

Cover Page



Universiteit Leiden



The handle <http://hdl.handle.net/1887/74054> holds various files of this Leiden University dissertation.

Author: Wit, M. de

Title: Advances in SQUID-detected magnetic resonance force microscopy

Issue Date: 2019-06-18

ADVANCES IN SQUID-DETECTED
MAGNETIC RESONANCE FORCE
MICROSCOPY

PROEFSCHRIFT

TER VERKRIJGING VAN
DE GRAAD VAN DOCTOR AAN DE UNIVERSITEIT LEIDEN,
OP GEZAG VAN RECTOR MAGNIFICUS PROF. MR. C.J.J.M STOLKER,
VOLGENS BESLUIT VAN HET COLLEGE VOOR PROMOTIES
TE VERDEDIGEN OP DINSDAG 18 JUNI 2019
KLOKKE 15:00 UUR

DOOR

MARTIN DE WIT

GEBOREN TE KATWIJK AAN ZEE
IN 1991

Promotor: Prof. dr. ir. T.H. Oosterkamp

Promotiecommissie: Dr. J.P. Davis (University of Alberta, Edmonton, Canada)
Prof. dr. J.A. Marohn (Cornell University, Ithaca, USA)
Prof. dr. E.R. Eliel
Dr. M.I. Huber
Prof. dr. J.M. van Ruitenbeek

Casimir PhD Series, Delft-Leiden 2019-14

ISBN 978-90-8593-400-4

An electronic version of this thesis can be found at <https://openaccess.leidenuniv.nl>

The work described in this thesis was performed at the Huygens - Kamerlingh Onnes Laboratory, Leiden University, Niels Bohrweg 2, 2333 CA, Leiden.

This research is funded by the Netherlands Organisation for Scientific Research (NWO).

The cover shows an abstract illustration of the mechanical vibration isolation, one of the main achievements of this research resulting from the close collaboration between the scientists and technicians in our lab. *Designed by Ilse Modder, www.ilsemodder.nl*

Copyright © 2019 Martin de Wit
Printed by: Gildeprint - Enschede

CONTENTS

1	Introduction	1
1.1	Development and applications of MRFM	2
1.2	Principles of MRFM	4
1.3	Sensitivity limit and the Oosterkamp approach	6
1.4	Thesis Outline	8
2	Instrumentation: Fermat and Yeti	11
2.1	Introduction.	12
2.2	MRFM detection chip	13
2.3	Cantilever	18
2.4	Fermat	21
2.5	Cryostat Yeti	32
3	Vibration isolation with high thermal conductance for a cryogen-free dilution refrigerator	37
3.1	Introduction.	38
3.2	Filter design.	39
3.3	Practical design and implementation	43
3.4	Experimental results	47
3.5	Conclusions	54
4	Feasibility of imaging in nuclear Magnetic Resonance Force Microscopy using Boltzmann polarization	57
4.1	Introduction.	58
4.2	Methods.	59
4.3	Frequency shifts measured in copper	67
4.4	Demonstration of volume sensitivity.	70
4.5	Imaging protons	72
4.6	Conclusions	76
4.7	Relevant NMR parameters of copper	77
4.8	Spin diffusion length for copper	77

5	Density and T_1 of surface and bulk spins in diamond in high magnetic field gradients	79
5.1	Introduction.	80
5.2	Methods.	81
5.3	Results and discussion	87
5.4	Summary and outlook	91
5.5	Vacuum properties of the cantilever	93
5.6	Fits with constant T_1 times	94
6	Flux compensation for SQUID-detected Magnetic Resonance Force Microscopy	95
6.1	Introduction.	96
6.2	Circuit and calibration	98
6.3	Results	101
6.4	Conclusions and outlook	103
7	Dissipation of the alternating magnetic field source	105
7.1	Introduction.	106
7.2	Calorimetry at mK temperatures	106
7.3	Characterization of dissipation.	110
7.4	Models for the origin of dissipation	113
7.5	Suggestions to reduce dissipation	120
7.6	Reducing the effects of dissipation.	121
7.7	Conclusions	122
8	Double-magnet cantilevers for increased magnetic field gradients	125
8.1	Introduction.	126
8.2	Intuition about magnetic field gradients.	127
8.3	Signal-to-noise ratio	129
8.4	Fabrication of double-magnet cantilevers	130
8.5	Magnetic field distribution	132
8.6	Enhanced coupling strength to pickup loop.	134
8.7	Spin-induced dissipation	135
8.8	Conclusions	139
9	Valorisation: the easy-MRFM	141
9.1	Necessity for a new characterization tool	142
9.2	Progress of the easy-MRFM	143
9.3	Future applications	146

A	Feedback cooling of the cantilever’s fundamental mode	147
A.1	Cantilever temperature and thermal noise force	148
A.2	Feedback cooling of the cantilever’s fundamental mode	151
B	Limitations of the mechanical generation of radio-frequency fields	155
B.1	Off-resonant coupling.	156
B.2	Non-linearities	158
B.3	Temperature dependence of quality factor	158
C	Quenching of SQUID modulation under radio-frequency interference	161
C.1	Quenched SQUID modulation	162
C.2	Possibilities	163
D	Fabrication recipes	165
D.1	Detection chip	166
D.2	Double layer resists for sputtering	167
D.3	Specific samples.	169
D.4	Considerations for double-layer detection chips	170
	Bibliography	173
	Samenvatting	193
	Curriculum Vitae	201
	List of Publications	203
	Acknowledgements	205

1

INTRODUCTION

In this thesis, we will cover some of the latest advances in Magnetic Resonance Force Microscopy, a technique that detects the tiny forces exerted by electrons or nuclei to obtain information about the structure or properties of a wide variety of samples. In this chapter, we give a coarse overview of the history of MRFM, followed by the motivation of the strategy followed by the Oosterkamp group to improve upon the existing technique. We end by giving an outline for the rest of this work.

1.1 DEVELOPMENT AND APPLICATIONS OF MRFM

The concept of Magnetic Resonance Force Microscopy was first described by Sidles, who envisioned MRFM as a technique that might resolve the structure of biological samples, such as proteins or virus particles [1]. Traditionally, these kinds of samples were studied using X-ray crystallography or Nuclear Magnetic Resonance (NMR) [2]. However, these techniques suffer from a number of drawbacks that limit the number of structures that can be resolved. As an example, NMR and the related Magnetic Resonance Imaging (MRI) use a radio-frequency magnetic field to excite the nuclear spins in a sample and measure their properties. The weak interactions between these fields and spins allow the samples to be investigated in a non-invasive way. However, the weak interaction also means that these techniques are inherently insensitive, and therefore require a large number of spins to generate a sufficiently large signal to be detected. Sidles suggested that the sensitivity of NMR could be enhanced by uniting it with Atomic Force Microscopy (AFM). This combined technique would use spin manipulation protocols from NMR, but the resulting state of the spins in the proteins would be detected by measuring forces using a mechanical resonator.

From this original conception in 1991, progress was quick. In 1992, the first Electron Spin Resonance (ESR) signal was detected by Rugar et al. [3], soon to be followed by the first successful imaging of a sample of the organic chemical compound DPPH with a lateral resolution of 5 μm [4]. Even though the signal from nuclear spins is almost three orders of magnitude smaller than that from electrons, the first nuclear MRFM experiment on protons was achieved in 1994, once again by Dan Rugar and colleagues at IBM [5]. Via the development of ever more sensitive cantilevers for the detection of the force signals [6, 7] and more sophisticated protocols to manipulate the spins [8–11], in 2004 single electron spin sensitivity was demonstrated [12]. With the goal of single electron spin resolution achieved, more effort was invested in optimizing the sensitivity for nuclear experiments [13, 14], including isotope-selective imaging [15]. The experiment that came closest to Sidles' original idea was performed in 2009, when Degen et al. managed to create a three-dimensional reconstruction of the Tobacco Mosaic Virus (TMV) with a spatial resolution better than 5 nm [16]. At the moment, the record for the spatial resolution (in one dimension) is set at 2 nm using a polystyrene-coated silicon nanowire [17]. Between 1992 and 2018, the sensitivity of MRFM has been improved by seven orders of magnitude, equivalent to a doubling of the sensitivity on average every 21 months during this period.

Note that during this development of imaging using MRFM, many groups often switched from the sample-on-tip geometry, in which the sample is attached to the cantilever and is then positioned near a small nanomagnet (pioneered by the IBM

group), to the magnet-on-tip geometry, in which the nanomagnet is attached to the cantilever and positioned near a sample (first used by Wago et al. [18] and Bruland et al. [19]), and back. In principle the sample-on-tip geometry has the best prospects for the application of imaging, as this approach is less sensitive to effects that reduce the quality factor of the cantilever, and higher magnetic field gradients can be achieved using surface-mounted nanomagnets. For this reason, this was the geometry used for the TMV experiment. However, this geometry severely limits the generality of the samples that can be investigated. The desire for generality favors the magnet-on-tip geometry, since having the sample on a surface other than the cantilever allows for more flexibility in terms of sample preparation.

Recent progress towards imaging has been slow compared to the early years. When we take the work by Mamin et al. on CaF_2 from 2007 as an intermediate benchmark, we find that in the period 1992-2007 the sensitivity doubled on average every 15 months, while in the period 2007-2018 this only happened every 51 months. It took 9 years for a group to improve upon the 5 nm resolution achieved in the TMV experiment. As is often the case with new technologies, the initial steps to increase the performance are clear and significant. However, keeping up the high rate of progress is extremely challenging, and it is unclear how to move from the ideal proof-of-principle systems to the real-world samples. Furthermore, imaging based on MRFM seems to have lost momentum compared to other techniques, such as (three-dimensional) electron microscopy techniques [20–24] and (scanning) NV-centers [25–27].

Now, this is not to say that MRFM has run its course. An alternative application of MRFM has gained popularity, namely to investigate condensed matter samples. Research is done on a variety of phenomena, such as ferromagnetic resonance [28–31], spin diffusion in strong field gradients [32–34], and spin-lattice relaxation times in small samples [35–37]. In our group, we try to take advantage of our low operating temperatures in combination with the capability to measure sub-surface effects. For these reasons, Wagenaar has suggested experiments on LAO-STO, high-temperature superconductors, and 3D topological insulators [37, 38].

1 1.2 PRINCIPLES OF MRFM

To understand the main principle of MRFM, we can simply deconstruct the name of the technique:

MAGNETIC: Consider a single spin with magnetic moment $\mu_s = S\hbar\gamma$, where S is the spin quantum number, \hbar is the reduced Planck constant, and γ is the gyromagnetic ratio, an isotope-dependent constant. For simplicity we will consider spins with $S = 1/2$, as is the case for electrons and protons. When we place the spin in a static magnetic field B_0 , the spin aligns either parallel (“up”) or anti-parallel (“down”) to this field, where the anti-parallel state has a slightly higher energy than the parallel state, with the energy difference given by $\Delta E = 2\mu_s B_0$.

RESONANCE: The spin can be manipulated using an alternating magnetic field B_1 (also called B_{RF}), but only when the frequency of this field matches the Larmor frequency of the spin, given by $\omega_L = \gamma|B_0|$. Equivalently, one can say that the energy of the pulse has to match the energy difference between the spin states. When the spin is positioned in the proximity of a small magnetic particle, the B_0 field varies spatially, which means the Larmor frequency of the spin becomes a function of position with respect to the magnetic particle. In that case, the frequency of the B_1 field, ω_{RF} , can be used to determine the distance of the spin to the magnetic particle.

FORCE: The magnetic moment of the spin is detected via the force it exerts when placed in a magnetic field gradient, such as the one created by the a small magnetic particle. The force is then given by $F = \mu_s (\nabla \cdot \mathbf{B}_0) \equiv \mu_s G$. In a field gradient $G = 0.1$ MT/m, the force exerted by a single spin ranges from 10^{-21} N for nuclear spins to 10^{-17} N for electron spins. These minute forces are detected by placing either the sample or the magnet at the end of a very soft cantilever. The force exerted by the sample on the tip results in a displacement of the cantilever tip, which can be detected using, for instance, a laser reflecting from the surface of the cantilever.

MICROSCOPY: The principles outlined above for the detection of a single spin remain valid when we consider an ensemble of spins. Again, the spins will align in the B_0 field either in the up or down state, where the population difference between the states is dictated by the Boltzmann polarization. For $S = 1/2$ particles, the equilibrium distribution follows from statistical mechanics, and is described by $N_+/N_- = e^{-(\mu_s B_0/k_B T)}$,

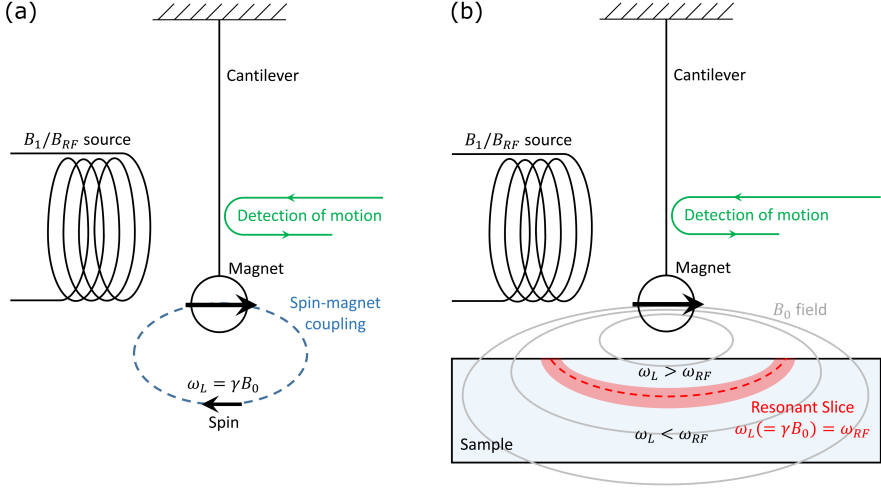


Figure 1.1: (a) Schematic of the MRFM setup and a single spin. The vital components of the setup are shown: the cantilever, B_1 field source, a detection mechanism (e.g. laser interferometer), and a small magnetic particle. (b) Schematic of the MRFM setup indicating the resonant slice, the region in space where $\omega_{RF} = \gamma B_0$.

where N_+/N_- is the ratio of spin up to spin down, $k_B = 1.38 \cdot 10^{-23}$ J/K is the Boltzmann constant, and T is the temperature of the spin ensemble. The signal now originates from all spins within the volume of space where $\gamma B_0 = \omega_{RF}$, the so-called resonant slice. This means that the spatial location of the addressed spins can be controlled by changing the frequency of the B_1 field, or by changing the position of the sample with respect to the magnet. It is possible to make a three-dimensional image of the sample by measuring the force signal for various positions of the magnet with respect to the sample. The resulting force map can be translated to a spin-density map using a deconvolution procedure [16, 39, 40]. The high field gradients mean that this reconstruction can have a spatial resolution as small as several nanometers.

The described measurement principle is shown in Fig. 1.1. The figure shows the so called “magnet-on-cantilever” geometry that is used in the rest of this thesis. Fig. 1.1(a) shows the vital components of an MRFM setup: a soft cantilever as force sensor, a source for the B_1 field required to manipulate the spin, a detection mechanism to read out the motion and properties of the cantilever, and a small magnet to generate large magnetic field gradients which are the origin of the force interaction, and give MRFM its high spatial resolution. In our case, the small magnet is also responsible for the generation of the B_0 field, as we do not apply an additional external magnetic field. Fig. 1.1(b) shows an example of a resonant slice. Only spins within this slice are resonant with the applied B_1 field and contribute to the signal.

1.3 SENSITIVITY LIMIT AND THE OOSTERKAMP APPROACH

As MRFM is inherently a force-detection technique, the fundamental limit for the sensitivity is set by the thermal force noise. The thermal force noise for a cantilever is given by:

$$\sqrt{S_F} = \sqrt{4k_B T \Gamma BW} = \sqrt{4k_B T \frac{k_0}{\omega_0 Q} BW}, \quad (1.1)$$

where Γ is the damping rate, k_0 is the stiffness of the cantilever, $\omega_0 = 2\pi f_0$ is its resonance frequency, Q is the quality factor, and BW is the measurement bandwidth. This force noise induces thermal fluctuations of the cantilever position as well as frequency noise. Using the force exerted by a magnetic moment in a magnetic field gradient we find that the minimal detectable magnetic moment in a unit bandwidth is given by:

$$\mu_{\min} = \frac{1}{G} \sqrt{4k_B T \frac{k_0}{\omega_0 Q}} \quad (1.2)$$

From this equation, it is clear that there are several routes to take if one wants to increase the sensitivity of MRFM. First, one should maximize the magnetic field gradients, which range from about 0.1 - 30 MT/m [19, 41, 42]. We take a closer look at how to maximize the magnetic field gradient in Ch. 8. Second, one has to use a cantilever with extreme dimensions (very long, very thin, and narrow) to minimize k/ω_0 , and with a very low intrinsic damping to obtain a high quality factor. This last requirement is often at odds with the demand that cantilevers are thin [43]. Finally, the temperature of the resonator has to be as low as possible, as this means a lower average thermal energy.

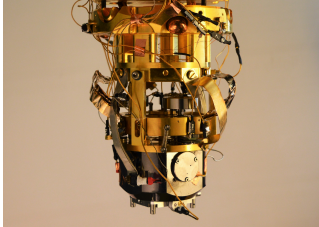
THE OOSTERKAMP APPROACH: Our main focus is to reduce the operating temperature of the MRFM setup. The low temperature not only reduces the force noise, but is also useful for reducing the relaxation rates of spins and increasing the Boltzmann polarization, and thereby the signal when Boltzmann-based protocols are used (as discussed in Ch. 4). There are multiple MRFM setups in the world that are operated in a dilution refrigerator, but this is not enough to achieve true milliKelvin temperatures in full operation. Several technical innovations to the setup are required to achieve this:

- The temperature of the cantilever in conventional MRFM is limited by the power input from the laser used for the read-out of the cantilever motion. Even for incident laser powers as low as 1 nW, no effective cantilever temperatures below 100 mK have been reported using laser read-out [44–46]. For this reason, we have implemented a SQUID-based detection scheme. Here the motion of the cantilever is measured using a superconducting pickup loop connected to a SQUID that detects the flux changes from the moving magnet at the end of the cantilever. Using this scheme, cantilever temperatures below 20 mK have been achieved [47, 48]. Details about this scheme are given in Ch. 2.
- Apart from thermal fluctuations, the cantilever can also be excited by mechanical vibrations, for instance originating from the cryostat. A sophisticated vibration isolation is required to provide sufficient attenuation of external vibration at the cantilevers resonance frequency. However, often the (soft) vibration isolation reduces the thermal conductance between the MRFM setup and the cooling mechanism, e.g., the mixing chamber of a dilution refrigerator. Therefore, we have developed a mechanical vibration isolation that combines good vibrational properties with a high thermal conductance, as discussed in Ch. 3.
- It has proven very challenging to generate B_1 fields of sufficient amplitude for many MRFM protocols without significant dissipation. We have attempted to reduce this dissipation by using a superconducting microwire as source for the B_1 field [37, 49]. Furthermore, we have developed a method for the mechanical generation of RF fields using the higher modes of the cantilever [50]. This approach will be further discussed in Ch. 4.

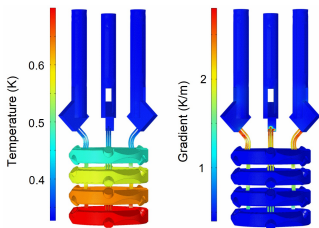
Using these technical innovations, the Oosterkamp group currently has the only operational setup in which a temperature down to 20 mK for both the cantilever and the sample is achieved during MRFM experiments. However, it has been found that the low temperatures also pose significant challenges. Spin-mediated dissipation of the cantilever energy, resulting in lower quality factors, is an increasingly important effect at lower temperatures [34, 51, 52]. Furthermore, even though we use a superconducting RF source, significant dissipation is observed even for modest RF amplitudes and frequencies, as discussed in Ch. 7.

1.4 THESIS OUTLINE

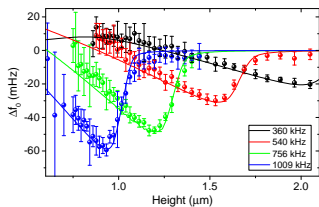
The thesis is structured as follows.



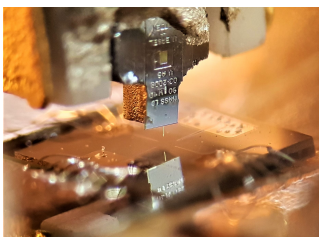
CHAPTER 2 introduces the experimental setup. It covers the most important components, such as the detection chip and the magnetically-tipped cantilever. The cantilever's response to a driving force is described starting from the equations of motion. Subsequently, it covers the positioning stages and methods, and the modifications made to the dilution refrigerator.



CHAPTER 3 presents the newly developed vibration isolation. It starts from a general design principle based on the analogy between electrical and mechanical filters, followed by a detailed account of the final implementation. The effectiveness is shown using SQUID vibration spectra and the cantilever's thermal properties.

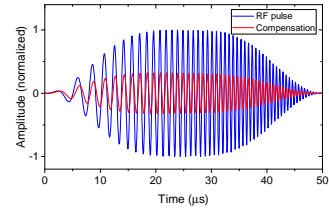


CHAPTER 4 shows the feasibility of Boltzmann-polarization-based imaging in MRFM. We study the time-dependent behaviour of both on- and off-resonant spins when excited by RF magnetic fields. The results are confirmed using frequency shift signals measured using the mechanical generation of RF fields. A volume sensitivity of $(40 \text{ nm})^3$ is achieved. We end with estimates of the expected volume resolution for a proton sample.

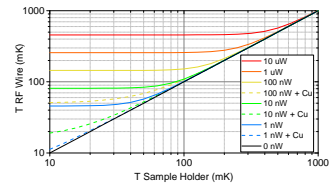


CHAPTER 5 is devoted to the study of surface and bulk spins in diamond. Ultra sensitive magnetic force microscopy at milliKelvin temperatures reveals that a high magnetic field gradient suppresses spin diffusion, increasing relaxation times of surface spins. The technique offers a valuable tool for characterizing dilute spin systems, which could yield insight on how to reduce dissipation in qubits and other nanodevices.

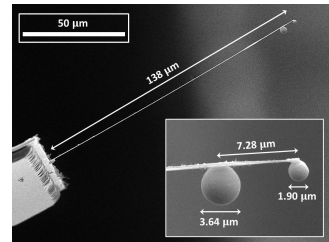
CHAPTER 6 describes the developed flux compensation scheme used to reduce the crosstalk between the SQUID-based read-out and the generated RF fields. The full electrical scheme of the RF- and detection circuits is described, together with the operation principle and calibration methods for the compensation. The effectiveness of the cancellation of flux crosstalk is shown by comparing the performance of the SQUID (i.e. modulation depth and noise) with and without an active compensation scheme.



CHAPTER 7 contains calorimeter measurements of the dissipated power when an RF current is passed through a superconducting RF wire. Various sources of dissipation are discussed, such as eddy currents induced in surrounding metals and flux-vortex flow in the superconductor itself. The chapter concludes with a number of suggestions to reduce the dissipated power and to limit the resulting increase in the temperature of the detection chip and sample.



CHAPTER 8 reports on our attempts to obtain higher magnetic field gradients whilst reducing the typically associated drawbacks. It is based on cantilevers with two affixed magnets, one with a small diameter to increase the maximum field gradient and thereby the spin signal, and one with a larger diameter several micrometers away from the tip of the cantilever to maintain a high coupling to the detection mechanism. The chapter presents the basic scaling laws concerning the magnet radius, and calculations of the expected influence on the MRFM experiment.



CHAPTER 9 concludes the thesis with a description of the progress of the easy-MRFM. The proof-of-principle is given, together with suggestions to improve the performance. This new device could make the technique of MRFM more widely available for other research groups, and could shed light on some of the big issues currently plaguing many nanodevices.



2

INSTRUMENTATION: FERMAT AND YETI

In this chapter, we cover all vital components of the new MRFM setup (Fermat) and the cryostat in which it was operated (Yeti). The chapter is intended to explain the design choices made for the various components. Hopefully, this will enable future operators to understand the design of the setup in detail and to prevent them from repeating our mistakes. This may guide them to further improve MRFM.

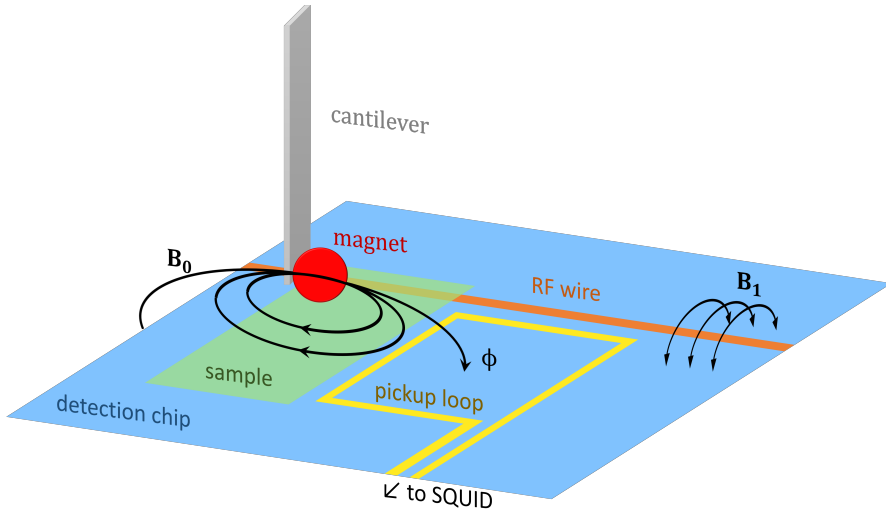


Figure 2.1: Operating principle of the SQUID-detected low temperature MRFM setup as used in the Oosterkamp group. Spins in a sample can be investigated via their coupling to an ultrasoft magnetically-tipped cantilever, the motion of which is measured using a superconducting pickup loop.

2.1 INTRODUCTION

In this work, we have designed and operated a new MRFM, based on the old system used in our group [38, 53, 54]. The name of the new MRFM is Fermat. The philosophy behind the setup is based on the idea of a low operation temperature, as introduced in Ch. 1. The main components of the MRFM are shown in Fig. 2.1. The system is based on an ultrasoft cantilever with a small magnetic particle attached to the unclamped end. This magnet is approached to within a micrometer of the sample located on a detection chip. The magnetic field originating from the magnet couples to the spins in the sample, which leads to a static force due to the polarization of the spins. An RF wire is used to apply radio-frequency pulses to alter the magnetization of the spins, and thereby the force acting on the magnet and cantilever. This results in changes in the amplitude or resonance frequency of the cantilever. A pickup loop is used to detect the motion of the cantilever through the position-dependent flux induced by the magnet. This flux is then sent to a DC-SQUID for ultra sensitive detection.

The magnetic field originating from the magnet is called the B_0 field, in analogy to conventional NMR. The B_0 field is used to create the Boltzmann polarization of

the spins in the sample. Furthermore, the small radius of the magnet results in large magnetic field gradients, which can be as large as $1 \text{ T}/\mu\text{m}$. These magnetic field gradients create a distribution of Larmor frequencies in the sample. This allows one to select which spins are affected by the RF pulse by choosing the pulse frequency accordingly, which is the basis for high resolution magnetic resonance imaging. The magnetic field created using the RF wire is typically labeled B_1 (following the NMR convention) or B_{RF} .

In this chapter, we discuss the most relevant components of the new MRFM setup Fermat and the dilution refrigerator Yeti in which it is operated. We start by considering the latest design for the detection chip, followed by the properties of the cantilever. Then we discuss the mechanical details of Fermat, with emphasis on the positioning and detailed design aspects. We finish by briefly showing the dilution refrigerator in which the MRFM is installed, with a focus on the vibration isolation.

2.2 MRFM DETECTION CHIP

As indicated in Fig. 2.1, we rely on a SQUID-based detection scheme. A vital component in this is the so-called detection chip. The detection chip is typically made of high-resistivity silicon with a native oxide¹, on top of which we have fabricated a pickup loop and RF wire. The pickup loop and RF wire are fabricated starting from a 350-400 nm thick NbTiN layer, grown by D.J. Thoen from the Technical University of Delft [55]. The detailed cleanroom recipe used for the fabrication can be found in appendix D. A scanning electron microscopy image of the latest generation of detection chips is shown in Fig. 2.2. In order to understand the full design of the detection chip, several considerations have to be taken into account, some of which we will discuss here.

RF WIRE: The central part of the RF wire is a $300 \mu\text{m}$ long segment with a width of $1.0 \mu\text{m}$ and a thickness of about 300 nm . The decision to go for a width of $1 \mu\text{m}$ was a compromise between a desired low current density, for which a wide RF wire is necessary, and minimal Meissner effect, which was shown to lead to serious deflections of the cantilever when it is brought close to the RF wire [53]. For these dimensions, we have measured a direct critical current $I_C = 28.3 \text{ mA}$ at 4.2 K , corresponding to a critical current density of about $9 \cdot 10^6 \text{ A}/\text{cm}^2$, similar to what is found in literature for high quality NbTiN [56]. When we approximate the shape of the RF wire as an

¹Exception: the diamond detection chip used in Ch. 5

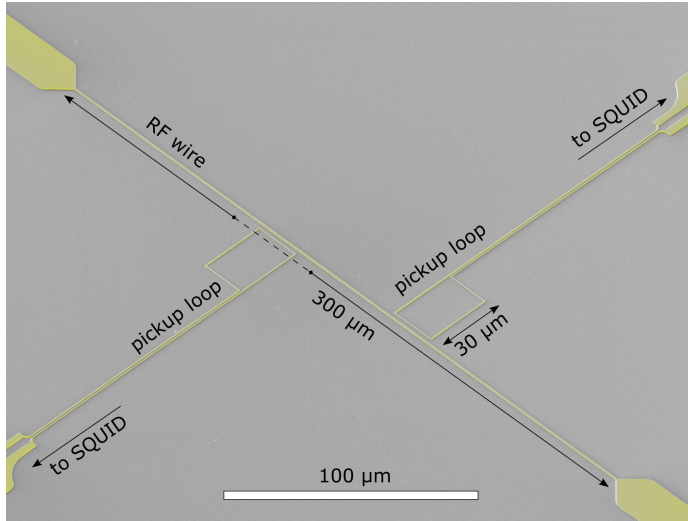


Figure 2.2: Scanning electron microscope image of the detection chip, taken with a tilt angle of 45 degrees. The NbTiN RF wire and pickup loops are shown in yellow. Samples should be placed close to the RF wire for maximal B_{RF} , and close to the pickup loop for minimal detection noise.

infinitely thin wire of infinite length, the magnetic field at a distance r from the wire is given by:

$$B_{\text{RF}}(r) = \frac{\mu_0 I}{2\pi r} \quad (2.1)$$

Thus, a maximum current of 28 mA can be used to generate a rotating frame magnetic field of 2.8 mT at a distance of 1 μm from the center of the RF wire. Note that the approximation for the shape of the wire breaks down when the distance to the wire becomes similar to the width. A field of 2.8 mT would be just enough to perform MRFM experiments on CaF_2 based on the cyclic inversion of the fluoride spins [57]. More properties of the RF wire and connecting circuit are discussed in detail in Ch. 7. In this chapter we also consider the measured dissipation on the RF wire, and discuss possible origins.

PICKUP LOOP: The detection of the motion of the cantilever is done by measuring the flux induced in a pickup loop by the magnetic field originating from the magnet at the end of the cantilever. The pickup loop is made of the same NbTiN as the RF wire in the same fabrication procedure. Once again, we want to minimize the Meissner repulsion between the magnet and superconducting lines. Therefore the lines of the pickup loop have a width of only 500 nm. The latest design for the pickup

loop is a single turn loop with dimensions $20 \times 30 \mu\text{m}^2$. The pickup loop is placed at a distance of $2.5 \mu\text{m}$ from the RF wire, as this would allow MRFM experiments as close to the RF wire as possible while at the same time having a strong flux coupling to the pickup loop for minimal detection noise. The downside of placing the pickup loop this close to the RF wire is an increase in the flux crosstalk resulting from the generated B_{RF} . However, a flux compensation scheme has been developed to counter this flux crosstalk, as discussed in Ch. 6. Preferably, the pickup loop is placed even closer to the RF wire.

The coupling between the pickup loop and the magnet on the end of the cantilever is straightforward to calculate. In the presence of a magnetic field \mathbf{B} , the flux through a loop is given by

$$\Phi_p = \int \mathbf{B} \cdot d\mathbf{a} = \int (\nabla \times \mathbf{A}) \cdot d\mathbf{a}, \quad (2.2)$$

where the integral is over the entire area of the pickup loop, and in the second step we have rewritten the magnetic field in terms of the vector potential \mathbf{A} . We can use the Curl Theorem to simplify the calculation:

$$\Phi_p = \oint \mathbf{A} \cdot d\mathbf{l} \quad (2.3)$$

Now the calculation is reduced to some relatively simple line integrals, given that the vector potential is known. When we assume the magnet to be perfectly spherical, an assumption that is justified in Sec. 2.3, from a magnetic point of view it can be described as a perfect dipole with a certain magnetic dipole moment \mathbf{m} . Then, the vector potential is given by[58]:

$$\mathbf{A}_{\text{dip}}(\mathbf{r}) = \frac{\mu_0}{4\pi} \frac{\mathbf{m} \times \hat{\mathbf{r}}}{r^2} = \frac{\mu_0}{4\pi} \frac{\mathbf{m} \times \mathbf{r}}{r^3} \quad (2.4)$$

Clearly, the precise coupling depends on the position and direction of magnetization of the magnetic particle with respect to the pickup loop.

2.2.1 Detection circuit

The induced flux in the pickup loop now has to be transferred to the SQUID. For this, we use a two-stage detection system, as was described in detail by Wijts (2013) [53]. The idea behind using a two-stage detection system is to reduce the inductance mismatch between the low inductance pickup loop and the relatively large inductance of the SQUID input coil and the wires connecting the pickup loop to the SQUID input coil. This is done by inserting an intermediary transformer with L_{f1} and L_{f2}

	Parameter	Value
L_p	inductance pickup loop	0.08 nH
L_{par}	parasitic inductance	1-2 nH
L_{f1}	primary inductance flux transformer	0.72 nH
L_{f2}	secondary inductance flux transformer	360 nH
L_{in}	inductance SQUID input coil	150 nH
L_c	inductance calibration transformer	5 nH
κ_f	flux transformer coupling parameter	~ 0.9
M_f	mutual inductance flux transformer	14.5 nH
M_i	mutual inductance SQUID input coil	2.44 nH

Table 2.1: definition of the symbols from Fig. 2.3, and the actual values as used in the Fermat setup, where we use Magnicon two-stage current sensor C70M116W and the Minigrail style transformer.

the inductances of the primary and secondary coils of the transformer. The schematic of the circuit is shown in Fig. 2.3. The induced flux in the SQUID Φ_{SQ} resulting from a flux Φ_p in the pickup loop for this system is given by:

$$\Phi_{\text{SQ}} = \frac{M_f M_i}{L_1 L_2 - M_f^2} \Phi_p, \quad (2.5)$$

with L_1 the inductance of the pickup loop circuit, given by $L_1 = (L_p + L_{\text{par}} + L_{f1})$, with L_{par} the parasitic inductance of the bonding wires between the pickup loop and the transformer. L_2 is the inductance of the SQUID input coil circuit, given by $L_2 = (L_{f2} + L_c + L_{\text{in}})$, where we neglect the parasitic inductance in this circuit. L_c is the inductance of the calibration transformer that can be used to inject flux into the SQUID input coil circuit for calibration or crosstalk compensation. The mutual inductance of the flux transformer is given by $M_f = \kappa_f \sqrt{L_{f1} L_{f2}}$, with $\kappa_f \sim 0.9$ the transformer coupling parameter. All symbols and corresponding values (when possible) are given in Table. 2.1. Depending on the estimated value for the parasitic inductance and the coupling parameter, inserting these numbers into Eq. 2.5 results in a flux transfer efficiency of about 3-4%. We can derive a similar equation for the coupling between the calibration circuit and the SQUID, which we can consider as a single-stage system due to the 1:1 transformer:

$$\Phi_{\text{SQ}} = \frac{M_i}{L_{f2} + L_c + L_{\text{in}}} \Phi_{\text{cal}}, \quad (2.6)$$

for which we then find a flux transfer efficiency of 0.47%.

In the actual experiment, the detection chip, flux transformer, and SQUID chip carrier² are placed right next to each other, and interconnected with as many parallel wirebonds as possible to reduce the parasitic inductance. The SQUID input coil can

²Magnicon CAR-1

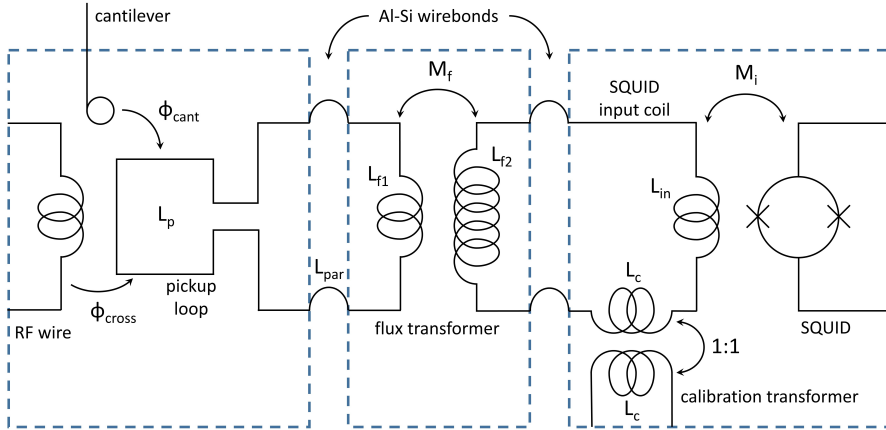


Figure 2.3: Schematic of the circuit used for the SQUID-based detection scheme. The flux in the pickup loop originating from the magnet on the cantilever or from the RF wire is transferred via a gradiometric flux transformer to the SQUID input coil. The calibration transformer can be used to calibrate the cantilever-pickup loop coupling or to compensate flux crosstalk.

be connected via two niobium terminals. The SQUID response is measured using NbTi in CuNi wiring connected to the Magnicon SQUID electronics³. The output of the SQUID electronics is connected via an SR560 low noise voltage preamplifier to a data acquisition card (DAQ).

MULTILAYER FABRICATION: There is plenty of room for improvement of the detection chip. Efforts have been made to create multilayer NbTiN detection chips, as discussed by de Voogd (2017) [59]. These initial attempts were unsuccessful, probably due to contamination of the second NbTiN layer, which resulted in extremely low critical current densities⁴. However, fine tuning this fabrication process would offer two interesting possibilities: First of all, the ability to make gradiometric pickup loops or pickup loops which cross the RF wire can be used to significantly reduce flux crosstalk from the RF wire. This would allow for experiments to be done much closer to (or on top of) the RF wire, resulting in higher B_{RF} fields at the position of the sample. Secondly, creating an optimized on-chip transformer would drastically reduce the parasitic inductance, which could lead to a more than 10-fold increase of the flux coupling between the pickup loop and the SQUID.

³Magnicon XXF-1

⁴Tests of the first generation of multilayer devices in liquid helium showed critical current densities below 10^4 A/cm².

2.3 CANTILEVER

The final sensitivity of the MRFM experiment is mainly dominated by the properties of the cantilever used to detect the forces. One of the most commonly used cantilevers in the MRFM community was developed by Chui et al. at IBM [7]. It was the cantilever of choice in some of the most significant achievements of MRFM [12, 14, 16], and also the one traditionally used in our group. This type of cantilever is made from single crystal silicon. It is 100 nm thick and has a (constant) width of 5 μm . The cantilevers are produced in three different lengths: 140, 170, and 200 μm . The choice for the dimensions of the cantilever is mainly determined by the desire for a low intrinsic damping and low spring constant, the latter of which is given by [60]

$$k_0 = \frac{1}{4} \frac{Ewd^3}{l^3}, \quad (2.7)$$

with w , d , and l the width, thickness, and length of the cantilever, respectively, and E the Young's modulus of the material, a value which for silicon is reported to be between 160 and 200 GPa, depending on the crystal orientation [61]. An additional factor of 1.030 might be added to equation 2.7, to indicate that the fundamental flexural mode is 3% stiffer than a beam that is statically bent [62].

Inserting all values for our cantilevers, taking a Young's modulus of 180 GPa for silicon, Eq. 2.7 leads to a theoretical bare spring constant of 30 to 80 $\mu\text{N/m}$, depending on the selected length. Furthermore, the IBM type cantilevers are known to have very low intrinsic damping, typically on the order of 10^{-13} kg/s [38, 63].

ALTERNATIVES: In the search for an alternative to the single crystal silicon cantilevers⁵, we have investigated the low temperature properties of silicon nitride (Si_3N_4) cantilevers. High stress silicon nitride is well known for its extremely low damping, and has been used to make MHz frequency drum resonators with Q-factors exceeding 10^8 [64]. The high quality factors are typically attributed to the fact that most of the dissipation in Si_3N_4 is related to deformations and bending of the material. This is suppressed by placing the material under high in-plane stress. It was hoped that the damping remains low for soft Si_3N_4 cantilevers. The Si_3N_4 cantilevers were manufactured by NuNano, and can be ordered with extremely low specified spring constants, even well below 1 $\mu\text{N/m}$. We have investigated cantilevers with a specified spring constant of 20 $\mu\text{N/m}$.⁶

⁵Not only is our stock dwindling, we have observed whisker-like residue on the surface of the cantilever, which we fear might reduce the quality factors.

⁶NuNano Ltd, NuVOC series SELECT100-H. Dimensions 130 x 1 x 0.1 μm^3 , unloaded resonance frequency 8 kHz.

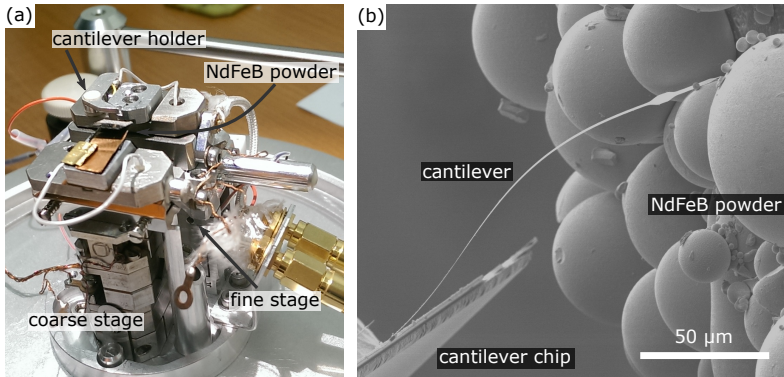


Figure 2.4: (a) Photo of the home-built nanomanipulator, with the main components labeled. (b) SEM image of a cantilever in contact with the NdFeB powder on the nanomanipulator just before starting the EBID.

At a base temperature of 40 mK, we observed a quality factor of $2.6 \cdot 10^4$ at a resonance frequency of 1644 Hz, similar to the single crystal cantilevers. In this respect, as well as in terms of the force sensitivity, the silicon nitride cantilevers appear to be a viable alternative to the IBM type cantilevers [65]. However, it should be noted that the electrical resistivity of Si_3N_4 is expected to be orders of magnitude larger than that of the silicon used for the IBM cantilevers [66]. This was evident while imaging the cantilever with the Scanning Electron Microscope (SEM), where charging of the cantilevers posed a challenge [67]. As this charging might lead to electrostatic non-contact friction of the cantilever [68], this could be a serious drawback of using silicon nitride. For this reason, all experiments described in this thesis were performed using the IBM type single crystal silicon cantilevers.

2.3.1 Attaching magnets

In the Oosterkamp group, we use the magnet-on-cantilever approach to do MRFM experiments. We attach these micrometer-sized magnets in a SEM using a nanomanipulator [69] (see Fig. 2.4(a)). We use this manipulator to approach the cantilever towards a $\text{Nd}_2\text{Fe}_{14}\text{B}$ powder⁷. A micron-sized spherical particle from this powder is attached using Electron Beam Induced Deposition (EBID) of platinum. After the particle has been attached, it is magnetized in the desired direction in a 5 T field at room temperature. The expected remanent magnetization of the particle after this process is about 1.3 T [70]. The process can be seen in figure 2.4 (b).

⁷Magnequench, MQP-S-11-9

The resonance frequency can be determined within the SEM by driving the cantilever electrostatically. By measuring the resonance frequency before and after the magnetic particle is attached, the spring constant of the cantilever can be determined using the added mass method[60]. The resonance frequency of a cantilever loaded with a known additional mass m_a is given by

$$f_{\text{loaded}} = \frac{1}{2\pi} \sqrt{\frac{k_0}{m_{\text{bare}} + m_a}} \quad (2.8)$$

By using that $m_{\text{bare}} = k_0/(2\pi f_{\text{bare}})^2$, we can rewrite Eq. 2.8 in term of the spring constant to obtain

$$k_0 = (2\pi)^2 \frac{m_a}{\left(\frac{1}{f_{\text{loaded}}^2} - \frac{1}{f_{\text{bare}}^2}\right)} \quad (2.9)$$

The value for the stiffness obtained from this measurement can be compared with the numerical result of Eq. 2.7 and with finite element analysis.

2.3.2 Description of the cantilever motion

Nearly all MRFM measurements are done by driving the cantilever with a small amplitude near the resonance frequency, either using electrostatic interactions, a piezoelectric element, generated magnetic fields [50], or by the spins directly [71]. In all these cases, the motion of the cantilever is well-described by a simple damped-driven harmonic oscillator, with an equation of motion given by

$$F_{\text{ext}} = m\ddot{x} + \Gamma\dot{x} + k_0x, \quad (2.10)$$

where F_{ext} is the force exerted on the cantilever, m the effective mass, and Γ the damping rate of the resonator. Assuming a sinusoidal driving force, $F_{\text{ext}}(\omega) = F_0 e^{i\omega t}$, the amplitude of the steady-state oscillation is given by:

$$A(\omega) = \frac{F_0}{k_0} \frac{\omega_0^2}{\sqrt{(\omega_0^2 - \omega^2)^2 + \left(\frac{\omega_0\omega}{Q}\right)^2}}, \quad (2.11)$$

with $\omega_0 = 2\pi f_0 = \sqrt{\frac{k_0}{m}}$, and Q the quality factor, given by $Q = m\omega_0/\Gamma$.⁸

It is now easy to see why MRFM is capable of detecting such minuscule forces. First of all, the low spring constant means that a small force is converted to a large

⁸The quality factor Q is formally defined as 2π times the energy stored in the resonator divided by the energy lost per oscillation cycle.

amplitude⁹. Secondly, we can compare the amplitudes of the cantilever when driven on-resonance ($\omega = \omega_0$) and off-resonance. We then find that when an external force, for example a spin signal, is on-resonance with the cantilever, it leads to an amplification of the amplitude equal to the quality factor, which can be greater than $5 \cdot 10^4$ for the type of cantilevers used.

When we look at frequencies close to the resonance frequency ($\omega_0 \approx \omega$) and at a high quality factor cantilever with low damping ($\Gamma/2m \ll \omega_0$), Eq. 2.11 can be approximated by

$$A(\omega) \simeq \frac{F_0}{k_0} \frac{\omega_0/2}{\sqrt{(\omega_0 - \omega)^2 + \left(\frac{\omega_0}{2Q}\right)^2}}, \quad (2.12)$$

which shows that when measuring the transfer function of the cantilever, the square of the signal can be fitted by a Lorentzian function to obtain the relevant properties of the resonator.

Alternatively, one can fit the phase instead of the amplitude to obtain the same properties. While sweeping the frequency over the resonance frequency, the phase changes by π . The measured phase curve can be fitted to the following equation: [72]

$$\phi(\omega) = \phi_0 + \arctan \left[2Q \left(1 - \frac{\omega}{\omega_0} \right) \right] \quad (2.13)$$

which directly indicates that the slope of the linear regime close to the resonance frequency is proportional to the Q-factor. An example of a typical measurement of the properties of the cantilever, including a combined fit to the square of Eq. 2.12 and to Eq. 2.13, can be seen in Fig. 2.5.

2.4 FERMAT

The detection chip and cantilever discussed in the previous sections are placed in the new MRFM setup, named Fermat. A schematic of Fermat with the most important components labeled is presented in Fig. 2.6(a). In this section we discuss these components one by one. We start by considering the cantilever holder. Secondly, we discuss the positioning system, which consists of the piezoknob-based coarse positioning stage, and the piezostack-based finestage. Here we will look at both the mechanics

⁹Assuming a detection noise floor of $10 \text{ pm}/\sqrt{\text{Hz}}$, femtoNewton forces can be detected

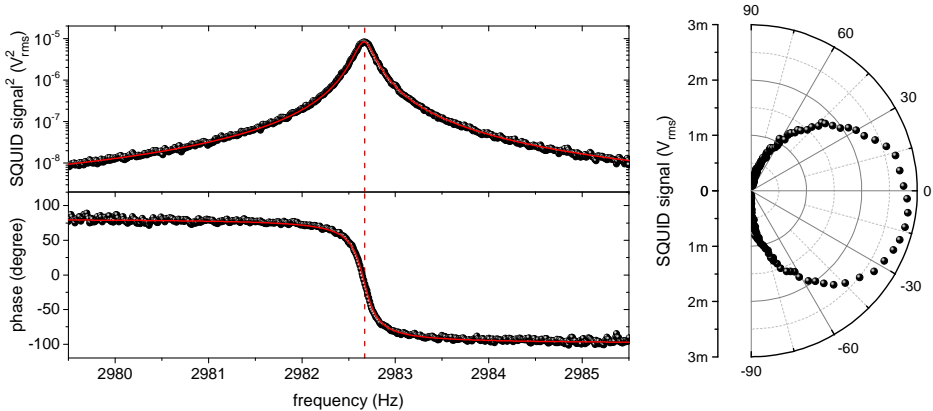


Figure 2.5: Measurement of the transfer function of a cantilever. (Top left) the amplitude and (bottom left) phase of the SQUID signal versus the piezo drive frequency. The solid red lines are fits according to the square of Eq. 2.12 and to Eq. 2.13, the dashed red line indicates the resonance frequency. On the right, the data from the figures (a) and (b) are plotted in a polar plot, where a harmonic oscillator gives a circle. For this particular measurement, $f_0 = 2982.67$ Hz, and $Q = 14.5 \cdot 10^3$.

as well as how to determine the position of the cantilever with respect to the sample. Finally, we discuss the sample holder and thermalization. A photograph of the fully assembled MRFM is shown in Fig. 2.6(b).

2.4.1 Cantilever holder

The cantilever, described in Sec. 2.3, is mounted at the end of the cantilever holder, shown in Fig. 2.7. The bulk of the cantilever holder is made of gold-plated bronze because of its high stiffness and reasonable thermal conductance at low temperatures. At the end of the holder, a small slot houses a piezoelectric element¹⁰. This piezo is electrically insulated from the rest of the cantilever holder, and is capped by a thin metal plate to reduce stray electric fields.

The cantilever is placed in a PEI holder glued to the top of the piezo, and held in place using a brass leaf spring. This leaf spring, in turn, is clamped rigidly into a copper core inside the bronze housing. The copper core is electrically insulated from the housing by a thin layer of stycast. A silver wire can be attached to the end of the copper core, which is used to thermalize the cantilever and to apply a voltage bias to the cantilever. This last feature can be useful when charging of the cantilever or

¹⁰PI PL022.31 PICMA-Chip Ceramic Insulated Piezo Actuator

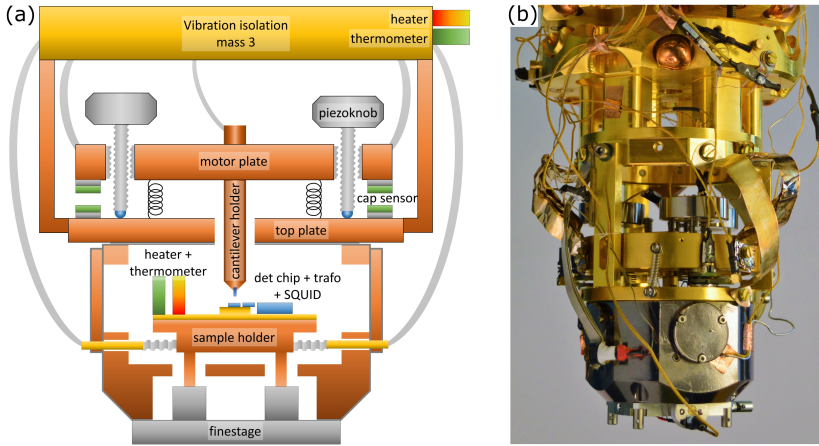


Figure 2.6: (a) Schematic overview of Fermat, with the most important components labeled. In this section, we will discuss in detail the cantilever holder, positioning (piezoknobs + finestage), and sample holder. (b) Photograph of Fermat as it was operated in the summer of 2018, during which the data for Ch. 3 and Ch. 4 were obtained.

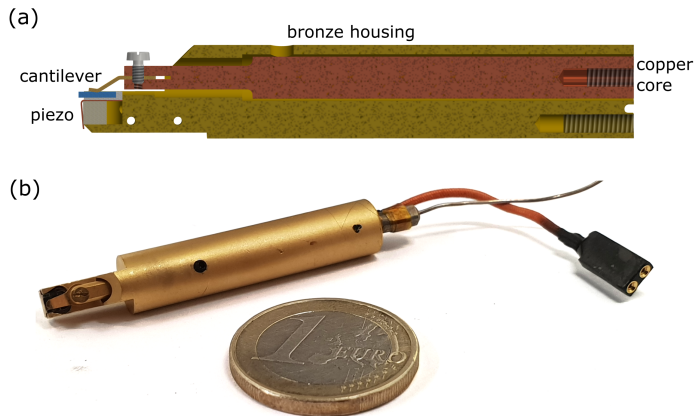


Figure 2.7: (a) Design and (b) photograph of the cantilever holder used in Fermat. Also visible are the silver wire used for thermalization and the cantilever-piezo connector.

sample is an issue.¹¹ To date, it has never been necessary to use this feature.

A photograph of the actual cantilever holder is shown in Fig. 2.7(b) next to a 1 euro coin for scale. Also visible is a silver wire (annealed to increase the thermal conductance) and the connector for the piezoelectric element. The cantilever holder is placed into the motor plate from Fig. 2.6. Three adjustment screws can be used to horizontally translate the cantilever holder in the motorplate, a useful feature when doing the room temperature alignment of the cantilever with respect to the pickup loop before cooling down, as discussed further in Sec. 2.4.3.

2.4.2 Piezoknobs and finestage

Moving the cantilever with respect to the sample is done using two separate positioning stages. The fine positioning of the cantilever requires reproducible nanometer accuracy, and is done using a piezostack-based finestage. This finestage is used to move the sample holder with respect to the cantilever holder, and was described in detail by previous PhD students from our group [53], to which we refer the interested reader. For coarse positioning we use an improved version of the piezoknob-based positioning stage used in the old MRFM setup in our group [38, 53, 54]. The new stage, shown in Fig. 2.8, also uses JPE piezoknobs mounted on spindles¹². A piezoknob is a stick-slip-based motor which uses piezoactuators to apply a torque on an axis called the spindle. Three of these motors are positioned in a triangular geometry, where the cantilever holder is located at the Fermat point of this triangle¹³. The spindles are mounted in nuts, both made of steel coated with diamond-like-carbon to reduce friction, with a thread spacing of 250 μm . At the end of each spindle there is a small aluminum-oxide sphere which rests on two parallel hardened steel rods (see Fig. 2.9(a)). Rotating the piezoknobs changes the effective length of the spindles and induces a tilt of the motor plane, which in turn moves the cantilever.

The idea of this new triangular geometry was to increase the reliability of the motors, but even now the reliability remains an issue. In Fig. 2.9 signs of wear are visible both on the steel rods and on the tip of the spindle (in this earlier version, the tip was made from silicon nitride). To reduce wear and increase the reliability of the motors, we have replaced the silicon nitride tips on the spindles with aluminum-oxide tips. Additionally, we have added extra weight around the piezoknobs to increase the

¹¹Fluctuating charges are often held responsible for non-contact friction and increased frequency noise in MRFM.

¹²Janssen Precision Engineering, CLE 2601

¹³The name Fermat for the new MRFM setup is based on this triangular layout.

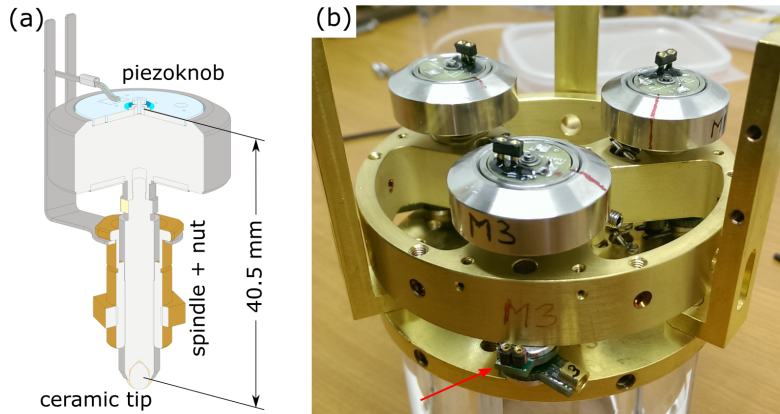


Figure 2.8: (a) Design of the JPE CLA 2601 piezoknobs (figure adapted from JPE). The sliding contact visible in the design is disabled in the actual implementation. (b) Photograph of the piezoknobs-based coarse positioning stage used in Fermat. The red arrow indicates one of the capacitors used for the absolute positioning.

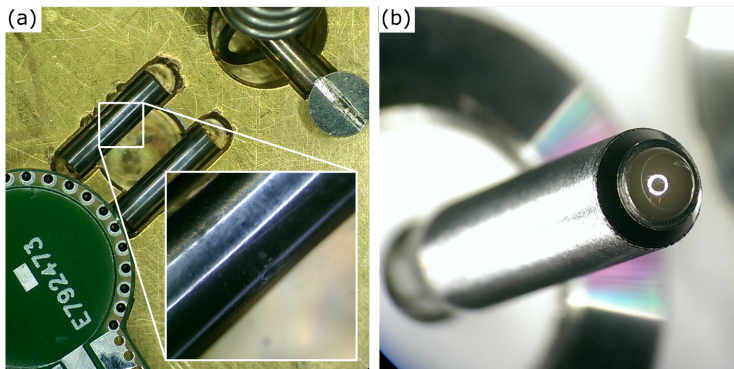


Figure 2.9: Optical microscope images of the observed wear on (a) the steel rods and (b) the silicon nitride spindle tips. After these observations, the silicon nitride tips were replaced by aluminum-oxide ceramic tips.

inertia. Furthermore, we have reduced the pre-stress necessary for the operation of a stick-slip motor to the lowest possible value. Finally, we have disabled the sliding contact typically used for operation of the piezoknobs, and instead allow the cables and motor to rotate freely. After these changes, the motors have become more reliable, working with a typical low-temperature efficiency of 50.000 steps per rotation, equivalent to a change in effective spindle length of about 5 nm per step. The dissipation has been measured to be less than 1 mJ/step, sufficiently low that continuous operation of the piezoknobs in a dilution refrigerator is possible. For

example, at a step rate of 10 Hz, the generated heating power is 10 mW, equivalent to the cooling power of our cryostat at 300 mK.

2

ABSOLUTE POSITION: Moving the piezoknobs has the effect of tilting the motor plate, thereby moving the cantilever below it. The absolute position of the cantilever can be measured using three sets of capacitor plates, one located next to each of the spindles (see the red arrow in Fig. 2.8(b)). By measuring the capacitance with sub-attoFarad resolution using an Andeen-Hagerling 2500a 1kHz automatic capacitance bridge, the length of all spindles can be calculated. From these lengths the tip position can be calculated with a precision of about 50 nm. The calculation translating the length of the different spindles to the relative position of the tip of the cantilever is very similar to the calculation described by de Voogd [59]. We have defined the right-handed coordinate system in such a way that from the center of the pickup loop the X-axis points towards motor 1 and the Z-axis is directed upwards. The X-direction is also the soft-direction of the cantilever.

2.4.3 Alignment and positioning

ALIGNMENT AT ROOM TEMPERATURE: The cantilever is aligned above the detection chip at room temperature using an optical microscope. In this alignment, one has to take into account thermal drift during cooldown, due to the different thermal expansion coefficients of the various components. Typically we measure a horizontal drift of about 50 μm in the direction away from the finestage piezo's, dominated by the contraction of the aluminium finestage. The vertical thermal drift is less than 20 μm . Note that the measured height using the capacitance read-out indicates a change in Z of about 50 μm , but this is due to the high thermal contraction of the capacitor-plates, made out of FR-4. This means that the measured increase in spindle length is actually an increased spacing between the capacitor plates. With this knowledge, the room temperature alignment procedure is the following:

1. Use the piezoknobs to place the cantilever at a height of approximately 50 μm above the surface of the pickup loop, with all spindles at the same length (measured using the capacitance read-out) to minimize the tilt of the cantilever with respect to the surface.
2. Use the adjustment screws (see Sec. 2.4.1) to horizontally move the cantilever such that it is in the center of the pickup loop. This location is then defined as $(X, Y, Z) = (0, 0, 50)$.

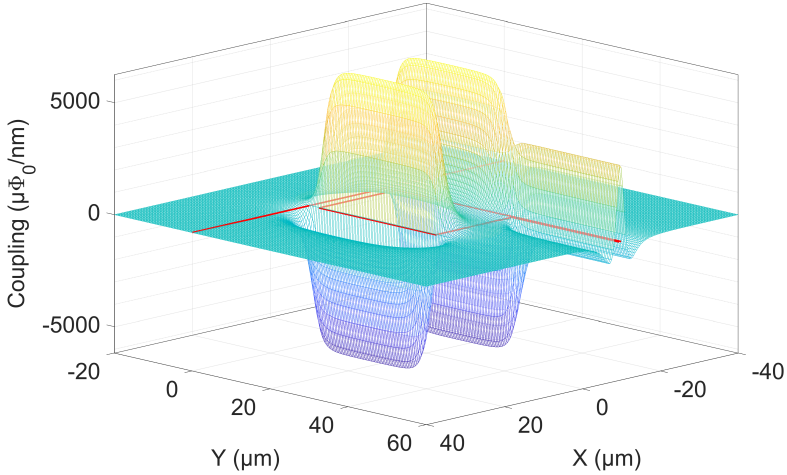


Figure 2.10: Calculated flux coupling in $\mu\Phi_0/\text{nm}$ between the magnetic particle (radius $1.7\ \mu\text{m}$) and the SQUID at a surface-to-surface distance of $1.0\ \mu\text{m}$. We have assumed a flux coupling efficiency between the pickup loop and the SQUID of 3.7%. A negative coupling corresponds to a 180 degree phase shift of the measured signal with respect to the driving signal send to the piezo. The location of the pickup loop and RF wire is shown in red.

3. Use the piezoknobs to move the cantilever to position $(X, Y, Z) = (50, -50, 50)$, as this is the approximate position where the center of the pickup loop will be after all thermal contraction.

LOW TEMPERATURE POSITIONING: Following the alignment procedure outlined before, the cantilever will be within tens of micrometers of the pickup loop after cooldown. At this point, in order to find the position of the cantilever relative to the pickup loop and sample, we combine the absolute positioning using the capacitance measurement with our knowledge about the coupling between the motion of the magnetic particle at the end of the cantilever and the pickup loop, as described in Sec. 2.2. A calculation of this coupling in the XY plane at a surface-to-surface separation of $1.0\ \mu\text{m}$ is shown in Fig. 2.10. For this calculation we have assumed a flux coupling efficiency $\eta = 3.7\%$, and a magnetic particle with a radius of $1.7\ \mu\text{m}$. A negative coupling in Fig. 2.10 should be interpreted as a 180-degree phase shift between the measured SQUID signal and the driving signal sent to the piezo. Especially the crossings from a positive to a negative coupling are clear indications of the exact location of the edges of the pickup loop in the X-direction. For the Y-direction, we look for an optimum in the coupling strength to find the center of the pickup loop.

In principle, the map from Fig. 2.10 can be used to find the exact position with

respect to the pickup loop when all experimental parameters are completely under control. However, in practice this is not the case, as for instance the direction of the magnetization of the magnet might not be perfectly aligned with respect to the pickup loop. Furthermore, the piezoknob coarse positioning stage described in the previous section is not as stable as it should be. The combination of some space between the spindles and nuts and the low pre-stress allow for some horizontal play when the motors are used. The capacitance measurement is not sensitive to horizontal shifts of the capacitor plates, meaning that the final position accuracy in the horizontal plane is at best $5 \mu\text{m}$. Therefore, we need to find additional ways to determine the position with respect to the pickup loop and sample, which does not involve moving the coarse stage.

POSITIONING CHECKS: We have devised three checks that can be used to decrease the uncertainty in the actual position.

The first check is to drive the cantilever using the cantilever piezo, and measure the sign (phase) of the coupling. As can be seen from Fig. 2.10, the sign indicates whether you are inside or outside of the pickup loop in the X direction.

The second check is to apply a DC current and thus a DC field using the RF wire. A slight tilt of the moment \mathbf{m} of the magnet on the cantilever with respect to the RF wire induces a vertical force given by $F_z = \frac{\partial}{\partial z} (\mathbf{m} \cdot \mathbf{B}_{\text{DC}})$. The force induces a frequency shift given by

$$\Delta f_{\text{DC}} = f_0 \left(\sqrt{1 + \frac{y_0 F_z l^2}{E d^3 w}} - 1 \right), \quad (2.14)$$

with $y_0 = 0.295$ for the fundamental mode [74]. The force has an opposite sign at opposite sides of the RF wire. So, the sign of the DC field induced frequency shift indicates whether the cantilever is positioned to the left or to the right of the RF wire.

Finally, driving the cantilever using the RF wire induces a torque $\tau = \mathbf{m} \times \mathbf{B}_{\text{RF}}$. For our geometry with the magnetic moment aligned in the X-direction (parallel to the RF wire) the resulting cantilever amplitude is then given by

$$A = \frac{m_x B_z l^2}{E w d^3}, \quad (2.15)$$

with B_z the vertical component of the magnetic field (see Eq. 2.1) at the location of the magnet. A plot of the expected cantilever amplitude when torsionally driven using the RF wire is shown in Fig. 2.11(a). We can combine this position-dependent cantilever

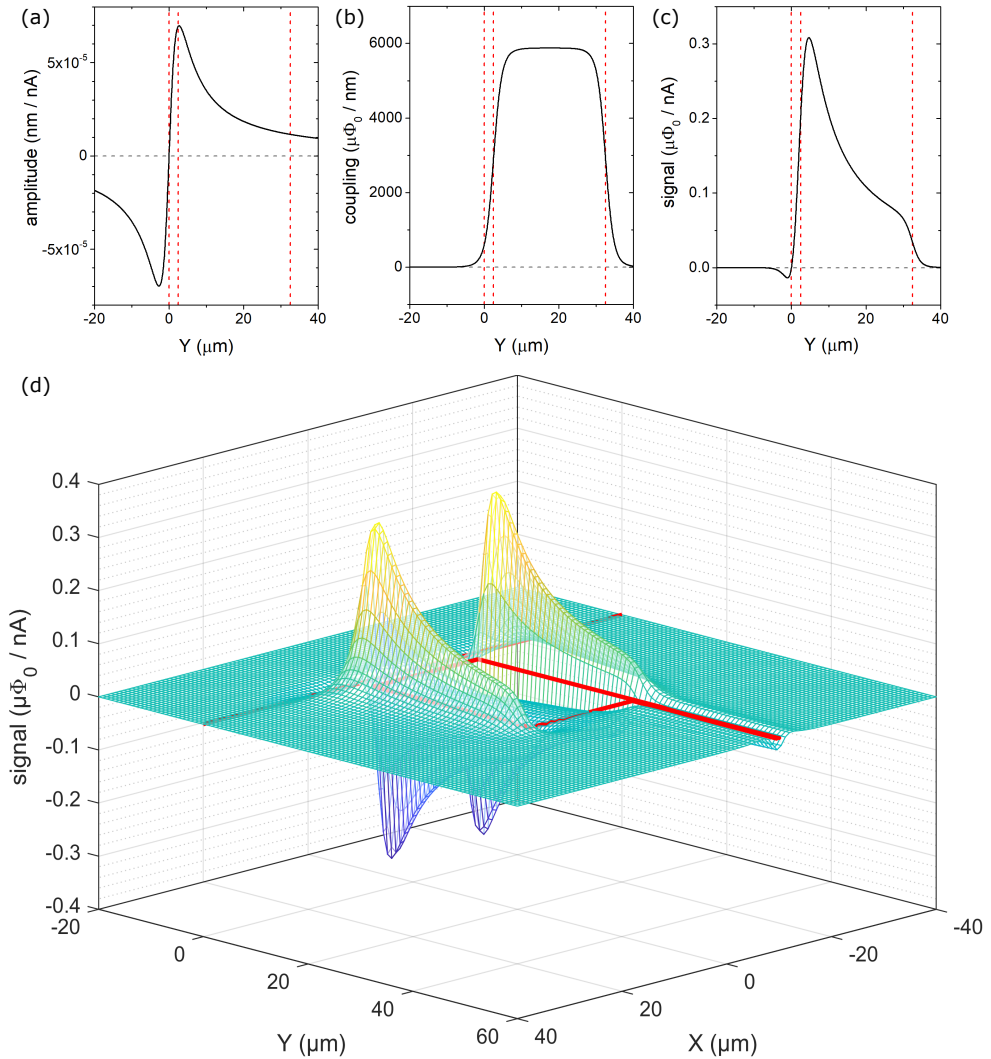


Figure 2.11: Calculations along a line perpendicular to the RF wire, $2 \mu\text{m}$ outside of the pickup loop, at a height of $1.0 \mu\text{m}$ above the pickup loop, showing (a) the amplitude of the cantilever when torsionally driven by a 1 nA current, without taking into account the Q-factor, (b) the coupling between the magnetic particle (radius $1.7 \mu\text{m}$) and the SQUID, assuming a flux coupling efficiency of 3.7% , and (c) the expected signal measured in the SQUID. The dashed red lines indicate the position of the RF wire and pickup loop. Figure (d) shows the same calculation as shown in (c), but now calculated for the full XY plane at a height of $1.0 \mu\text{m}$ above the surface. The solid red lines indicate the position of the RF wire and pickup loop.

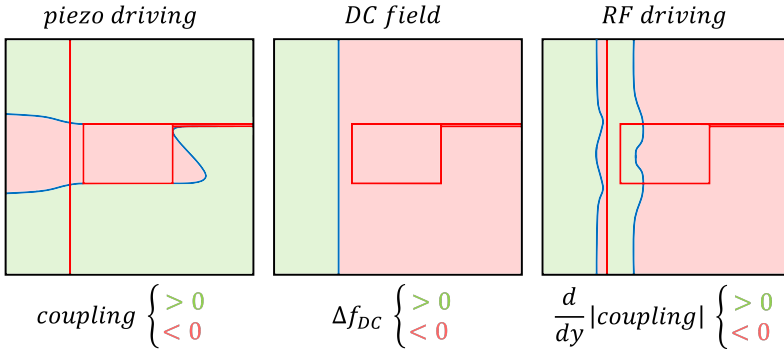


Figure 2.12: Drawings of the three checks which together can be used to obtain the approximate position above the detection chip without using the coarse positioning stage. The sign conventions are arbitrary, as these depend on the specific experimental parameters, and should be determined in advance.

amplitude with the position-dependent coupling (Fig. 2.11(b)) to obtain a map of the flux induced by the driven cantilever versus position. This map, calculated for a surface-to-surface separation of $1.0 \mu\text{m}$, is shown in Fig. 2.11(d). When the signal is measured at several positions using the finestage, the sign of the slope of the coupling gives additional information about the distance to the RF wire. Note that in this calculation we neglected the effects of a small misalignment of the magnetic moment with respect to the RF wire. Furthermore, we ignore the direct crosstalk between the RF wire and the pickup loop. However, since this crosstalk has a constant amplitude and phase in the narrow frequency range required for this measurement, this can be easily corrected for.

A summary of the three checks is shown in Fig. 2.12. It should be clear that combining all three checks divides the detection chips into 12 segments which can be distinguished from each other by the combination of all checks. Note that the sign convention used in Fig. 2.12 is chosen arbitrarily, so the actual signs should be determined in advance once.

2.4.4 Sample holder and temperature control

An overview of the sample holder with all relevant components labeled is shown in Fig. 2.13. The sample holder, made of gold-plated copper for maximum heat conductance to the sample, carries the detection chip, flux transformer, and SQUID, as well as

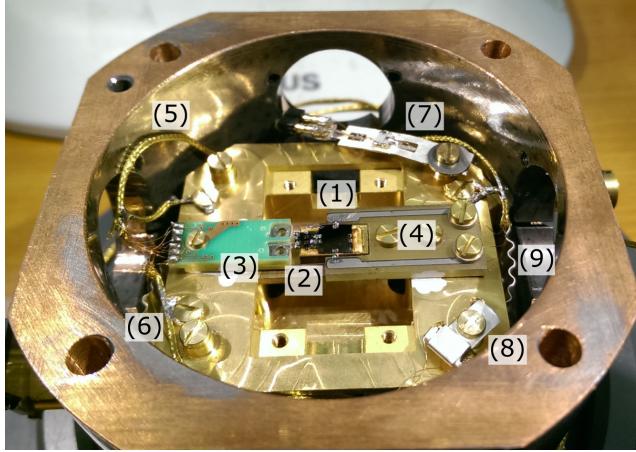


Figure 2.13: Photograph of the sample holder of Fermat with the most important components labeled: (1) detection chip; (2) gradiometric transformer as described in section 2.2.1; (3) SQUID in CAR-1 carrier; (4) Nb foil for RF circuit; (5) SQUID wiring (4 twisted pairs, NbTiN in Cu, gold-plated copper shielding); (6) connection to compensation coil; (7) AR3 low temperature thermometer; (8) 100 Ω -heater; (9) Corrugated silver foil for thermalization.

the sample thermometer¹⁴ and heater¹⁵. The sample holder is placed in the housing of Fermat, made of tantalum-coated copper. The tantalum coating was chosen for magnetic shielding of the SQUID, as tantalum is a superconductor with a critical temperature of approximately 4.5 K with a critical field of 83 mT. To connect the microscopic RF wire to the macroscopic wiring, we use aluminium wirebonds to two niobium strips on a FR-4 substrate. The wiring is then connected via a clamping contact using niobium screws and rings.

As noted before, the sample holder is placed on the aluminium finestage. As this aluminium becomes superconducting and thus is a very poor heat conductor, the sample holder is thermalized using corrugated silver foil connected to silver strips, which in turn are attached directly to the bottom mass of the vibration isolation. A tuned PID temperature controller is used to control the temperature of the sample holder with a temperature stability better than 10 μ K at low temperatures, and very short time constants, as shown in Fig. 2.14, where we show the time response of the measured sample holder temperature (blue line) and applied power (red line) to a change in the temperature setpoint (black line). The short time constant indicates high thermal conductance and a low heat capacity of the sample holder.

¹⁴HDL AR3, calibrated for temperatures 10 mK - 1 K, read-out using a Picowatt AVS-47

¹⁵SMD 100 Ω with silver housing

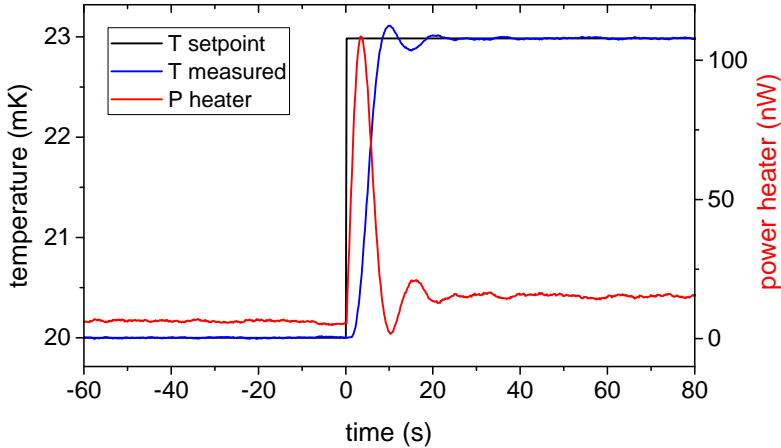


Figure 2.14: Thermal response of the sample holder to a change in the PID temperature setpoint (black line). The measured temperature (blue line) reaches a stable temperature within seconds due to the finely tuned PID controlling the heater power (red line) with nW accuracy.

2.5 CRYOSTAT YETI

CRYOGEN-FREE DILUTION REFRIGERATOR: All experiments described in this thesis have been performed in a dilution refrigerator¹⁶, nicknamed Yeti. The design of the cryostat can be seen in Fig. 2.15. It has a base temperature of approximately 8 mK, with a measured cooling power of 1100 μW at 120 mK. A two-stage pulsetube cryocooler¹⁷ is used to cool the cryostat to liquid helium temperatures. The advantage of using a pulsetube (PT) is that no cryogenic liquids are required, which cuts down on the operating costs and extends the length of experiments at the lowest temperatures. However, because a PT relies on varying helium pressure between 7 and 22 bar [75], using it comes at the expense of increased vibrations [76, 77].

REDUCING VIBRATION LEVELS: To reduce the vibration levels at the coldest plate, often called the mixing chamber plate (MC-plate), a number of vibration isolation measures have been taken, all highlighted in the subfigures in Fig. 2.15. The modifications were described in detail by Den Haan et al. for the older cryostat in the lab, nicknamed Olaf, the little snowman [77]. To reduce the effect of mechanical noise from external sources like pumps and people, the cryostat is suspended from a

¹⁶Leiden Cryogenics CF-CS81-1400-Maglev

¹⁷Cryomech, PT420

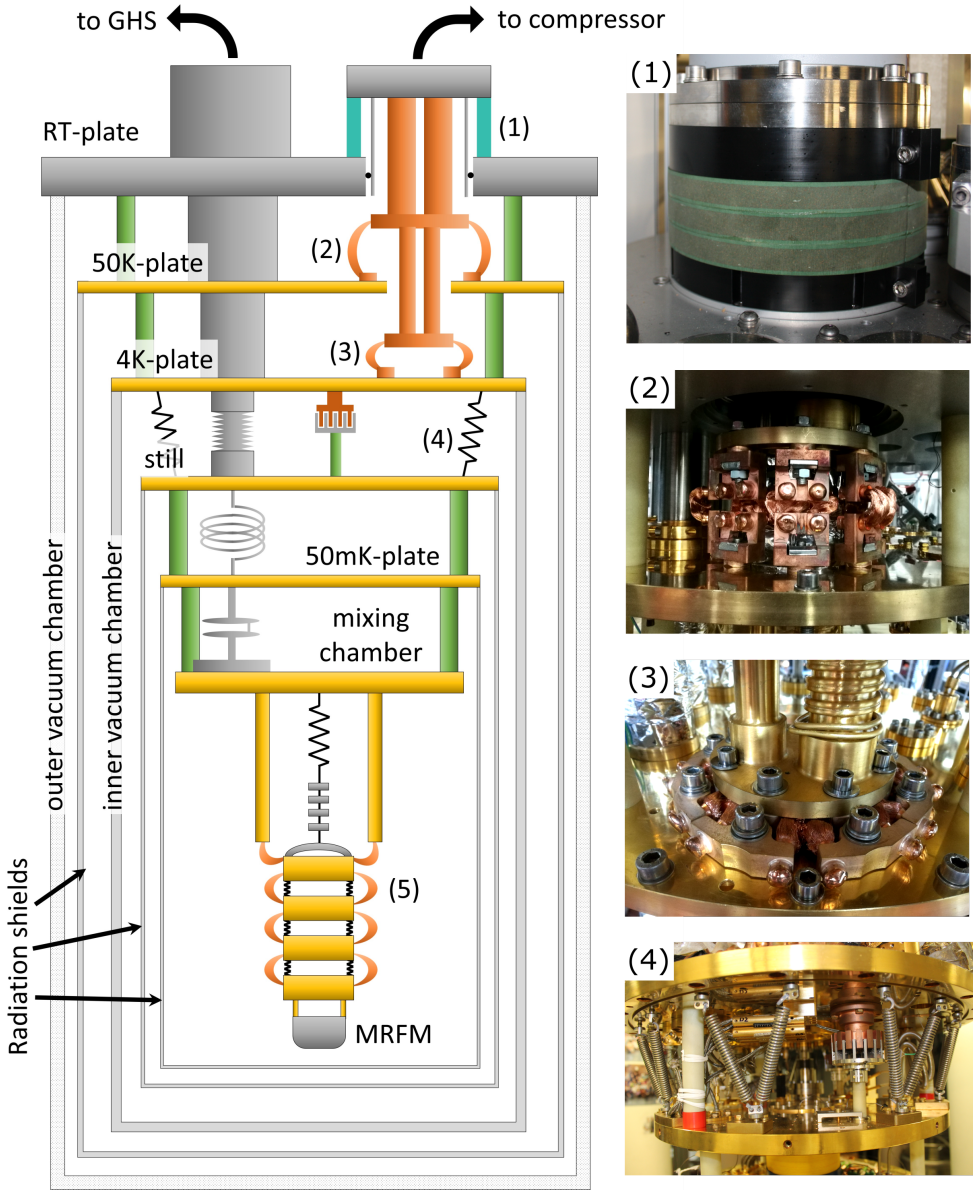


Figure 2.15: Schematic overview of the Yeti dilution refrigerator. The various vibration isolation measures are indicated by the numbers: (1) The vibration damping foam used to dissipate the motion of the pulsetube (PT); (2) Soft vertical heatlinks which connect the 50K-plate to the PT 50K-stage; (3) The “cartwheel-design” heatlinks connecting the 4K-plate to the PT 4K-stage; (4) The suspension of the still from springs. Two cylindrical eddy current dampers are installed to dissipate the vibrational energy. The still is interconnected using a flexible bellow. Note that the red blocks in the picture are removed before cooldown; (5) Low temperature multi-stage vibration isolation, explained in detail in Ch. 3.

heavy concrete temple, which in turn rests on a foundation separated from the rest of the building. The idea here is that external forces acting on a stiff, heavy system introduce only little displacement. This method is generally used to damp external vibrations, but is not sufficient when the main source of noise is located within the cryostat itself, as is the case with a pulsetube.

The hoses connecting the compressor of the PT to the rotary valve used to vary the helium pressure make a large loop (diameter ~ 2 m). The top of the loop is suspended from the ceiling with ropes, and the bottom of the loop buried in loose sand to dampen the vibrations from the compressor. The hoses are placed inside an acoustic isolation box which is in part intended to reduce acoustic noise in the cryostat, but is mainly needed for the comfort of the cryostat operator.

The PT itself is mechanically disconnected from the 4K-plate, 50K-plate, and RT-plate. At the RT-plate, the PT is placed on vibration damping foam to dissipate mechanical energy¹⁸. At the 4K-plate and the 50K-plate, soft copper heatlinks are placed in order to obtain a high thermal conductance in combination with a low stiffness. The heatlinks are TIG welded in argon to prevent oxidation during welding. The bolts that connect the heatlinks to the plates are fastened using a torque of 33 Nm. All clamping contacts contain molybdenum washers to increase the force of the thermal contact. We obtain a measured heat-conductance between the 4K-plate and the 4K-stage of the PT of 6.7 W/K, very close to the 7.9 W/K measured when the PT was still rigidly connected. The 4K-plate has a new base-temperature of 4.8 K because of the high thermal load coming from the large number of cables.

To further reduce vibrations that couple into the cryostat via paths other than the stages of the PT, the rigid G10 poles between the 4K-plate and the still-plate are disconnected from the still-plate. Instead, the bottom three plates of the cryostat are suspended from 18 stainless steel springs¹⁹. The springs are mounted in 9 pairs, and are placed at an inward angle of 12 degrees, and a sideways angle of 21 degrees to prevent low-frequency horizontal and rotational motion. The total suspended mass is assumed to be about 130 kg, including the experiments. The total system should behave like a second order low-pass filter with a corner frequency of approximately 3.3 Hz, a value chosen such that it is in between the PT higher harmonics at 2.8 and 4.2 Hz. Preferably, one would like the corner frequency to be well below the PT fundamental frequency of 1.4 Hz, but this was not possible given the limits on the maximal extension of the springs. Two eddy current dampers are placed off-axis between the still-plate and the 4K plate to dampen the residual motion of the still-plate with respect to the 4K-plate. The eddy current dampers can be used as "touch

¹⁸Bilz Vibration Technology AG, Insulation pads B30

¹⁹Amatec E0500-075-3000S, spring constant 3.03 N/mm, initial tension 10.2 N.

sensors” by checking whether there is an electrical connection between the two halves of the damper.

The final component of the vibration isolation is a three-stage mechanical low-pass filter suspended from the mixing chamber. The design and performance of this system are discussed in Ch. 3.

3

VIBRATION ISOLATION WITH HIGH THERMAL CONDUCTANCE FOR A CRYOGEN-FREE DILUTION REFRIGERATOR

We present the design and implementation of a mechanical low-pass filter vibration isolation used to reduce the vibrational noise in a cryogen-free dilution refrigerator operated at 10 mK, intended for scanning probe techniques. We discuss the design guidelines necessary to meet the competing requirements of having a low mechanical stiffness in combination with a high thermal conductance. We demonstrate the effectiveness of our approach by measuring the vibrational noise levels of an ultrasoft mechanical resonator positioned above a superconducting quantum interference device (SQUID). Starting from a cryostat base temperature of 8 mK, the vibration isolation can be cooled to 10.5 mK, with a cooling power of 113 μW at 100 mK. We use the low vibrations and low temperature to demonstrate an effective cantilever temperature of less than 20 mK. This results in a force sensitivity of less than 500 $\text{zN}/\sqrt{\text{Hz}}$, and an integrated frequency noise as low as 0.4 mHz in a 1 Hz measurement bandwidth.

This chapter has been published as M. de Wit, G. Welker *et al.*, “Vibration isolation with high thermal conductance for a cryogen-free dilution refrigerator”, *Review of Scientific Instruments*, Vol. 90, p. 015112, Jan. 2019

3.1 INTRODUCTION

In recent years, there is ever-increasing interest in the ability to work at very low temperatures with minimal mechanical noise. This is evidenced by the large number of low-temperature instruments developed for this purpose in a variety of scanning probe techniques, such as Scanning Tunneling Microscopy (STM) [78–89], Atomic Force Microscopy (AFM) [90, 91], Magnetic Resonance Force Microscopy (MRFM) [16, 37, 92], and other scanning probe techniques [93–96]. Other examples include instruments intended to investigate the quantum properties of macroscopic objects where resonators with extremely low mode temperatures are required [97, 98]. However, vibration sensitive measurements at low temperatures remain a technological challenge, one of the reasons being the added vibrational noise introduced by the cooling equipment.

The specific vibrational requirements vary depending on the technique. STM and the related Scanning Tunneling Spectroscopy (STS) are notoriously sensitive to changes in the tip-sample distance z . The tunneling current is exponentially dependent on this distance [99], leading to a required stability below 1 pm within the bandwidth (BW) of the I/V converter (typically a few Hz to several kHz) [83, 84, 86]. For techniques like AFM, Magnetic Force Microscopy (MFM), and MRFM, the low frequency stability criteria are less strict, with $\delta z \leq 10$ pm [77, 90, 91]. Additionally, these techniques also require low vibration levels near the resonance frequency of the cantilever (typically 1-100 kHz). The upper limit on the allowed vibration noise around the cantilever frequency can be derived from the thermal displacement noise. This depends on the cantilever's properties and operating temperature. For our specific MRFM setup, we aim for vibrations near the resonance frequency on the order of tens of femtometers per unit bandwidth at a temperature of 100 mK.

Global solutions that attenuate vibrations outside of the cryostat work very well for a wide variety of systems. Common measures include, e.g., mounting of the cryostat on a heavy platform, placing pumps in separate rooms or using sand to dampen vibration transfer via vacuum lines [84–88]. However, a local solution within the cryostat may be required when, for instance, it is not possible to create a stiff mechanical loop between the tip and the sample, or when the cryostat is based on a cryocooler, e.g., a pulsetube, in which case significant vibrations are generated within the cryostat itself [76, 100]. In these cases, one has to solve the combined problem of obtaining a high thermal conductance with low vibration noise, which is generally considered hard to do [101, 102]. The reason for this is that most vibration isolation systems are based on a mechanical low-pass filter with a corner frequency well below the desired operating frequency of the instrument, which means the stiffness of the

vibration isolation should be low. However, the thermal conduction scales with the cross-sectional area of the thermal link, and is therefore higher for a stiff connection. These conflicting requirements for the stiffness of the vibration isolation often lead to a compromise for one of the two properties [103–105]. Here we present a design which optimizes both aspects.

The vibration isolation presented in this article is intended to be used for a low temperature MRFM setup, where an ultrasoft resonator is used to measure the properties of various spin systems [106]. Due to the low stiffness and high quality factor of the resonator, the system is extremely sensitive to small forces [48], and therefore to vibrations. We explain the correspondence between electrical and mechanical networks, as this analogue proves to be very useful for calculating the optimal design of our mechanical filter. The filter we present here was designed to fit in an experimental space of 55 cm length and to carry a load of several kilograms. It should be effective in the frequency range starting from 50 Hz up to about 100 kHz. However, our general design principles also allow us to build a filter with a different bandwidth, tailored to the frequency range needed in scanning probe techniques such as STM/STS and AFM or for experiments working towards macroscopic superpositions. We will demonstrate the effectiveness of the vibration isolation by analyzing the displacement noise spectrum and thermal properties of the MRFM resonator, showing that our method has allowed us to successfully combine a high thermal conductance and low mechanical vibrations.

3.2 FILTER DESIGN

Commonly, the development of mechanical vibration isolation relies heavily on finite element simulations to determine the design parameters corresponding to the desired filter properties. In these simulations, the initial design is tweaked until the desired filter properties are found. Instead, we determined the parameters of our mechanical filter by first designing an electrical filter with the desired properties, and then converting this to the mechanical equivalent using the current-force analogy between electrical and mechanical networks. This allows us to precisely specify the desired filter properties beforehand, from which we can then calculate the required mechanical components. We therefore find the optimal solution using analytical techniques rather than using complex simulations. As we will see later, this also allows us to use our design principle across many frequency scales without requiring a new finite element analysis. The corresponding quantities for the analogy between electrical and mechanical circuits are found in Table. 3.1. We choose the current-force analogy

Electrical		Mechanical	
Variable	Symbol	Variable	Symbol
Current	I (A)	Force	F (N)
Voltage	U (V)	Velocity	v (m/s)
Impedance	Z (Ω)	Admittance	Y (s/kg)
Admittance	Y (1/ Ω)	Impedance	Z (kg/s)
Resistance	R (Ω)	Responsiveness	1/D (s/kg)
Inductance	L (H)	Elasticity	1/k (m/N)
Capacitance	C (F)	Mass	m (kg)

--	--

Table 3.1: Table of corresponding electrical and mechanical quantities.

over the voltage-force analogy [107] because the former conserves the topology of the network.

To design our desired filter, we follow the method of Campbell for the design of LC wave-filters [108]. Campbell's filter design method is based on two requirements:

- The filter is thought to be composed out of an infinite repetition of identical sections, as shown in Fig. 3.1(a), where a single section (also called unit cell) is indicated by the black dotted box.
- The sections have to be dissipationless to prevent signal attenuation in the pass-band. Therefore the impedances of all elements within the section have to be imaginary.

Following these requirements, the edges of the transmitted frequency band of the filter are defined by the inequality

$$-1 \leq \frac{Z_1}{4Z_2} \leq 0 \quad (3.1)$$

The iterative impedance is the input impedance of a unit cell when loaded with this impedance. In order to prevent reflections within the pass-band, the signal source and the load should have internal impedances equal to Z_{iter} . The iterative impedance should be real and frequency-independent, because this maximizes the power transfer within the pass-band and is easiest to realize.

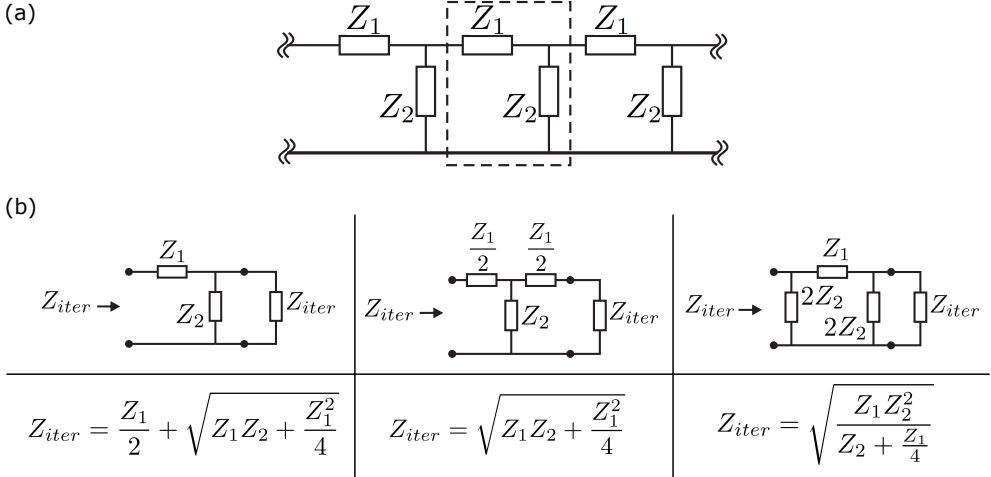


Figure 3.1: a) General scheme of a filter composed of identical sections, with one unit cell indicated by the black dotted box. b) Three options for the design of the unit cell for an LC filter, with below the corresponding values for the iterative impedance Z_{iter} .

There are three principle choices for the unit cell, all given in Fig. 3.1(b). The total attenuation is determined by the number of unit cells. Each unit cell acts like a second order filter, adding an extra 40 dB per decade to the high frequency asymptote of the transfer function. This attenuation is caused by reflection, not by dissipation, which is very important for low-temperature applications.

The design of the mechanical filter is straightforward when we use the third option from Fig. 3.1(b) with $Z_1 = \frac{1}{Y_1} = i\omega L$, and $Z_2 = \frac{1}{Y_2} = \frac{1}{i\omega C}$. The resulting electrical low-pass filter is shown in Fig. 3.2(a). Note that the two neighboring $2Z_2$ in the middle add up to Z_2 . We can use Eq. 3.1 to calculate the band edges: $\omega_1 = 0$ and $\omega_2 = \frac{2}{\sqrt{LC}}$.

With the electrical filter figured out, we make the transfer to the mechanical filter according to the correspondence as outlined in Table. 3.1. As the electrical inductance corresponds to mechanical elasticity, the coils are replaced by mechanical springs with stiffness k . The capacitors are replaced by masses in the mechanical filter. Note that the first mass has the value $\frac{m}{2}$ due to the specific unit cell design. The current source becomes a force source and the electrical input and load admittances become mechanical loads (dampers). The final mechanical circuit is depicted in Fig. 3.2(b). Going to the mechanical picture also implies a conversion between impedance and admittance in Eq. 3.1:

$$-1 \leq \frac{Y_1}{4Y_2} \leq 0 \tag{3.2}$$

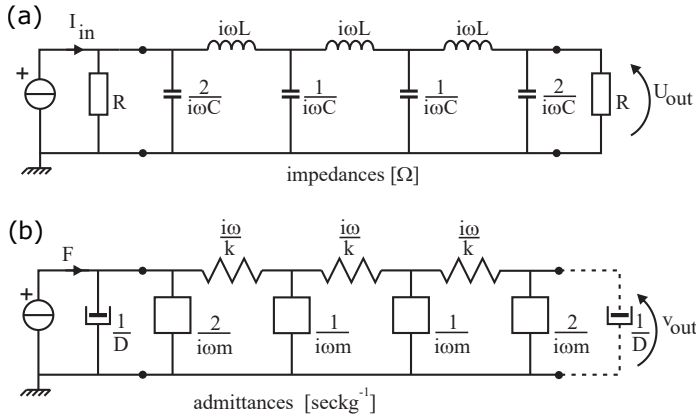


Figure 3.2: a) Electrical filter consisting of two unit cells. b) Corresponding mechanical filter.

With $Y_1 = \frac{k}{i\omega}$ and $Y_2 = i\omega m$, this leads to the band edges $\omega_1 = 0$ and $\omega_2 = 2\sqrt{\frac{k}{m}}$.

We now have a design for the unit cell of a general mechanical low-pass filter. The bandwidth and corner frequency are determined by the choice of the stiffness k and mass m , which can be tailored to the needs of a specific experimental setup. In practice, only corner frequencies between a few Hz and 50 kHz can be easily realized. At too low frequencies, the necessary soft springs will not be able to support the weight anymore, whereas above 50 kHz, the wavelength of sound in metals comes into play, potentially leading to the excitation of the eigenmodes of the masses.

A second practical challenge is the realization of the damper at the end of the filter. It should be connected to the mechanical ground, just as an electrical load is connected to the electrical ground. This is, however, not possible, because this mass reference point is defined by earth's gravity. The alternative to a damper as a real-valued load is using a purely reactive load: more mass. Simulations show that adding mass to the $\frac{m}{2}$ of the filter's last mass does not significantly alter the frequency characteristics of the filter, and even increases the attenuation. There is no strict limit on the weight of the added mass. In fact, adding more will, in principle, improve the filter. In practice, the limit depends on the choice of springs, which should be able to carry the weight whilst staying in the linear regime. The downside of replacing the damper with mass is that we lose the suppression of the resonance frequencies of the filter. We have chosen a final mass with a weight equal to the previous mass. The circuit diagram and schematic for the final design of the mechanical low-pass filter is shown in Fig. 3.3. Note that the damper at the input is missing, for experimental reasons which will be explained in Sec. 3.4.2.

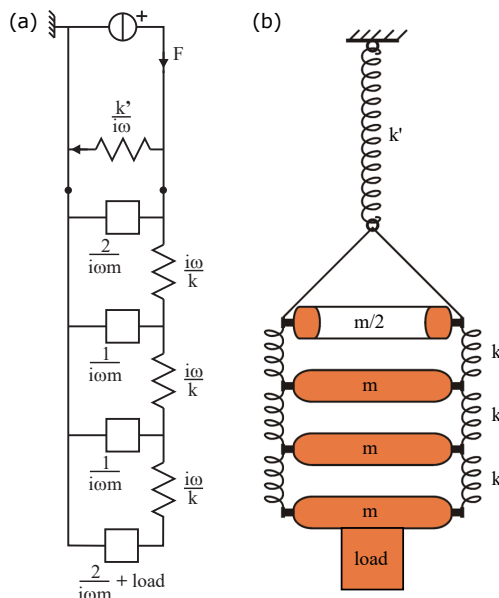


Figure 3.3: (a) Circuit diagram and (b) schematic overview of the mechanical low-pass filter based on the outlined theory. Note that the damper at the input is missing.

3.3 PRACTICAL DESIGN AND IMPLEMENTATION

Our setup is based on a Leiden Cryogenics CF-1400 dilution refrigerator with a base temperature of 8 mK and a measured cooling power of 1100 μW at 120 mK. The cryostat was modified to reduce the vibration levels at the mixing chamber following the approach outlined by Den Haan et al. [77] for a different cryostat in our lab. We have mechanically decoupled the two-stage pulsetube cryocooler from the cryostat, and suspended the bottom half of the cryostat from springs between the 4K-plate and the 1K-plate. In the rest of this paper, we focus only on the implementation and performance of the mechanical low-pass filter below the mixing chamber.

The design of the vibration isolation based on the theory outlined in Sec. 3.2 can be seen in Fig. 3.4(a). The isolation consists of three distinct parts: the weak spring intended to carry the weight, the 50 Hz low-pass filter acting as the main vibration isolation filter, and an additional 10 kHz low-pass filter used to remove mechanical noise from the cold head of our pulsetube at 24 kHz.

The 50 Hz filter consists of 4 separate gold-plated copper masses, each connected by 3 springs. The top mass has half the weight of the other three masses, as dictated

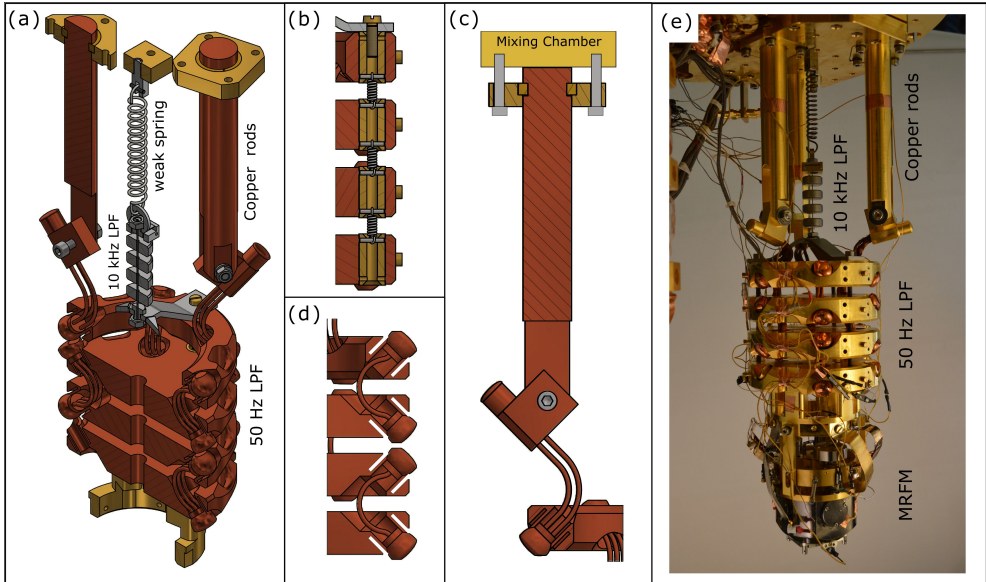


Figure 3.4: (a) Schematic drawing of the full design of the low temperature vibration isolation. It consists of a weak spring, a 10 kHz low-pass filter and a 50 Hz low-pass filter. The full length of the assembly is about 50 cm. The experiment can be mounted below the bottom mass. (b) Detailed schematic of the springs interconnecting the masses. The design is such that the springs can be replaced even after the filter is fully assembled and welded. (c) Detailed schematic of the thermal connection between the mixing chamber and the top mass. To get as little interfacial thermal resistance as possible, the copper rods are pressed directly against the mixing chamber. (d) Detailed schematic of the heatlinks interconnecting the masses. Of particular importance are the notches that concentrate the heat during the welding of the heatlinks. The heatlinks consist of three soft braided strands of copper. (e) Photo of the vibration isolation mounted on the mixing chamber of the dilution refrigerator.

by the theory. A variation in the masses of the different plates of up to 20% is allowed without a significant reduction in the isolating performance. As it might be desirable to tune the internal frequencies of this mass-spring system away from mechanical vibration frequencies of the cryostat, the springs, made of stainless steel, are fully modular and can easily be replaced even after assembly, as can be seen in Fig. 3.4(b). When multiple springs are used at each stage, the stiffness of all springs should be as equal as possible. In our design we have chosen a mass $m = 2$ kg, and springs with a stiffness $k = 16$ kN/m, leading to a combined stiffness of 48 kN/m. This choice leads to a corner frequency of $\omega_c/(2\pi) = 50$ Hz. We have chosen to use 3 filter stages as this should give sufficient attenuation above 100 Hz. The internal resonance frequencies of this filter have been measured at room temperature by applying a driving force at the top mass of the filter and using geophones to measure the response at the

bottom mass. The frequencies match well with the resonance frequencies obtained from the theoretical model, as shown in Fig. 3.5. The good agreement between theory and experiment in terms of the resonance frequencies gives confidence to also trust the model regarding the reduction of vibrations, where we expect over 100 dB of attenuation above 100 Hz. This level of attenuation is sufficient for our application with a resonator at a frequency of 3 kHz, but it is also possible to attain a larger attenuation at lower frequencies, as indicated in Sec. 3.2. The internal resonances can be suppressed by adding a well-designed damper, as demonstrated by the calculation shown as the red line in Fig. 3.5.

The 10 kHz filter consists of a stainless steel wire with a diameter of 1.0 mm connecting 4 stainless steel masses weighing 20 g each. The design of this second filter is also based on the previously outlined theory, just like the 50 Hz filter. This filter is necessary to remove noise that can drive high frequency internal filter modes, e.g. resonances of the masses. Once again, the theoretical internal resonances were verified experimentally, indicating that the electrical-to-mechanical filter correspondence holds for a wide range of frequencies.

Concerning the weak spring: we have chosen a stainless steel spring with a length of 100 mm and a spring constant of about 10 kN/m, leading to a resonance frequency of 4 Hz. However, it must be noted that this choice is not critical at all. A wide range of spring constants is allowed, as long as the weak spring can really be considered weak with regard to the springs interconnecting the masses. If a damper is added to the system, it should be in parallel to the weak spring. Note that no additional damping is necessary in parallel to the springs between the masses in order to damp all four resonances.

When mounting the experiment including its electrical wiring, care needs to be taken to attach each wire firmly to each of the masses. Otherwise, the wires create a mechanical shortcut, thereby reducing the efficiency of the vibration isolation.

In order to be able to cool the experiments suspended from the vibration isolation to temperatures as close to the temperature of the mixing chamber as possible, we have taken great care to maximize the thermal conductance. Since the biggest bottlenecks in the thermal conductance are the stainless steel weak spring and 10 kHz low-pass filter, we bypass these components by using three solid copper rods in parallel to the weak spring, each with a diameter of 25 mm and 175 mm length, which are connected to the top mass via three soft braided copper heatlinks. We are allowed to make this thermal bypass as long as the combined stiffness of the soft heatlinks and the weak spring remains low compared to the stiffness of the interconnecting springs. The soft braided copper heatlinks consist of hundreds of intertwined copper

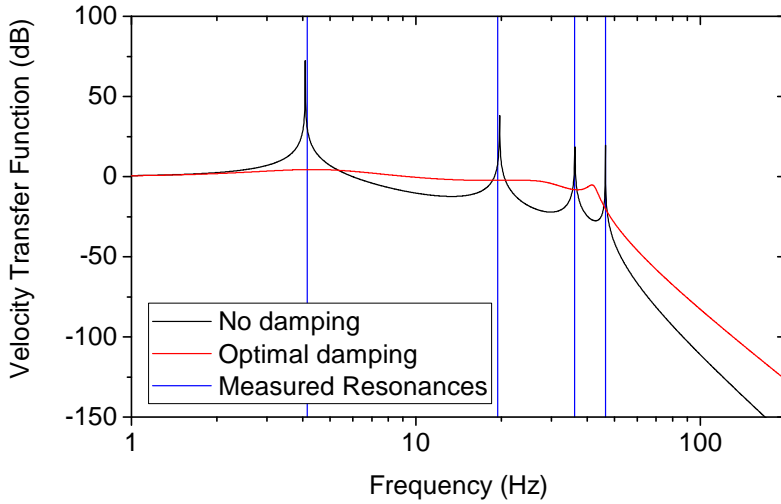


Figure 3.5: Theoretical velocity transfer function of the mechanical low-pass filter, calculated without damping (black line) and with optimal damping (red line). The vertical blue lines indicate the positions of the measured room-temperature resonance frequencies (total load 12 kg).

wires with a diameter of 0.1 mm. Using a bundle of thin wires leads to a much lower mechanical stiffness than when using a single thick wire. In order to avoid a large contact resistance between the mixing chamber and the copper rods, the rods are gold-plated and placed directly against the mixing chamber plate of the dilution refrigerator. All contact surfaces are cleaned by subsequently using acetone, ethanol, and isopropanol to remove organic residue, which can reduce the thermal conductance. A strong mechanical contact is achieved using the system shown in Fig. 3.4(c). All clamping contacts using bolts contain molybdenum washers, as these will increase the contact force during cooldown due to the low thermal contraction coefficient of molybdenum compared to other metals.

All masses are interconnected via three sets of three soft braided copper heatlinks which are tungsten inert gas (TIG) welded into the masses in an argon atmosphere to prevent oxidation. The welding of the copper was made possible by the notched structure of the welding joints in the masses (see Fig. 3.4(d)), which are intended to concentrate the heat during welding. The gold plating was removed from the welding joint prior to the welding to prevent diffusion of the gold into the heatlinks, which would reduce the thermal conductance. The experiment is rigidly attached to the bottom mass, which should now function as a cold and vibration-free platform.

3.4 EXPERIMENTAL RESULTS

To characterize the performance of the vibration isolation, we install a very soft cantilever (typically used for MRFM experiments) below the bottom mass. The cantilever has a spring constant $k_0 = 70 \mu\text{N/m}$, a resonance frequency f_0 of about 3009 Hz, and a quality factor Q_0 larger than 20 000 at low temperatures. A magnetic particle (radius $R_0 = 1.7 \mu\text{m}$) is attached to the end of the cantilever. We then compare two situations: In one configuration, the vibration isolation is operating as intended and as described in Sec. 3.3. In the other configuration, the vibration isolation was disabled by using a solid brass rod to create a stiff connection between the mixing chamber and the last mass of the vibration isolation. This simulates a situation where the experiment is mounted without vibration isolation. The vibrations of the setup are determined by measuring the motion of the cantilever using a superconducting quantum interference device (SQUID) [47], which measures the changing flux due to the motion of the particle. The sensitivity of this vibration measurement is limited by the flux noise of the SQUID, which can be converted to a displacement noise using the thermal motion of the cantilever and the equipartition theorem [48]. We start by demonstrating the thermal properties of the vibration isolation.

3.4.1 Thermal conductance

To verify the effectiveness of the thermalization, we have measured the heat conductance of our vibration isolation. For the base temperature of our cryostat, which is a mixing chamber temperature of approximately 8 mK, we find that the bottom mass of the vibration isolation saturates at 10.5 mK. This already indicates a good performance of the thermalization. We then use a heater to apply a known power to the bottom mass, while we again measure the temperature of the bottom mass and the mixing chamber. This allows us to quantify an effective cooling power at the bottom mass (defined as the maximum power that can be dissipated to remain at a set temperature). At 100 mK, we measure a cooling power of $113 \mu\text{W}$, which is significantly higher than that of comparable soft low temperature vibration isolations described in the literature [79, 105], and only about a factor of 7 lower than the cooling power of the mixing chamber of the dilution refrigerator at the same temperature.

The experimental data is compared to a finite element simulation using Comsol Multiphysics to determine the limiting factors in the heat conductance. The results of this analysis and the experimental data are shown in Fig. 3.6. We use a thermal conductivity that is linearly dependent on temperature as expected for metals [109],

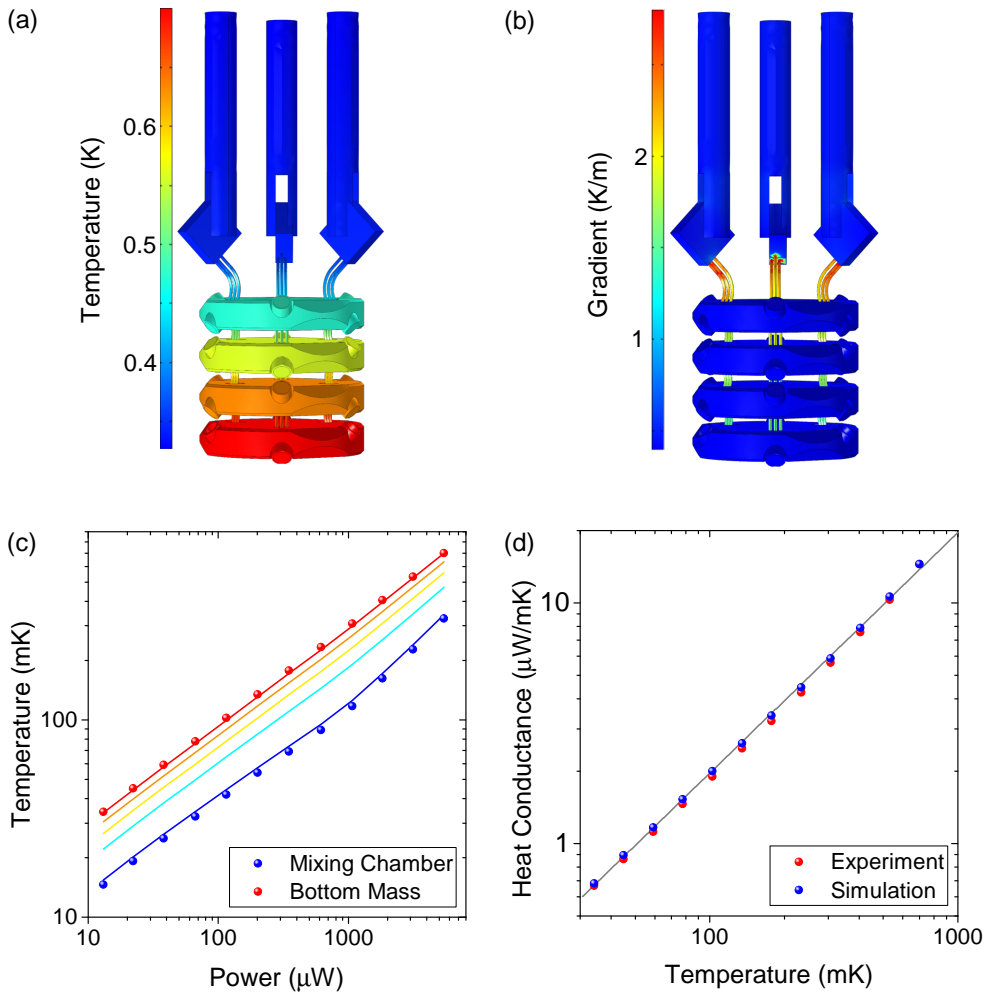


Figure 3.6: Measurements and finite element simulations of the thermal properties of the vibration isolation. A power is applied to the bottom mass, and the temperature of the bottom mass and the mixing chamber are measured. In the simulation, we insert the power and mixing chamber temperature, and calculate the corresponding temperature of the bottom mass to check the model. Results of the simulation for the (a) temperature and (b) temperature gradient are shown for a power of 5.4 mW. (c) Measured temperature of the mixing chamber and bottom mass as a function of the applied power. The solid lines are the simulated temperatures at each of the masses (red is the bottom mass, blue the bottom of the copper rod). At 100 mK, we find a cooling power of 113 μW at the bottom mass. (d) Heat conductance between the bottom mass and the mixing chamber as a function of the temperature of the bottom mass. The solid line is a linear fit to the data.

given by $\kappa = 145 \cdot T$. The proportionality constant of $145 \text{ Wm}^{-1}\text{K}^{-2}$ corresponds to low purity copper [110]. The simulated temperature distribution (for an input power of 5.4 mW) is shown in Fig. 3.6(a). The uniformity of the color of the masses indicates that the heatlinks interconnecting the masses are the limiting thermal resistance, something that becomes even more apparent from the plotted thermal gradient as shown in Fig. 3.6(b).

There is a good correspondence between the simulation and the experimental values for all applied powers, as shown in Fig. 3.6(c). Similar agreement is found when plotting the heat conductance between the bottom mass and the mixing chamber as a function of the temperature of the bottom mass (Fig. 3.6(d)). The assumption that the heat conductivity is linearly dependent on the temperature seems to hold over the full temperature range. As the model does not include contact resistance or radiation, but only the geometry and thermal properties of the copper, we can conclude that the thermal performance of the vibration isolation is limited purely by the thermal conductance of the braided copper. Furthermore, we do not expect that other sources of thermal resistance follow this particular temperature dependence [109]. So, the argon-welded connections appear to be of sufficient quality not to hinder the conductance. The performance can be improved further by making the heatlinks out of copper with a higher RRR value, and thereby a higher thermal conductivity.

3.4.2 SQUID vibration spectrum

The performance of the vibration isolation is shown in Fig. 3.7, where we plot the measured SQUID spectra for the two different situations: In the red data, the vibration isolation is in full operation. The black data show the situation when the vibration isolation is disabled. A clear improvement is visible for nearly all frequencies above 5 Hz. We focus on the region between 0 and 800 Hz to indicate how effective almost all vibrations are reduced to below the SQUID noise floor, and on the region around 3009 Hz as this is the resonance frequency of our cantilever. The conversion factor (c) between SQUID voltage and displacement is about 0.78 mV/nm for the black spectrum, and 0.56 mV/nm for the red spectrum, where the small difference is caused by a slightly different coupling between the cantilever motion and the SQUID for the two measurements. The different coupling is the result of a slightly different position of the cantilever with respect to the flux detector. Using these conversion factors, we find a displacement noise floor at 3 kHz below $10 \text{ pm}/\sqrt{\text{Hz}}$ for both spectra.

At frequencies below 5 Hz, the measured noise of the spectrum with vibration

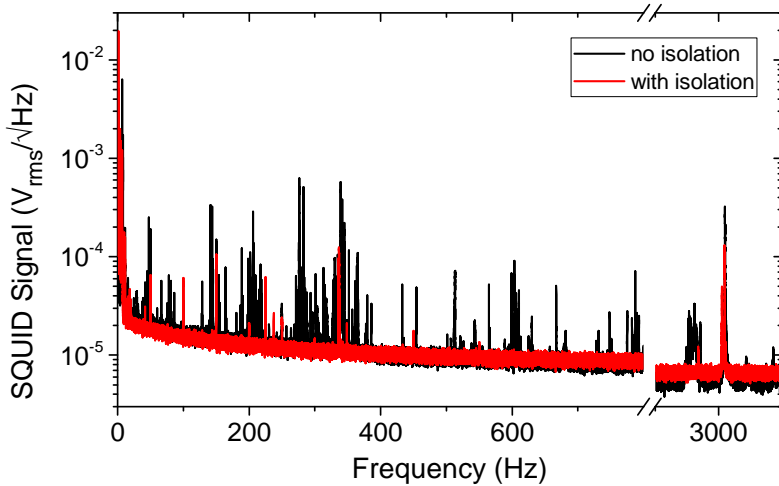


Figure 3.7: SQUID spectra $\sqrt{S_V}$ of the vibration noise measured at temperatures below 25 mK. The black data show the SQUID signal with the vibration isolation disabled using the brass rod, while in red we see the measured spectrum with proper vibration isolation.

isolation becomes larger than that of the spectrum without isolation. However, the amplitude of the vibrations in this frequency range is independent of the coupling between the cantilever motion and the SQUID, indicating that these peaks are not caused by tip-sample movement. Instead, we attribute them to microphonics due to motion of the wiring going to the experiment between the mixing chamber and the top mass of the vibration isolation. The low-frequency motion of the mass-spring system can be removed by using a properly designed damper in parallel to the weak spring, as is shown in Fig. 3.5. This damper would suppress internal resonances of the vibration isolation, for which we expect undamped Q-factors ranging from 100 to 1000 and thereby reduce the microphonics-induced noise.

In the presented experiment, a damper was not implemented for two reasons. First, the power dissipated by the damper would heat the mixing chamber of the cryostat, and thereby reduce the base temperature of the experiment. Secondly, the most commonly used damper at low temperatures is based on the induction of eddy currents by moving a magnet near a conductor. Due to the high sensitivity of our SQUID-based detection for fluctuating magnetic fields, a magnetic damper would deteriorate the detection noise floor in the MRFM experiments. We therefore settled for the internal damping in the weak spring, which is obviously sub-optimal.

3.4.3 Cantilever temperature and frequency noise

To further verify the effectiveness of the vibration isolation, we have measured the effective cantilever temperature, following the procedure outlined by Usenko et al. [47] Any excitation of the cantilever besides the thermal excitation increases the motional energy of the cantilever to values larger than the thermal energy of the surrounding bath, in our case the bottom mass of the vibration isolation. To measure this effective cantilever temperature, we vary the temperature of the bottom mass between 10.5 mK and 700 mK. At every temperature, we take thermal spectra of the cantilever motion. Using the equipartition theorem, we can derive an effective cantilever temperature from the integrated power spectral density [111]:

$$k_{\text{B}}T_{\text{eff}} = k_0 \langle x^2 \rangle = k_0 \int_{f_1}^{f_2} (S_x - S_0) df, \quad (3.3)$$

where f_1 and f_2 define a small bandwidth around the cantilever resonance frequency, S_0 the background determined by the SQUID noise floor, and $S_x = c^2 S_V$, with c^2 being the conversion factor between SQUID voltage and cantilever motion. In effect, we calculate the area of the cantilever peak since this is proportional to the mean resonator energy and thereby the temperature. The resulting cantilever temperature as a function of the bath temperature for the two configurations with and without vibration isolation is shown in Fig. 3.8(a). We calibrate the data by assuming that $T_{\text{eff}} = T_{\text{bath}}$ for the four highest temperatures, where T_{bath} is the temperature of the bottom mass.

Without the vibration isolation, we observe a large spread in the measured cantilever temperatures. The black data in Fig. 3.8(a) show an example of two data sets, one taken during the night with low effective temperatures and the other taken during the day, where the cantilever temperature is increased. As expected, vibrations are most detrimental at low bath temperatures. Figure 3.8(b) shows the deviation of the effective temperature from the bath temperature depending on the time of the day (for bath temperatures below 100 mK). The measured effective temperatures show a clear day-night cycle. During the day, the distribution of measured values is much broader than one would expect purely based on the statistical fluctuations of the thermal cantilever energy. In the worst cases, the effective cantilever temperature can exceed 1.5 K, which corresponds to an equivalent cantilever motion of 0.5 nm.

When using the vibration isolation, the effective cantilever temperature is nearly equal to the bath temperature for temperatures down to approximately 100 mK, as shown by the red data points in Fig. 3.8(a). This means that above 100 mK,

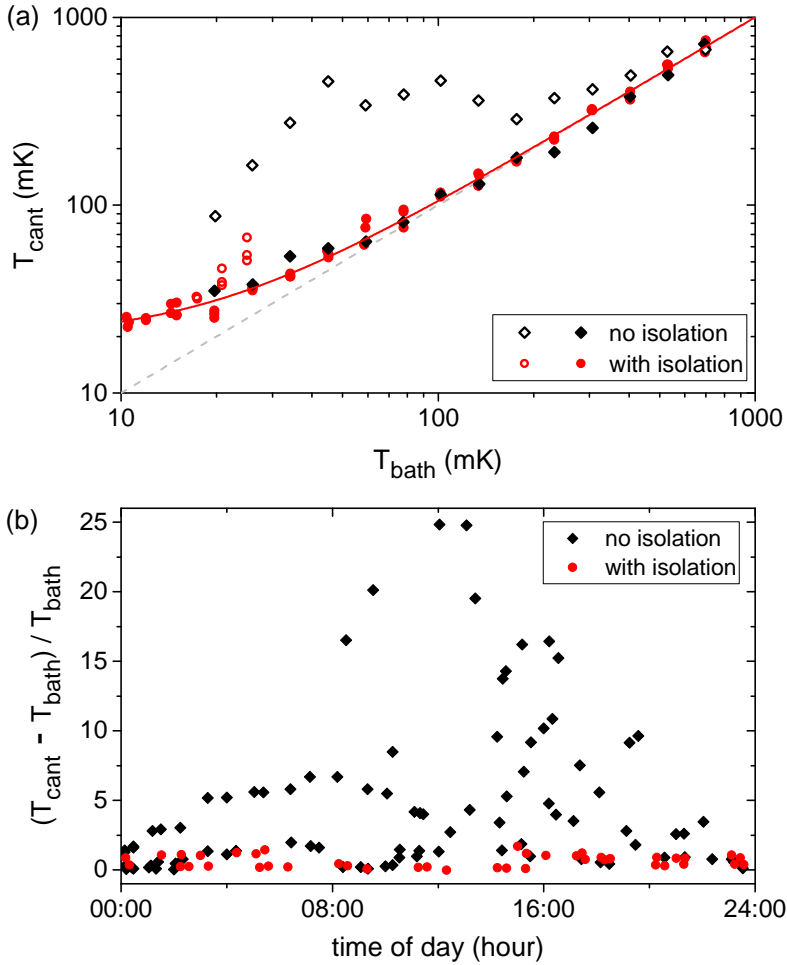


Figure 3.8: (a) Measurement of the effective cantilever temperature for various bath (bottom mass) temperatures. The black diamonds are data measured without vibration isolation, where the solid diamonds are measured during the night, and the open diamonds during the day. The red circles indicate the measured cantilever temperatures with proper vibration isolation. The open circles are measurements with an elevated cantilever temperature, as explained in the main text. (b) Deviation of the cantilever temperature from the bath temperature plotted against the time of day when the measurement was done. Only bath temperatures below 100 mK are considered. The black diamonds indicate the measurements without vibration isolation. The red circles were measured with vibration isolation.

the cantilever motion is thermally limited without being significantly disturbed by external vibrations. At lower temperatures, we measure effective temperatures that are slightly increased compared to the bath temperature. However, this increase is independent of the time of day at which the spectra were taken. The elevated effective temperatures are probably due to residual vibrations and a strongly decreasing heat conductivity at low temperatures. The red line is a fit to the data to a saturation curve of the form $T_{\text{eff}} = (T^n + T_0^n)^{1/n}$, where T_0 is the saturation temperature, and n is an exponent determined by the temperature dependence of the limiting thermal conductance. We obtain $T_0 = 19.7$ mK and $n = 1.5$. This saturation temperature implies an improvement of a factor of 75 when compared to the 1.5 K measured at certain times without the vibration isolation, and corresponds to an effective cantilever motion of 60 pm. Note that this is the total rms motion of the cantilever tip. To convert this to the displacement of the cantilever base, one needs to look at the motion spectral density of the tip and divide this by the transfer function of the cantilever. Exactly on resonance, the absolute rms motion of the tip is approximately $0.2 \text{ nm}/\sqrt{\text{Hz}}$. Using a Q of 20 000, this corresponds to a base vibration level of $10 \text{ fm}/\sqrt{\text{Hz}}$.

When performing the fit, several data points were not taken into account, indicated by open red circles in Fig. 3.8(a). Before taking those spectra, measurements at much higher temperatures had been performed and the system had not reached thermal equilibrium yet, leading to higher effective cantilever temperatures.

Note that we still observe some unwanted resonances close to the cantilever's resonance frequency, as visible in Fig. 3.7(a). These resonances prevent us from obtaining a reliable cantilever temperature when, due to a shifting cantilever frequency, these resonances start to overlap with the cantilever's resonance frequency. This indicates that there is room for even further improvements to get a cleaner spectrum.

For MRFM, the relevance of the low cantilever temperature can be demonstrated by looking at the frequency noise spectrum of the cantilever, as many MRFM protocols are based on detecting minute shifts of the resonance frequency [14, 37]. The frequency noise is measured by driving the cantilever to a calibrated amplitude $A = 60 \text{ nm}_{\text{rms}}$, using a piezoelement. A phase-locked loop (PLL) of a Zurich Instruments lock-in amplifier is used to measure the resonance frequency of the cantilever over time, from which we can calculate the frequency noise spectrum $S_{\delta f}$, which is shown in Fig. 3.9. The total frequency noise is given by the sum of three independent contributions [68]: the detector noise $S_{\text{det}} = \frac{S_{\text{xn}}}{A^2} f^2$ with S_{xn} being the position noise, the thermal noise $S_{\text{th}} = \frac{k_B T f_0}{2\pi A^2 k_0 Q}$, and a $1/f$ noise term $S_{1/f}$. In Fig. 3.9, the three terms are indicated by the blue, green, and orange solid lines, respectively, using a cantilever temperature of 15 mK, a measured $Q = 20500$, and a position noise $\sqrt{S_{\text{xn}}} = 9 \text{ pm}/\sqrt{\text{Hz}}$. The sum

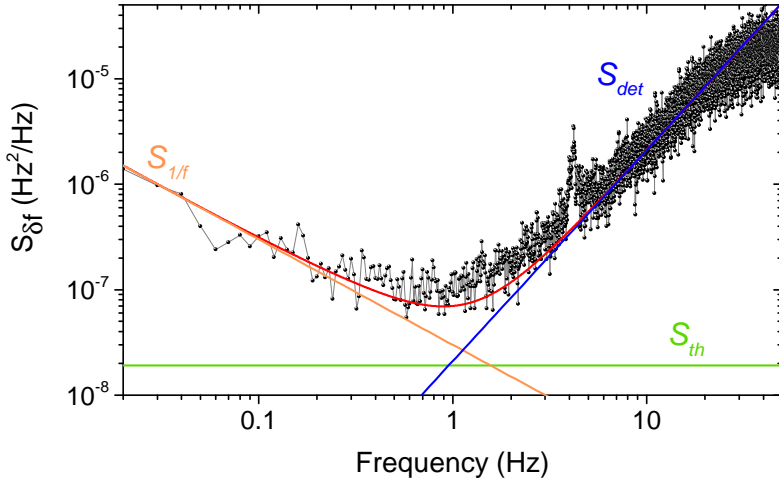


Figure 3.9: The frequency noise $S_{\delta f}$ of the MRFM cantilever with proper vibration isolation, measured at $T = 15$ mK. The cantilever is oscillated with an amplitude of $60 \text{ nm}_{\text{rms}}$. The frequency noise is composed of the detector noise S_{det} (blue), thermal noise S_{th} (green), and $1/f$ noise $S_{1/f}$ (orange). The sum of the three is shown in red. The frequency noise floor is found to be $0.3 \text{ mHz}/\sqrt{\text{Hz}}$.

of all individual contributions is shown in red. We find a total frequency noise of 0.4 mHz in a 1 Hz measurement BW. For a 3000 Hz resonator, this equates to a stability of 0.13 ppm . In typical frequency-shift-based MRFM experiments, the interaction between the cantilever and the spins in the sample induces frequency shifts of several mHz [11, 12, 35, 37]. Thus, the current frequency noise floor would allow for single-shot measurements or smaller sample volumes. Due to the relatively low cantilever amplitude and corresponding high detector noise, the detector noise was of similar magnitude as the thermal noise, so a further reduction of the noise floor is possible.

3.5 CONCLUSIONS

A mechanical vibration isolation intended for scanning probe microscopy experiments in a cryogen-free dilution refrigerator has been designed and constructed. The vibration isolation offers a large improvement in the measured vibrations in combination with an outstanding thermal conductance between the mixing chamber and the bottom of the isolation, with a base temperature of 10.5 mK at the bottom mass. The high cooling power of $113 \text{ }\mu\text{W}$ at 100 mK means that a low temperature can be maintained even for experiments where some power dissipation cannot be avoided. The

equivalence between electrical and mechanical filters offers a simple and convenient approach to precisely calculate all properties of a mechanical low pass filter in the design phase. The theory shows a large tolerance for the exact mechanical properties of all components, allowing for tailoring of the system to various environments.

Measurements of the effective temperature of a soft mechanical resonator indicate that an effective cantilever temperature of about 20 mK can be achieved. This combination of minimal vibrational noise and low energies in the resonator opens up the possibility for exciting experiments, for instance testing models of wave-function collapse [97, 98, 112], as well as scanning probe investigations of materials showing exotic behavior at very low temperature.

Furthermore, the ultralow frequency noise achieved using our new vibration isolation can be used for even more sensitive frequency-shift-based MRFM protocols, in which the coupling between the resonator and spins in the sample induces minute changes in the effective stiffness, and thereby the resonance frequency [11, 37, 113]. The lower cantilever effective temperature directly translates to a lower thermal force noise in the cantilever, given by $S_F = 4k_B T \Gamma BW$, with Γ being the damping of the resonator and BW the measurement bandwidth. For the experimental parameters described in Sec. 3.4.2 and the measured cantilever temperature of 20 mK, we find a force noise $\sqrt{S_F} \lesssim 500 \text{ zN}/\sqrt{\text{Hz}}$. This extreme force sensitivity would allow for the MRFM detection volume to be scaled down more and more towards single nuclear spin resolution.

4

FEASIBILITY OF IMAGING IN NUCLEAR MAGNETIC RESONANCE FORCE MICROSCOPY USING BOLTZMANN POLARIZATION

We report on magnetic resonance force microscopy measurements of the Boltzmann polarization of nuclear spins in copper by detecting the frequency shift of a soft cantilever. We use the time-dependent solution of the Bloch equations to derive a concise equation describing the effect of radio-frequent (RF) magnetic fields on both on- and off-resonant spins in high magnetic field gradients. We then apply this theory to saturation experiments performed on a 100 nm thick layer of copper, where we use the higher modes of the cantilever as source of the RF field. We demonstrate a detection volume sensitivity of only $(40 \text{ nm})^3$, corresponding to about $1.6 \cdot 10^4$ polarized copper nuclear spins. We propose an experiment on protons where, with the appropriate technical improvements, frequency-shift based magnetic resonance imaging with a resolution better than $(10 \text{ nm})^3$ could be possible. Achieving this resolution would make imaging based on the Boltzmann polarization competitive with the more traditional stochastic spin-fluctuation based imaging, with the possibility to work at milliKelvin temperatures.

This chapter has been published as M. de Wit *et al.*, “Feasibility of imaging in nuclear Magnetic Resonance Force Microscopy using Boltzmann polarization”, *Journal of Applied Physics*, Vol. 125, p. 083901, Feb. 2019

4.1 INTRODUCTION

Magnetic Resonance Force Microscopy (MRFM) is a technique that combines magnetic resonance protocols with an ultra sensitive cantilever to measure the forces exerted by extremely small numbers of spins, with the immense potential of imaging biological samples with nanometer resolution [4, 5, 62]. In the last 20 years, great steps have been taken towards this goal, with some milestones including the detection of a single electron spin [12], the magnetic resonance imaging of a tobacco mosaic virus with a spatial resolution of 4 nm [16], and more recently the demonstration of a one-dimensional slice thickness below 2 nm for the imaging of a polystyrene film [17]. The experiments are typically performed by modulating the sample magnetization in resonance with the cantilever, and then measuring either the resulting change in the oscillation amplitude (force-based) or the frequency shift (force-gradient based).

Both the force-based and force-gradient based experiments have some severe technical drawbacks, mainly associated to the cyclic inversion of the spin ensemble. For the coherent manipulation of the magnetization, alternating magnetic fields on the order of several mT are required [57, 114]. The dissipation associated with the generation of these fields is significant and prevents experiments from being performed at milliKelvin temperatures, even for low duty-cycle MRMF protocols like cyclic-CERMIT [11, 14]. Furthermore, the requirement that the magnetization is inverted continuously during the detection of the signal means only samples with a long rotating-frame spin-lattice relaxation time $T_{1\rho}$ are suitable.

For imaging of nuclei, previous experiments have almost exclusively focused on measuring the statistical polarization of the spin ensemble. However, the possibility to use the Boltzmann polarization instead would dramatically improve the efficiency of the measurement, as averaging N times enhances the power signal-to-noise ratio (SNR) by a factor of N for Boltzmann based measurements, compared to \sqrt{N} for statistical polarization signals. There have been MRFM experiments based on the Boltzmann polarization, for instance in order to measure the relaxation times of nuclei [11, 35, 37], but these experiments lacked the volume sensitivity required for imaging with a spatial resolution comparable to the statistical experiments.

In this work, we present measurements of the Boltzmann polarization of a copper sample at a temperature of 21 mK by detecting the frequency shift induced by a saturation experiment. We derive the time-dependent solution to the Bloch equations appropriate for typical MRFM experiments, obtaining a concise equation for the non-equilibrium response of both on- and off-resonant spins to a radio-frequent (RF) pulse. Furthermore, we demonstrate that we can use higher modes of the cantilever as the

source of the alternating field in order to generate the required RF fields to saturate the magnetization of the spins with minimal dissipation [50]. These results suggest that imaging based on the Boltzmann polarization could be possible, allowing for the first MRFM imaging experiments performed at temperatures down to 10 mK and using the magnet-on-tip geometry, as opposed to the sample-on-tip geometry more commonly found. We substantiate this claim by using the specifications of the current experiments to calculate the resolution for an imaging experiment on protons based on measuring the Boltzmann polarization.

4.2 METHODS

4.2.1 Experimental setup

We improve on earlier measurements in our group on nuclear spins in a copper sample. The setup and measurement procedure strongly resemble those used in that previous work [37]. The operating principle of the MRFM is shown in Fig. 4.1(a). The heart of the setup is a soft single-crystal silicon cantilever (spring constant $k_0 = 70 \mu\text{Nm}^{-1}$) [7] with a magnetic particle at the end with a radius $R_0 = 1.7 \mu\text{m}$, resulting in a natural resonance frequency $f_0 = \omega_0/(2\pi) \sim 3.0 \text{ kHz}$, an intrinsic Q-factor $Q_0 \sim 3 \cdot 10^4$, and a thermal force noise at 20 mK of $0.4 \text{ aN}/\sqrt{\text{Hz}}$. The magnet induces a static magnetic field B_0 which can be well approximated by the field of a perfect magnetic dipole. The strength of the field of the magnet reduces quickly as the distance to the center of the magnet increases, creating a large magnetic field gradient. For typical experimental parameters the magnetic field is of the order of a few tens to a few hundred mT, with magnetic field gradients of approximately $100 \text{ mT}/\mu\text{m}$. When the cantilever is placed at a height h above a sample, spins in the sample couple to the resonator via the magnetic field gradient, inducing a frequency shift (see Sec. 4.2.5). An RF pulse with frequency ω_{RF} can be used to remove the polarization of the spins that are resonant with this pulse, i.e. the spins that are within the resonant slice where $|B_0| = \omega_{\text{RF}}/\gamma$, with γ the gyromagnetic ratio of the spins (in Fig. 4.1(a) the resonant slice is marked in red). We will refer to this procedure as a saturation experiment or saturation pulse. The theoretical background of the saturation experiment is given in Sec. 4.2.4.

Our particular MRFM setup is designed to be operated at temperatures close to 10 mK using a detection scheme based on a pickup loop (shown in Fig. 4.1(b)) and superconducting quantum interference device (SQUID) [47]. Additionally, we use a superconducting NbTiN RF wire to send RF currents to the sample [55]. The MRFM setup is mounted at the bottom of a mechanical vibration isolation stage, and

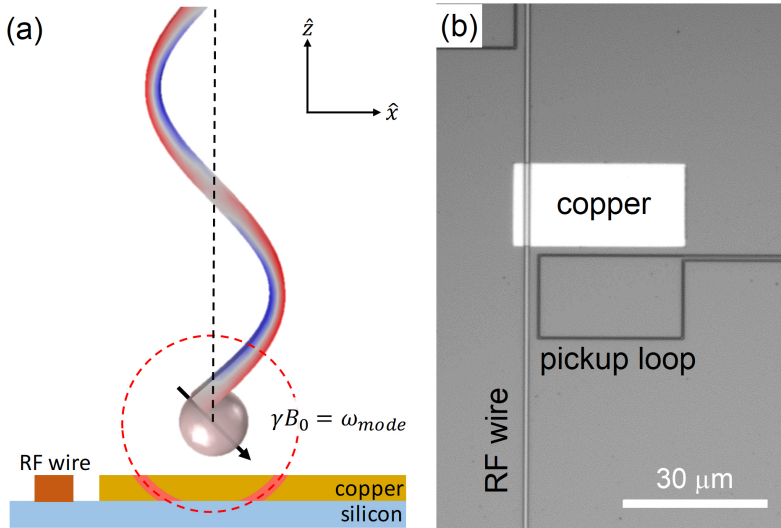


Figure 4.1: (a) Schematic of the measurement setup. An RF wire is used to generate an RF field B_{RF} directly or to excite higher modes of the cantilever to generate B_{RF} fields with minimal dissipation. The RF pulse removes the Boltzmann polarization of spins located within and near the resonant slice (red region), inducing mHz shifts of the cantilever’s fundamental resonance frequency. (b) Optical microscope image of the detection chip, showing the NbTiN pickup loop and RF wire, and the copper sample with a thickness of 100 nm.

the cryostat has been modified to reduce vibrations originating from the pulse tube refrigerator [77].

The RF pulse can be applied using two methods, both shown in Fig. 4.1(a). First of all, we can use an RF wire to send an alternating current, which generates a magnetic field directly. This allows for precise control of the pulse shape and amplitude, but at the cost of some heating of the sample due to AC dissipation in the superconducting RF wire. The amplitude of the RF field is given by $B_{RF} = \mu_0 I / 2\pi r$, with r the distance to the RF wire, dictating that all measurements have to be done as close to the RF wire as possible (preferably within several micrometers). At a distance of $5 \mu\text{m}$ from the RF wire, we can generate magnetic fields (in the rotating frame of the spins, see Sec. 4.2.4) of up to 0.3 mT. An alternative method to generate the required RF field is by using the higher modes of the cantilever, the proof of concept of which was recently demonstrated by Wagenaar et al. [50]. Generating RF fields using the higher modes can be done with a much smaller current in the RF wire to generate a magnetic drive field, or by using a piezo at the base of the cantilever, allowing experiments at larger distances from the RF wire, or even without one. In our experiment, we use a small current in the RF wire (on the order of $\sim 10 \mu\text{A}$) to

excite one of the higher modes of the cantilever, as illustrated in Fig. 4.1(a). The motion of the higher mode induces a small rotation of the magnet, which results in the generation of an amplified B_{RF} at the frequency of the excited higher mode perpendicular to the tip field. In this way, RF fields can be generated with negligible dissipation.

The copper sample used in the experiment is patterned on the detection chip close to both the RF wire and the pickup loop, as shown in Fig. 4.1(b). The copper sample is a sputtered film with a thickness of 100 nm, capped with a 20 nm layer of gold to prevent oxidation. The thickness of the sample was chosen to be 100 nm in order to reduce eddy currents in the copper, which deteriorate the Q-factor of the cantilever and thereby the measurement sensitivity (for metal films with a thickness less than the skin depth, eddy current dissipation scales with the cube of the thickness [115]). Copper overlaps with the RF wire in order to give the sample a well defined potential. Besides the thermal conductance of the silicon substrate, there is no additional thermalization used to cool the copper. The cantilever can be positioned above the copper with a lateral accuracy of several micrometers. The relevant nuclear magnetic resonance (NMR) properties of copper for an MRFM experiment are detailed in the supplementary material.

4.2.2 Frequency noise

We have employed a series of improvements to the setup to enhance the frequency noise floor of the measurement, and thus increase the sensitivity. The improvement is obvious when looking at the noise spectrum of the frequency, as shown in Fig. 4.2. The spectrum is measured by driving the cantilever with an amplitude of 43 nm_{rms} and tracking the resonance frequency using a phase-locked loop (PLL) of a Zurich Instruments lock-in amplifier with a detection bandwidth of 40 Hz. The PLL feedback signal is sent to a spectrum analyzer. In black we see the frequency noise spectrum of the current setup, while in red we see the frequency noise spectrum from the experiment in 2016 on a 300 nm thick copper film performed in our group [37]. Both spectra were measured at a height of 1.3 μm above a copper sample. The total frequency noise is given by the sum of the thermal noise, the detection noise, and the 1/f noise typically attributed to the sample [37, 116]:

$$P_{\delta f}(f) = P_{\delta f}^{\text{thermal}} + P_{\delta f}^{\text{det}} f^2 + P_{\delta f}^{\text{sample}} f^{-1} \quad (4.1)$$

The noise reduction of nearly 2 orders of magnitude is due to a combination of several technical improvements. Improved vibration isolation and cantilever thermalization have reduced the thermodynamic temperature of the cantilever from 132 mK to less

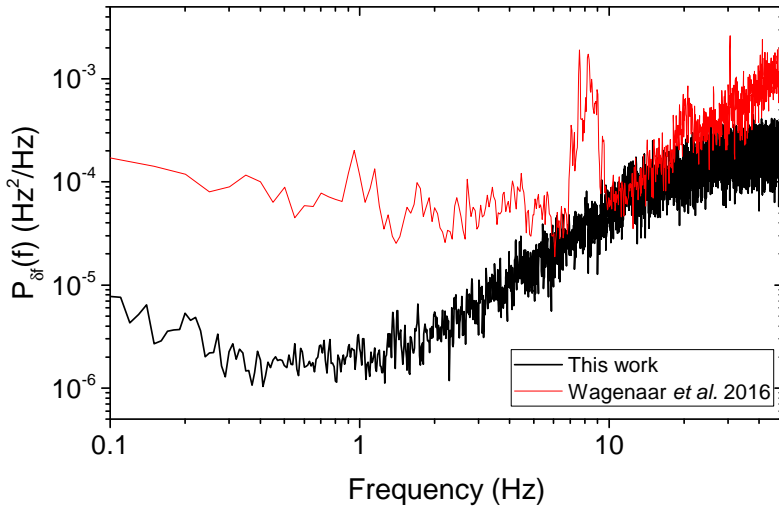


Figure 4.2: Frequency noise spectrum $P_{\delta f}$ measured at a height of $1.3 \mu\text{m}$. In red we see the frequency noise spectrum from the initial experiment in our group, measured with a cantilever amplitude of $110 \text{ nm}_{\text{rms}}$ [37]. In black we see the current experiment, measured with a cantilever amplitude of $43 \text{ nm}_{\text{rms}}$. The roll-off of the noise at higher frequencies in the black spectrum is due to the bandwidth of the PLL, which was set at 40 Hz .

than 50 mK . An improved design of the pickup loop resulted in an amplitude detection noise floor of $30 \text{ pm}/\sqrt{\text{Hz}}$, determined from the measured transfer between the cantilever motion and the SQUID's output voltage. This allows for a much lower cantilever drive amplitude with the same detection frequency noise. The biggest improvement seems to be the reduction of the thickness of the copper film. Because the dissipated power of the eddy currents in the film scales strongly with the thickness of the film, we find that the measured Q-factor at $1.3 \mu\text{m}$ from the sample has increased from 317 for the 300 nm film to almost 5000 for the 100 nm film. This reduces all three contribution to the frequency noise, particularly the $1/f$ noise which is mainly attributed to eddy currents in the sample¹. The thermal noise floor using these parameters is estimated to be $0.7 \text{ mHz}/\sqrt{\text{Hz}}$, so the data in Fig. 4.2 are not thermally limited. With a 1 Hz detection bandwidth, the integrated frequency noise is as low as 1.8 mHz .

¹The conjecture that the eddy currents dominate the $1/f$ noise follows from the dependence of the $1/f$ noise on the Q-factor, as discussed in Fig. 2 in the paper by Wagenaar et al. [37].

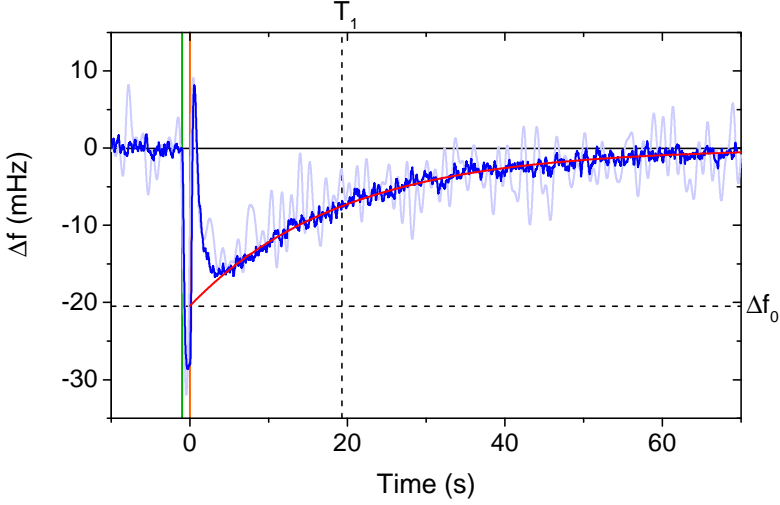


Figure 4.3: Example of a typical measurement (at $T = 40$ mK) where we show the frequency shift Δf with respect to the equilibrium frequency f_0 . The light blue line shows a single measurement of the frequency shift (after a 1 Hz low-pass filter). The dark blue line shows 50 averages. The red solid line is an exponential fit to the data following Eq. 4.2. The green and orange vertical lines indicate the start and end of the saturation pulse.

4.2.3 Measurement procedure

A typical saturation recovery measurement (performed at a temperature $T = 40$ mK) is shown in Fig. 4.3. Again a PLL is used to measure the frequency shift $\Delta f = f(t) - f_0$. At $t = 0$, an RF pulse with a certain duration t_p and strength B_{RF} is turned on. The start and end are indicated by the green and orange vertical lines in Fig. 4.3. During the pulse, we observe frequency shifts that we attribute to a combination of electrostatic effects and slight local heating of the sample. After the pulse, the frequency shift relative to f_0 is measured. The obtained recovery curve can be fitted to

$$\Delta f(t) = \Delta f_0 e^{-(t-t_0)/T_1}, \quad (4.2)$$

with Δf_0 the direct frequency shift at time t_0 , the end of the pulse. The light blue curve in Fig. 4.3 shows the result of a single measurement of the frequency shift (with a 1 Hz low-pass filter), and the dark blue curve shows the result of 50 averages. In red we show the best fit to the data using Eq. 4.2.

4.2.4 Spin dynamics in MRFM

In order to fully understand the observed frequency shifts, we need to find the final magnetization of the spins coupled to the magnetic field of our cantilever after a saturation pulse. The behaviour of spins in alternating magnetic fields is well understood from conventional NMR, but the analysis is often limited to steady-state solutions [117]. This limit works well for most NMR applications where the alternating fields are of sufficient strength and duration that the magnetization of the spin ensemble has reached an equilibrium during the pulse, but this does not necessarily work for MRFM due to the large magnetic field gradient, resulting large number of off-resonant spins, and the often weak oscillating magnetic fields. Therefore, we will derive equations for the time dependence of the magnetization of spins during an RF pulse, also for spins not meeting the resonance condition. These equations are then used to derive the effective resonant slice thickness in an MRFM experiment, a crucial component trying to decrease the detection volume and thereby optimize the imaging resolution.

The time evolution of spins subjected to a large static magnetic field (B_0) and a small alternating magnetic field (B_{RF}) perpendicular to the static field has long been understood using the Bloch equations [118]. In the rotating frame, the equations of motion of the magnetization $\mathbf{m}(t)$ subjected to an effective magnetic field $\mathbf{B}_{\text{eff}} = (B_0 - \omega/\gamma)\hat{\mathbf{k}} + B_{\text{RF}}\hat{\mathbf{i}}$ are given by

$$\begin{aligned}\frac{dm_x}{dt} &= -\Delta\omega m_y - \frac{m_x(t)}{T_2} \\ \frac{dm_y}{dt} &= \omega_1 m_z + \Delta\omega m_x - \frac{m_y(t)}{T_2} \\ \frac{dm_z}{dt} &= -\omega_1 m_y - \frac{m_z(t) - m_0}{T_1}\end{aligned}\tag{4.3}$$

Here γ is the gyromagnetic ratio of the spins, T_1 and T_2 are the spin-lattice (longitudinal) and spin-spin (transverse) relaxation times, the detuning $\Delta\omega \equiv \omega - \omega_0$ with $\omega_0 = \gamma B_0$ the Larmor frequency, and $\omega_1 \equiv \gamma B_{\text{RF}}$. m_0 is the initial magnetization in thermal equilibrium. $\hat{\mathbf{k}}$ is the unit vector pointing in the direction of the B_0 field. To solve this system of differential equations, it is convenient to rewrite them in vector notation as

$$\dot{\mathbf{m}} = A\mathbf{m} + \mathbf{b},\tag{4.4}$$

with the source term $\mathbf{b} = \frac{m_0}{T_1} \hat{\mathbf{k}}$, and A given by

$$A = \begin{pmatrix} -\frac{1}{T_2} & -\Delta\omega & 0 \\ \Delta\omega & -\frac{1}{T_2} & \omega_1 \\ 0 & -\omega_1 & -\frac{1}{T_1} \end{pmatrix} \quad (4.5)$$

The steady state solution is now easy to derive by solving the differential equation after setting $\dot{\mathbf{m}} = 0$. Note that m_x and m_y are rotating with the Larmor frequency around the z-axis. As the resonance frequencies of the cantilevers used in MRFM are typically much lower than the Larmor frequency, any coupling of these two components to the cantilever averages out over time. Therefore, we are only interested in the z-component of the magnetization, which is the same in the rotating frame as in the laboratory frame [117, 119]:

$$\begin{aligned} m_{z,\infty} &= \frac{1 + \Delta\omega^2 T_2^2}{1 + \Delta\omega^2 T_2^2 + \omega_1^2 T_1 T_2} m_0 \\ &\equiv p_z m_0 \end{aligned} \quad (4.6)$$

In the last line we defined p_z as the fraction of the magnetization that is removed by the B_{RF} field if it is left on continuously.

In MRFM experiments the steady state solution described by Eq. 4.6 is often not enough, as the RF pulses are not necessarily of sufficient strength and duration to fully saturate the magnetization of a spin ensemble. The time-dependent solution where $\dot{\mathbf{m}} \neq 0$ is given by the sum of the homogeneous solution ($\mathbf{b} = 0$) and the non-homogeneous steady state solution:

$$\begin{aligned} m_z &= m_{z,\infty} + (m_0 - p_z m_0) e^{\lambda_z t} \\ &= p_z m_0 + (m_0 - p_z m_0) e^{-\frac{t}{T_1 p_z}}, \end{aligned} \quad (4.7)$$

where $\lambda_z = 1/(T_1 p_z)$ is the third eigenvalue of the matrix A . Inserting this equation into Eq. 4.4 confirms that it is a valid solution. The equation above gives the time-dependent z-magnetization of a spin ensemble after an RF magnetic field is turned on and left on. In deriving it, we have assumed that $T_2 \ll T_1$ and that the strength of the RF field is weak such that $\omega_1 T_2 \ll 1$. These assumptions give us a concise equation much more convenient for saturation experiments in MRFM than the expressions found in the general case [120, 121].

The consequences of Eq. 4.7 can be seen in Fig. 4.4. Depending on the precise pulse parameters, even the spins that do not meet the resonance condition by a detuning $\Delta\omega$ can lose (part of) their magnetization due to the RF pulse. The calculation is done assuming $T_1 = 25$ s and $T_2 = 0.15$ ms, typical values for copper at $T = 40$ mK

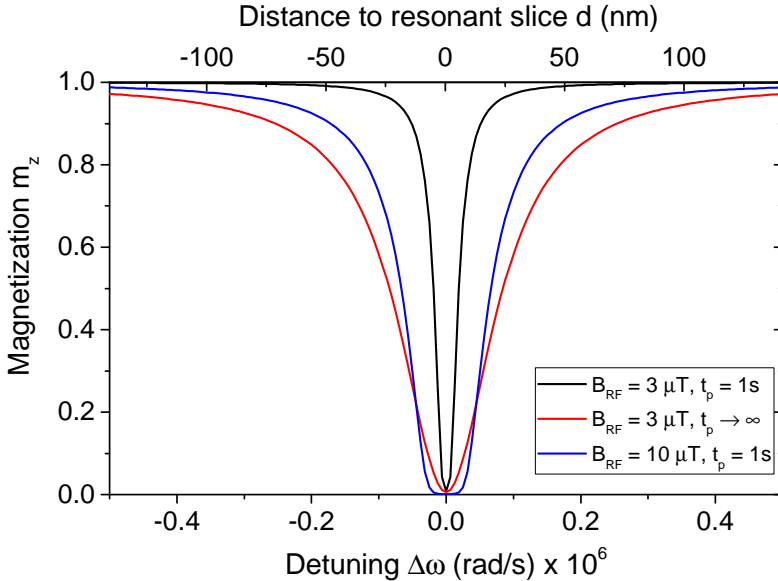


Figure 4.4: Calculated magnetization m_z after three different RF pulses: In black after a 1 s pulse with a strength of $3 \mu\text{T}$, in red an infinitely long pulse with the same strength, and in blue a 1 s pulse with a strength of $10 \mu\text{T}$. The bottom axis shows the detuning $\Delta\omega$, while the bottom axis shows the corresponding distance to the resonant slice, calculated using Eq. 4.8 assuming a magnetic field gradient $\nabla_r B_0 = 5 \cdot 10^4 \text{ T/m}$.

[37]. The detuning can be translated to a distance to the resonant slice (the region where $\Delta\omega = 0$) using

$$d \approx \frac{\Delta\omega}{\gamma \nabla_r B_0} \quad (4.8)$$

where $\nabla_r B_0$ is the gradient of the magnetic field in the radial direction.

4.2.5 Calculation of frequency shifts

To calculate the frequency shift Δf_0 due to the saturation of the magnetization of the spins in resonance, we first look at the shift of the cantilever resonance frequency due to the coupling with a single spin. For this we follow a recent theoretical analysis of the magnetic coupling between a paramagnetic spin and the cantilever by De Voogd et al. [52]. In our case, where the frequency of the RF pulse $\omega_{\text{RF}} \gg \frac{1}{T_2}$ and $\omega T_1 \gg 1$, a single spin induces a stiffness shift given by

$$\Delta k = \langle m \rangle \left(|B''_{\parallel B_0}| + \frac{1}{B_0} |B'_{\perp B_0}|^2 \right) \quad (4.9)$$

The primes and double primes refer to the first and second derivatives, respectively, with respect to the fundamental direction of motion of the cantilever. $|\mathbf{B}''_{||B_0}|$ is the component along B_0 . $|\mathbf{B}'_{\perp B_0}|$ is the perpendicular component. $\langle m \rangle$ is the mean Boltzmann polarization.

The effect of an RF pulse is to partially remove the magnetization of the spins by an amount given by:

$$\Delta m = \langle m \rangle - m_z \quad (4.10)$$

$$= \langle m \rangle (1 - p_z) \left(1 - e^{-\frac{t_p}{T_1 p_z}} \right), \quad (4.11)$$

where we set m_0 equal to $\langle m \rangle$, i.e., we assume the system is in thermal equilibrium before the pulse such that the initial magnetization is equal to the Boltzmann polarization. Please be reminded that Δm is position dependent via p_z due to the detuning $\Delta\omega$, which increases with the distance to the resonant slice and also depends on the precise RF pulse parameters. We can calculate the total measured frequency shift after an RF pulse by integrating over all spins in the sample including the position dependent demagnetization Δm

$$\Delta f_0 = -\frac{1}{2} \frac{f_0}{k_0} \rho \int \Delta m \left(|\mathbf{B}''_{||B_0}| + \frac{1}{B_0} |\mathbf{B}'_{\perp B_0}|^2 \right) dV, \quad (4.12)$$

with $\rho = 85$ spins/nm³ the spin density of copper. Alternatively, one can also sum the contribution of individual voxels, as long as the size of the voxels is small compared to the effective resonant slice width.

4.3 FREQUENCY SHIFTS MEASURED IN COPPER

In this section, we present measured frequency shifts using the higher modes of our cantilever as a source for the RF-field, on one hand to demonstrate that the higher modes can indeed be used to perform full-fledged saturation experiments in MRFM, and on the other to give some experimental verifications of the theory presented in the Sec. 4.2.

We demonstrate the effectiveness of using the higher modes of the cantilever as an RF field source, by exciting 4 different higher modes of the cantilever by sending a current of 21 μA_{rms} through the RF wire. The frequencies of the selected higher modes are 360 kHz, 540 kHz, 756 kHz, and 1.009 MHz. The positions of the resonant slices corresponding to these frequencies are shown in Fig. 4.5(a). The height of the

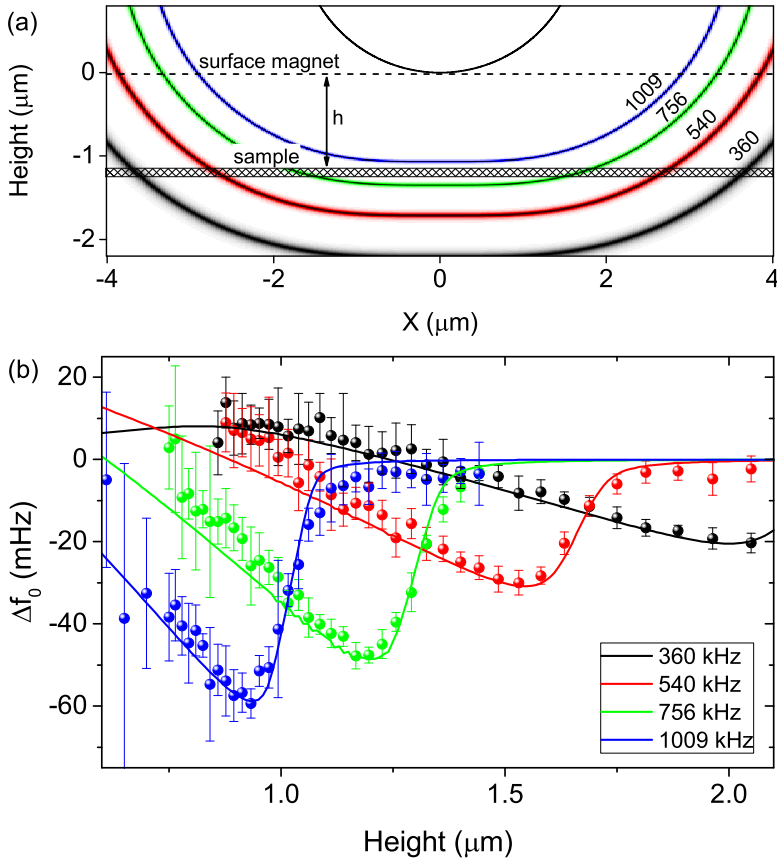


Figure 4.5: (a) Positions of the resonant slices corresponding to the cantilever higher modes at 360 (black), 540 (red), 756 (green), and 1009 (blue) kHz. The black sphere at the top of the image represents the cantilever magnet (radius $1.7 \mu\text{m}$, to scale). (b) Direct frequency shift Δf_0 versus height h after exciting the spins by using the RF wire to drive the higher modes of the cantilever indicated in (a), measured at $T = 30 \text{ mK}$. Solid lines are the calculated signals for a pulse duration $t_p = 0.3 \text{ s}$, and with B_{RF} a free parameter. The error bars indicate the standard deviation of 10 single-shot measurements.

magnet above the sample determines which of the resonant slices is in the sample, and how much signal each of these slices produces. In Fig. 4.5(b), we show the measured direct frequency shift Δf_0 as a function of the height for each of the higher modes, averaging over 10 single measurements. The error bars are determined by fitting 10 single-shot measurements and calculating the standard deviation of the fitted Δf_0 . The solid lines in the figure are the calculated signals based on Eq. 4.12 using $t_p = 0.3 \text{ s}$. As the precise amplitude of the mechanically generated RF field is difficult to control since it depends on the distance between the magnet and the RF wire, the

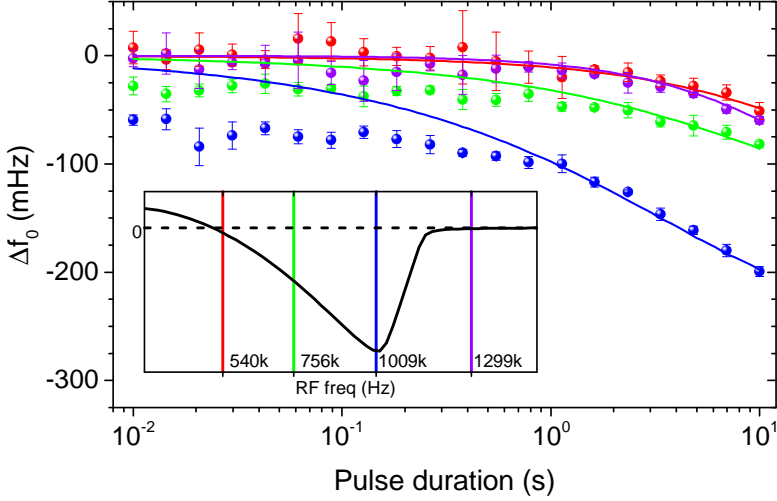


Figure 4.6: Effect of the excitation pulse duration t_p on the measured direct frequency shift Δf_0 for the higher modes of the cantilever at 540 (red), 756 (green), 1009 (blue), and 1299 (purple) kHz, measured at $h = 0.95 \mu\text{m}$ and $T = 30 \text{ mK}$. The inset shows the calculated direct frequency shift as a function of the RF frequency, and also shows the position of the higher modes in this calculation. As t_p increases, the resonant slice broadens and the direct frequency shift increases as expected from the resonant slice positions indicated in the inset. The error bars indicate the standard deviation of 5 single-shot measurements.

height of the magnet above the sample, and the Q-factor of the higher mode, the strength of the RF field is the only free fitting parameter.

From the fits we obtain fields of 38, 35, 38, and 33 μT for the 4 higher modes as mentioned before. Evidently, the different higher modes enter the sample at the predicted heights, with the correct overall magnitude of the direct frequency shift. The small deviation between the data and calculation at the lower heights probably results from a slightly changing B_{RF} . This measurement can be considered as a crude one-dimensional scan of the sample. Furthermore, considering that the current of 21 μA_{rms} corresponds to a field of only 0.2 μT at the position of the cantilever, 7 μm away from the RF wire, this measurement indicates that using the higher modes to generate the RF field results in an amplification of the RF field strength of more than a factor of 160. No heating was observed on the sample holder, indicating a dissipated power $< 1 \text{ nW}$.

We can further demonstrate the effect of the pulse parameters on the effective resonant slice width by doing a variation on the previous experiment. We now keep the sample at a constant height, and vary the duration of the RF current used to excite

each of the higher modes in order to broaden the resonant slice. By comparing the measured increase of the signal for the various higher modes to the signal we expect from Eqs. 4.7 and 4.12, we can confirm the applicability of these equations. This experiment is shown in Fig. 4.6. The inset shows the calculated frequency shift as a function of the RF frequency, as well as the position of the higher modes. From the inset we see that for short pulses (a narrow resonant slice) we expect no signal from the 540 kHz and 1.299 MHz higher modes, some signal from the 756 kHz higher mode, and most signal from the 1.009 MHz higher mode. This behaviour is also observed in the main figure, where the solid lines are the calculated frequency shifts based on Eq. 4.12. As t_p is increased, even the resonant slices whose center is not in the sample broaden enough that off-resonant spins start to create measurable frequency shifts, with a good correlation between theory and experiment. The mismatch between the measured and calculated signal for very short pulse durations is attributed to the large Q-factor of the higher modes, which can be as high as 10^6 , resulting in characteristic time constants of up to 1 s. In that case, driving the higher mode for a very short time still results in a long effective pulse duration determined by the slow ringdown of the higher mode.

4

4.4 DEMONSTRATION OF VOLUME SENSITIVITY

As shown in Fig. 4.2, we have a very clean frequency noise spectrum. To make full use of this, we have attempted to determine our optimal frequency resolution. To achieve this, we make a small adjustment to the measurement scheme, by switching off the cantilever drive a couple of seconds before we apply the RF pulse. The amplitude of the fundamental mode decays quickly due to the relatively low Q-factor of the fundamental mode close to the sample. By the time the pulse is sent, the amplitude of the cantilever is thermally limited to less than 0.1 nm. Directly after the pulse, the cantilever drive is switched back on to measure the resonance frequency shift. In this way, we prevent broadening of the resonant slice due to the cantilever amplitude of about $30 \text{ nm}_{\text{rms}}$, and are able to achieve very narrow resonant slices. Fig. 4.7 shows the relaxation curve measured at $T = 21 \text{ mK}$ and $h = 1.0 \text{ }\mu\text{m}$, after an 882 kHz RF pulse with $B_{\text{RF}} = 172 \text{ }\mu\text{T}$ and $t_p = 80 \text{ }\mu\text{s}$. The blue curve shows the result of 410 averages with a total measurement time of over 10 hours, while the red curve is a fit to the data following Eq. 4.2, from which we extract a direct frequency shift of -5.4 mHz . The inset shows the difference between the measured data and the fit, indicating that we can measure the frequency shift with a standard deviation of 0.1 mHz, consistent with the integrated frequency noise calculated from Fig. 4.2 and the number of averages.

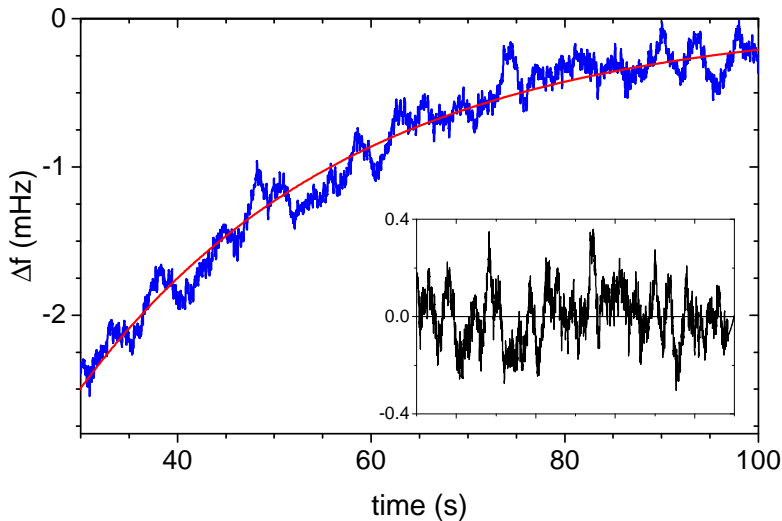


Figure 4.7: Relaxation curve (1 Hz low-pass filter, 410 averages) measured at $h = 1.0 \mu\text{m}$ and $T = 21 \text{ mK}$, for a pulse at frequency 882 kHz with $B_{\text{RF}} = 172 \mu\text{T}$ and $t_p = 80 \mu\text{s}$. The solid red line is a fit to Eq. 4.2, from which we extract $\Delta f_0 = -5.4 \text{ mHz}$. The inset shows the difference between the data and the exponential fit, indicating a standard deviation of the measured frequency shift of 0.1 mHz.

We can try to estimate the total detection volume that was necessary to generate this signal. In order to do so, we make the simplifying assumption that there exists a critical detuning $\Delta\omega_C$ such that all spins at a detuning smaller than the critical detuning (i.e. spins that feel a magnetic field between $B_0 - \Delta\omega_C/\gamma$ and $B_0 + \Delta\omega_C/\gamma$) are fully saturated, and spins at a detuning larger than the critical detuning are completely unaffected by the pulse. We then calculate the signal for various values of $\Delta\omega_C$ until we find the value for which the calculation matches the experiment. By dividing the sample in small voxels and summing all voxels that satisfy the condition specified above for the correct $\Delta\omega_C$, we find an estimate for the detection volume.

For the data presented in Fig. 4.7 we find that this signal is the result of a critical detuning $\Delta\omega_C/(2\pi) = 2.1 \text{ kHz}$, equivalent to a resonant slice with a full width of approximately 4 nm. This corresponds to a total detection volume of $(152 \text{ nm})^3$, with a noise floor equal to $(40 \text{ nm})^3$. This latter volume contains a total of $5.5 \cdot 10^6$ spins at a Boltzmann polarization of about 0.3%, corresponding to about $1.6 \cdot 10^4$ fully polarized copper nuclear spins².

²This noise floor can also be expressed in terms of the magnetic moment, leading to a value of approximately $2 \cdot 10^{-22} \text{ J/T}$.

Note that for very small resonant slice widths, spin diffusion might be a relevant factor [33]. However, only spin diffusion during the RF pulse influences the size of the detection volume. Since in this experiment the pulse duration is only 80 μs , we calculate that the spin diffusion length is less than 0.1 nm (see supplementary material for details about the expected spin diffusion), much smaller than the estimated resonant slice width of 4 nm.

4.5 IMAGING PROTONS

4

With the volume sensitivities achieved on copper as demonstrated in Sec. 4.4, it is worthwhile to discuss what such an experiment would look like for a sample containing protons, the prime target spin for imaging purposes. Therefore, in this section, we will calculate the signals that can be expected from a proton-rich sample, under the assumption that it is possible to achieve the same low frequency noise as in the current experiment on copper. ^1H spins have spin $S = 1/2$, gyromagnetic ratio $\gamma_{\text{H}}/(2\pi) = 42.6$ MHz/T, and a magnetic moment $\mu_{\text{H}} = 1.41 \cdot 10^{-26} \text{ J/T}$. For MRFM, proton spins are generally a bit more favourable than copper spins, as the higher gyromagnetic ratio and magnetic moment mean a higher Boltzmann polarization and a larger coupling between a single spin and the cantilever. We assume a proton spin density $\rho_{\text{H}} = 50$ spins/nm³, a typical value for biological tissue and polymers [16, 116]. Furthermore, we assume $T_1 = 30$ s and $T_2 = 0.1$ ms. Note that the exact values for the relaxation times do not matter that much as long as the conditions used for the derivation of Eqs. 4.7 and 4.9 are met, and the RF pulse duration is short compared to T_1 .

We calculate the total volume necessary to get a frequency shift of 1.8 mHz, a signal that can be measured in a single shot experiment assuming the SNR achieved on the copper, and 0.5 mHz, which can be measured within 30 minutes (~ 15 averages). The results can be found in Table 4.1. We considered three different experimental configurations, where we vary the size of the magnet in order to increase the field gradients and thereby the signal per spin. The first configuration is a replication of the experimental parameters as used for the copper measurement from Fig. 4.7: A saturation experiment performed at a height of 1.0 μm and a temperature of 21 mK. The optimal signal at this height is found for an RF frequency of 3.5 MHz (about a factor of 4 higher than the RF frequency used for the copper due to the higher gyromagnetic ratio). The other two configurations are simulations with magnets with radii of 1.0 μm and 0.5 μm . To make a fair comparison, we calculate the signal for the same Larmor frequency 3.5 MHz, which dictates measurement heights of 0.56 μm and 0.24 μm . All unmentioned parameters are kept constant. The predicted detection

R_0 (μm)	h (μm)	$\nabla_r B_0$ ($\mu\text{T}/\text{nm}$)	V_{ss}	$V_{30\text{min}}$
1.7	1.00	100	$(84 \text{ nm})^3$	$(55 \text{ nm})^3$
1.0	0.56	170	$(59 \text{ nm})^3$	$(39 \text{ nm})^3$
0.5	0.24	370	$(39 \text{ nm})^3$	$(25 \text{ nm})^3$

Table 4.1: Calculated volume sensitivities V_{ss} (volume required for 1.8 mHz frequency shift) and $V_{30\text{min,DNP}}$ (volume required for a 0.5 mHz frequency shift). Calculations are done for sample temperature $T = 21$ mK and RF frequency $\omega_{\text{RF}}/(2\pi) = 3.5$ MHz. The radial magnetic field gradient $\nabla_r B_0$ is calculated at 50 nm below the surface of the sample.

volumes for the different configurations are shown in Table 4.1.

Clearly, decreasing the size of the magnetic particle will enhance the volume sensitivity, but there is a fundamental limit: the experiment described here relies on removing the Boltzmann polarization of the sample, but as the detection volume goes down, we enter the regime where statistical polarization becomes dominant. The critical volume V_c for this transition is given by [122]

$$V_c = \frac{4}{\rho_{\text{H}}} \left(\frac{k_{\text{B}}T}{\hbar\gamma B_0} \right)^2, \quad (4.13)$$

where it is assumed that the thermal energy is much larger than the Zeeman splitting. For a temperature of 21 mK and a Larmor frequency of 3.5 MHz, $V_c \sim (11 \text{ nm})^3$. Below this detection volume, measurements of the direct frequency shift would average to zero.

However, further enhancement of the volume sensitivity can still be achieved by increasing the Boltzmann polarization of the protons. This can be done by working at higher Larmor frequencies by decreasing the tip-sample separation, or by applying a strong external magnetic field. An external magnetic field of 8 T would increase the Boltzmann polarization by roughly a factor of 100, but applying external magnetic fields in combination with our SQUID-based detection is challenging due to our extreme sensitivity to magnetic noise. An appealing alternative is to use dynamical nuclear polarization (DNP), as was recently demonstrated for MRFM by Isaac et al. [116]. For suitable samples, e.g. nitroxide-doped polystyrene, DNP can be used to transfer polarization from electron spins to nuclei. The maximum enhancement of the nuclear polarization that can be achieved using this mechanism is given by $\epsilon = \gamma_e/\gamma_{\text{H}} = 660$. However, for protons at a Larmor frequency of 3.5 MHz and temperature of 21 mK the initial Boltzmann polarization is about 0.4%, so our maximal enhancement is limited to a factor 250. Table 4.2 shows the calculated volume sensitivities if we are able to use DNP to enhance the nuclear polarization, for the

R_0 (μm)	h (μm)	DNP _{eff} (%)	$V_{\text{ss,DNP}}$	$V_{30\text{min,DNP}}$
1.7	1.00	10	(21 nm) ³	(14 nm) ³
1.7	1.00	100	(13 nm) ³	(8.7 nm) ³
1.0	0.56	10	(15 nm) ³	(10 nm) ³
1.0	0.56	100	(9.4 nm) ³	(6.1 nm) ³
0.5	0.24	10	(9.6 nm) ³	(6.2 nm) ³
0.5	0.24	100	(6.1 nm) ³	(4.0 nm) ³

Table 4.2: Calculated volume sensitivities $V_{\text{ss,DNP}}$ and $V_{30\text{min,DNP}}$ including DNP to enhance the nuclear polarization with an efficiency DNP_{eff}. Calculations are done for sample temperature $T = 21$ mK and RF frequency $\omega_{\text{RF}}/(2\pi) = 3.5$ MHz.

cases where we achieve DNP efficiencies of 10% and 100%. Even for the more realistic assumption of 10% efficiency, we find that a volume sensitivity below (10 nm)³ could be possible. This voxel size would make imaging based on measurements of the Boltzmann polarization a viable approach to image biological samples, without the demand for high RF field amplitudes and continuous application of this field, as was the case for previous amplitude-based imaging [16].

Of course, there are some potential pitfalls that should be considered. First of all, we have assumed that the frequency noise spectrum shown in Fig. 4.2 can be maintained. However, large 1/f noise has been reported at 4K on insulating samples like polymers, attributed to dielectric fluctuations [68, 123]. This frequency noise scales with the square of the charge difference between the sample and the tip. Therefore, we believe it can be avoided, either by properly grounding both the tip and sample, but also by biasing the tip to tune away any charge difference [124, 125].

A second limitation is that for the current experiment we require T_1 times to be between several seconds and minutes. When T_1 is shorter than several seconds, it becomes comparable to other time constants in our setup (e.g., the thermal time constant of the sample holder), making it difficult to extract the signal. When T_1 becomes longer than minutes, averaging measurements to increase the SNR will become very time-consuming, although the total measurement time may come down by using multiple resonant slices [126, 127]. Plus, as the duration of a measurement increases, 1/f noise will increasingly become a limiting factor. T_1 times within the desired range for suitable proton samples are reported at low temperatures [113, 116]. For very pure samples with long T_1 times, appropriate doping of the sample with impurities can be used to reduce the relaxation time [128].

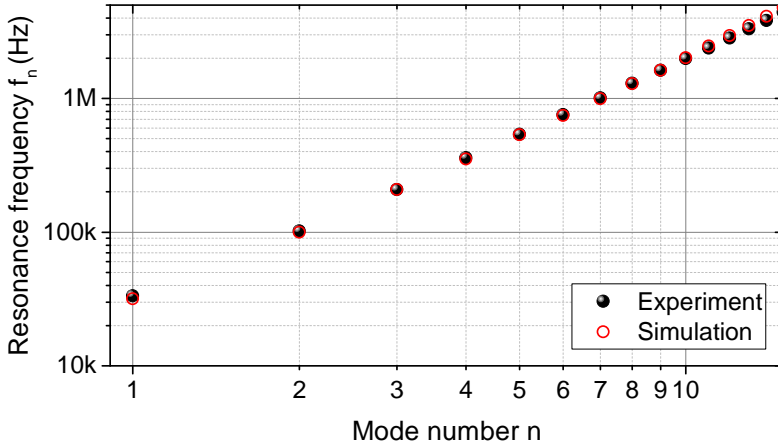


Figure 4.8: Measured higher mode resonance frequencies of the cantilever, together with the mode frequencies obtained from finite element calculations. The highest resonance mode investigated is the 15th mode located at $f_{15} = 4.4$ MHz. In the simulations we only consider higher modes that vibrate in the soft direction of the cantilever.

The final challenge is to maintain the low operating temperatures required for the low frequency noise floor while sending RF pulses in the MHz range. The power dissipated by the RF pulse, even when using a superconducting RF wire, increases with the frequency. To apply a 0.1 mT RF pulse at a sample located 5 μm from the RF wire at 3.5 MHz, we measure a dissipation of approximately 3 μW in our setup. A continuous power pulse with this level of dissipation would locally heat the sample to over 100 mK. We can avoid this source of dissipation by using the higher modes of the cantilever, which can be excited up to the 15th mode at 4.4 MHz and possibly beyond. In Fig. 4.8 we show the frequencies of the higher flexural modes together with the calculated frequencies obtained from finite element calculations. The estimated dissipation from the motion of a higher mode is well below 1 fW, since we measure the higher modes to have Q-factors approaching one million. Note that exciting the higher modes becomes harder for higher mode numbers, as the rotation angle of the magnet (that partially determines the magnitude of the generated RF field) scales with the inverse of the torsional stiffness $\kappa_n \propto n^4$. For the presented mode numbers this can be compensated by increasing the amplitude of the driving force. We do expect, however, that non-linearities of the cantilever will be the fundamental limit for the maximum fields that we can generate using the higher modes [50].

4.6 CONCLUSIONS

We have used the time-dependent solution of the Bloch equation to derive a concise equation to calculate the frequency shifts in MRFM experiments, and applied this to saturation experiments on a thin copper film. By using the higher modes of the cantilever as a source for the RF fields, we have demonstrated that it is possible to make one-dimensional scans of the copper film with near-negligible dissipation, and that the measured direct frequency shifts are well reproduced by the presented theory. Finally, we have shown that we have measured a frequency-shift signal with a volume sensitivity of $(40 \text{ nm})^3$. We have done all this at temperatures as low as 21 mK, made possible by the SQUID-based detection of the cantilever motion and the low power saturation protocol in combination with the mechanical generation of the RF fields.

The achieved volume sensitivity opens up the way for imaging based on measurements of the Boltzmann polarization, which could allow for high resolution imaging due to the direct gain from lower temperatures, and the favourable averaging compared to statistical polarization based imaging. We have shown that modest technical changes to our current setup can allow for experiments on protons with a spatial resolution of $(25 \text{ nm})^3$, and that increasing the polarization, for instance using DNP, can improve the resolution even further to below $(10 \text{ nm})^3$. The magnet-on-tip geometry allows for a larger choice in available samples, as it is still an open question whether interesting biological samples can be attached to an ultrasoft MRFM cantilever for approaches using the sample-on-tip geometry. When it is possible to measure on different samples with the same low frequency noise as achieved in the current experiment, high-resolution Boltzmann-polarization-based magnetic resonance imaging at milliKelvin temperatures in a magnet-on-tip geometry could become a reality.

SUPPLEMENTAL MATERIAL

4.7 RELEVANT NMR PARAMETERS OF COPPER

The relevant NMR properties for both isotopes of copper are given in Table 4.3. In all calculations, we assume a combined spin density $\rho = 85$ spins/nm³, and spin-lattice relaxation times T_1 dictated by the Korringa relation $TT_1 = 1.2$ sK [129].

Parameter	Variable	⁶³ Cu	⁶⁵ Cu
Spin	S	3/2	3/2
Natural abundance		69 %	31 %
Gyromagnetic Ratio	$\gamma/(2\pi)$	11.3 MHz/T	12.1 MHz/T
spin-spin relaxation time	T_2	0.15 ms	0.15 ms

Table 4.3: Overview of the relevant NMR parameters for the two isotopes of copper. [109, 129, 130]

4.8 SPIN DIFFUSION LENGTH FOR COPPER

When attempting to measure the signal from very narrow resonant slices, spin diffusion might be a relevant factor, as the transfer of polarization from spins within the resonant slice to spins outside of the resonant slice would increase the effective detection volume. Spin diffusion can be suppressed in high field gradients [32–34]. Assuming a spin density of 85 spins/nm³ and a nearest-neighbor distance $a = 0.256$ nm, we calculate that this requires field gradients of at least 1.3 MT/m. So the field gradients in the presented experiments are insufficient to suppress the spin diffusion.

We can find the expected diffusion length following the calculation by Wagenaar et al.[37], who assumes a transition rate $W = 1/30T_2$ [131]. For $T_2 = 0.15$ ms this leads to a diffusion constant $D = Wa^2 = 15$ nm²/s and a diffusion length $l_D = \sqrt{Dt_p}$. Thus, for a pulse duration $t_p = 80$ μ s, we find a diffusion length of 0.04 nm. Since the diffusion transports polarization away from the resonant slice in both directions, this leads to a broadening of the resonant slice of 0.08 nm.

5

DENSITY AND T_1 OF SURFACE AND BULK SPINS IN DIAMOND IN HIGH MAGNETIC FIELD GRADIENTS

Small spin ensembles play an important role in many areas of condensed matter physics. Here we present a method to measure spin densities in very dilute spin systems. We report on surface and bulk spin density measurements of diamond, using ultra-sensitive magnetic force microscopy with magnetic field gradients up to $0.5 \text{ T}/\mu\text{m}$. At temperatures between 25 and 800 mK, we measure the shifts in the resonance frequency and quality factor of a cantilever with a micromagnet attached to it. A recently developed theoretical analysis allows us to extract a surface spin density of $0.072 \text{ spins}/\text{nm}^2$ and a bulk spin density of 0.4 ppm from this data. In addition, we find an increase of the T_1 time of the surface spins in high magnetic field gradients due to the suppression of spin diffusion. Our technique is applicable to a variety of samples other than diamond, and could be of interest for several research fields where surface, interface or impurity bulk spin densities are an important factor.

This chapter has been published as M. de Wit, G. Welker *et al.*, “Density and T_1 of surface and bulk spins in diamond in high magnetic field gradients”, *Phys. Rev. Applied*, Vol. 10, p. 064045, Dec. 2018

5.1 INTRODUCTION

Noise coming from paramagnetic impurities is a widespread phenomenon that is relevant to fields ranging from magnetometry to solid-state qubits [132, 133]. An example is NV^- centers in diamond (from now on referred to as “NV-centers”), which have become one of the workhorses in quantum technology. Interaction with paramagnetic impurities is considered one of the main factors that induce decoherence of the NV-center [134]. This decoherence is faster for shallow NV-centers close to the surface and slower for NV-centers in the bulk of the diamond sample, because shallow NV-centers are under the influence of a layer of electron spins at the surface of the diamond [132, 135]. Understanding and potentially eliminating this source of decoherence has been a long-standing goal of the field [136]. Here we present a method to measure the impurity spin density, where the sensor is decoupled from the diamond sample. We use an ultrasoft cantilever with an attached micromagnet that couples to the spins via dipole-dipole interaction. The method is easily transferable to a wide range of samples [51].

Multiple experiments have been conducted to measure the diamond surface impurity spin density and to characterize the properties of this two-dimensional electron spin bath, such as correlation times of the fluctuating spins [135, 137–140]. The measured spin densities differ and range from 0.01 to $0.5 \mu_B/\text{nm}^2$. Most of these experiments were done at room temperature, except for one measurement at 10 K [138]. All mentioned studies used NV-centers to probe the surface electron spin bath. The technological challenge of measuring surface or bulk spin densities on samples other than diamond can be met by use of a scanning NV-center approach [137]. Unfortunately, the detection range of a scanning NV-center approach is limited to a few nanometers. Our method is capable of sensing spins at micrometer distances.

We do our experiments at milliKelvin temperatures, where no surface spin-density measurements on diamond have been performed yet. The low temperature in combination with a high magnetic field gradient allows us to measure with an extremely low force noise [48]. In addition, it allows us to interact with electron spins that can easily be polarized by small magnetic fields and to disregard all physical processes involving phonons. This makes our method suitable for measuring spin densities in very dilute spin systems. In particular, it is of interest for the fields of quantum computation devices [141, 142], magnetometry [143], and magnetic resonance force microscopy (MRFM) [106], as surface and bulk impurity spins play an important role there.

Our group has previously demonstrated surface spin-density measurements of dan-

gling bonds on a silicon oxide surface [51]. Here we present spin-density measurements of paramagnetic impurities on a diamond surface and also expand our method to probe impurity spins in the bulk of the sample. We show that strong magnetic field gradients influence the T_1 relaxation time of the impurity spins and that this effect is an important ingredient to understand the system.

5.2 METHODS

5.2.1 Experimental setup

In our experiments we use a commercially available diamond sample with a size of $2.6 \times 2.6 \times 0.3 \text{ mm}^3$ and that is specified to have less than 1 ppm of nitrogen impurities¹. One surface is polished twice to a surface roughness $R_a < 5 \text{ nm}^2$. We clean the diamond subsequently in acetone, 2-propanol, fuming nitric acid, hydrofluoric acid, and water to start the fabrication process with a clean surface and without oxides. On the surface we fabricate a niobium titanium nitride (NbTiN) pickup loop and RF-wire, the latter of which is not used in the present experiment [55]. After fabrication, the sample is exposed to air for several months. Before mounting of the sample, it is ultrasonically cleaned in acetone, and thereafter in 2-propanol to remove organics and dust.

The measurements are performed with a MRFM setup comparable to the one used in earlier experiments [51]. To establish the magnetic interaction, we use a spherical (Nd,Fe)B particle (from now on simply referred to as the “magnet”) with a diameter of $2.99 \text{ }\mu\text{m}$. This magnet is glued with platinum by electron-beam-induced deposition (EBID) to the end of an ultrasoft cantilever with a length of $166 \text{ }\mu\text{m}$, width of $5 \text{ }\mu\text{m}$, and thickness of 100 nm [7]. This geometry leads to an intrinsic spring constant $k_0 = 5.0 \times 10^{-5} \text{ N/m}$ with a corresponding natural frequency of 2850 Hz (see Supplemental Material Fig. 5.7 for the properties of the cantilever measured versus temperature at $5 \text{ }\mu\text{m}$ height, far away from the sample). After the magnet is attached, it is placed in an external field of 5 T , leading to a magnetic moment \mathbf{m} of $1.5 \times 10^{-11} \text{ Am}^2$ pointing along the direction of movement of the cantilever (Fig. 5.1(a)). The magnetic particle is responsible for the B field, which polarizes the spins in the sample but also creates large magnetic field gradients of up to $0.5 \text{ T}/\mu\text{m}$.

The magnetized cantilever is mounted above the sample and can be moved with

¹SC Plate CVD, <100>, PL, from Element Six

²Second polish: scaife polishing from Stone Perfect

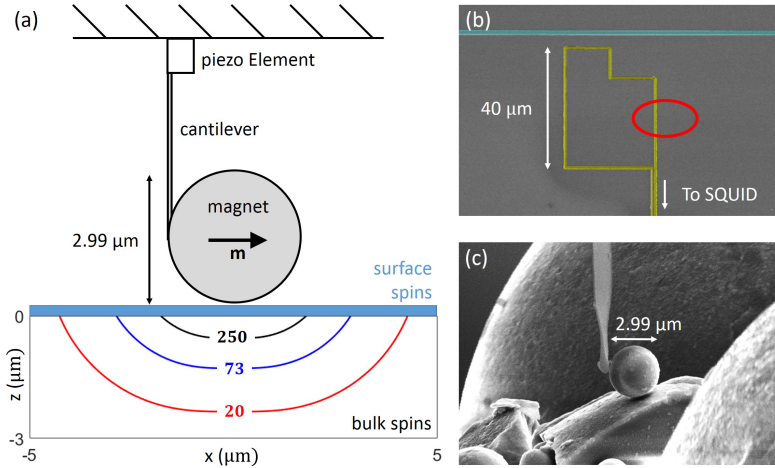


Figure 5.1: (a) Setup: A magnetic particle with a diameter of $2.99\ \mu\text{m}$ attached to the end of a soft MRFM cantilever is positioned above the diamond sample, where it induces a high magnetic field gradient (solid colored lines, unit $\text{mT}/\mu\text{m}$). The bulk of the diamond contains nitrogen impurities with an associated electron spin. On the surface we find an impurity layer containing paramagnetic electron spins, indicated in blue. (b) False-color scanning-electron-microscope image of the nanofabricated structures on top of the diamond sample. The pickup loop used for the read-out of the cantilever is shown in yellow. In blue there is a NbTiN RF wire, which is not used in the current experiment. The measurements described in this work are done at the location marked by the red circle. (c) Scanning-electron-microscope image of the tip of the cantilever and a NdFeB particle after the electron-beam-induced deposition (EBID).

respect to the sample with use of a modified piezoknob-based cryogenic positioning stage³. The absolute tip position is measured with three capacitive sensors, while the precise distance between the surface of the magnet and the surface of the diamond is calibrated by gently lowering the magnet until the two touch, using the piezoknobs.

The motion of the cantilever is measured with a SQUID-based read-out [47], where we detect the changing magnetic flux in the pickup loop (yellow in Fig. 5.1(b)) due to the moving magnet. We can determine the linear response of the cantilever by driving a small piezo element at the base of the cantilever. When we sweep the drive frequency and measure the cantilever response using a lock-in amplifier, we obtain the resonance frequency and quality factor by fitting the square of the SQUID output with a Lorentzian, as seen in Fig. 5.2.

The full experimental setup is mounted at the mixing chamber of a cryogen-free

³Cryo Positioning Stage - High Resonance (CPSHR), from Janssen Precision Engineering B.V.

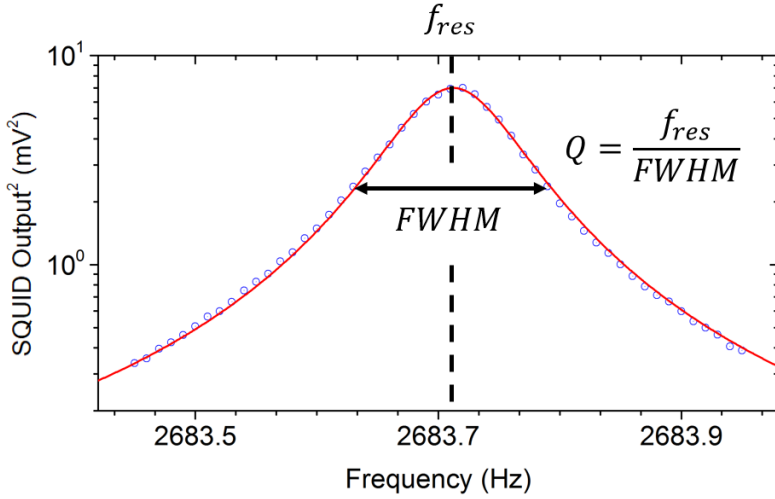


Figure 5.2: Example of a frequency sweep measured at a tip-sample separation of $3.4 \mu\text{m}$ at a temperature of 25 mK . The resonance frequency and quality factor are obtained by the fitting of the data to a Lorentzian (solid red line).

dilution refrigerator with vibration isolation [77], and with a base temperature of 10 mK . The gold-plated copper sample holder is thermally connected to the mixing chamber with a silver strip. A heater and calibrated low-temperature thermometer are used to control the temperature of the sample holder. Because of the limited thermal conductance between the mixing chamber, the sample holder, and the diamond sample itself, the sample temperature typically saturates at approximately $25\text{--}30 \text{ mK}$.

5.2.2 Spin-bath - cantilever coupling

When the tip of the cantilever is positioned close to the sample, it couples to the electron spins via the magnetic field that originates from the magnet. The motion of the cantilever changes the direction and strength of this field. The electron spins will follow the varying magnetic field, but with a lag due to their relaxation times T_1 and T_2 . This effect will, in return, change the motion of the cantilever. De Voogd *et al.* [52] investigated the complete spin-cantilever system while taking into account the intrinsic damping of the cantilever and the spin-lattice relaxation. They derived an expression for the change of the resonance frequency $\Delta f = f_{\text{res}} - f_0$, where f_{res} is the resonance frequency taking into account the interaction with the spins, and f_0 is the resonance frequency of the cantilever. Only spins with $T_1 \gtrsim 1/\omega_0$, with $\omega_0 = 2\pi f_0$, contribute to the frequency shift. A similar expression is found for the inverse quality

factor $\Delta \frac{1}{Q} = \frac{1}{Q} - \frac{1}{Q_0}$, with Q_0 the cantilever's bare quality factor. The spin-mediated dissipation $1/Q$ is significant only when $T_1 \approx 1/\omega_0$. We now give the expressions for Δf and $\Delta \frac{1}{Q}$ for our specific sample.

In our sample, we expect two main sources for the signal: spins in the bulk and spins on the surface of the diamond. First, we expect a contribution from the free electron spins associated with the nitrogen impurities in the bulk of diamond (P1 and P2 centers). The T_1 relaxation time of the dilute electron spins in the bulk of diamond has been reported to increase to several seconds at low temperatures [144]. Since this means that the spin-lattice relaxation is negligible on timescales comparable to the cantilever period, there is no dissipation path for the cantilever through the spin to the lattice at the cantilever's resonance frequency. Hence, we expect the bulk spin-induced shift of the quality factor to be zero. Taking these assumptions into account, we find the contributions of the spins in the bulk to be

$$\Delta f_{\text{bulk}} = \frac{f_0}{2k_0} \frac{\rho \mu_{\text{B}}^2}{k_{\text{B}} T} \int_V d^3 \mathbf{r} \mathcal{C}(\mathbf{r}), \quad (5.1)$$

and

$$\Delta \frac{1}{Q}_{\text{bulk}} = 0, \quad (5.2)$$

where

$$\mathcal{C}(\mathbf{r}) = \frac{|\mathbf{B}'_{\parallel \hat{\mathbf{B}}_0}|^2}{\cosh^2\left(\frac{\mu_{\text{B}} B_0}{k_{\text{B}} T}\right)}, \quad (5.3)$$

ρ is the bulk spin density, μ_{B} is the Bohr magneton, and T is the temperature of the spin bath. The integral is over the entire volume of the sample.

Since our sample is exposed to air before the experiment, we expect a second contribution from a layer of surface spins that can be expected on any surface that has been exposed to air for extended times [145]. As these are dilute paramagnetic spins, we expect these spins to have T_1 times in the millisecond range. In the case that T_1 is similar to $\frac{1}{\omega_0}$, these spins create an additional dissipation path for the cantilever. Therefore, these spins should cause additional shifts given by

$$\Delta f_{\text{surf}} = \frac{f_0}{2k_0} \frac{\sigma \mu_{\text{B}}^2}{k_{\text{B}} T} \int_S d^2 \mathbf{r} \mathcal{C}(\mathbf{r}) \frac{(\omega_0 T_1(\mathbf{r}))^2}{1 + (\omega_0 T_1(\mathbf{r}))^2}, \quad (5.4)$$

and

$$\Delta \frac{1}{Q}_{\text{surf}} = \frac{1}{k_0} \frac{\sigma \mu_{\text{B}}^2}{k_{\text{B}} T} \int_S d^2 \mathbf{r} \mathcal{C}(\mathbf{r}) \frac{\omega_0 T_1(\mathbf{r})}{1 + (\omega_0 T_1(\mathbf{r}))^2}, \quad (5.5)$$

where σ is the surface spin density. We have placed the term containing $\omega_0 T_1$ inside the integral to reflect the fact that T_1 may depend on the magnetic field gradient. The integral is over the entire surface of the sample.

To calculate the expected frequency shift and additional dissipation, accurate values are needed for the magnetic moment and the shape and size of the magnetic field. In our experiment, since the magnetic particle is almost perfectly spherical, we can calculate the field as if it originates from a magnetic dipole. In the coordinate-free form, this is given by [146]

$$\mathbf{B}(\mathbf{r}) = \frac{\mu_0}{4\pi} \frac{1}{r^3} [3(\mathbf{m} \cdot \hat{\mathbf{r}}) \hat{\mathbf{r}} - \mathbf{m}], \quad (5.6)$$

where \mathbf{m} is the magnetic moment of the magnet. From this field, we can calculate all relevant derivatives as required for Eq. 5.3.

5.2.3 Spin diffusion in high magnetic field gradients

The theory presented so far describes the spin-cantilever interaction for a constant T_1 of the spins. For most applications (e.g., in bulk techniques with homogeneous external fields) this is a good approximation. However, this approximation does not hold when dilute spins are placed in large magnetic field gradients, as is the case in our experiment. These gradients can increase the relaxation times by suppressing spin diffusion, a concept first derived by Bloembergen [131]. Spin diffusion in diamond was studied by Cardellino *et al.* [33].

In this model, it is assumed that different spins can have different relaxation times depending on their local environment. This results in the presence of fast-relaxing spins that can rapidly thermalize to the lattice, and slow-relaxing spins that are badly coupled to the lattice. After a perturbation of the thermal equilibrium, relaxation of the polarization of this sample to equilibrium occurs via spin diffusion which couples the slower-relaxing spins to the faster-relaxing spins through flip-flop interaction, reducing the overall relaxation time of the sample.

However, spin diffusion can be suppressed by application of a large magnetic field gradient, which reduces the probability of two spins exchanging energy by introducing a difference in field felt by neighboring spins. An Ansatz for the suppression of the spin diffusion can be obtained by calculation of the normalized overlap integral between the line shapes of two spins [32]:

$$\Phi(\bar{a}G) = \frac{\int F(B')F(B' - \bar{a}G)dB'}{\int F^2(B')dB'}, \quad (5.7)$$

where G is the gradient of the magnetic field strength at the position of the spins, $\bar{a} \simeq 0.5 \bar{r}$ is the approximate average spacing between spins in the radial direction with \bar{r} the nearest-neighbor distance under the assumption of a cubic lattice, and $F(B)$ is the resonance line shape of the spins. We look at the spacing in the radial direction, since this direction has the largest magnetic field strength gradients, and therefore the highest suppression of spin diffusion. Since we are considering a layer of spins on the surface of the diamond, the total number of spins is too small to measure the actual spectra of the surface spins by bulk techniques such as ESR, so we assume these spins have a Lorentzian profile

$$F(B) = \frac{1}{\pi} \frac{\left(\frac{\Delta B_{\text{dd}}}{2}\right)}{B^2 + \left(\frac{\Delta B_{\text{dd}}}{2}\right)^2}, \quad (5.8)$$

with a linewidth given by [117, p. 128]:

$$\Delta B_{\text{dd}} = 3.8\mu_0\gamma_e\hbar/4\pi\bar{r}^3, \quad (5.9)$$

where $\gamma_e/2\pi = 28.0$ GHz/T is the electron gyromagnetic ratio. Because the convolution of two Lorentzian profiles with width Δ is itself a Lorentzian with width 2Δ , we can evaluate Eq. 5.7, from which we find that

$$\Phi(\bar{a}G) = \frac{1}{1 + (\bar{a}G/\Delta B_{\text{dd}})^2} = \frac{1}{1 + (G/G^*)^2}, \quad (5.10)$$

where $G^* = \Delta B_{\text{dd}}/\bar{a}$ is a measure for the gradient when the quenching becomes significant, from now on called the “critical gradient”. In short, it is the gradient for which the difference in the field at neighboring spins becomes larger than the spin linewidth. $\Phi(\bar{a}G)$ can be seen as a flip-flop suppression factor. When $\Phi(\bar{a}G)$ is 0, flip-flops are fully suppressed, and when $\Phi(\bar{a}G)$ approaches 1, spins can exchange energy and flip-flops are possible. Thus, we find that the relaxation time is given by

$$T_1(G) = \left\{ \frac{1}{T_1^{\text{ff}}} \frac{1}{[1 + (G/G^*)^2]} + \frac{1}{T_1^*} \right\}^{-1}, \quad (5.11)$$

where T_1^{ff} is the reduced T_1 time due to flip-flops between neighboring spins and T_1^* is the intrinsic relaxation time of the system when the flip-flops are completely quenched. This is only a heuristic description of the effects of spin diffusion, and does not take into account the direction of the gradient or the effects of the spin-bath polarization on the flip-flop rate.

5.3 RESULTS AND DISCUSSION

For our experiments, we change the height (distance between the two surfaces of the diamond and the magnet) and vary the temperature from 25 mK to 800 mK. At every height-temperature combination, the resonance frequency and quality factor are measured as described in Sec. 5.2.1.

5.3.1 Frequency shift and dissipation

The results of the measurements of the frequency shift are shown in Fig. 5.3. The solid lines indicate the results of the fits according to Eqs. 5.1 and Eq. 5.4, with the total frequency shift given by $\Delta f = \Delta f_{\text{bulk}} + \Delta f_{\text{surf}}$. We calculate f_0 at each height by extrapolating the measured frequency-shift data to higher temperatures.

The two-dimensional and three-dimensional integrals over $\mathcal{C}(\mathbf{r})$ are calculated with the magnetic field distribution defined by Eq. 5.6. As mentioned before, both integrals are calculated over the entire surface and volume, respectively, but they converge within several micrometers from the magnet due to the strong distance-dependence of $\mathcal{C}(\mathbf{r})$. The only free parameters remaining in the model are the two spin densities ρ and σ for the bulk and the surface, respectively, and the T_1 time of the surface spins, which for now is fixed at 0.5 ms. As the term $(\omega_0 T_1)^2 / [1 + (\omega_0 T_1)^2]$ converges to 1 for $\omega_0 T_1 \gg 1$, the effect of the T_1 time on the total frequency shift can be ignored, so the precise value for the T_1 time is important only in the analysis of the temperature-dependent change of the quality factor.

A complication in fitting the values for the two spin densities, is that the functions for Δf_{bulk} and Δf_{surf} are not independent. To determine the precise values, we fix ρ and fit σ as a shared fit parameter over the temperature traces for all heights. Next, we vary ρ to minimize the average fitting error. This method yields global values of $\rho = 0.4$ ppm, compatible with the specifications of the diamond sample, and $\sigma = 0.072$ spins/nm², in line with previously measured surface spin densities [139]. The dashed line in Fig. 5.3 shows the frequency shift due to the bulk spins at a height of 20 nm for this concentration, signifying that even very low spin densities have a substantial effect on the total frequency shift.

The measured changes of the quality factor for each height and temperature are shown in Fig. 5.4. The total value for the inverse quality-factor is given by $\frac{1}{Q} = \frac{1}{Q_0} + \Delta \frac{1}{Q_{\text{surf}}}$, where Q_0 is the quality factor of the resonator without coupling to the

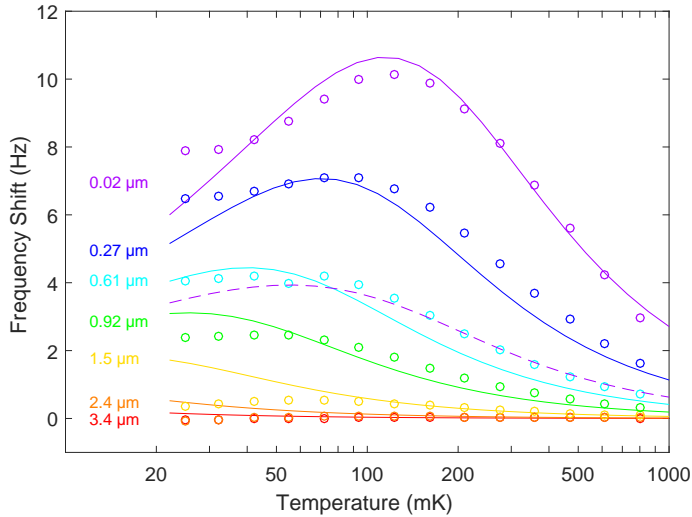


Figure 5.3: Data (circles) and theory (lines) for the frequency shift of the cantilever versus temperature when the cantilever is positioned near the surface of the diamond sample. The dashed line shows the contribution from the bulk spins in the diamond only. The solid lines are calculated with $\sigma = 0.072$ spins/nm² and $\rho = 0.40$ ppm.

spin-bath. Q_0 can be obtained by extrapolation of the measured dissipation to high temperatures. For a height of 3.4 μm we find that Q_0 is 24 000, and for a height of 2.4 μm , we find Q_0 to be 18 500. For all smaller heights we fix Q_0 to 18 500. These values are lower than the vacuum quality-factor (at a height of 5 μm , we find Q_0 is 35 000, see Fig. 5.7), and we ascribe this to some other long-range effect (e.g., electrostatic interactions [147, 148]).

To fit the data to Eq. 5.5, we fix the spin densities of both the surface and the bulk to the values obtained from the frequency-shift analysis. Our attempt to fit these data using Eq. 5.5 with a constant T_1 time independent of position did not yield a good match with the data. This is illustrated by the dashed line in Fig. 5.4, which shows the result of the calculation at a height of 20 nm, with $T_1 = 1.3$ ms. A clear deviation between the data and calculated values at low temperatures is visible. Repeating the calculation for each available height separately results in different T_1 times. We find that T_1 increases from 0.4 ms at a large height to 1.3 ms at a small height (see Fig. 5.8 for the fitting results obtained with constant T_1 times). This observation is a strong indication of the suppression of the spin diffusion by the high magnetic field gradient.

We include this effect by inserting Eq. 5.11 into Eq. 5.5, yielding a position-dependent T_1 time bound by T_1^* in the high gradients close to the magnet, and T_1^{ff} for

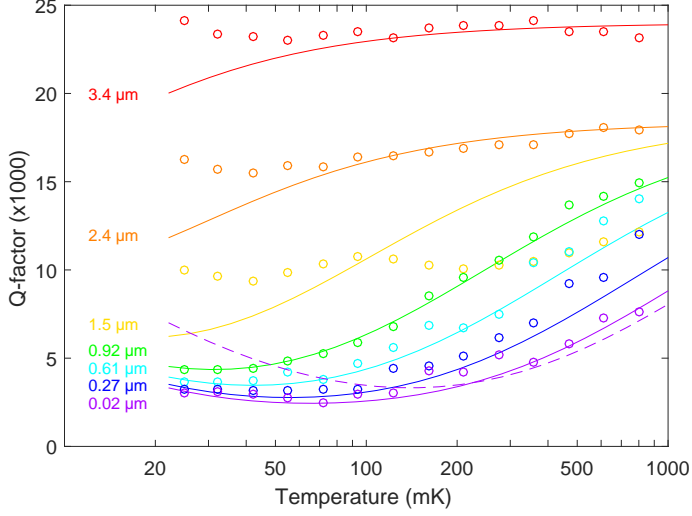


Figure 5.4: Data (circles) and theory (lines) for the change in the quality factor of the cantilever versus temperature when the cantilever is positioned near the surface of the diamond sample. The solid lines are calculated with the spin densities obtained from the frequency data, including the effects of spin diffusion using $T_1^* = 10$ ms and $T_1^{\text{ff}} = 0.45$ ms. The dashed line shows the expected quality factor at a height of $0.02 \mu\text{m}$ calculated with a constant $T_1 = 1.3$ ms.

spins far away from the magnet. Using the surface spin density $\sigma = 0.072$ spins/ nm^2 obtained from the frequency-shift data, we find that in our case $\bar{r} = \sigma^{-1/2} = 3.7$ nm, resulting in a linewidth of $\Delta B_{\text{dd}} = 0.14$ mT according to Eq. 5.9. This leads to a critical gradient $G^* = 73$ mT/ μm , a value smaller than the maximum field gradients in our setup as indicated in Fig. 5.1(a). The resulting dependence of the T_1 time on the magnetic field strength gradient is shown in Fig. 5.5.

To obtain reliable values for the relaxation times T_1^{ff} and T_1^* , we use an interesting feature of the coupling between the spins and the magnet. Fig. 5.6 shows the spatial distribution of \mathcal{C} for various temperatures, calculated at a constant tip-sample separation of 20 nm, indicating the position of the spins contributing most to the signal. It is clear that as the temperature of the sample decreases, the average location of contributing spins moves away from the cantilever. This immediately implies that at low temperatures, most of the contributing spins are located in a region with a magnetic field gradient below G^* , which means that spin diffusion is not suppressed, and thus their relaxation time approaches T_1^{ff} . Equivalently, at high temperatures, the spins that contribute the most are close to the magnet in a high magnetic field gradient, meaning flip-flops are quenched and $T_1 \approx T_1^*$. This allows us to fit T_1^{ff} and T_1^* almost independently. The solid lines in Fig. 5.4 show the final calculations including the

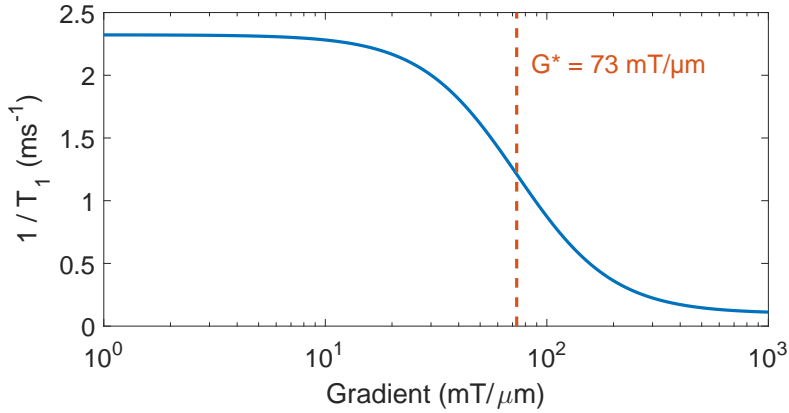


Figure 5.5: Plot of the inverse of the T_1 time calculated from Eq. 5.11, using $G^* = 73$ mT/ μm , $T_1^{\text{ff}} = 0.45$ ms, and $T_1^* = 10$ ms.

5

effects of spin diffusion using $T_1^* = 10$ ms and $T_1^{\text{ff}} = 0.45$ ms.

We select a value of 10 ms for T_1^* . Higher values for T_1^* do not significantly change the dissipation, because T_1^* becomes too far away from the cantilever period. In other words, the dissipation of the cantilever mediated by the spins peaks when T_1 matches the cantilever period, so we are only sensitive to T_1 times of up to several milliseconds. Spins with a T_1 time greater than several milliseconds do not contribute to the enhanced dissipation, but they do change the resonance frequency.

There are still some unexplained features in the data. First, there is a clear difference between data and theory for large tip-surface separations at low temperatures. It seems that the quality factor of the silicon cantilever increases when the temperature decreases (see Supplemental Material Fig. 5.7 for the data showing the increasing Q factor at low temperatures measured at a height of 5 μm), presumably due to the freezing out of the quantum fluctuators on the surface of the silicon beam [149]. Furthermore, the measurements at a height of 1.5 μm also strongly deviate from the fit for both the resonance frequency and the quality factor. This could be because this measurement is performed directly above a superconducting line of the pickup loop, which might lead to a lower density of paramagnetic electron spins on and beneath the superconductor. The low quality factor can then be explained by the increased coupling with the pickup loop, which leads to additional dissipation of the cantilever energy via the inductive coupling to resistive elements. We did not take the data measured at this height into account in our final analysis.

As the measured data as a function of temperature (for each height) show a clear

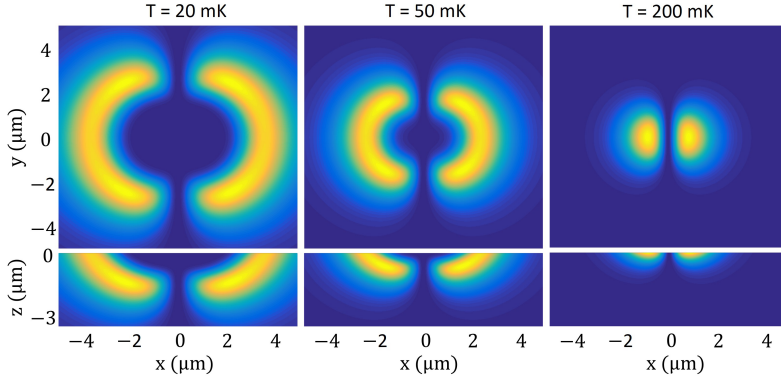


Figure 5.6: Simulation of the relative contribution of spins at different locations, calculated for a tip-sample separation of 20 nm. Yellow indicates regions of maximal coupling, while blue indicates a very low coupling between a spin and the cantilever.

nontrivial curve that matches the magnetic interaction as described by De Voogd et al., we are confident that the observed effects can be ascribed to paramagnetic spins. Other dissipation channels, such as dielectric fluctuations, are estimated to be smaller than what we find. In an improved version of our experiment, we would like to apply an external magnetic field, although this is a large technical challenge because the SQUID detection is very sensitive to noise in the applied external magnetic field.

5.4 SUMMARY AND OUTLOOK

In conclusion, by using our MRFM setup as an ultra sensitive, long-range magnetic force microscope, we are able to measure the amount of nitrogen impurities in our diamond sample, resulting in a bulk spin density of only 0.4 ppm. This shows that our method allows us to characterize samples containing low spin densities over a field of view of several micrometers. Furthermore, we characterize the paramagnetic electron-like spins on the surface of the diamond, yielding a density of 0.072 spins/nm^2 , and T_1 times of several milliseconds, heavily influenced by the presence of spin diffusion. As it is the fluctuation of these spins that is typically held responsible for the reduced performance of a variety of nanodevices such as qubits and superconducting resonators, we believe that our technique offers a useful tool to characterize the properties of the surface spin system and understand the resulting dissipation in these devices.

As the flip-flop interaction between the surface spins on the diamond can be reduced by use of a high gradient, it could be possible to improve the coherence of

various diamond-based devices. The idea of suppressing flip-flop induced spin-bath fluctuations for this purpose has been demonstrated before by increasing the polarization of the spin bath to more than 99% [144]. However, this works only for low temperatures and high magnetic fields. This is not the case for gradient-based quenching of flip-flops. Furthermore, since the required magnitude of the critical gradient depends on the spin density, relatively modest magnetic field strength gradients are required to isolate a single spin from its environment in very pure samples. For example, to suppress spin diffusion in a diamond sample with a nitrogen spin density of 1 ppm, it is sufficient to have a gradient of 1 mT/ μm .

A potential near-future application of this technique could be the testing of various sample preparation steps that are typically used to enhance the performance of nanodevices. As an example, we expect that a short chemical wet etch of diamond using hydrofluoric acid should reduce the density of the unpaired spins on the surface, resulting in the case of MRFM in a higher quality factor of the resonator close to the surface and in the case of shallow NV-centers in enhanced correlation times. Our technique would allow us to test the effect of this etch in any intermediate state of the fabrication of one of these devices, allowing better optimization of the fabrication process.

SUPPLEMENTAL MATERIAL

5.5 VACUUM PROPERTIES OF THE CANTILEVER

To exclude the possibility that the mechanical properties of the cantilever might be dependent on the temperature, even at temperature well below 1 K, we have measured the resonance frequency and Q-factor of the cantilever at a height of approximately 5 μm for various temperatures below 1 K. A height of 5 μm is sufficiently far away from the sample that we expect no significant coupling between the spins and the magnetic tip of the cantilever. The results of this measurement are presented in Fig. 5.7. The properties of the cantilever were obtained using the same method as described in Sec. 5.2.1.

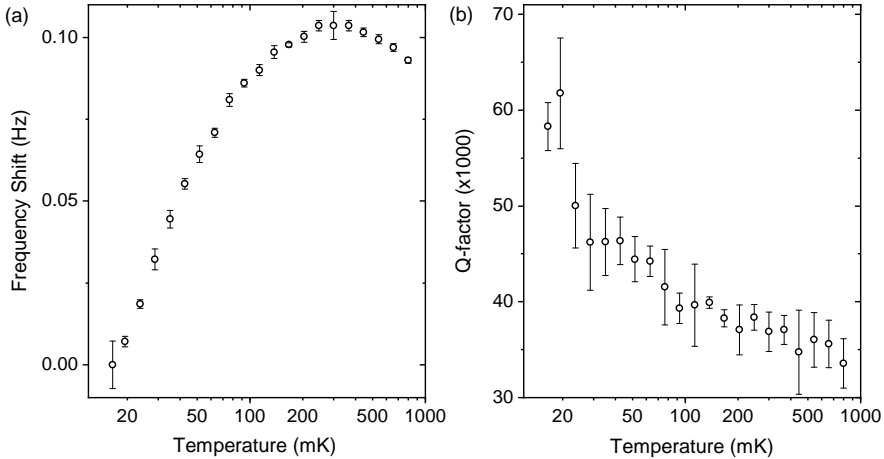


Figure 5.7: Properties of the cantilever measured at a height of 5 μm for various temperatures. The resonance frequency (a) changes by approximately 100 mHz with respect to a reference frequency of 2749.01 Hz. The Q-factor (b) is constant at a value of 35 000 for temperatures above 100 mK, but increases for lower temperatures.

We find that between 16 mK and 800 mK, the resonance frequency shifts by approximately 100 mHz, which is only a fraction of the total frequency shifts measured close to the sample, where spins influence the resonance frequency. We therefore conclude that the mechanical properties of the cantilever, e.g. the Young's modulus and thereby the intrinsic stiffness, do not change significantly within the presented temperature range.

For the Q-factor we find that it is stable at approximately 35 000 for temperatures above 100 mK, and increases to 60 000 for lower temperatures. This rising Q-factor is a possible explanation for the mismatch between the calculation and experiment in the low temperature, large height region of Fig. 5.4, as we pointed out at the end of Sec. 5.3. At small heights, the spin-mediated dissipation is much larger than the intrinsic dissipation in the cantilever, and the changing vacuum Q-factor becomes irrelevant.

5.6 FITS WITH CONSTANT T_1 TIMES

In Sec. 5.3, we note that if we fit the data of Fig. 5.4 using a constant T_1 for each height, we find a clearly increasing T_1 for decreasing height. For completeness, we show the result of this initial analysis in Fig. 5.8, where the circles indicate the data, and the solid lines the theory. As indicated in the main text, a clear deviation at low temperatures is visible. The height of each measurement and the value for T_1 which best fits the data can be found next to the lines. As can be seen, the best fit for a constant T_1 increases from 0.4 ms at a height of 3.4 μm to 1.3 ms at a height of 20 nm. To explain why the T_1 time of a spin close to the magnet is larger than that for a spin far away, we decided to study the effects of the magnetic field gradient on the spin diffusion, the result of which is presented in Sec. 5.3.

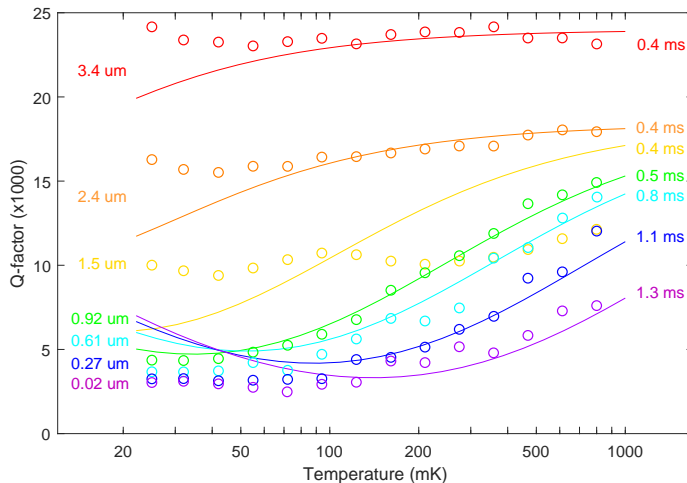


Figure 5.8: Initial analysis of the data from Fig. 5, where we use a constant T_1 for each height. The number on the right of each line shows the best-fit value for T_1 , showing a clear trend of increasing T_1 for decreasing height.

6

FLUX COMPENSATION FOR SQUID-DETECTED MAGNETIC RESONANCE FORCE MICROSCOPY

One of the major challenges in performing SQUID-detected Magnetic Resonance Force Microscopy (MRFM) at milliKelvin temperatures is the crosstalk between the radio-frequency (RF) pulses used for the spin manipulation and the SQUID-based detection mechanism. Here we present an approach based on balancing the flux crosstalk using an on-chip feedback coil coupled to the SQUID. This approach does not require any additional components near the location of the sample, and can therefore be applied to any SQUID-based detection scheme to cancel predictable RF interference. We demonstrate the effectiveness of our approach by showing that we can almost completely negate flux crosstalk with an amplitude of up to several Φ_0 . This technical achievement allows for complicated magnetic resonance protocols to be performed at temperatures below 50 mK.

This chapter has been published as M. de Wit *et al.*, “Flux compensation for SQUID-detected Magnetic Resonance Force Microscopy”, *Cryogenics*, Vol. 98, p. 67-70, Jan. 2019

6.1 INTRODUCTION

Magnetic Resonance Force Microscopy (MRFM) is a technique intended for nanoscale Magnetic Resonance Imaging (MRI) [14, 16, 62]. It is based on measuring the forces between spins in the sample and a small magnetic particle attached to the end of a soft cantilever (in the magnet-on-cantilever geometry) [41]. A variety of radio-frequency (RF) pulses can be used to manipulate the spins in the sample to generate the signal [11, 12]. The motion of the cantilever, which contains the spin signal, is typically read out using laser interferometry [106].

The fundamental force sensitivity of MRFM is determined by the thermal force noise. Therefore, one would like to operate the MRFM at the lowest possible temperatures. In order to prevent heating, we use a superconducting microwire as the source for the RF pulses. Furthermore, we have replaced the laser interferometer, which heats the cantilever and sample [44], by a SQUID-based detection scheme [47]. In this scheme, the motion of the cantilever is determined by measuring the flux induced by the magnetic particle in a superconducting pickup loop, which is coupled to the input coil of a SQUID. A photograph of the experimental setup used in this detection scheme is shown in Fig. 6.1(a), with a zoom-in on the MRFM detection chip containing the RF wire and pickup loops shown in Fig. 6.1(b). Due to these adjustments, the SQUID-detected MRFM can be operated at experimentally verified temperatures below 50 mK [37, 49].

The extreme sensitivity of the SQUID that we rely on to measure the sub-nanometer motion of the cantilever also has a disadvantage: SQUIDs are notoriously sensitive to electromagnetic interference [150, 151]. Interference of sufficient intensity reduces the extent to which the SQUID voltage changes in response to an applied flux. From now on the response of the SQUID voltage to applied flux will be called the 'SQUID modulation'. The time-dependent modulation voltage of a SQUID subjected to a low-frequency applied flux Φ_a and additional RF interference with amplitude Φ_{RF} is given by [152]:

$$V(t) = \Delta V_0 \cos\left(\frac{2\pi\Phi_a(t)}{\Phi_0}\right) J_0\left(\frac{2\pi\Phi_{\text{RF}}}{\Phi_0}\right), \quad (6.1)$$

with ΔV_0 the peak-to-peak modulation depth without RF interference, J_0 the zeroth order Bessel function, and $\Phi_0 = 2.068 \cdot 10^{-15}$ Wb, the magnetic flux quantum. The reduced SQUID modulation results in an increase in the measured SQUID noise floor. RF interference that originates from environmental sources can be reduced by using magnetic shielding. However, in the MRFM experiment there is also a local source of RF interference which cannot be avoided by using shielding: the direct

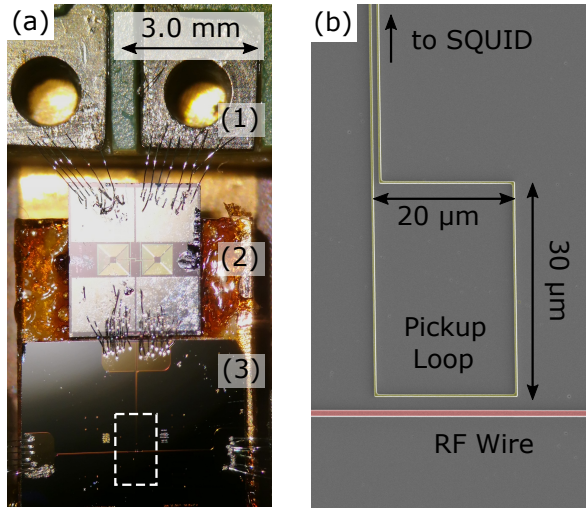


Figure 6.1: (a) Optical microscope image of (1) the niobium terminals connected to the SQUID input coil, (2) the gradiometric transformer used for the impedance matching, and (3) the MRFM detection chip. The white dashed boxed indicates the location of the zoomed-in image shown in (b) (not to scale). (b) Scanning electron microscope image of the detection chip, showing the NbTiN pickup loop (yellow) and RF wire (red).

crosstalk between the RF pulse and the pickup loop, as discussed in the next section. The presence of this crosstalk is detrimental for MRFM experiments, as it prevents measurements of the spin signal during the pulse, an absolute necessity in many MRFM protocols.

This challenge was also encountered and overcome in the field of SQUID-detected NMR, where the high sensitivity of the SQUIDs offers the possibility to work at very low fields and low frequencies [153–156]. In order to protect the SQUID from RF interference, a variety of solutions have been developed, but most can be subdivided into two classes. The first class of solutions involves disabling the SQUID by using diodes or Q-spoilers to block high currents [157–160]. This type of solutions is relatively easy to implement, but prevents measurements of the NMR signal during the RF pulse. The second class of solutions is based on sending a copy of the RF pulse with the appropriate phase and amplitude to an additional coil in the detection circuit [153, 161–163]. This balancing coil is often placed around or near the pickup coil which couples the measured NMR signals to the input coil of the SQUID.

In this chapter, we describe the measurement scheme used to remove the crosstalk in our SQUID-detected MRFM setup, where we use an on-chip feedback coil in the SQUID input coil circuit to balance nearly all crosstalk before it reaches the SQUID.

We start by explaining the compensation method and calibration of the required balancing pulses. We then demonstrate the effectiveness of our approach by showing the reduction in measured crosstalk in the full MRFM setup. The application of this technique to SQUID-detected MRFM is vital for the operation of MRFM at milliKelvin temperatures.

6.2 CIRCUIT AND CALIBRATION

As introduced in the previous section, RF pulses are required to manipulate the spins in the sample, which we generate by sending an alternating current through a superconducting RF wire [49]. In order to coherently modulate the magnetization of the spins, alternating magnetic fields B_{RF} on the order of several mT are necessary [57, 114]. To generate a 1 mT field (in the rotating frame of the spins) at a distance of 1 μm from the RF wire, a current with peak amplitude $I = 10 \text{ mA}_{\text{pk}}$ is required. Given this current and the geometry of the system, the flux crosstalk between the RF pulse and the pickup loop is given by:

$$\Phi_{\text{RF}} = \eta_{\Phi} \int_{\text{area}} B_{\text{RF}}(\vec{r}) dA \approx \eta_{\Phi} w I \frac{\mu_0}{2\pi} \ln\left(\frac{r_2}{r_1}\right), \quad (6.2)$$

where $w = 20 \mu\text{m}$ is the width of the pickup loop, μ_0 is the vacuum permeability, and $r_1 = 2.5 \mu\text{m}$ and $r_2 = 32.5 \mu\text{m}$ are the distance between the near and far edges of the pickup loop, respectively. We have assumed that all flux enters via the rectangular pickup loop, as we have minimized the parasitic area enclosed by the supply wires.

η_{Φ} is the efficiency of the coupling between the pickup loop and the input coil of the SQUID. To optimize this efficiency, we use a gradiometric transformer to match the inductances of the pickup loop and the SQUID, see Fig. 6.1(a). For a single transformer circuit, as shown in Fig. 6.2, the efficiency is given by [164]:

$$\eta_{\Phi} = \frac{M_f M_i}{(L_p + L_{\text{par}} + L_1)(L_2 + L_i) - M_f^2}, \quad (6.3)$$

in which the various inductances L and mutual inductances M are defined in Fig. 6.2. L_{par} is the parasitic inductance within the pickup loop circuit, which is dominated by the wirebonds between the detection chip and the transformer. We use a sub-optimally designed gradiometric transformer to match the impedance of the pickup loop and input coil, resulting in $\eta_{\Phi} \approx 3.5\%$. Using this efficiency together with the other experimental parameters, we find from Eq. 6.2 that a 10 mA current induces a crosstalk in the SQUID of $\Phi_{\text{RF}} = 3.6 \cdot 10^{-15} \text{ Wb} \sim 1.8 \Phi_0$. Given that the SQUID noise

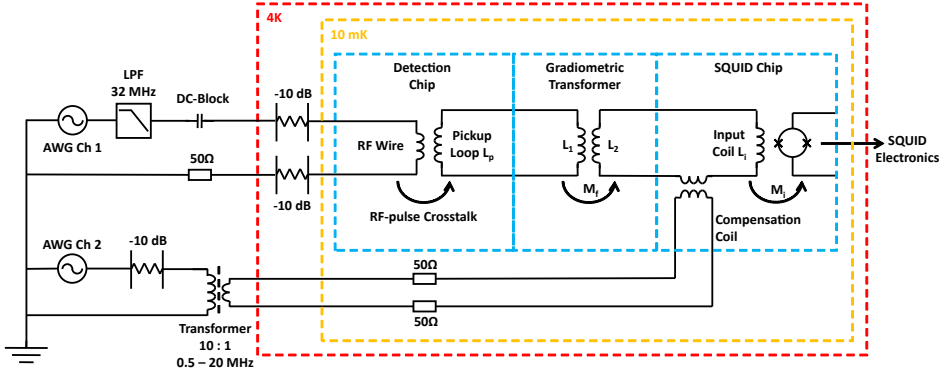


Figure 6.2: Schematic of the electronic circuit used for the flux compensation. The red and yellow dashed boxes indicate different stages of the cryostat, the blue dashed boxes indicate the detection chip, transformer chip, and SQUID chip, all connected using Al-Si(1%) wirebonds.

floor at temperatures below 4 K is generally less than $1\text{-}2 \mu\Phi_0/\sqrt{\text{Hz}}$, this crosstalk is quite significant.

To solve this issue, we use an additional feedback transformer to precisely cancel this crosstalk flux in the SQUID, using the electrical circuit shown in Fig. 6.2. We use a SQUID with an on-chip additional feedback transformer¹. A dual-channel arbitrary waveform generator (AWG) is used to send both the RF pulse and the compensation pulse. The first channel is used to send the current to the RF wire. This current is intended to generate the magnetic fields to perform NMR protocols, but also creates unwanted crosstalk flux in the pickup loop. Low temperature attenuators are used to reduce the noise originating from the room temperature electronics and filters. The second channel is used to send a compensation pulse with precisely the correct gain and phase shift to the compensation coil in order to balance the crosstalk of the RF pulse. A ferrite core transformer is used to decouple the highly sensitive feedback transformer from low-frequency noise on the electrical ground of the cryostat. As the compensation coil is so strongly coupled to the input coil of the SQUID, 50 Ohm resistors are used to attenuate the current at the 10 mK plate of the dilution refrigerator to suppress noise currents in the compensation circuit.

The required gain and phase shift are calibrated by using a lock-in amplifier to measure the crosstalk in the SQUID during a continuous, constant frequency RF signal. The amplitude $R(f)$ and phase $\phi(f)$ of the compensation pulse is varied until a minimum in the measured crosstalk is obtained. Because of the frequency dependence of the transfer functions of the various circuits, this calibration must be

¹Magnicon integrated 2-stage current sensor C70M116W

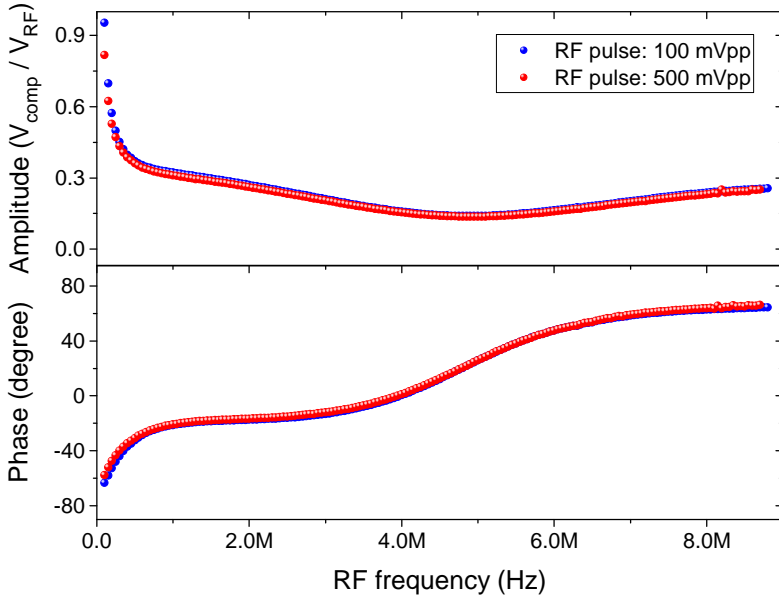


Figure 6.3: Calibrated amplitude $R(f)$ (top) and phase $\phi(f)$ (bottom) of the compensation pulse for an RF pulse with reference phase 0. Both the amplitude and phase result from the combination of the transfer functions of the RF circuit and the compensation circuit, as shown in Fig. 6.2.

repeated for the full RF pulse frequency range required for the experiments, the result of which is shown in Fig. 6.3. The blue and red curves are measured for different RF signal amplitudes. The good correspondence between the two shows that the SQUID does not suffer from large non-linearities in this range.

It is straightforward to use the calibration from Fig. 6.3 to properly compensate the flux from pulses consisting of a single frequency, as required for e.g. saturation experiments [37]. However, it can also be used to compensate for the crosstalk from more complex RF pulses, such as the pulses required for adiabatic rapid passage (ARP), the technique used to coherently flip the magnetization of a spin ensemble [57, 165]. An ARP pulse consists of a frequency-chirp combined with an amplitude envelope, an example of which is given by the blue curve in Fig. 6.4. In this particular example, the amplitude envelope is of the WURST kind [166, 167], given by $A(t) = 1 - \left| \cos\left(\frac{\pi t}{t_p}\right) \right|^4$, where the pulse starts at $t = 0$ and ends at $t = t_p$.

In order to find the appropriate compensation pulse for an arbitrary RF pulse, we take the discrete Fourier transform of the RF pulse, and multiply each frequency component with the corresponding calibrated amplitude and phase represented as the

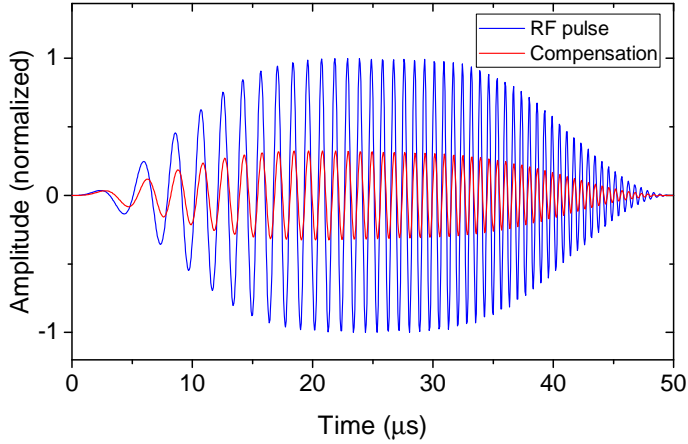


Figure 6.4: Example of a complex RF pulse, typically used for ARP protocols in MRFM, plus pre-calculated compensation pulse using the Fourier transform method. The RF pulse consists of a WURST amplitude envelope and a linear frequency chirp from 100 kHz to 1.9 MHz.

complex number $z(f) = R(f)e^{i\phi(f)}$. The required compensation pulse is obtained by taking the inverse Fourier transform to return to the time-domain. The resulting compensation pulse for the example ARP pulse is shown in red in Fig. 6.4.

6.3 RESULTS

To demonstrate the effectiveness of the flux crosstalk compensation method, we show the response of the SQUID to external flux in Fig. 6.5. All experiments in this section were performed at a temperature of 20 mK, stabilized using a PID controller. We apply a test flux $\Phi_a \sim 2 \Phi_0$ in the SQUID at a frequency of 23 Hz. The reference modulation without RF pulse is shown in black, where we find the SQUID modulation depth, amplified by the SQUID electronics, to be $5.9 V_{pp}$. When switching on the RF pulse with a frequency of 1.908 MHz and a peak-to-peak amplitude of $0.88 \Phi_0$, the measured modulation depth is significantly reduced, as can be seen from the red curve. The SQUID's noise susceptibility, which can be quantified by looking at the slope of the modulation, is increased by a factor of 8. By sending the suitable compensation pulse, we are able to restore the SQUID modulation, as shown by the blue curve. The compensation, and corresponding canceling of the flux crosstalk in the SQUID input circuit, leads to a recovery of the SQUID noise level to within 3% of that without RF pulse. To allow for easier comparison, we have shifted the different curves in the

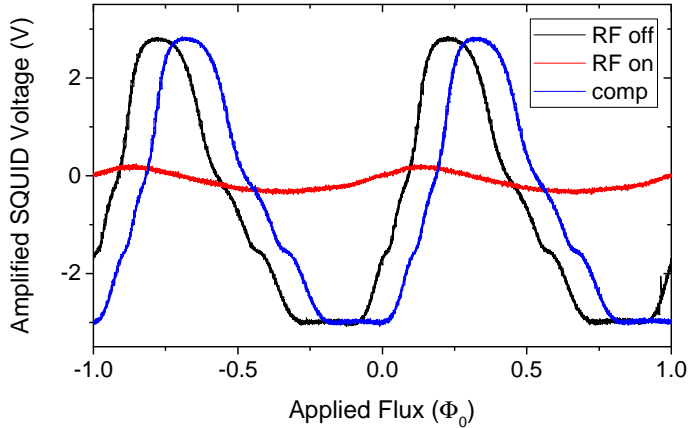


Figure 6.5: Effects of a 1.908 MHz, $0.88 \Phi_0$ pulse on the SQUID modulation. The modulation without RF field is shown in black. The red curve shows the suppressed modulation with an unbalanced RF flux crosstalk, while the blue curve shows the restored modulation with optimized compensation.

6

figure along the horizontal axis. This does not influence the actual experiment.

The previous experiment showing the SQUID modulation depth gives an idea of the effect of the RF pulse on the SQUID noise floor, i.e., the ability to measure at frequencies that are not equal to the frequency of the RF pulse. A direct visualization of the effect of the compensation at the RF pulse frequency is shown in Fig. 6.6, where we see a small part of the SQUID spectra during the application of a 118 kHz, 0.3 mA_{pp} RF pulse, with and without compensation. Each spectrum has been averaged 100 times with a total measurement time of 1000 seconds. The measured integrated flux crosstalk has been reduced from $74 \text{ m}\Phi_{0,\text{pp}}$ without compensation to below $42 \text{ }\mu\Phi_{0,\text{pp}}$ with compensation. Thus, the crosstalk has been reduced to less than 0.1% of the uncompensated value. The remaining flux crosstalk is the result of a small drift in the transfer functions of the RF wire or compensation circuits due to heating of the low temperature attenuators. We expect that this problem is reduced for pulses of shorter duration. Note that in order to reach these levels of crosstalk reduction, the compensation pulse amplitude has to be calibrated to an accuracy better than 0.1%, and the phase to better than 0.1 degree.

The RF frequency of 118 kHz was selected in order to prevent aliasing in the data acquisition. However, note that the compensation scheme can in principle be applied over a large bandwidth, from DC up to at least tens of MHz. In the current experiment, this bandwidth is limited by the DC block in the RF circuit, and the bandwidth of the SQUID feedback of about 20 MHz.

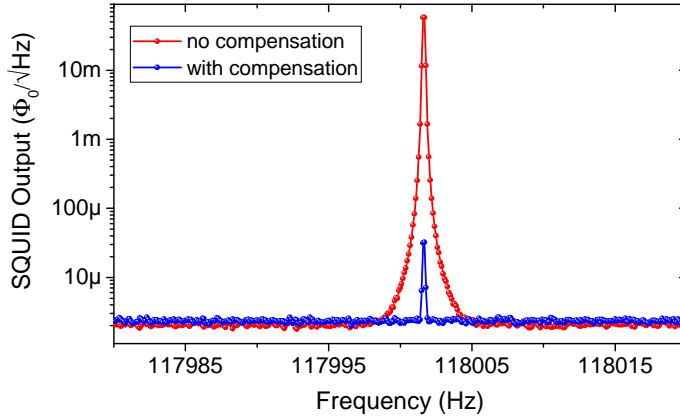


Figure 6.6: Demonstration of the reduction of crosstalk by compensating the RF pulse. The measured flux crosstalk has been reduced from $74 \text{ m}\Phi_{0,\text{pp}}$ without compensation to less than $42 \text{ }\mu\Phi_{0,\text{pp}}$ with compensation.

Note that the compensation scheme is suitable for low temperature operation, as it generates only very little dissipation. Compensating a $10 \text{ mA}_{\text{pk}}$ RF current requires a balancing current of about $200 \text{ }\mu\text{A}_{\text{pk}}$ in the low temperature compensation coil circuit. Given that this current dissipates over the two $50 \text{ }\Omega$ resistors, this leads to a power dissipation of less than $2 \text{ }\mu\text{W}$ at the 10 mK plate. This power is sufficiently small that this will not significantly heat up the 10 mK plate.

6.4 CONCLUSIONS AND OUTLOOK

We have presented a crosstalk compensation scheme that is easy to implement without any local adjustments near the sample or pickup loops. The compensation scheme allows for relatively strong RF pulses without any adverse effect on the SQUID sensitivity. This means that data acquisition with the SQUID does not have to be interrupted or compromised during RF pulses. This is a vital requirement for MRFM experiments, and initially was considered one of the major arguments against a SQUID-detected MRFM setup. Furthermore, even though our approach is very similar to what is done in the SQUID-detected NMR community, our approach to balance the crosstalk at the location of the SQUID instead of near the sample could allow for a broader application of the balancing technique.

An extended application would be to use this scheme to cancel noise in an applied external magnetic field. An external magnetic field in MRFM is useful due to the

enhancement of the Boltzmann polarization, leading to a larger signal for the same volume of spins. However, the application of an external magnetic field when using a SQUID is not an easy task, because of the extreme sensitivity of the SQUID to both the magnitude of the field as well as the magnetic field noise. The problem that a SQUID cannot be operated in large external fields can be solved by placing the SQUID outside of the external field in a low field region of the cryostat [168], and only placing the pickup loop and transformer in the high field region (at the cost of a slightly increased parasitic inductance in the input coil circuit). This leaves the second problem of the magnetic field noise. Suppose we use a gradiometric pickup loop with a parasitic area of only $1 \mu\text{m}^2$ coupled to the SQUID with an efficiency of 1%. Then, applying a 1 T external magnetic field without degradation of the SQUID noise floor requires a field stability of about 0.1 ppm. This is well beyond the stability of present-day magnet power supply systems, which is of the order of 10 ppm [169]. A potential solution would be to use a persistent current switch, but achieving this at 10 mK is still technologically challenging [170]. Alternatively, one could redirect a part of the current from the external magnetic field to the compensation coil, after proper attenuation and phase shifting. Any noise in the power supply of the external magnet will now be compensated at the SQUID level. When the current from the magnet power supply is low-pass filtered to a bandwidth of 10 Hz, even a delay of 100 μs is acceptable to obtain a noise reduction of over a factor of 100. In combination with the other proposed solutions this should be sufficient to be able to place the pickup loop in an external field of potentially up to 1 T without a reduction in the SQUID sensitivity.

The possibility to continue to measure with the SQUID even during an RF protocol opens the way to perform MRFM experiments that rely on continuous application of ARP pulses at low temperatures. The fundamental limit of sensitivity of an MRFM experiment is dictated by the thermal force noise $\sqrt{S_F} = \sqrt{4k_B T \Gamma BW}$, with Γ the damping of the cantilever and BW the measurement bandwidth. Thus, lower operating temperatures in principle allow for measurements on smaller spin ensembles, and would be a new step towards the imaging of a single nuclear spin.

7

DISSIPATION OF THE ALTERNATING MAGNETIC FIELD SOURCE

Concerning the operation of a Magnetic Resonance Force Microscope at milliKelvin temperatures, one of the main challenges is the induced dissipation while creating the radio-frequency field necessary to manipulate the spins. Even though we use a superconducting RF wire, we still measure a significant dissipation which limits the ultimate operating temperature, the source of which remains unidentified. In this chapter, we present our attempt to shed some light on this problem, by carefully characterizing the amplitude- and frequency-dependent dissipation, and discussing a variety of possible sources.

7.1 INTRODUCTION

One of the crucial components of the MRFM setup is the source used to generate the B_1 field, which is necessary to manipulate the spins in the sample. There are two main approaches to making the microwave source. The first is based on (superconducting) microwave resonators, whose high quality factors amplify the generated magnetic fields, but at the cost of a limited bandwidth [63]. Alternatively, one can use an RF current passing through a microwire, allowing a larger operating bandwidth, but large currents are required to generate sufficient fields.

When operating an MRFM at low temperatures, it turns out that the dissipation of the RF source is the main limiting factor. For instance, Poggio et al. [57] generated a 4 mT field at the location of the sample by passing 20 mA through a copper microwire at a current density of $\sim 10^7$ A/cm². However, in doing so, they had a dissipated power of 350 μ W. When measuring in a dilution refrigerator with a cooling power of only several μ W at the mixing chamber at 15 mK, this is unacceptable. Therefore, our setup uses a superconducting microwire made of NbTiN in order to reduce the dissipation [49]. However, even when using a superconducting RF source an increase in sample temperature is observed during pulses. As a varying sample temperature strongly affects an MRFM measurement (i.e. by changing the Boltzmann polarization of the spin ensemble or inducing shifts of the resonance frequency and quality factor of the cantilever), it is paramount to solve this issue.

In this chapter, we investigate the dissipation when sending alternating currents through our RF microwire by using our MRFM setup as a calorimeter. We then compare this measured dissipation to various possible mechanisms which could cause dissipation due to an alternating current. In doing so we try to understand the origin of the dissipation and, hopefully, find a solution to this longstanding problem.

7.2 CALORIMETRY AT MK TEMPERATURES

7.2.1 Cryogenic dual-compensated calorimeter

In order to measure the dissipated power at low temperatures, we use our MRFM setup as a dual compensated calorimeter. The operating principle of such a calorimeter is shown in Fig. 7.1. The idea is straightforward: two temperature controllers are

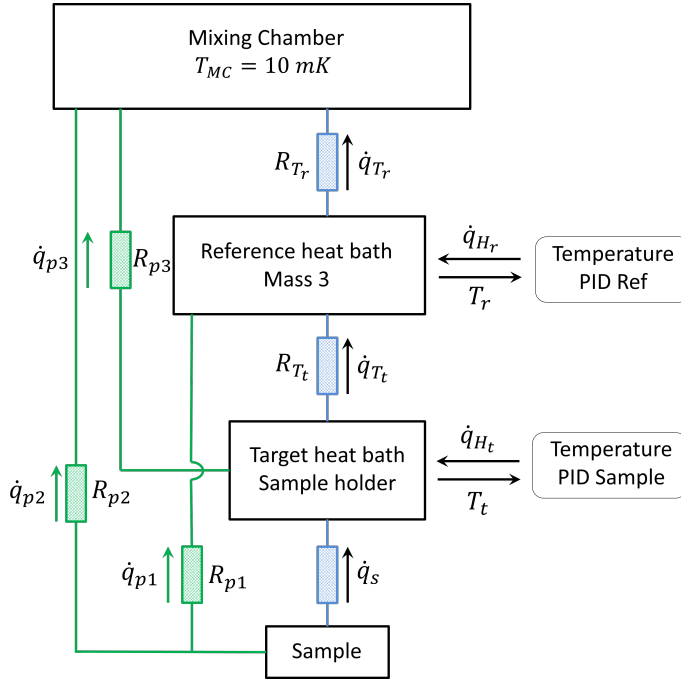


Figure 7.1: Schematic of the operation principle of a dual compensated calorimeter. The blue parts indicate the intended heatlinks between the different calorimeter stages, while the parts in green are parasitic thermal connections. A dual temperature controller maintains both the target and reference heat bath at constant temperatures.

used to hold the target (T_t) and reference (T_r) heat baths at a constant temperature, with T_t slightly above T_r . The total heat flow to and from the target heat bath is given by:

$$\dot{q}_{H_t} = \dot{q}_s - \dot{q}_{T_t} - \sum_n \dot{q}_{pn} \quad (7.1)$$

where \dot{q}_s is the power from the sample that reaches the target heat bath, \dot{q}_{T_t} the heat flow from the target to the reference heat bath, \dot{q}_{H_r} the power used by the temperature controller to maintain constant temperature, and \dot{q}_{pn} are all parasitic heat flows that bypass one or both of the heat baths. Because we keep T_t and T_r constant, all thermal conductivities of the various materials stay the same during the measurement. If we also assume that the sum of all parasitic heat losses is small and constant, we can directly measure the power dissipated on the sample, since this can be measured as a decrease of the control power required to keep the target heat bath at a constant temperature.

The measurement protocol depends on differential measurements of the required

heating power on the sample, with the reference bath always at a constant temperature. First, the reference power (P_1) required to keep the sample holder at a certain setpoint temperature is measured without any heating on the sample. Second, the reference power is switched off, and the target bath is allowed to cool down to the temperature of the reference bath. Third, dissipation on the sample is switched on, in our case by sending continuous RF power through the RF wire. When the temperature without feedback is stable, the temperature controller is switched on, and the new required power (P_2) to heat the sample holder to the temperature setpoint is determined. The power dissipated by the sample is now given by the difference between P_1 and P_2 .

In reality, we did not use a dedicated calorimeter setup for the experiments presented in this chapter. Instead, we simply used the Fermat MRFM setup, where the sample holder is used as the target heat bath, while we use the bottom mass of the vibration isolation (mass 3) as the reference heat bath. The heat conductance between the two baths has been measured for different temperatures, the result of which is shown in Fig. 7.2. The linear dependency on the temperature matches electronic thermal conductance at low temperatures [109], while the magnitude of the measured value indicates that the conductance is limited by the brass screw used to connect the sample holder to the outer housing of Fermat: An M2 brass screw with a length of 1 cm would lead to a thermal conductance of approximately 10 nW/mK at a temperature of 100 mK. An AR3 low temperature thermometer¹ is used in combination with a 100 Ohm heating element to control the temperature between 15 mK and 1 K. The final achieved power resolution varies between 1 and 100 nW depending on the setpoint temperature of the sample holder, and the ferocity of the PID controller.

7.2.2 NbTiN RF wire

The RF wire under investigation in this chapter can be seen in Fig. 7.3(a), and consists of two leads with dimensions $2000 \times 20 \times 0.3 \mu\text{m}$, and a constriction with dimensions $300 \times 1.0 \times 0.3 \mu\text{m}$. The transition between the leads and the constriction has rounded corners to prevent current crowding which reduces the critical current [171]. It was fabricated according to the recipe outlined in appendix D, based on NbTiN films grown by David Thoen [55]. The superconducting properties of the RF wire were measured in a vacuum chamber inside a liquid helium dewar. A DC transport critical current of 28.3 mA was measured, equivalent to a critical current density of $9 \cdot 10^6 \text{ A/cm}^2$ (see Fig. 7.3(b)). The residual DC resistance well below the critical current is less than 0.1 m Ω .

¹Supplied by Hightech Development Leiden (HDL), calibrated range 10 mK - 1.1 K.

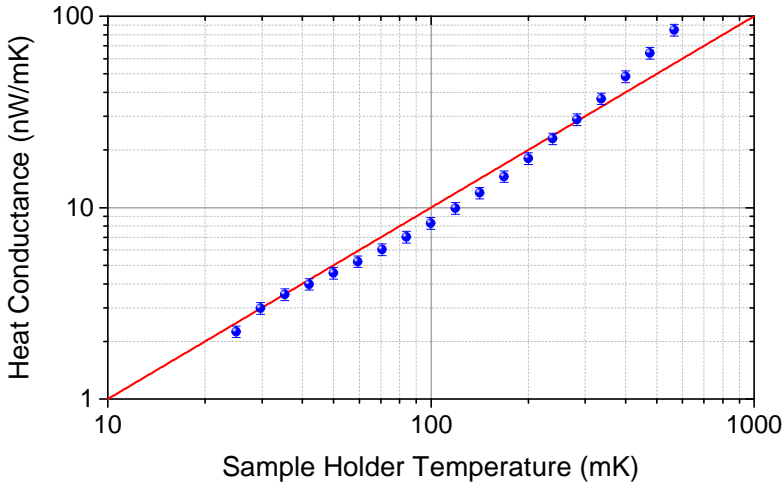


Figure 7.2: Thermal conductance between the sample holder and mass 3. The red line indicates the expected linear dependence between the heat conductance and temperature. The error bars are based on the uncertainties in the thermometer calibration and low temperature resistance of the heater.

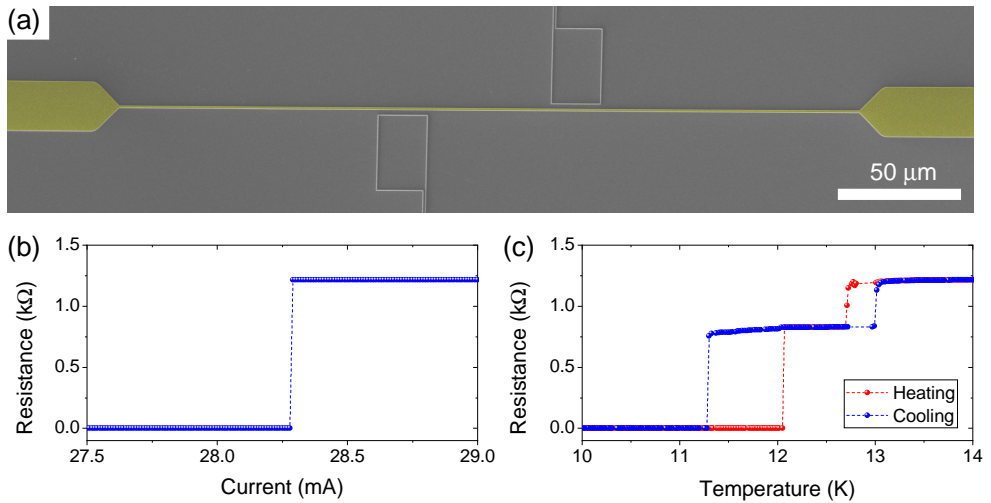


Figure 7.3: Properties of the RF wire under investigation. (a) Scanning electron microscope image of the RF wire (yellow), consisting of a narrow part with dimensions $300 \times 1.0 \times 0.3 \mu\text{m}$, and two leads with dimensions $2000 \times 20 \times 0.3 \mu\text{m}$. (b) Measurement of the critical current at 4.2 K and a pressure of $\sim 10^{-3}$ mbar. (c) Measurement of the critical temperature, where the red curve is measured during heating, and the blue curve is measured during cooling.

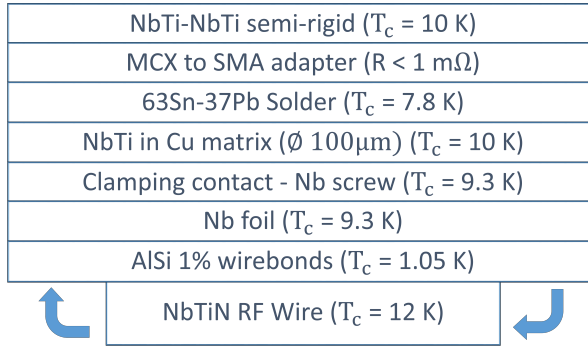


Figure 7.4: List of all components of the RF circuit from the mixing chamber (top) to the sample (bottom).

The superconducting transition temperature of the RF wire can be seen in Fig. 7.3(c). The two distinct steps correspond to slightly different critical temperatures for the constriction and leads of the RF wire, where the RF wire is responsible for the lower temperature step as surface impurities have more effect on narrow structures. The difference between heating and cooling is due to the thermal delay between the sample holder and the RF wire. We deem the heating curve to be more reliable, leading to a critical temperature of ~ 12 K, slightly less than the value reported for the full wafer [55].

7.3 CHARACTERIZATION OF DISSIPATION

We have used the setup described in the previous section to measure the dissipated power in the RF wire for various (RF) currents. The most straightforward experiment is simply sending a direct current I in order to determine the resistance R in the system following a Joule heating model where $P = RI^2$. Fig. 7.5 shows the result of this experiment, where we observe a power dissipation of up to tens of nanoWatts, and where the red solid line represents the Joule heating model with a residual resistance of 0.9 m Ω . A residual resistance this low is nearly unavoidable in any circuit with transitions between materials, and in this case might be explained by, for instance, the oxide layer on the niobium at the clamping contact transition to the copper/NbTi wire (see Fig. 7.4).

When the direct current is replaced by an alternating current, Joule heating hardly changes. For an alternating current $I(t) = I_0 \cos(\omega t)$, the dissipated power is given

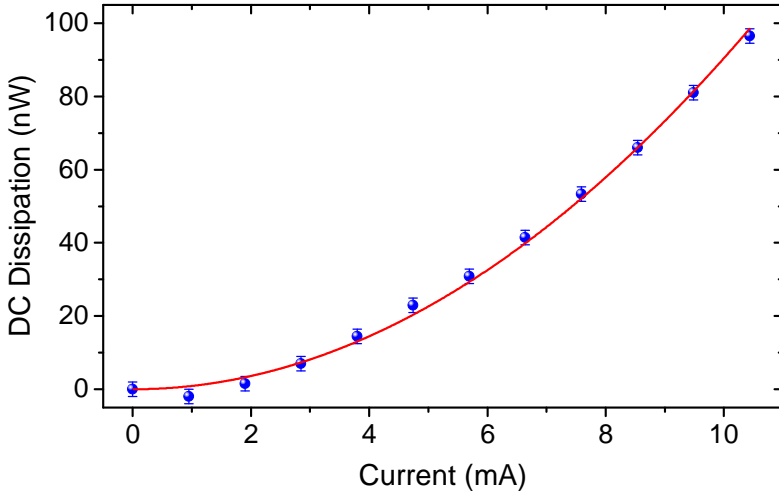


Figure 7.5: Measured dissipation at the sample holder versus direct current. The red line is a parabolic fit to a simple Joule heating model with a residual resistance of roughly $0.9 \text{ m}\Omega$. The error bars are estimated from the noise on the applied power.

by:

$$P(t) = RI^2(t) = RI_0^2 \cos^2(\omega t) = RI_0^2 \left(\frac{1}{2} + \frac{1}{2} \cos(2\omega t) \right) \quad (7.2)$$

Evidently, we obtain an oscillating power with an average of $P = RI_{\text{rms}}^2$. This in turn would lead to a final temperature consisting of a constant temperature increase with respect to the surroundings, plus an alternating component oscillating with frequency 2ω . However, if this frequency is larger than the inverse thermal time constant of the system (e.g. the sample holder), this alternating component will be averaged out. What allows us to distinguish AC Joule heating from other effects, is that the Joule heating is independent of the frequency of the current. Therefore, when we measure the dissipation as a function of frequency, it should only show up as a dissipation background, equal at all frequencies.

In Fig. 7.6 we have measured the dissipation resulting from a 200 kHz alternating current with varying amplitude. The inset shows similar data, but measured at different (higher) frequencies (with an inferior power resolution). The solid lines are fits to the data to a model $P = c(f)I^2$. So, the dissipation scales in the same way as expected from Joule heating, but the magnitude of the measured dissipation is much larger than what was observed for DC in Fig. 7.5. Therefore, we have to look for an additional source of dissipation which seems to be dominant in our setup.

More insight on the matter might be obtained from the influence of the RF fre-

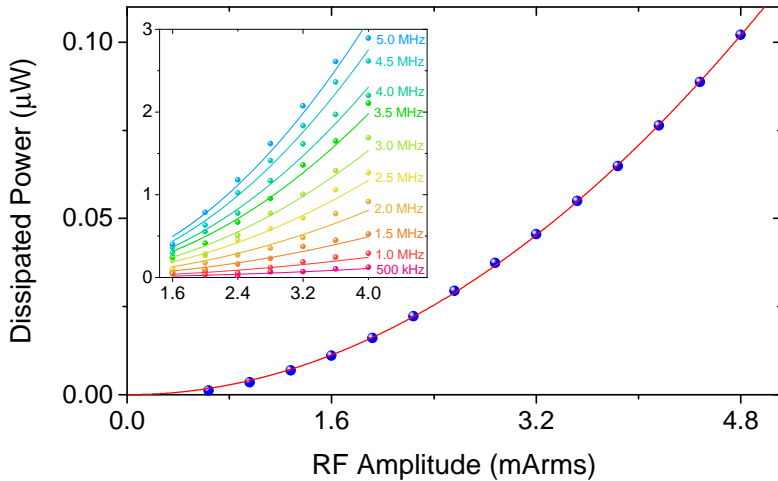


Figure 7.6: Dissipated power vs amplitude of the RF current at a frequency of 200 kHz at a sample holder temperature of 50 mK. The red line represents a quadratic relation between the amplitude and power. At 200 kHz, the dissipation is 4 times the DC dissipation. Inset: the same measurement at different RF frequencies and at a sample holder temperature of 70 mK.

quency. We have varied the RF frequency from 100 kHz to 20 MHz at a constant current of 1.6 mA_{rms}. The measured dissipation for all frequencies is shown in Fig. 7.7. Measurements were done at a sample holder temperature of 150 mK (blue), 300 mK (green), and 500 mK (orange). From the nice overlap between the different curves, we can conclude that the temperature does not influence the amount of power dissipated. The red solid lines are fits to a simple power law $P = cf^b$, with c a free fitting parameter, and $b = 0, 1$, and 1.5 . We find that at low frequencies, the power scales linearly with the RF frequency, but as the applied frequency increases the dependency changes to $P \propto f^{1.5}$. The inset shows more measurements of the dissipated power vs frequency for different RF currents, but this does not seem to affect the measured frequency-dependence. The solid lines are fits to the data of a powerlaw with $b = 1.5$.

Let us summarize what we have learned from the experimental data in this section. The dissipation can be divided into an AC and DC component. The DC component corresponds to Joule heating over a 0.9 mΩ resistive component somewhere on or near the sample holder. The dissipated power from the AC component seems to be independent of temperature (for temperatures below 500 mK), and scales quadratically with the amplitude of the RF current. The frequency dependence of the dissipation seems to vary between $P \propto f$ and $P \propto f^{1.5}$, depending on the actual RF frequency. We can now use this data to speculate about the source of the (AC) dissipation.

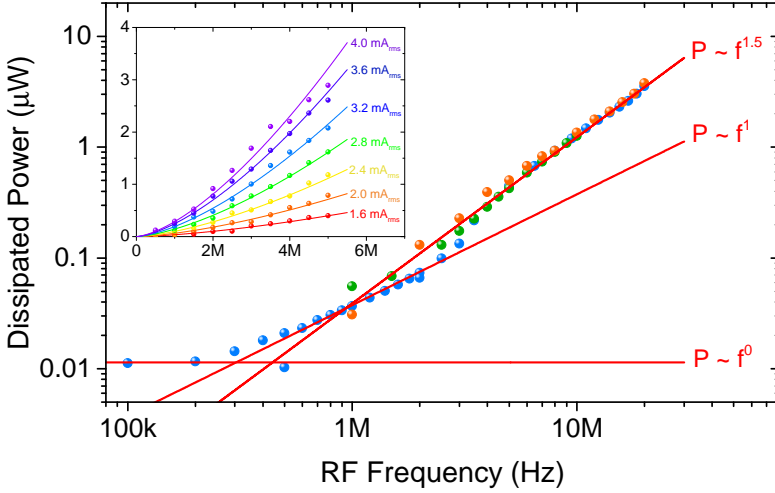


Figure 7.7: Dissipated power vs frequency of the RF current, measured at $1.6 \text{ mA}_{\text{rms}}$. The red lines indicate fits to a simple power law $P = cf^b$ for $b = 0, 1$, and 1.5 . Data was measured at a sample holder temperature of 150 mK (blue), 300 mK (green), and 500 mK (orange). Inset: the same measurement but at different RF amplitudes, measured at 300 mK .

7.4 MODELS FOR THE ORIGIN OF DISSIPATION

When looking for the origin of the dissipation in our RF wire, there are two main suspects: losses due to eddy currents in surrounding metals, and dissipation within the superconductor itself.

7.4.1 Eddy currents and skin effect

When a time-varying magnetic field is present in a conducting material, eddy currents are generated to compensate for the changing flux. As the conductivity of normal metals has a finite value, these eddy currents are subsequently dissipated into heat. In general, analytical calculations of eddy currents are complicated, but using the appropriate limits and approximations they are certainly possible [172]. An important concept is the skin depth which describes the attenuation of the free space magnetic field within a material [173]:

$$\delta = \sqrt{2\rho/\omega\mu}, \quad (7.3)$$

where ρ is the resistivity of the material, and ω is the angular frequency of the alternating magnetic field. μ is the magnetic permeability of the material, which we

will set equal to μ_0 since we only look at nonmagnetic materials. The precise value for the skin depth is difficult to calculate because often the low temperature resistivity of, e.g., copper is not known, since this depends on the residual resistivity ratio (RRR) of the particular copper component [174]. For the MHz frequencies we typically use in our MRFM experiments, the skin depth is of the order of 10 μm .

A particularly nice analysis is given by Meyer et al., who calculate the dissipated power due to eddy currents in two limits. If the thickness of a metal plate is much larger than the skin depth (the inductive limit, $d \gg \delta$), most eddy currents flow across the surface of the plate, and the dissipated power is given by: [115]

$$P = A \left(\frac{B_0}{\mu_0} \right)^2 \left(\frac{\rho}{\delta} \right) \propto \sqrt{\omega\rho}, \quad (7.4)$$

where B_0 is the amplitude of the alternating magnetic field in free space, and A is the area of the plate. The opposite limit is when the metal plate is so thin compared to the skin depth that the plate practically becomes transparent to the field (the resistive limit, $d \ll \delta$). In that case the dissipation scales strongly with the thickness of the plate:

$$P = A \left(\frac{B_0}{\mu_0} \right)^2 \left(\frac{d}{\delta} \right)^3 \frac{\rho}{6\delta} \propto \frac{\omega^2 d^3}{\rho}. \quad (7.5)$$

We can use Eqs. 7.4 and 7.5 to check if eddy current dissipation is the main source of heating in our experiment by comparing the predicted and measured power laws. Note that these equations assume a varying magnetic field that is homogeneously distributed in free space, which is not the case in our setup where all magnetic fields are very local.

When looking at potential sources for eddy current dissipation in our setup, there are two likely candidates: a thin metallic sample right next to the RF wire, and the copper sample holder underneath the detection chip.

For a metallic sample with a thickness of 100 nm, we are in the resistive limit, so we can use Eq. 7.5 while taking into account that the magnetic field of the RF wire decreases with distance ²:

$$P = l \left(\frac{1}{\mu_0} \right)^2 \left(\frac{d}{\delta} \right)^3 \frac{\rho}{6\delta} \left(\frac{\mu_0 I}{2\pi} \right)^2 \int \frac{1}{r^2} dr, \quad (7.6)$$

where the integral is taken over the entire width of the sample, and l is the length of the sample along the RF wire. The resulting dissipation for the expected lower

²The magnitude of the magnetic field of a wire carrying a current I is simply given by $|B| = \frac{\mu_0 I}{2\pi r}$, with r the distance from the wire.

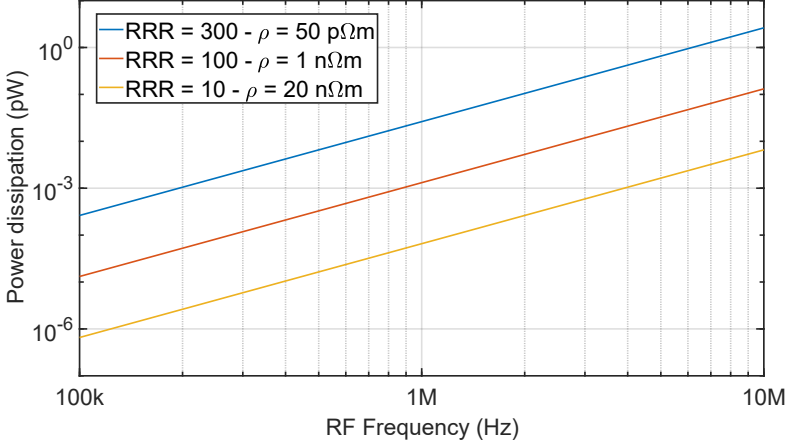


Figure 7.8: Calculation of the dissipation induced by eddy currents due to a $10 \text{ mA}_{\text{pk}}$ current in the RF wire for a metallic sample of thickness 100 nm for different RRR values.

and upper limits of the RRR value of the copper is seen in Fig. 7.8. Even for pretty extreme parameters of a peak current of $10 \text{ mA}_{\text{pk}}$ at a frequency of 10 MHz, the dissipation only reaches pW levels.

For eddy currents induced in the sample holder, we are well in the inductive limit. In this case we can modify 7.4 by once again taking into account the magnetic field distribution to calculate the dissipation:

$$P = \left(\frac{1}{\mu_0} \right)^2 \frac{\rho l}{\delta} \left(\frac{\mu_0 I}{2\pi} \right)^2 \int \frac{1}{(d^2 + r^2)} dr \quad (7.7)$$

Here d is the thickness of the detection chip (the minimal distance between the sample holder and RF wire), and the integral is taken over the full width of the sample holder. Once again, we have calculated the expected dissipation for typical RF pulse parameters, the result of which can be seen as the blue curve in Fig. 7.9. The red curve in this figure is the result of a finite element analysis using COMSOL Multiphysics for the same system with the same settings. Both methods show the same $\sqrt{\omega}$ dependency, and in absolute values they are within a factor of 2 of each other. The absolute value for the dissipation is between 10 and 100 nW, so the effects of eddy currents in the sample holder are certainly present, but are still small compared to the dissipation measured in the setup.

Based on these calculations, we conclude that both the frequency-dependence and absolute values of the eddy current losses indicate that they are not responsible for the observed dissipation during the MRFM experiments.

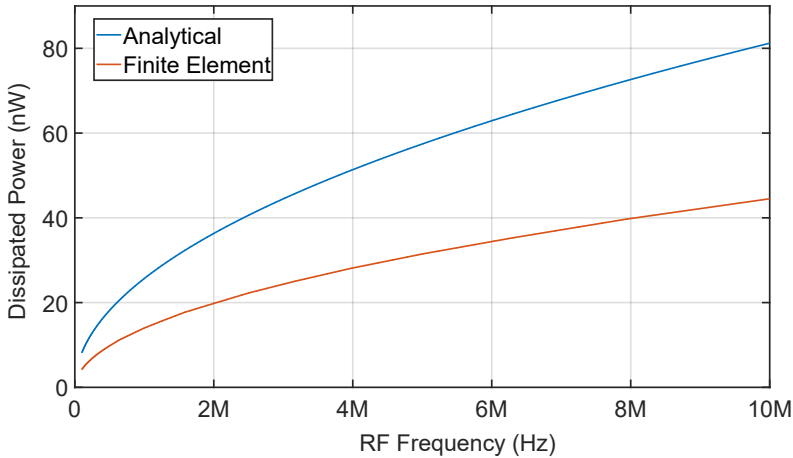


Figure 7.9: Calculation of the dissipation due to a $10 \text{ mA}_{\text{pk}}$ current induced by eddy currents in the sample holder located 0.5 mm below the RF source, assuming a resistivity of $1 \text{ n}\Omega\text{m}$ ($\text{RRR} = 100$).

7.4.2 Dissipation in type-II superconductors

A completely different line of thought is that the dissipation originates within the superconductor. We will consider two different mechanisms for losses in a superconductor carrying an alternating current. The first is based on the presence of quasiparticles in the superconducting condensate, and the second on the movement of flux vortices penetrating the superconductor. As we are only trying to identify potential origins of the dissipation, the theoretical description of these models will be minimal. For a more in-depth analysis, the reader is referred to more specialized work like Tinkham [175] and Annett [176].

THE QUASIPARTICLE MODEL: For high frequency currents, we can use the two-fluid model to predict that normal electrons (the quasiparticles) within the superconducting condensate can give rise to a finite amount of dissipation [175]. The normal and superconducting electrons can be seen as two parallel conduction channels, one resistive (dissipation) and one inductive (no dissipation), leading to a total conductivity given by

$$\sigma(\omega) = \sigma_1(\omega) - i\sigma_2(\omega), \quad (7.8)$$

with $\sigma_1 = n_n e^2 \tau_n / m$ the conductivity of the normal channel and $\sigma_2 = n_s e^2 / m\omega$ the conductivity of the superconducting one. τ_n is the scattering relaxation time of the normal electrons, and n_n and n_s are the densities of the normal and superconducting

electrons. At low frequencies, the inductive superconducting channel shorts the resistive one, but there is a crossover frequency above which the resistive channel becomes favourable. This crossover frequency is given by $\omega \approx (n_s/n_n)(1/\tau_n)$. This frequency is expected to be very high, due to the short τ_n , which is in the fs range [177], and due to the fact that in the BCS theory, $n_n \sim \exp(-\Delta/k_B T)$, so n_n goes exponentially to zero at low temperatures. However, even far below the crossover frequency, there will always be a nonzero dissipation from the normal component.

Following the argument above, given an imposed alternating current density J , the dissipation per unit volume is given by $Re(1/\sigma)J^2 = [\sigma_1/(\sigma_1^2 + \sigma_2^2)]J^2 \approx (\sigma_1/\sigma_2^2)J^2$, where we assumed $\sigma_1 \ll \sigma_2$. Inserting the conductivities for both channels, we find:

$$\mathcal{P} = \frac{n_n \tau_n m}{n_s^2 e^2} \omega^2 J^2 \quad (7.9)$$

Thus, the dissipation in this model should be proportional to the square of both the frequency and the amplitude of the AC current.

When we compare this model to the experiments described in this chapter, we find that the model matches in terms of the current-dependence of the dissipation. However, we do not observe a quadratic dependence on the frequency. Giving an actual number for the dissipation based on this equation is difficult, but since we measure at temperatures far below the energy gap of NbTiN ($\Delta \sim 1.76 k_B T_c \approx k_B \cdot 26$ K) [55] we expect n_n to be extremely small, and thus the dissipation to be small as well. We therefore deem it unlikely that this is the main origin of the observed dissipation.

THE VORTEX MODEL: A defining property of type-II superconductors is their capability to carry supercurrents at relatively high magnetic fields. The explanation for this was given by Abrikosov, who hypothesized that quantized magnetic vortices are allowed to enter the superconductor when it is subjected to a magnetic field between the lower (H_{c1}) and upper (H_{c2}) critical field [178]. However, several theories are now holding these vortices responsible for the observed dissipation in superconductors. When a current density J is applied, a Lorentz force $F_L = \Phi_0 J$ acts on the vortex³ [179]. Here $\Phi_0 = h/2e$ is the magnetic flux quantum. When this force is smaller than the pinning force holding the vortex in place, the vortex will make a small oscillation around its pinning site, similar to a particle trapped in a potential U_0 . Thermally assisted flux creep is possible when the temperature $T \gg U_0/k_B$, but in our temperature regime it is estimated that this motion of vortices does not lead to significant

³Actually, this is the Lorentz force per vortex per unit length.

dissipation. This situation changes when the current density is increased and the Lorentz force becomes larger than the pinning force, in which case the vortices start to move [180]. This leads to the dissipation of energy, as experimentally observed by Raes et al. [181].

In the Bardeen-Stephen model for the case of free vortex flow without pinning it is assumed that the core of the moving vortex with radius ξ is fully normal [182]. Dissipation occurs due to ordinary resistive processes in the core. Following this model, it is found that the power dissipated per unit volume due to the flow resistance ρ_f is given by [179]:

$$\mathcal{P} = J^2 \rho_f = J^2 \rho_n \frac{B}{H_{c2}}, \quad (7.10)$$

with $B = \Phi_0/a_0^2$, where a_0 is the spacing between vortices. So, in the Bardeen-Stephen model, dissipation rises quadratically with the RF current. Note that the dissipation is a fraction B/H_{c2} of the dissipation in the normal state with resistance ρ_n . Additionally, as the origin of the dissipation in this model is a viscous flow of the vortex, the power dissipation is also quadratic with the velocity of the vortex, and thereby quadratic with the frequency of the RF current.

We can try to calculate an order of magnitude number for the dissipation due to the flux flow mechanism described above. For this, we calculate the upper critical field

$$B_{c2} = \mu_0 H_{c2} = \frac{\Phi_0}{2\pi\xi^2} \sim 20 \text{ T}, \quad (7.11)$$

where $\xi = 3.8 \text{ nm}$ is the BCS coherence length of NbTiN [183, 184]. When we assume that the vortices have entered the RF wire during cooldown in the earth's magnetic field, and that all losses occur within the narrow part of the RF wire, the dissipated power is on the order of $1 \mu\text{W}$, which is definitely in the right ballpark.

As we measure an exponent of the frequency-dependence of the power dissipation between 1 and 1.5, it remains unclear via what mechanism the vortices induce losses. Anyway, the influence of vortices can be checked by applying a direct current in combination with the RF current. The idea here is that as soon as the field induced by the wire itself surpasses H_{c1} , additional vortices will enter the wire. The first critical field of the NbTiN can be calculated using [176]

$$H_{c1} = \frac{\Phi_0}{4\pi\mu_0\lambda^2} \ln\left(\frac{\lambda}{\xi}\right), \quad (7.12)$$

where $\lambda = 260$ to 300 nm is the London penetration depth [55, 185]. Using these values, we find a critical magnetic field $B_{c1} = \mu_0 H_{c1} \sim 8 \text{ mT}$. The current necessary

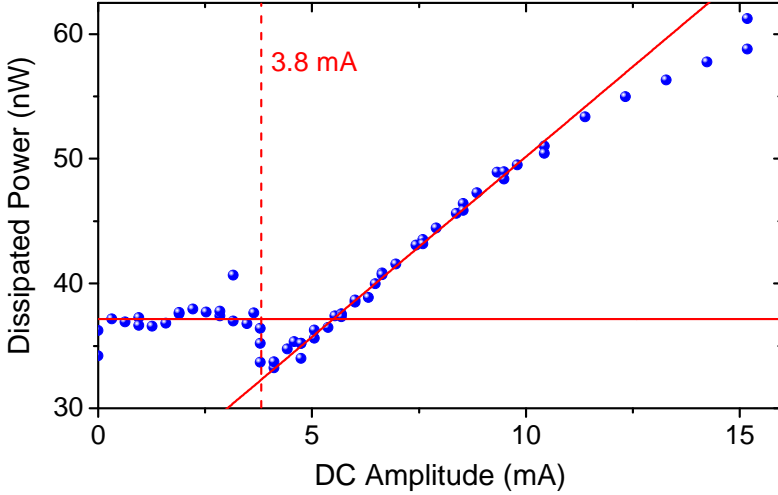


Figure 7.10: Measurement of the dissipation due to an RF current of $1.6 \text{ mA}_{\text{rms}}$ at 1 MHz as a function of the applied direct current.

to create this field at the surface of a wire of radius R_0 is given by [175]

$$I_{c1} = \frac{2\pi R_0 B_{c1}}{\mu_0} \left(\frac{2}{3}\right)^{3/2}, \quad (7.13)$$

leading to a critical current of 3.3 mA. Here we assume the wire to be cylindrical with a diameter equal to the thickness (so $R_0 = 150 \text{ nm}$). When the applied direct current gets above this value, the dissipation should increase linearly with the number of vortices, and thus with the amplitude of the direct current [186].

A direct current with a peak value of 50 mA was added to the RF current using a bias tee. After attenuation at the 4K plate of the cryostat, this leaves a current of up to 16 mA. To subtract the Joule heating, we again relied on differential measurements, where we first measure the dissipation with only the direct current, and subsequently with both the DC and AC at the same time. As can be seen in Fig. 7.10, indeed the measured dissipation stays constant up to a direct current of about 4 mA, after which it increases linearly with the applied current. The measurement was performed with an alternating current of $1.6 \text{ mA}_{\text{rms}}$ at 1 MHz, with a sample holder temperature of 70 mK to optimize the power resolution.

Interestingly, coinciding with the onset of the linear increase in the dissipation is a distinct dip of roughly 5 nW. Possibly, this is caused by the transition from flux penetrating the edges of the RF wire to flux vortices which completely penetrate the superconductor, which might lead to a more favorable overall field distribution.

7.5 SUGGESTIONS TO REDUCE DISSIPATION

It has become clear that the dissipation observed in the MRFM RF wire can originate from a number of possible sources, where we estimate the effects of flux vortices to be dominant. In order to reduce the dissipation, there are several technical options to consider:

- Reducing the Joule heating: we have measured a residual resistance of $0.9 \text{ m}\Omega$ in our RF circuit, which we attribute to one or several of the transitions between different materials and to the connectors in the circuit. The residual resistance can be improved by replacing all clamping contacts by spotwelded connections [170], or by moving all connections as close to the mixing chamber as possible, where more cooling power is available to remove generated heat.
- Reducing eddy current losses: As we have seen, the largest part of eddy current losses is expected to be induced in the copper sample holder. Increasing the distance between the RF wire and metal components in the setup would reduce these losses. However, as the magnetic field generated by a wire falls off linearly with the distance to the wire, large separations are needed to get a significant improvement. This could be done by placing the detection chip on top of a sapphire sample holder. Alternatively, one could try to shield the normal metals from the magnetic field by coating the bottom of the detection chip with a layer of superconducting material with a thickness much larger than the London penetration depth. However, both of these options will probably reduce the thermalization of the sample.
- Reducing flux vortices losses: When we assume the movement of flux vortices to be responsible for the power dissipation, there are two things we can do. The first is to reduce the total number of vortices. Stan et al. have shown that the maximum field you can apply before vortices enter a thin superconducting strip is given by $B_m \approx \Phi_0/w^2$, with w the width of the strip [186]. So, by reducing the width of the RF wire, the number of vortices at a given field can be reduced. The downside to this is that a narrow RF wire has a higher current density, which could enhance the flux flow of the remaining vortices, and reduces the maximal B_1 field. A similar effect can be achieved by making a laminar RF wire, where the thickness d of each layer is well below the London penetration depth. Then, the first critical field is enhanced via

$$H_{c1} = \frac{2\Phi_0}{\pi d^2} \ln\left(\frac{d}{\xi}\right), \quad (7.14)$$

which prevents vortices from entering [187]. The second approach is to enhance the pinning of the vortices, and thereby reduce vortex motion. This can be done by intentionally introducing defects in the superconductor [188–190] or applying the appropriate external magnetic fields [191, 192].

- Reducing dielectric losses: This is a topic we did not cover before, but it has been reported that the presence of the dielectric substrate, in our case the SiO_2 , can cause dissipation in superconducting resonators [52, 193, 194]. It is not clear if this type of dissipation is currently an issue in our RF wire. As a precaution, it might be possible to etch away the substrate near the RF wire to create a trenched microwire. Removing the dielectric from areas with high electric field gradients has been shown to improve the performance of superconducting devices [195].

7.6 REDUCING THE EFFECTS OF DISSIPATION

If all of the proposed solutions fail, there is a low tech solution: accept the dissipation, but guide the heat away from the sample. For low levels of dissipation, this can be done by covering the RF wire with a gold or copper layer with its own thermalization channels. For a 300 nm thick copper layer with a width of 300 μm and a total length of 2.5 mm we expect a thermal resistance of 3 mK/nW, where we assume the thermal conductivity to be ~ 10 W/mK at 100 mK. This rough estimate is backed up by a more accurate finite element analysis of the local temperature of the RF wire for various RF powers, as can be seen in Fig. 7.11. In this analysis a power P is applied at the RF wire, which is placed on top of a silicon chip with $\kappa_{\text{Si}} \propto T^3$, as expected for insulating materials [196]. The bottom of this chip is assumed to be perfectly thermalized to the sample holder.

It shows that even with very moderate dissipated powers the local temperature of the RF wire increases far above the temperature of the sample holder. Adding additional heat conductance by covering the RF wire with copper as described above is a significant improvement, and is therefore highly recommended. For the copper thermalization, we assume that the edge of the copper is properly thermalized to the sample holder, and $\kappa_{\text{Cu}} \propto T$. The simulation shows that the improvement is a combined effect of direct cooling via the copper and a larger effective contact area to the silicon substrate.

Alternatively, it might be possible to keep the RF source separated from the sample, for instance by putting it on a different chip or by switching to a more

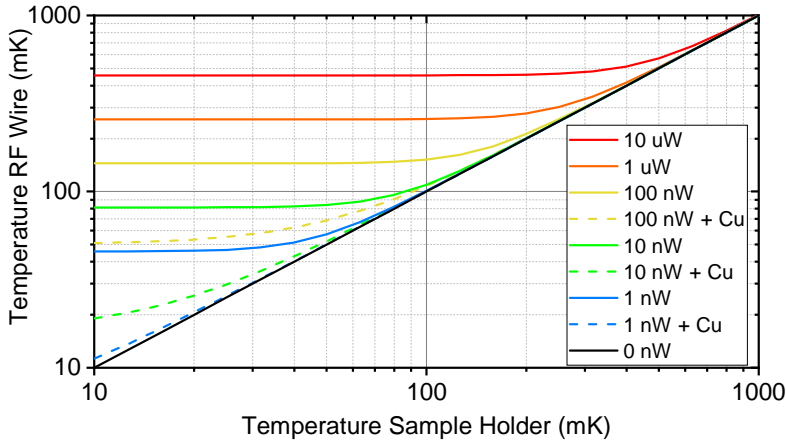


Figure 7.11: Finite element analysis of the local temperature of the RF wire while applying various powers, with and without additional copper thermalization.

long-ranged RF source. For high dissipation, this might be a better alternative, but it remains technically challenging to prevent a parasitic heat flow to the sample. Furthermore, a more long-ranged RF field would cause eddy current dissipation in surrounding metals to increase.

7

7.7 CONCLUSIONS

In this chapter, we have described the possibility of using Fermat as a highly sensitive calorimeter to measure the dissipation induced by the RF fields generated by the RF wire. We have measured this dissipation for various RF amplitudes and frequencies, concluding that the dissipation scales with I^2 and f^n , where n was found to vary between 1 (at low frequency) and 1.5 (at high frequency). We did not find a temperature dependence for temperatures below 500 mK. We evaluated various models for the dissipation, including eddy current losses and the intrinsic dissipation in superconductors when carrying an AC current. Our conclusion is that eddy currents only contribute to a small part of the observed dissipation, so completely removing these will only give a marginal improvement. We hypothesize that the dissipation is caused by the presence of flux vortices within the superconducting RF wire, but we were so far unable to match our data to a specific mechanism.

We have proposed some technical adjustments which might reduce the (effects of the) dissipation. When the NbTiN is indeed the source of the dissipation, we would

advise to start by fabricating detection chips with an additional thermalization of the RF wire. The gold thermalization is easy to implement, and based on the simulations it should offer a significant reduction of the sample temperature resulting from the dissipated power.

We end this chapter by calculating whether the measured dissipation allows to do an imaging experiment on protons with a B_1 field of 4 mT. At a distance of 0.5 μm from the RF wire, this requires a current of 20 mA_{pk} . The Larmor frequency of protons in a field of 100 mT is roughly 4 MHz. We extrapolate that a continuous power RF pulse with these parameters would dissipate roughly 30-40 μW , which would rule out continuous power protocols. Fortunately, most MRFM protocols have a low duty-cycle. For instance, cyclic-CERMIT has a duty cycle of only 0.5%, as the RF power is only switched on once every several cantilever periods [14].

Assuming that by using a properly chosen MRFM protocol, we can reduce the dissipation to 1 μW . According to the simulations in Fig. 7.11, this would allow sample temperatures close to 100 mK, which is already quite good. We can improve on this by increasing the thickness of the RF wire from 300 nm to 1 μm , as this would reduce the dissipation by an additional factor of 10 according to Eq. 7.10. The resulting 100 nW dissipation would heat the sample to about 50 mK. Therefore, based on these estimates, we are cautiously optimistic that the proposed technical improvements will reduce the dissipation from the RF wire, and enable a full fledged milliKelvin MRFM experiment.

8

DOUBLE-MAGNET CANTILEVERS FOR INCREASED MAGNETIC FIELD GRADIENTS

Ever since its first conception, the goal of MRFM was to reach levels of sensitivity sufficient to measure the properties of a single nuclear spin [1]. One of the approaches to increase the sensitivity of MRFM is to increase the spin signals by increasing the magnetic field gradients. In this chapter, we motivate this approach, and describe our attempt to increase the magnetic field gradient in such a way that it requires minimal change to the experimental setup, and reduces the effects of potential drawbacks.

8.1 INTRODUCTION

There has been a wide variety of methods to maximize the magnetic field gradients in MRFM. The standard approach of growing a magnetic structure on top of the RF source is widely used and has been very successful [16, 57, 197]. The fabrication of these structures is relatively straightforward, and by creating sharp edges, very large field gradients of up to 6 MT/m can be achieved using a variety of magnetic materials, such as dysprosium and iron-cobalt. The most extreme example of this approach was the utilization of a commercial disk drive write head, resulting in a record magnetic field gradient of 28 MT/m, with the added advantage of dynamic control of the gradient with frequencies up to 1 GHz [42]. However, this approach has the drawback of a complex resonant slice shape, and positioning the sample to within 100 nm of these structures can be challenging.

A more innovative approach of creating the magnetic field gradients is by using a current-focusing field gradient source (CFFGS), in which a constriction in a current-carrying wire is used to generate time-dependent field gradients of up to 1 MT/m, but at the cost of significant dissipation [17, 114, 198]. The maximum field gradients are limited by the breakdown current density in the wire. Once again, the experiment has to be performed very close (within 50 nm) to the wire.

The methods described above are all based on the sample-on-tip approach for MRFM. There has also been work focused on the magnet-on-tip approach. Micron-sized SmCo-particles have been used to generate gradients of up to 0.5 MT/m [19, 63, 199]. Higher field gradients can be achieved by using focused ion beam milling to shape magnetic particles [200–202] or using e-beam lithography [203], with the record set at 5.4 MT/m [41]. A big issue for all of these approaches is the positioning of the magnetic tip with respect to the sample. Furthermore, due to our SQUID-based detection, the problem is intensified as we are even incapable of detecting the cantilever motion at all when the cantilever is not positioned close enough to the pickup loop.

In an attempt to evade this issue, we have decided to combine two NdFeB magnets with different radii on the same cantilever: a small one to create higher field gradients than our group has achieved in the past, and a large one to have a high coupling to the SQUID-based detection system, which eases positioning and reduces the detection noise. This approach requires minimal changes to the experimental setup, and reduces the effects of potential drawbacks. We calculate the expected magnetic fields originating from these new cantilevers, and how this influences the flux coupling to the pickup loop. We end the chapter by analyzing how the spin-induced dissipation

is affected by the higher magnetic field gradients.

8.2 INTUITION ABOUT MAGNETIC FIELD GRADIENTS

The purpose of this section is to create some intuition about how the signals in MRFM scale with the size of the magnet used to generate the magnetic field gradient. In this section we will use the following simplifications:

- To be completely correct one has to always consider only the component of the force in the soft-direction of the cantilever, which in our case is the horizontal direction parallel to the magnetization of the magnet. However, in order to be able to gain some insight in the various scaling laws, we will consider the magnetic field gradient in the radial direction instead. This simplification will be justified in Sec. 8.5.
- We neglect the dynamics of the spin in the cantilever's magnetic field, assuming that the moment of the spin $\boldsymbol{\mu}_s$ is always perfectly aligned with the field. In that case, the interaction between the spin and the magnetic field can be determined from the interaction energy $E = -(\boldsymbol{\mu}_s \cdot \mathbf{B})$, instead of from the full analysis by De Voogd et al. [52].

An intuitive picture of how the radius of the magnet influences the expected signals is given by Garner [204]. When a single spin with magnetic moment $\boldsymbol{\mu}_s$ is placed in a magnetic field \mathbf{B} originating from the magnet on the tip of the cantilever, this creates a force between the spin and the cantilever, given by:

$$\mathbf{F} = \nabla (\boldsymbol{\mu}_s \cdot \mathbf{B}) = \boldsymbol{\mu}_s \cdot \nabla \mathbf{B} \quad (8.1)$$

This force induces a shift of the stiffness of the cantilever:

$$k_s = \boldsymbol{\mu}_s \cdot \nabla^2 \mathbf{B} \quad (8.2)$$

which results in a measurable frequency shift according to

$$\Delta f = \frac{1}{2} \frac{k_s}{k_0} f_0 \quad (8.3)$$

To use these equations, we need to know the distribution of the magnetic field originating from the magnet. As discussed in Ch. 2, we can describe the spherical

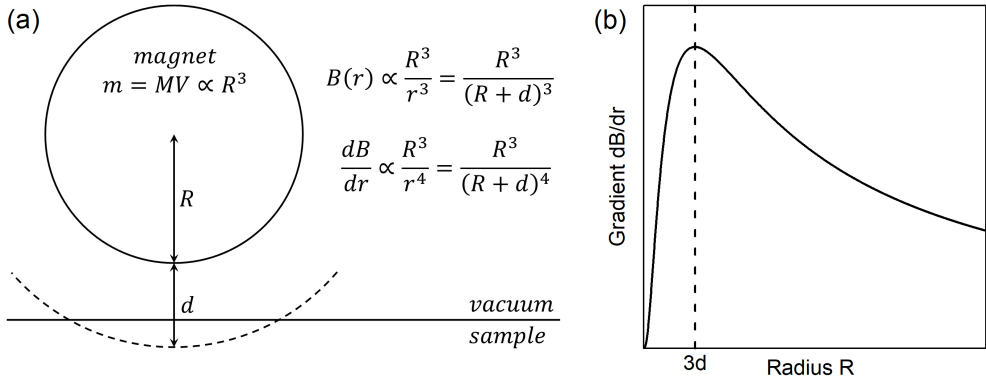


Figure 8.1: (a) Schematic of a magnet with radius R positioned above a sample with a resonant slice at a distance d from the surface of the magnet. (b) Calculated gradient versus radius of the magnet for a given d . The gradient is maximal for $R = 3d$.

magnet at the tip of the cantilever as a magnetic dipole with magnetic moment \mathbf{m} , for which the field is given by [146]

$$\mathbf{B}(\mathbf{r}) = \frac{\mu_0 \mathbf{m}}{4\pi r^3} [3(\hat{\mathbf{m}} \cdot \hat{\mathbf{r}}) \hat{\mathbf{r}} - \hat{\mathbf{m}}] \quad (8.4)$$

Here $r = |\mathbf{r}|$ is the distance to the center of the magnet positioned at the origin, which can be rewritten as $r = R + d$, with R the radius of the magnet and d the distance between the surface of the magnet and the resonant slice. The situation is sketched in Fig. 8.1(a). The magnetic moment, in turn, can be rewritten in terms of the saturation magnetization $M = \mathbf{B}_r/\mu_0$ and the volume V of the spherical magnet¹:

$$\mathbf{m} = \frac{\mathbf{B}_r}{\mu_0} V = \frac{4\pi}{3} \frac{1}{\mu_0} \mathbf{B}_r R^3 \quad (8.5)$$

Thus, $\mathbf{B} \propto R^3/(R+d)^3$. Considering this, the first derivative of the magnetic field, for simplicity calculated in the radial direction, then scales as

$$\frac{\partial \mathbf{B}}{\partial r} \propto \frac{R^3}{r^4} = \frac{R^3}{(R+d)^4} \quad (8.6)$$

Let us now consider the implications of these equations for maximizing the magnetic field gradient, and thereby the MRFM signals. First, imagine that we can perform our experiment right at the surface of the magnet, so $d = 0$. Then the gradient scales as R^{-1} , and we should take the smallest possible magnet to obtain the largest magnetic field gradient.

¹For our magnetic material, NdFeB, B_r is equal to 1.15 - 1.3 T [51, 59]

However, in practice it is not possible to measure so close to the surface of the magnet, as non-contact friction reduces the sensitivity of the experiment [51, 52, 68]. When we therefore demand that d is a constant value larger than 0, we can maximize the gradient to find that for a given d there is an optimal radius $R = 3d$ [204]. A plot of the gradient is shown in Fig. 8.1(b). When the radius is much smaller than $3d$, the gradient roughly scales with R^3 , as the decreasing radius reduces the magnetic moment. So, for measurements where $d > R/3$, one would be better off using a larger magnet. On the other hand, when the radius is much larger than $3d$, the gradient scales with R^{-1} , and a smaller magnet would give a higher signal per spin. So, decreasing the size of the magnetic particle is only beneficial when the experiment can be performed within $d < R/3$.

There is a second important aspect to consider, namely the total MRFM signal. Let's say that we are always measuring at a distance d that is proportional to the radius. In other words, when the radius is increased, the distance between the magnet and the sample is increased proportionally. Then the force per spin increases as the size of the magnetic particle is reduced, proportional to R^{-1} . However, the volume of the resonant slice, and thus the number of spins within it, increases with the size of the magnetic particle, proportional to R^3 . Therefore, even though the signal per spin and the volume sensitivity are improved, the total MRFM signal in the experiment decreases when a smaller magnet is used.

8.3 SIGNAL-TO-NOISE RATIO

As usual in MRFM, the right experimental parameters depend on the specific experiment in mind. A measurement based on using spins to drive the amplitude of the cantilever, a so-called force measurement, has different optimal parameters than a frequency shift measurement.

We start from the assumption that our experiment is thermally limited, i.e. the dominant noise factor is the thermal force noise, given by

$$S_F = 4k_B T \Gamma \quad (8.7)$$

with $\Gamma = k/(\omega_0 Q)$ the damping of the cantilever. The signal-to-noise ratio (SNR) for a force experiment on a single spin with magnetic moment μ_s is then given by

$$\text{SNR}_F = \mu_s \frac{\partial \mathbf{B}}{\partial x} (4k_B T \Gamma BW)^{-\frac{1}{2}} \quad (8.8)$$

with BW the bandwidth of the measurement².

For a frequency shift measurement we want to find the frequency noise. First, we can calculate the noise in the stiffness of the cantilever using Hooke's law as transfer function, leading to

$$S_k = \frac{S_F}{A^2} = \frac{4k_B T \Gamma}{A^2} \quad (8.9)$$

with A the rms amplitude of the cantilever motion. From this, we can find the frequency noise using

$$S_{\delta f_0}(f) = \left(\frac{1}{2} \frac{f_0}{k_0}\right)^2 S_k = \frac{k_B T \Gamma f_0^2}{k_0^2 A^2} \quad (8.10)$$

Note that this equation is only valid for $f \gg f_0/(2Q)$. We can combine this with Eqs. 8.2 and 8.3 to find the frequency shift SNR:

$$\text{SNR}_{\delta f_0} = \frac{f_0 \mu_s}{2 k_0} \frac{\partial^2 \mathbf{B}}{\partial x^2} \left(\frac{k_B T \Gamma f_0^2 BW}{k_0^2 A^2} \right)^{-\frac{1}{2}} \quad (8.11)$$

Using Eqs. 8.8 and 8.11, we can compare the relative signal-to-noise ratios of the two experiments for different experimental parameters when both experiments are operated in the thermal limit:

$$\frac{\text{SNR}_F}{\text{SNR}_{\delta f_0}} \propto \frac{R_0}{A} \quad (8.12)$$

8

Here we assume the experiments are performed at the optimal height as described in Sec. 8.2. Frequency shift experiments become more interesting for smaller magnets and large driving amplitudes. However, given that the radius of the magnetic particle is on the order of several micrometers, and that the driven cantilever amplitude is roughly 1 - 100 nm, direct force measurements remain more sensitive for our range of experimental parameters.

8.4 FABRICATION OF DOUBLE-MAGNET CANTILEVERS

Based on considerations from the previous sections, we have fabricated MRFM cantilevers that combine a small diameter particle at the tip of the cantilever for a high

²Here we assume a single-shot experiment (no averaging) where we reduce the spin magnetic moment to zero, as would be the case in a saturation experiment.

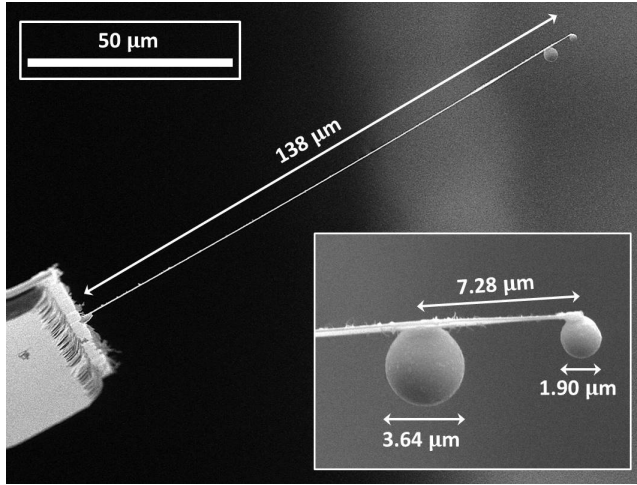


Figure 8.2: Scanning electron microscope image of the double magnet cantilever. The inset shows a zoom on the tip of the cantilever.

field gradient with a larger diameter particle a bit higher up the cantilever to maintain a high coupling strength to the SQUID. In selecting the appropriate combination of cantilever and magnet sizes, a trade-off is made between the sensitivity, for which a low stiffness is required, and keeping the resonance frequency high enough to stay within the effective range of the vibration isolation. We aim for finished cantilevers with a resonance frequency close to 3 kHz, similar to the conventional cantilevers in our group.

In total, three cantilevers were made with slightly different parameters. In the remainder of this chapter, we will base our calculations on the parameters of one of these finished double-magnet cantilevers, which is shown in Fig. 8.2. This new cantilever has a length of 138 μm and carries two magnets: at the very end, a small magnet with radius $R_1 = 0.95 \mu\text{m}$, and at about 7.3 μm from the tip a second larger magnet with a radius $R_2 = 1.82 \mu\text{m}$. The magnets are attached to the cantilever using the same method as described in Sec. 2.3.

The resonance frequency of the cantilever can be calculated using the familiar equation $\omega_0^2 = k_0/m$, but with a modified effective mass which takes into account the new mass distribution $\rho(l)$. When we assume the magnetic particles to be point masses, we find for the effective mass

$$m = \int_0^l \frac{x^2}{l^2} \rho(x) dx = m_1 \frac{x_1^2}{l^2} + m_2 \frac{x_2^2}{l^2} + \frac{\rho_{\text{Si}} l w t}{4}, \quad (8.13)$$

with m_1 and m_2 the masses of the small and large magnets, respectively, and x_1

and x_2 their respective positions measured from the base of the cantilever. The last term represents the effective mass of the silicon cantilever itself, with ρ_{Si} the density of silicon³. Using this equation with the parameters obtained from Fig. 8.2, the calculated natural frequency of the double-magnet cantilever is 3086.7 Hz, very close to the 3085.1 Hz measured at 4 K.⁴

8.5 MAGNETIC FIELD DISTRIBUTION

The main purpose of the large top magnet is to increase the coupling strength between the cantilever and the SQUID, as will be discussed in Sec. 8.6. However, a potential downside is that the large magnet might have an effect on the field at the position of the sample, thereby complicating the shape of the resonant slice. To check this, we calculate the total magnetic field resulting from both particles. A contour plot of the field distribution is shown in Fig. 8.3(a). The figure shows that the field of the large top particle falls off sufficiently quick that the amplitude and shape of the resonant slices (constant B_0) below the bottom magnet are hardly affected, allowing us to do our simulations using a simple single dipole model. This is confirmed in figure 8.3(b), where we compare the magnitude of the field directly below the bottom magnet with and without the top magnet. We find that at small heights, where all of the experiments are performed, the magnitude of the magnetic field is unaltered by the presence of the large upper magnet.

Of course, the main goal of going for smaller magnetic particles is to increase the magnetic field gradient. Fig. 8.4(a) shows a contour plot of the derivative of the magnetic field in the X-direction for a magnet with a radius of $0.95 \mu\text{m}^5$. As expected, the derivative is zero directly below the magnet, but increases to values of several hundred mT/ μm at positions right in front of or behind the magnet.

A cross section of the contour plot along the line $Z = R_0/3$ is shown in Fig. 8.4(b), calculated for two magnets with different radii of $0.85 \mu\text{m}$ and $1.9 \mu\text{m}$. From this image, we find the following: First of all, the maximum field gradient is indeed inversely proportional to the radius of the magnet; secondly, the distance to the optimum of $\partial B/\partial x$ scales with the radius of the magnet, so a smaller particle reduces the effective field of view of the MRFM. Both of these observations match the predictions from Sec. 8.3 where we looked at the radial component of the magnetic field gradient, showing

³ $\rho_{Si} = 2330 \text{ kg/m}^3$ and $\rho_{NdFeB} = 7400 \text{ kg/m}^3$.

⁴Note: this calculation is only valid for the fundamental mode.

⁵reminder: the Z-direction is the vertical direction along the axis of the cantilever, and the X-direction is pointed along the soft direction of the cantilever and the magnetization of the magnets.

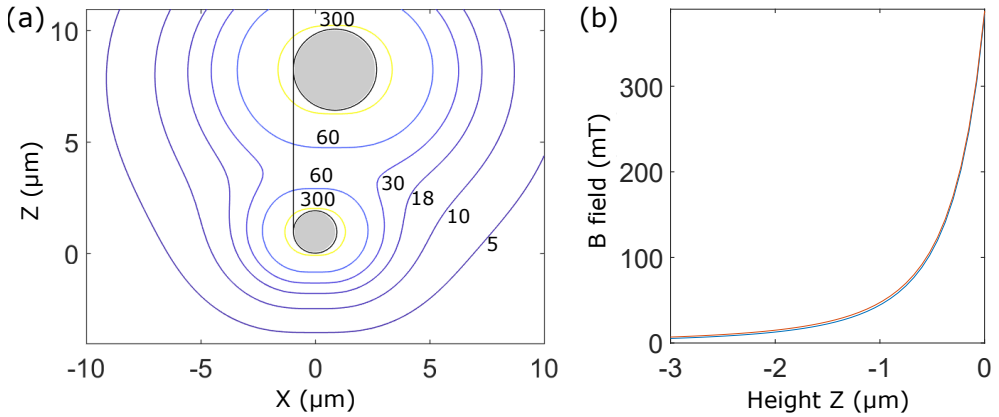


Figure 8.3: (a) Contour plot of the magnetic field distribution around the new cantilever (radii $0.95\ \mu\text{m}$ and $1.82\ \mu\text{m}$). The gray circles indicate the positions of the magnets. The labels indicate the magnitude of the field (mT) for the different contour lines. (b) B-field versus the distance between the sample and the surface of the magnet for a single magnet (blue) and the double magnet (red) configurations, calculated directly below the magnet.

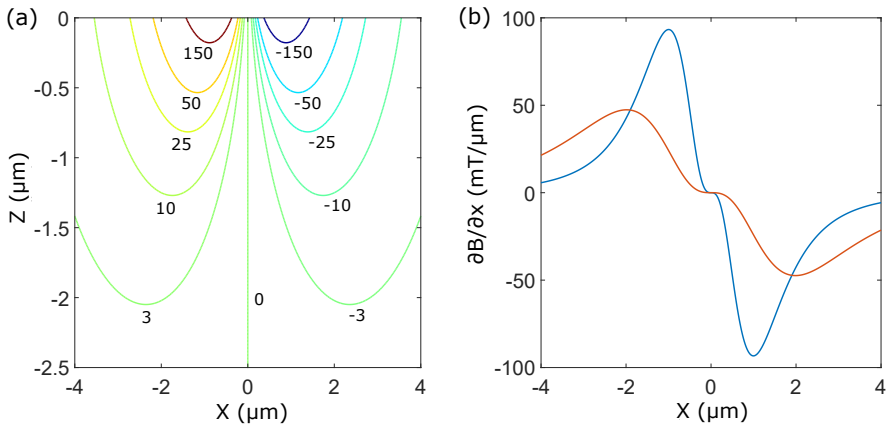


Figure 8.4: (a) Contourplot of $\partial B/\partial x$ in the $Y = 0$ plane for a magnet with radius $0.95\ \mu\text{m}$. The labels indicate the magnitude of $\partial B/\partial x$ in units $\text{mT}/\mu\text{m}$. The surface of the magnet is located at $Z = 0$. (b) Cross-section of Fig. (a) for two different magnets, one with radius $0.95\ \mu\text{m}$ (blue) and the other with radius $1.9\ \mu\text{m}$ (red), along $Z = R_0/3$ (following Garner). As predicted, the magnitude of $\partial B/\partial x$ scales with the inverse of the radius of the magnet, while the distance between the center of the magnet and the optimum of $\partial B/\partial x$ scales linearly with the radius.

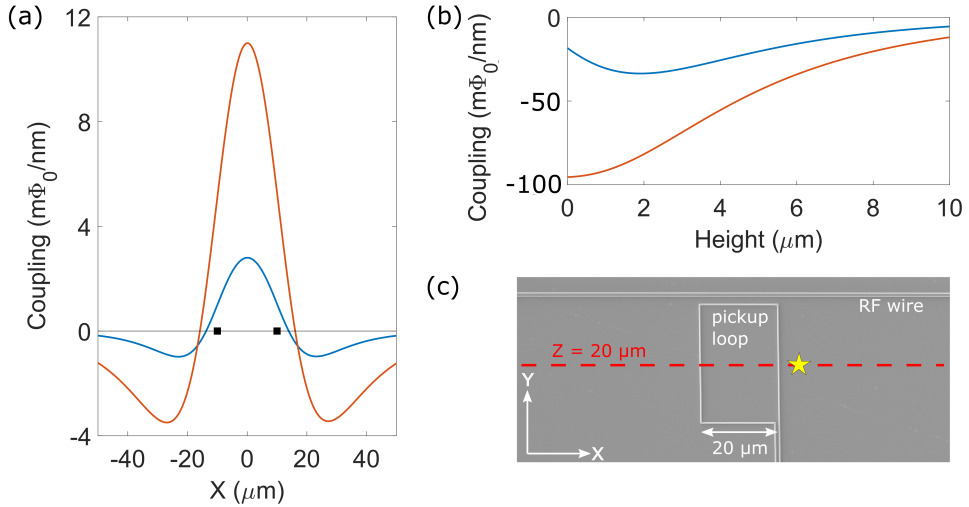


Figure 8.5: Calculation of the improved coupling of the double magnet cantilevers (solid red) compared to a single magnet cantilever (solid blue), with (a) the coupling along the red dashed line in (c) at $20\ \mu\text{m}$ above the surface, and (b) the coupling versus the height at the position marked by the star in (c), $5\ \mu\text{m}$ outside the pickup loop at $X = 15\ \mu\text{m}$.

that this was a valid simplification to find the general scaling laws concerning the radius of the magnet.

8.6 ENHANCED COUPLING STRENGTH TO PICKUP LOOP

Where traditional MRFM setups utilizing a laser readout of the cantilever motion have a constant detection sensitivity, with our SQUID readout this sensitivity is highly dependent on the position of the magnetic particle with respect to the pickup loop, and on the amplitude of the oscillation of the cantilever. This coupling is obviously very small when the cantilever is far away from the pickup loop, as is the case when we are still determining the exact position of the cantilever. A bit less obvious is the fact that the coupling also becomes small when the magnet is very close to the surface of the detection chip. This is because the vertical component of the magnetic field from the magnet is zero in the horizontal plane crossing the magnet. Both of these situations with low coupling should be improved by the second magnet: In the far-field limit the second particle increases the total magnetic moment and thereby the coupling, and close to the pickup loop, when the bottom magnet is nearly touching the surface of the chip, the top particle is still high above the pickup loop with a strong coupling.

These intuitive ideas are checked by a calculation of the coupling from both particles using the equations outlined in Sec. 2.2. The result is shown in Fig. 8.5. The coupling at large distances from the pickup loop (20 μm above the pickup loop) is shown in Fig. 8.5(a), where we find that the ratio between signals of the single and double magnet cantilever is simply equal to the ratio of the volumes of the magnets, since to first order the coupling is proportional to the magnetic moment $m = V \frac{B_r}{\mu_0}$, with B_r the saturation magnetization. Fig. 8.5(b) shows the coupling versus the height at a typical position where an MRFM experiment could be performed. While it is clear that the coupling for the single magnet decreases rapidly as the height of the magnet is reduced, the coupling of the double magnet to the pickup loop keeps rising, with a maximum increase in coupling of a factor of 3.

We can get some intuition about these values for the coupling by looking at the signals that we would get from the thermal motion of the cantilever. A cantilever with spring constant $k_0 = 80 \mu\text{N/m}$ at a temperature of 20 mK has a mean thermally driven amplitude of about 50 pm. In order to be able to detect the thermal motion, this motion has to be multiplied by the coupling strength, and then compared to the SQUID flux noise floor of about $1 \mu\Phi_0/\sqrt{\text{Hz}}$, while taking into account that we only have about 3% of efficiency in transferring the signal from the pickup loop to the SQUID (see Sec. 2.2.1). So, a detection noise of $1 \mu\Phi_0/\sqrt{\text{Hz}}$ at the SQUID means a detection limit of about $30 \mu\Phi_0/\sqrt{\text{Hz}}$ at the pickup loop. This implies that the coupling has to be larger than

$$\frac{30 \mu\Phi_0}{50 \text{ pm}} = 0.6 \text{ m}\Phi_0/\text{nm} \quad (8.14)$$

for the thermal motion to be detectable within a 1 Hz bandwidth.

8.7 SPIN-INDUCED DISSIPATION

We will now present experimental data demonstrating that the new double-magnet cantilevers work, i.e. retain their magnetization, based on measurements of the spin-induced dissipation of the cantilever when coupled to the 2D spin system on the surface of a silicon substrate. This experiment was first performed by Den Haan et al. using a force sensor with a single magnet[77]. In Ref. [77], it is described how the coupling between paramagnetic spins and the magnet on the cantilever opens a dissipation channel for the energy in the cantilever, inducing a shift of the inverse quality factor given by:

$$\Delta \frac{1}{Q} = C \frac{2\pi f_0 T_1}{1 + (2\pi f_0 T_1)^2}, \quad (8.15)$$

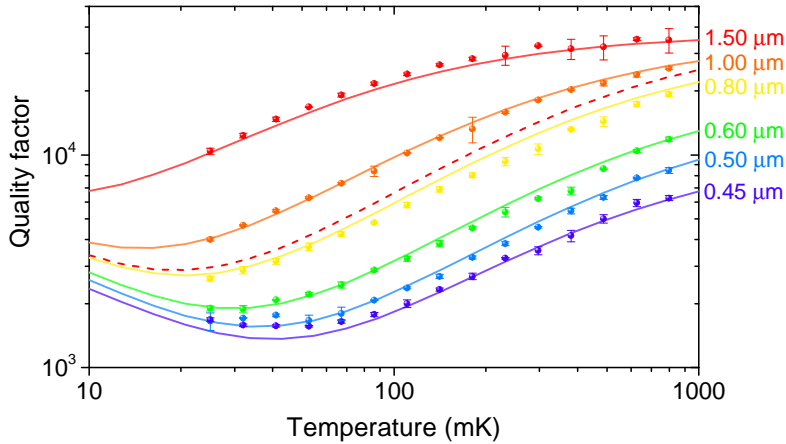


Figure 8.6: Quality factor versus temperature for the new double-magnet cantilever coupled to the electron spins on a silicon substrate. The solid lines are fits to the data for a collective spin density σ and relaxation time T_1 . Q_0 is extrapolated from the high temperature limit for each height individually. The dashed red line shows the results of a calculation for a 3.4 μm diameter magnet at $h = 1.5 \mu\text{m}$ for identical parameters.

with

$$C = \frac{\sigma\mu^2}{k_0 k_B T} \int_S \frac{\left(\hat{\mathbf{B}}(\mathbf{r}) \cdot \frac{\partial \mathbf{B}(\mathbf{r})}{\partial x} \right)^2}{\cosh^2 \left(\frac{\mu B(\mathbf{r})}{k_B T} \right)} d^2 \mathbf{r} \quad (8.16)$$

The quality factor of the cantilever is then given by $Q^{-1} = Q_0^{-1} + \Delta Q^{-1}$. Using this theory, Den Haan et al. were able to extract a spin density of 0.14 spins/ nm^2 , with a spin-lattice relaxation time $T_1 = 0.39$ ms.

We have repeated this experiment with the double-magnet cantilever shown in Fig. 8.2 positioned above one of the silicon detection chips. The measurement consists of measuring the properties (resonance frequency and quality factor) of the cantilever for various temperatures and heights above the surface, in our case by performing frequency sweeps around the cantilever resonance frequency using a piezoelectric element to drive the cantilever. The resulting quality factor measured in this experiment is shown in Fig. 8.6. During this experiment, some unintended charging of the cantilever tip or sample induced large $1/f$ frequency noise, leading to sudden jumps in the cantilever resonance frequency every couple of minutes. For this reason, we were unable to obtain reliable frequency shift data. The $1/f$ noise does not influence the measurement of the cantilever quality factor, as long as no frequency jump occurred during the sweep.

The solid lines in Fig. 8.6 are fits to Eq. 8.15, assuming a magnet with a radius of $0.95 \mu\text{m}$ and a saturation magnetization of 1.15 T . We cannot extract independent values for the spin density and relaxation time, as this requires reliable frequency shift data. When only the quality factor data is available, the two parameters can balance each other. However, in the limit of $\omega_0 T_1 \ll 1$, the shift of the inverse quality factor is proportional to σ/T_1 , so this factor is still a meaningful way to compare the dissipative properties of various surfaces. For the data presented in Fig. 8.6, we find $\sigma/T_1 = 1.04 \text{ nm}^{-2}\text{ms}^{-1}$, a value three times higher than what was reported by Den Haan et al., indicating that the surface of the used detection chip was contaminated, most likely caused by residue of e-beam lithography resist on the surface of the chip. However, considering the poor quality of the surface, the smaller magnets indeed lead to less dissipation of the energy in the cantilever for equal heights, as visible when comparing the solid red line in Fig. 8.6 with the dashed red line, which indicates the calculated quality factor using the same parameters as the other curves but for a magnet with a radius of $1.7 \mu\text{m}$.

In the analysis of this data, we have made the following assumptions:

- The minima of the dissipation curves can be used to calibrate the height or saturation magnetization of the magnet. We had to add 300 nm to the assumed height to match the data with the calculations. This height error can be caused by a systematic error in our height calibration method⁶, or by a dead layer of the magnet, which reduces the effective radius and then requires a higher saturation magnetization. We believe the problem lies in the height calibration, as the MRFM experiments described in Ch. 4 showed a similar height mismatch.
- Q_0 has been determined individually for each height curve, by extrapolation of the data to high temperatures using that the spin-dependent dissipation has a $1/T$ dependence for high T . We find a quality factor of over $37\,000$ for the largest heights, and a gradually decreasing quality factor as the height decreases. We attribute this temperature-independent dissipation to the fluctuating charges at the cantilever frequency, whose low frequency counterparts are held responsible for the $1/f$ frequency noise.

The results from Fig. 8.6 suggest big improvements in the quality factor close to the sample when using smaller magnets. This is made more explicit in Fig. 8.7(a), where we show the calculated spin-induced dissipation for the cantilever coupled to

⁶The height calibration consists of a touch measurement, where the cantilever is slowly approached to the surface until it's motion cannot be detected anymore. Errors can be introduced when, for instance, charging causes the cantilever to bend when close to the sample, or when the cantilever is not aligned perfectly perpendicular to the surface of the detection chip.

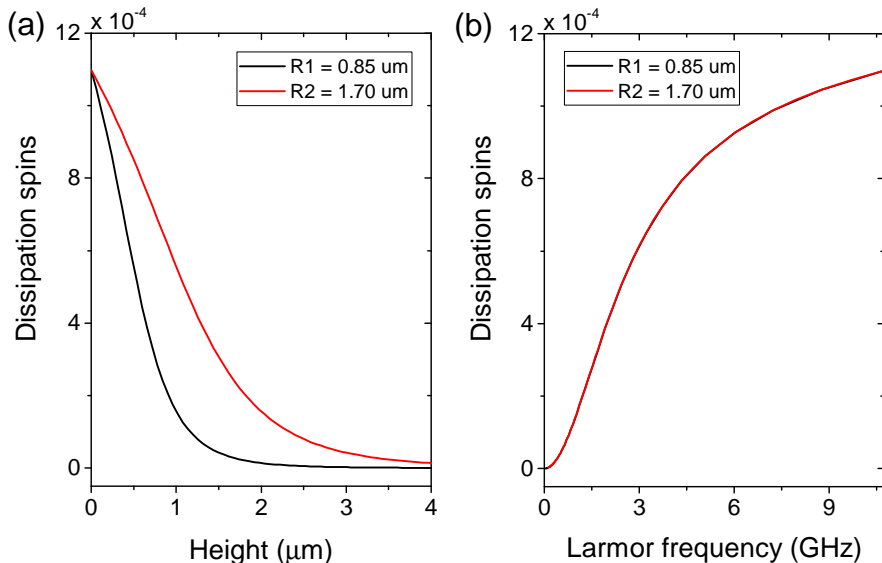


Figure 8.7: Calculation of the spin induced dissipation ($= \Delta Q^{-1}$) using the parameters found in Fig. 8.6 for two different magnet radii, plotted versus (a) the height above the sample and (b) the Larmor frequency of the electron spins in the field from the two magnets.

a 2D spin system at a temperature of 30 mK as a function of the height. However, this presentation of the data is misleading since this compares equal heights. In reality, when using a smaller magnet the experiments have to be performed at smaller distances. Therefore, a better comparison is by looking at constant Larmor frequencies instead, as shown in Fig. 8.7(b). The translation between height and Larmor frequency was done by calculating the magnitude of the magnetic field directly below the magnet for all heights.

We find that the spin-induced dissipation presented in this way is completely independent of the radius of the magnet. This can be understood following the same arguments we used in Sec. 8.3. The dissipation per spin is determined by the square of the field gradient, which is roughly proportional to R_0^{-2} when evaluated at a constant Larmor frequency⁷. At the same time, the total number of spins for a 2D system scales as R_0^2 , so the increasing dissipation per spin is perfectly balanced by the decreasing number of contributing spins, making the total dissipation independent of the radius of the magnet.

Note that this finding is only valid when the dissipation originates from a 2D system. In the case that the dissipation originates from the bulk of the sample a

⁷This is equivalent to using a height proportional to the radius.

smaller magnet will lead to reduced dissipation proportional to the radius, and thus a higher quality factor.

8.8 CONCLUSIONS

To summarize, we have succeeded in the fabrication of MRFM cantilevers with two magnetic particles, one at the end of the tip with a small radius to generate large field gradients, and a second larger particle several micrometers higher on the cantilever to reduce the detection noise. Initial experiments measuring the spin-induced dissipation show that the new cantilevers are fully functional and should be suited for MRFM experiments. To date, the true MRFM experiments have yet to be done.

With the enhanced field gradients, more sensitive MRFM experiments become possible. In Ch. 4, the prospects for these new cantilevers for the imaging of protons is discussed. However, one should keep in mind that even though the signal per spin increases, the total signal is decreased due to the small detection volumes. Furthermore, the issue of a reduced quality factor of the cantilever by the magnetic coupling to an approximately 2D spin-system is not solved by using these new cantilevers.

A follow up to the fabrication of these cantilevers to get even higher field gradients was attempted in collaboration with the Marohn Group from Cornell University. Although some cantilevers were made, unfortunately they broke before they could be tested in our MRFM setup [205].

9

VALORISATION: THE EASY-MRFM

Magnetic Resonance Force Microscopy is a technique with immense potential, but in practice it is hindered by the complexity of the setup and strong restrictions on possible samples. For these reasons only approximately 10 groups work on this technique worldwide, and MRFM setups are not commercially available. In this valorisation chapter, we explain the necessity for a more simplified MRFM setup, if necessary with a slightly reduced functionality. This would make the technique more broadly applicable, in which case it could offer invaluable information to a variety of fields, some of which will be exemplified at the end of this chapter. We show current progress in the development of this new instrument, and describe the modifications required to reach the desired specifications for full operation.

9.1 NECESSITY FOR A NEW CHARACTERIZATION TOOL

The current performance of many nanodevices is limited by the presence of fluctuating two-level systems (TLS) that couple to the device. These systems are often associated with the presence of dangling chemical bonds on the surface of the substrate or inside the device itself. Examples of the limited performance of devices include the reduced coherence times in superconducting qubits [193, 206–211], the short T_2 times of shallow NV-centers [135, 137–139, 212, 213], and excess flux noise in SQUIDs and Josephson junctions [214–217].

Attempts to solve these issues follow two general approaches. On the one hand people try to reduce the device’s sensitivity to the noise by tweaking the design [195, 218, 219]. On the other hand they try to remove the source of the noise by changing materials and fabrication procedures [141, 220, 221]. However, real progress is hindered by the fact that we are blind to the effects of various adjustments until the finished device is tested, as only the final performance of the device gives a decisive answer. This means improvements are costly and time-consuming, as changes to one of the first steps of the production still require the completion of all subsequent steps. Additionally, when it is suspected that the unwanted electron spins are introduced in one of the fabrication steps, it is currently very challenging to find out which particular step is responsible. What is needed is an independent characterization tool that is capable of quantifying the impact of an action at any stage in the device fabrication process on the density of two level systems.

Our magnetic resonance force microscope (MRFM) might be a viable option for this purpose. We have demonstrated that we are able to do ultra sensitive magnetic force microscopy measurements on dilute paramagnetic spin systems to extract spin densities, spin-lattice relaxation times, and even rudimentary dynamics such as spin diffusion. Over the years, we have used this technique on a variety of samples, such as the dangling bonds in the native oxide of silicon [77], the surface spins and (N^-) bulk spins in diamond [34], and the Fe^{3+} defects in the bulk of single-crystal strontium titanate ($SrTiO_3$) [53]. In our group, the ultra sensitive magnetic force technique has become a standard sample characterization before the start of MRFM experiments.

The method of the characterization of a sample’s spin properties is based on the observation that the resonance frequency and damping of the magnetically-tipped cantilever are altered by the vicinity of nearby spins. By measuring the temperature- and distance-dependence of both the resonance frequency and the damping of the cantilever at very low temperatures (< 250 mK), the density and T_1 times of the spins on the surface and in the bulk of a sample can be determined [52]. The lowest

surface spin density that we have found was 0.07 spins/nm². In other words, these surface spins are on average 4 nm apart. The sensitivity of our method would be sufficient to detect 100 times fewer spins than this, i.e. electron surface spins that are up to 40 nm apart on average.

However, our current MRFM setup is ill-suited as a general sample characterization tool, since measurements can only be done in the proximity of a pickup loop necessary for the detection of the motion of the magnetically-tipped cantilever. This means that either the sample has to be placed on a detection chip, or a superconducting pickup loop has to be fabricated on the sample. Using optical detection instead would not allow to reach the low temperatures that are called for to polarize the magnetic spins with the field of our magnetic particle. An additional drawback is that changing the sample requires a partial deconstruction of the setup, so it takes at least several days. This makes the current setup incompatible with, for instance, testing surface treatments concerning the removal of oxide layers, where a fast throughput time is essential.

Therefore, we have developed a new setup, called the easy-MRFM, that is still compatible with milliKelvin operating temperatures (and therefore is still based on SQUID technology), and where all vital MRFM components are separated from the sample. This opens the possibility to characterize more general samples with a higher turn-over rate.

9.2 PROGRESS OF THE EASY-MRFM

The idea of the easy-MRFM is to fabricate a superconducting pickup loop on a silicon arm that can be placed next to the cantilever, rather than fabricating the pickup loop on the sample itself. This would allow for detection of the motion of the cantilever with a constant coupling independent of the position of the cantilever with respect to the sample. The ability to measure the properties of the cantilever is all that is required for the magnetic force measurements to extract the spin densities of the sample under investigation. More complex MRFM protocols, requiring radio-frequency (RF) pulses, can be performed by using the higher modes of the cantilever for the mechanical generation of RF fields [50].

The first prototype of the easy-MRFM is shown in Figs. 9.1(a)-(d). It was designed to be a module for the current MRFM setup, where it can simply be exchanged with the old cantilever holder without major adjustments. As a result, the entire easy-

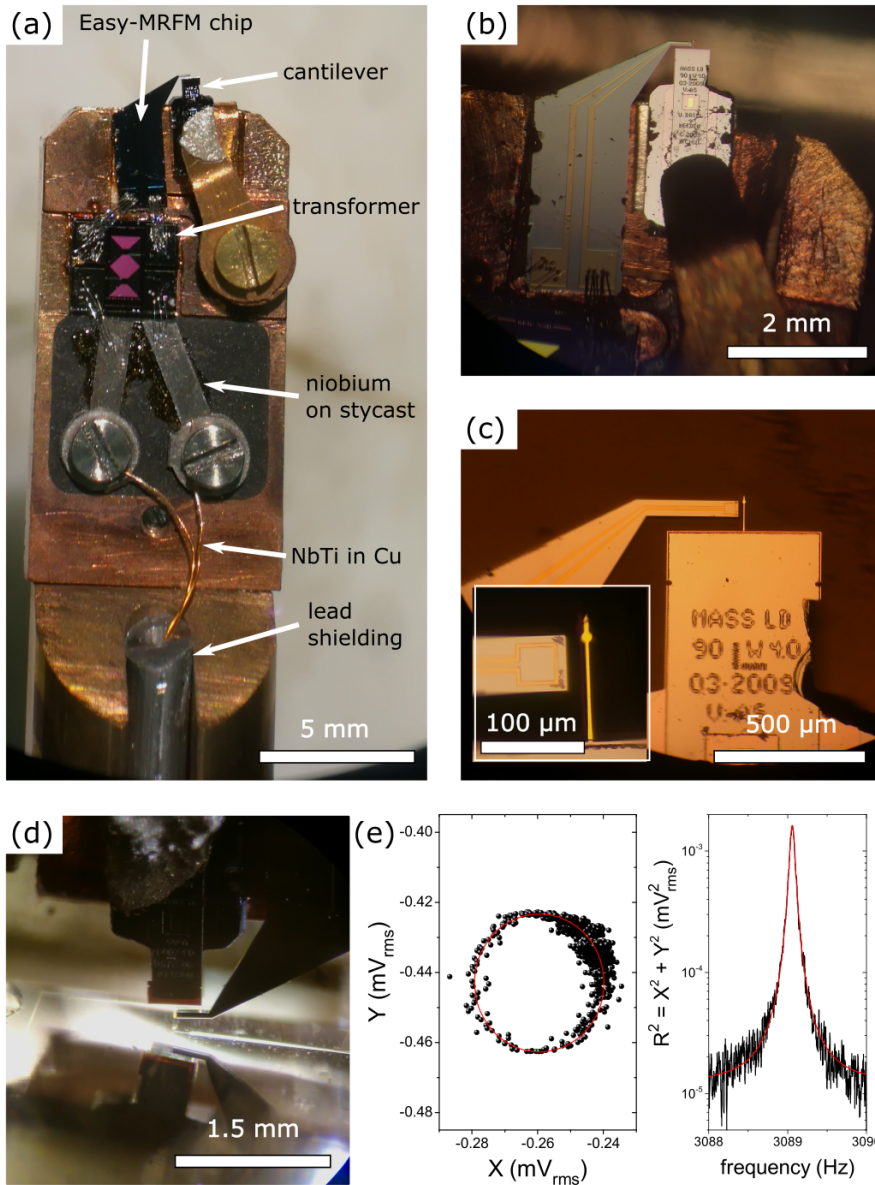


Figure 9.1: (a) Photograph of the easy-MRFM prototype with the most important components labeled. (b) Easy-MRFM detection chip and cantilever. (c) Alignment of the cantilever with respect to the pickup loop with area $(40 \mu\text{m})^2$. (d) Easy-MRFM positioned above a conventional MRFM detection chip before cooling down. (e) Detected cantilever response to a driving force. The left image shows the polar plot (raw data), the right image shows the squared amplitude response, corrected for the direct crosstalk between the drive and detection circuits. The solid red line is a Lorentzian fit to the data.

MRFM has a diameter of only 8 mm. The prototype contains the cantilever chip, mounted on top of a piezoelectric element, the easy-MRFM detection chip made of 100 nm thick NbTiN, fabricated by Delft Circuits [222], and a gradiometric transformer to match the detection chip pickup loop to the input coil of a SQUID, which is placed in a superconducting shielding several centimeters away from the tip of the easy-MRFM. The cantilever, which is one of the double-magnet cantilevers described in Ch. 8 of this thesis, can be placed within a distance of 50 μm from the pickup loop (see the inset of Fig. 9.1(c)).

Initial results show that it is possible to detect the driven motion of the cantilever and extract its properties, as shown in Fig. 9.1(e). Despite large crosstalk, we can extract the properties of the cantilever which gives access to the two parameters, f_{res} and Q , that are necessary to extract a spin density. In the right image of Fig. 9.1(e) we have manually subtracted the offset due to the crosstalk. The same can be achieved using a circle fit to the cantilever signal in the polar plot [72]. Protocols for the fits to the polar plot data are available [65].

Even though this data gives the proof-of-concept for the easy-MRFM, further optimization is desirable. The coupling between the magnetically tipped cantilever and the detection pickup loop is currently too small to see the thermal motion of the resonator (required to calibrate the absolute coupling strength). Furthermore, the low coupling requires the cantilever to be driven to a large amplitude for its motion to become detectable. This large amplitude may induce non-linearities in the cantilever, which hinder the determination of the cantilever's resonance frequency and quality factor. For these reasons, the coupling should be improved by at least one order of magnitude. This can be done by optimizing the position of the cantilever with respect to the pickup loop, increasing the radius of the magnet at the end of the cantilever, or improving the matching between the pickup loop and the input coil of the SQUID. The latter can be done by reducing the parasitic inductance and tweaking the design of the transformer.

When the easy MRFM is operational, the turn-over rate will be dictated by the cooldown time of the dilution refrigerator in which it is operated, which is several days. The turn-over rate can be improved further by mounting the instrument on a cold-insertable probe [223], in which case samples can be exchanged without the need to open the cryostat. Then it should become possible to determine spin densities on one sample per day.

9.3 FUTURE APPLICATIONS

When the easy-MRFM is further developed into a mature technique, applications can be found in many fields of physics and industry. In the greater quantum computation community, it could be used to pinpoint the critical fabrication steps that should be removed, adapted, or included to remove the dangling bonds responsible for the low coherence times. As a pilot experiment we propose to measure the spin density on a thin layer of NbTiN, a common material used for superconducting qubits, before and after the in-situ application of a small amount of hydrofluoric acid to remove the surface layer on top of the NbTiN.

Apart from the prospect of using the easy-MRFM technology to specifically address the problem of unwanted electron spins in quantum computation devices, we believe that it may also be useful to study chemically amplified resists after they have been illuminated with UV light. The radicals that are produced in the process have an unpaired electron [224–226]. It is estimated that a typical density of broken bonds is about $10^{20} \text{ cm}^{-3} = 0.1 \text{ nm}^{-3}$ [227]. At this density, these radicals should be readily detectable as a frequency shift of our magnetic force sensor. Any additional information about the detailed response of the resist to various radiation doses could be invaluable for improving the performance of the new high resolution resists.

A

FEEDBACK COOLING OF THE CANTILEVER'S FUNDAMENTAL MODE

The fundamental sensitivity of MRFM is limited by the thermal force noise. This noise can be reduced by lowering the temperature of the cantilever. However, this is complicated by the limited thermal conductance of all the different components combined with the constant influx of power from various sources. This can create large temperature gradients between the experiment's vital components, such as the sample and the cantilever, and the source of cooling (e.g. the mixing chamber). To give an example from Poggio et al.: in a cryostat with a base temperature of 250 mK, the cantilever temperature saturated at 2.2 K due to the laser used for the detection of the cantilever [44].

In this appendix, we discuss our efforts to cool the cantilever, focusing on the achieved cantilever temperature and thermal force noise, and the feedback cooling of our resonator to an effective mode temperature below 150 μ K. Note that the experiments in this chapter were performed in one of the older versions of the setup than that explained in Ch. 2. All relevant experimental details will be discussed.

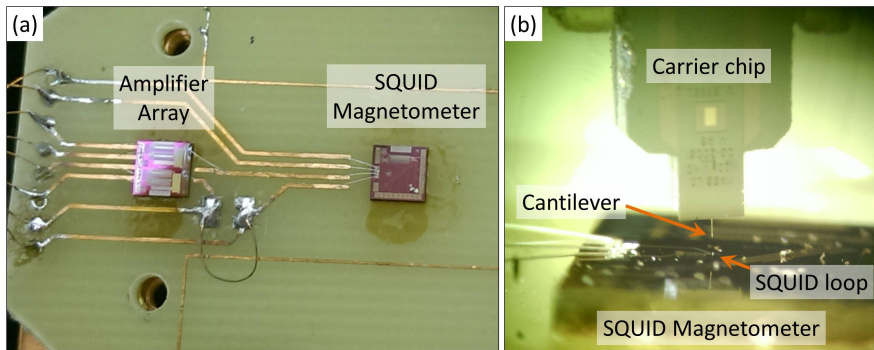


Figure A.1: Setup used for the experiments described in this section. (a) Photograph of the improvised two-stage SQUID, consisting of a magnetometer coupled to a SQUID array. (b) Optical microscope image of the cantilever placed directly above the SQUID loop of the magnetometer.

A.1 CANTILEVER TEMPERATURE AND THERMAL NOISE FORCE

In order to achieve the lowest possible cantilever temperature, several measures were taken to ensure a good thermalization to the mixing chamber of the dilution refrigerator. First of all, the silicon chip which supports the cantilever is attached to a copper block using a brass spring, and further thermalized using some silver epoxy at the base of the chip. This copper block is directly connected to the mixing chamber via a silver wire with a diameter of 1 mm and a length of about 30 cm. When we assume the silver is the limiting factor in the thermal conductance, this configuration leads to an optimal power tolerance of 3 nW/mK at 100 mK. However, since this estimate ignores the thermal resistance at the interfaces of different components and materials, the actual thermal conductance should be much lower.

To determine the lowest temperature at which the cantilever saturates, we place the cantilever directly above a SQUID¹ (see Fig. A.1) in order to maximize the coupling and thereby the SNR. We measure the thermal motion of the cantilever by looking at the power spectral density of the SQUID signal at different temperatures. Two representative curves measured at 12 mK and 500 mK can be seen in the upper image of Fig. A.2. The thermal motion of the cantilever's fundamental mode at 2727 Hz is clearly visible above the noise. We use a cantilever with a magnet with a radius of 1.5 μm , and a stiffness of 50 $\mu\text{N/m}$. The smaller bumps visible in the bottom

¹PTB GX1GFM Magnetometer, connected to a PTB 5X1GF4 SQUID series Array used as amplifier

curve are mechanical vibrations of the setup amplified by the transfer function of the cantilever.

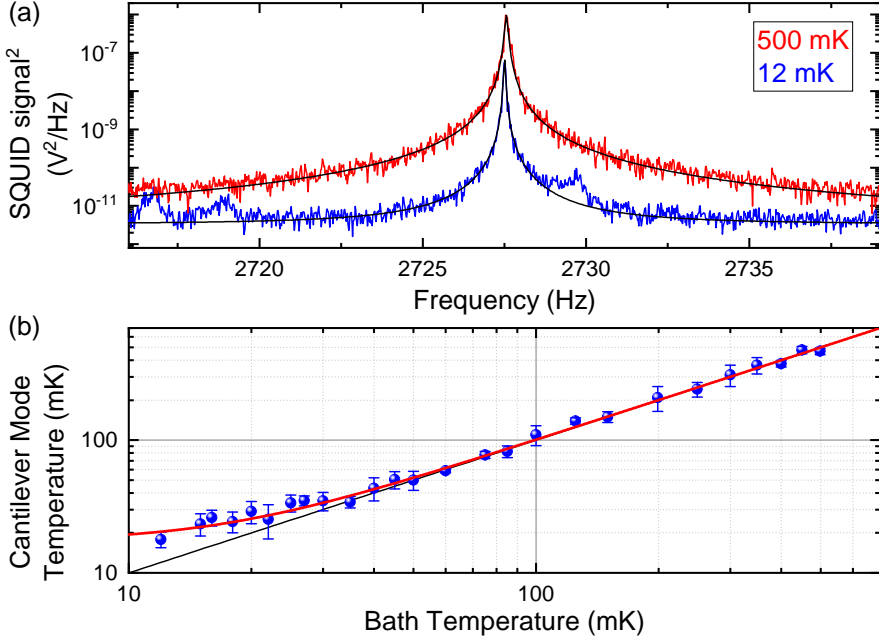


Figure A.2: (a) SQUID signal for two bath temperatures. The black lines are Lorentzian fits to the data. (b) Cantilever noise temperature calculated from the area beneath the peaks obtained from the fit. The red solid line is a fit to the data using Eq. A.2, with $T_0 = 17.3 \pm 3.3$ mK, and $n = 2.2 \pm 0.6$.

Once the coupling between the magnetic particle and the SQUID is known, the area obtained from a fit of the data to a Lorentzian peak can be used to calculate the effective mode temperature, and via the equipartition theorem² this can be translated to the mean square displacement of the resonator. The coupling, which depends on the position of the cantilever with respect to the SQUID, can be experimentally determined by using a calibration coil in the SQUID input coil circuit to drive the cantilever [53]. Alternatively, the coupling can be determined by assuming that at high temperatures the cantilever temperature is equal to the bath temperature. This gives us

$$\frac{1}{2}k\langle x \rangle^2 = \frac{1}{2}k_B T = \frac{1}{2}k_B \beta A \quad (\text{A.1})$$

²The equipartition theorem relates the thermal energy of a system to its average potential energy. In the case of an harmonic oscillator, it simply states that $\frac{1}{2}k_B T = \frac{1}{2}k\langle x \rangle^2$.

with β the conversion factor between the area and the temperature in units K/V^2 , and A the area under the curve of the power spectral density.

The measured cantilever noise temperature is shown in Fig. A.2(b). Our assumption that at high temperatures the cantilever temperature is equal to the bath temperature is justified by the linear behavior observed above approximately 50 mK, as indicated by the black diagonal line. Below this temperature, a saturation of the cantilever noise temperature can be observed. The red solid line is a fit to the data using a saturation curve [47]:

$$T_N = (T^n + T_0^n)^{1/n} \quad (\text{A.2})$$

The best fit to the data was obtained when using a saturation temperature $T_0 = 17.3 \pm 3.3$ mK, and an exponent $n = 2.2 \pm 0.6$, where the value of the exponent n is determined by the temperature dependence of the limiting thermal resistance. The acquired value for n indicates that the thermal conductance is due to conduction electrons [109], whereas the first Oosterkamp MRFM setup, which was used in the work of Usenko et al. [47], appeared to be limited by phonon processes or boundary effects. This difference could be due to the improved direct electrical connection of the cantilever to the mixing chamber via the silver wire and silver epoxy. Since the thermal conductance via electrons is much better than via phonons at low temperatures, this might also explain the reduction in the saturation temperature of the cantilever by nearly a factor of 2 when compared to the work by Usenko et al..

By using the conversion factor defined in Eq. A.1, we can now use the SQUID signal power spectral density to calculate the displacement noise, as shown in Fig. A.3.

With the data we have gathered so far, we can calculate some numbers which indicate the final measurement sensitivity of our setup, such as the thermal force noise, which is given by

$$\sqrt{S_F} = \sqrt{4k_B T \frac{k}{2\pi f_0 Q}} \quad (\text{A.3})$$

In recent years, several groups have reached astonishingly low values for the thermal force noise, reaching well within the zeptoNewton range, using a variety of resonator geometries [228–231]. However, most of these geometries are unsuited for MRFM. For our cantilever, assuming $k = 50 \mu\text{N}/\text{m}$, $f_0 = 2727$ Hz and $Q = 5 \cdot 10^4$ at low temperatures, we calculate a force noise $\sqrt{S_F} = 0.23$ aN/ $\sqrt{\text{Hz}}$. This value is very close to the lowest values ever reported for the soft cantilever geometries necessary for magnetic resonance force microscopy [45, 232, 233].

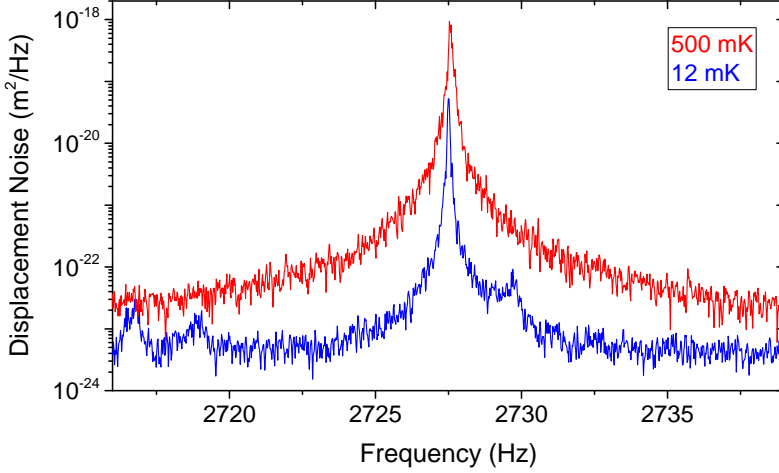


Figure A.3: Displacement spectra showing the thermal motion of the cantilever for temperatures of 500 mK (red) and 12 mK (blue).

A.2 FEEDBACK COOLING OF THE CANTILEVER'S FUNDAMENTAL MODE

Since the effective temperature of our resonator appears to be limited by the performance of the dilution refrigerator, the next step to reduce the motion of the resonator is to implement a technique called feedback cooling. In this technique, a high precision measurement of the motion of a resonator is used to perform active feedback on said motion, thus introducing an additional damping of the resonator. Feedback cooling is widely used for a variety of reasons:

- One of the ultimate goals is to use MRFM to detect the magnetic moments of individual nuclei with Ångström-scale spatial resolution. Detecting such small forces requires the smallest possible spring constant. However, since the mean-square amplitude of a cantilever's Brownian motion is given by $\langle x^2 \rangle = k_B T / k$, reducing the spring constant might lead to a thermal motion exceeding the desired imaging resolution [234]. Furthermore, the Brownian motion of the resonator also introduces a fluctuation of the polarizing field felt by the spins with an amplitude of $B_x = x_{\text{rms}} \partial B / \partial x$ [235]. To solve these issues feedback cooling must be used to reduce the cantilever's motion to within an acceptable range.
- As the quality factor of a resonator increases, its bandwidth is reduced. Since

the amplitude of a resonator decays with a typical time $\tau = Q/\pi f_0$, the time between independent measurements becomes very large. By reducing the quality factor using feedback, the decay time can be kept short, which increases the bandwidth of the experiment without sacrificing the force sensitivity [57].

- A cold resonator with a low number of phonons is useful for a variety of experiments exploring the limits of quantum mechanics [236–238]. This topic is extensively covered in the thesis of de Voogd [59].

The setup used for the feedback cooling experiment was the same as the one used in the previous section on the effective cantilever temperature, but at a position with a slightly better coupling to the pickup loop, which affects the detection noise floor.

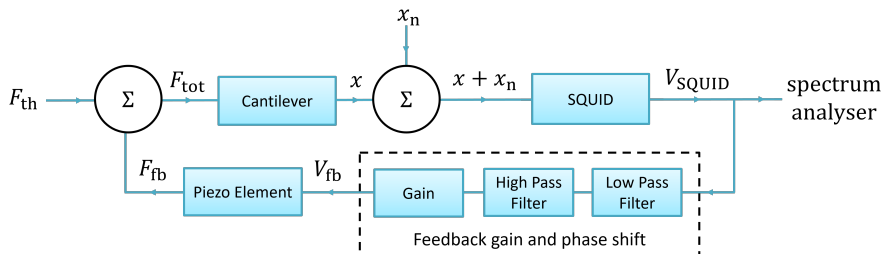


Figure A.4: Diagram of the experimental setup used for the feedback cooling

In order to perform the feedback, the SQUID signal containing the information about the cantilever motion is sent through a low-pass filter followed by a high-pass filter³ to add a gain and phase shift. The bandwidth of both filters is adjusted to obtain the desired phase shift with a random attenuation. This signal is then sent to an amplifier with a tunable gain⁴. This altered signal is then sent to a piezoelectric element which is mechanically coupled to the cantilever. A diagram of this setup can be seen in Fig. A.4. When the phase shift is set in such a way that the feedback is negative, this scheme results in a damping of the cantilever motion, proportional to the velocity of the cantilever. Simultaneously, the SQUID signal is sent to a spectrum analyzer to measure the resulting cantilever motion.

The response of the cantilever to this feedback signal can be calculated from an equation of motion very similar to the one defined in Eq. 2.10, but with an additional force term [44]:

$$m\ddot{x} + \Gamma\dot{x} + kx = F_{\text{tot}} = F_{\text{th}} - g\gamma(\dot{x} + \dot{x}_n), \quad (\text{A.4})$$

³SRS SIM965 Analog Filter

⁴SRS SIM911 BJT Preamplifier

where F_{th} is the random thermal force, g the gain of the feedback, and x_n is the detector displacement noise. The reason this last term is present here and not in Eq. 2.10, is that now also the detector displacement noise is coupled back to the cantilever motion via the feedback mechanism.

Considering this equation of motion, the spectral density of both the actual displacement and the measured displacement of the cantilever can be calculated, following Poggio et al. [44]. The actual displacement spectral density is given by

$$S_x(\omega) = \left[\frac{1/m^2}{(\omega_0^2 - \omega^2)^2 + (1+g)^2 \frac{\omega_0^2 \omega^2}{Q_0^2}} \right] S_F + \left[\frac{g^2 \omega_0^2 \omega^2 / Q_0^2}{(\omega_0^2 - \omega^2)^2 + (1+g)^2 \frac{\omega_0^2 \omega^2}{Q_0^2}} \right] S_{x_n}, \quad (\text{A.5})$$

and the measured displacement spectral density by

$$S_{x+x_n}(\omega) = \left[\frac{1/m^2}{(\omega_0^2 - \omega^2)^2 + (1+g)^2 \frac{\omega_0^2 \omega^2}{Q_0^2}} \right] S_F + \left[\frac{[(\omega_0^2 - \omega^2)^2 + \omega_0^2 \omega^2] / Q_0^2}{(\omega_0^2 - \omega^2)^2 + (1+g)^2 \frac{\omega_0^2 \omega^2}{Q_0^2}} \right] S_{x_n}, \quad (\text{A.6})$$

with S_{x_n} the spectral density of the detection noise, and $S_F = 4k_B T \Gamma$ the standard thermal force spectral density with T the cantilever temperature at zero gain.

The result of the feedback cooling of the cantilever, starting from a Q-factor of $5.2 \cdot 10^4$ at a temperature close to 20 mK is shown in Fig. A.5. The solid lines are fits to the data according to Eq. A.6. Fitting the data can be challenging due to the high number of parameters and, especially in the case of the purple curve, the low SNR. In the procedure we followed, we fix the parameters for the mass and spring constant by calculating them based on the cantilever geometry. For T , we take the calibrated cantilever temperature based on the procedure described in section A.2. We fix Q_0 at the value obtained from a Lorentzian fit to the data at zero gain. This only leaves three parameters free: the resonance frequency f_0 , the gain g , and the detection noise S_{x_n} .

This procedure works well for all but the highest gain data. To get a reliable value for the gain for this data, we also fix f_0 and S_{x_n} to the values found for the second highest gain. The gain we obtain in this way can then be used to calculate

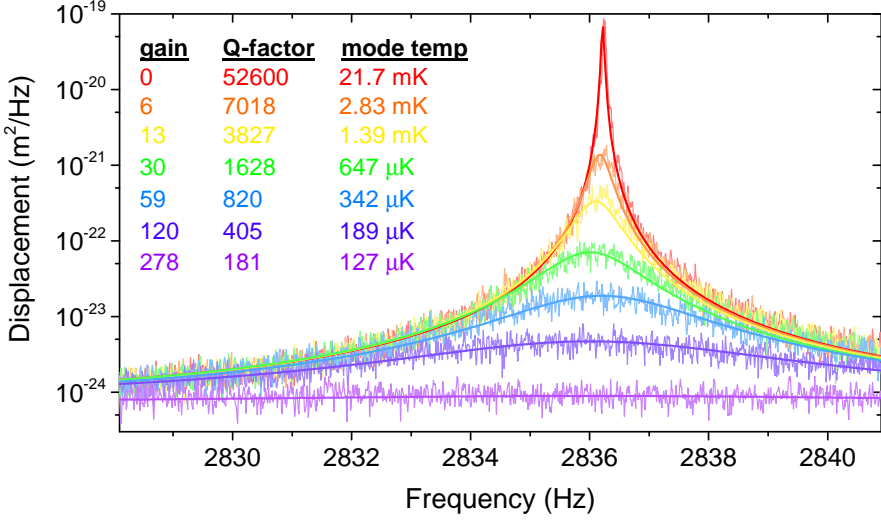


Figure A.5: The main result of the feedback cooling, indicating a final mode temperature of 127 μK . The solid curves are fits to equation A.6. The Q factors of all curves (apart from the bottom one) are obtained from a Lorentzian fit to the data.

the Q using $Q = Q_0/(1 + g)$ [48, 239].

The fit values obtained from Fig. A.5 can be used to calculate the final mode temperature achieved by the feedback cooling, using [44]

$$T_{\text{mode}} = \frac{T}{1 + g} + \frac{k\omega_0}{4k_B Q_0} \left(\frac{g^2}{1 + g} \right) S_{x_n}, \quad (\text{A.7})$$

from which we find that at our maximum gain (limited by the detection noise) we have achieved a mode temperature of 127 μK . The minimal achievable temperature is given by

$$T_{\text{min}} = \sqrt{\frac{k\omega_0 T}{k_B Q_0}} S_{x_n} = 122 \mu\text{K}, \quad (\text{A.8})$$

given our parameters and measured force noise.

This mode temperature corresponds to a phonon occupation number

$$N_{\text{phonons}} = \frac{k_B T_{\text{mode}}}{\hbar\omega_0} = 937, \quad (\text{A.9})$$

at a thermal force noise of 0.23 $\text{aN}/\sqrt{\text{Hz}}$ and a displacement noise floor of 840 $\text{fm}/\sqrt{\text{Hz}}$.

B

LIMITATIONS OF THE MECHANICAL GENERATION OF RADIO-FREQUENCY FIELDS

While the higher modes have the potential for generating very large B_1 fields with very little dissipation, we have also encountered some serious drawbacks of the presence and use of the higher modes. In this appendix, we will demonstrate some of these limitations based on saturation experiments performed on copper, as described in Ch. 4.

B.1 OFF-RESONANT COUPLING

The first issue we discuss is the unintended driving of one or more of the higher modes, even when the applied RF pulse is far off-resonance with the higher mode. During the pulse, the cantilever higher mode acts like a forced damped harmonic oscillator, with equation of motion

$$\ddot{x}(t) + \Gamma\dot{x}(t) + \omega_0^2 x(t) = \frac{F_0}{m} \cos(\omega t), \quad (\text{B.1})$$

with m the mass of the oscillator, $\omega_0^2 = k/m$ the natural frequency, Γ the damping, and F_0 the amplitude of the external force. For $\omega \neq \omega_0$, no damping, and the initial conditions where the cantilever is stationary at $t = 0$, the general solution is given by

$$x(t) = 2A_0 \sin\left[\frac{(\omega_0 + \omega)t}{2}\right] \sin\left[\frac{(\omega_0 - \omega)t}{2}\right], \quad (\text{B.2})$$

with

$$A_0 = \frac{F_0/m}{\omega_0^2 - \omega^2}. \quad (\text{B.3})$$

So, if $\omega \approx \omega_0$, we can look at $x(t)$ as the product of a slow modulation with an amplitude $2A_0 \sin((\omega_0 - \omega)t/2)$, and a rapid oscillation with amplitude $\sin((\omega_0 + \omega)t/2)$. The amplitude of the modulation increases as ω approaches ω_0 . When $\Gamma > 0$, the motion decays to zero as time progresses, resulting in a steady oscillation with amplitude

$$A(\omega) = F_0 / [m^2(\omega_0^2 - \omega^2)^2 + \Gamma^2\omega^2]^{(-1/2)} \quad (\text{B.4})$$

When the pulse is switched off, the cantilever motion starts to decay following

$$x(t) = A_1 \exp(-\omega_0 t/2Q) \cos(\omega_0 t), \quad (\text{B.5})$$

where A_1 is the amplitude of the cantilever at the end of the pulse. We assume weak damping.

We demonstrate the effect of this behaviour in Fig. B.1(a), where we show the direct frequency shift after an RF pulse with a frequency of 950 kHz, which is in between the higher modes at 756 kHz and 1009 kHz, and very short pulse durations. We observe an oscillation of the direct frequency shift, which in the past was wrongfully interpreted as a potential Rabi oscillation [205]. The period of the oscillation is 18 μ s, which indicates that it originates for the beating with the higher mode at 1.009

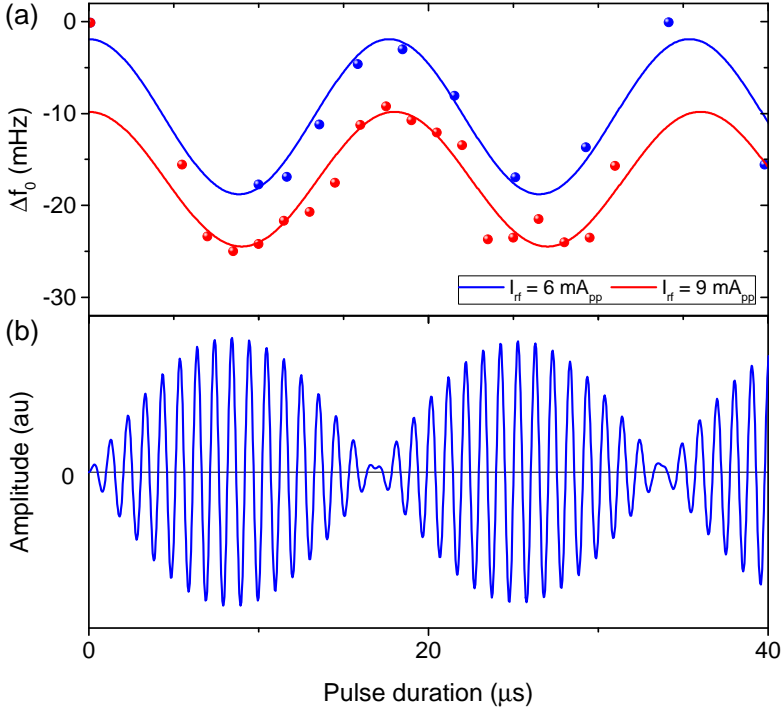


Figure B.1: (a) Direct frequency shift Δf_0 versus pulse duration at RF frequency $f_{RF} = 950 \text{ kHz}$, $T = 30 \text{ mK}$, and $h = 0.95 \mu\text{m}$, for 2 different B_1 fields. The solid curves are fits to a simple cosine, from which we extract oscillation periods of 17.7 ± 0.3 and $18.0 \pm 0.2 \mu\text{s}$ for the 6 and 9 mA_{pp} data sets, respectively. (b) Simulation of the motion $x(t)$ of the 1.009 MHz higher mode when excited by a 950 kHz drive force.

MHz, 59 kHz off-resonance. Fig. B.1(b) shows the simulated amplitude of the 1.009 MHz higher mode when excited with a periodic driving force at 950 kHz.

Thus, the ‘‘Rabi’’ oscillations observed for very short pulse times are in reality caused by the motion of one or more of the higher modes, generating a B_{RF} field with an amplitude which varies with the slow beating frequency, and with a duration determined by the exponential decay with characteristic time $\tau = Q/\pi f_n$.

B.2 NON-LINEARITIES

The second issue is the inherent non-linearity of the higher modes of the cantilever. In Fig. B.2(a) we vary the frequency of the drive field we use to excite the higher mode at 756 kHz. We drive the higher mode using RF currents of about $3 \mu\text{A}_{\text{pp}}$ (black), $10 \mu\text{A}_{\text{pp}}$ (red), and $30 \mu\text{A}_{\text{pp}}$ (green). The solid lines in the figure are guides to the eye. The asymmetry of the curves shows that even at extremely small driving amplitudes the non-linearities of the cantilever dominate the total B_{RF} field.

In Fig. B.2(b) we see a measurement where we drive the same higher mode, but now far away from the sample. In this case, we drive the mode using the cantilever piezo, and we measure the response using the induced magnetic field in the pickup loop. Also far from the surface we observe a clear non-linearity, indicating that at least parts of the non-linearity are an inherent property of the cantilever. We assume that the non-linearities are caused by stress at the surface of the cantilever, which would mean this issue intensifies for higher mode numbers. The slight mismatch between the mode frequency in both figures is attributed to a small sample-induced frequency shift in the top figure.

B.3 TEMPERATURE DEPENDENCE OF QUALITY FACTOR

Finally, we report a large temperature-dependence of the quality factor of the higher modes on the cantilever temperature. Measurements of the temperature-dependence of the Q-factor for the 756 kHz mode is shown in Fig. B.3(b). The solid red line in this curve indicates a $1/T$ dependence. The precise origin of the dissipation responsible for this Q-factor is unknown. For low temperatures, the Q-factor increases to over $5 \cdot 10^5$, with a characteristic time $\tau > 0.2$ s. For higher frequency modes, Q-factors in excess of 1 million have been observed.

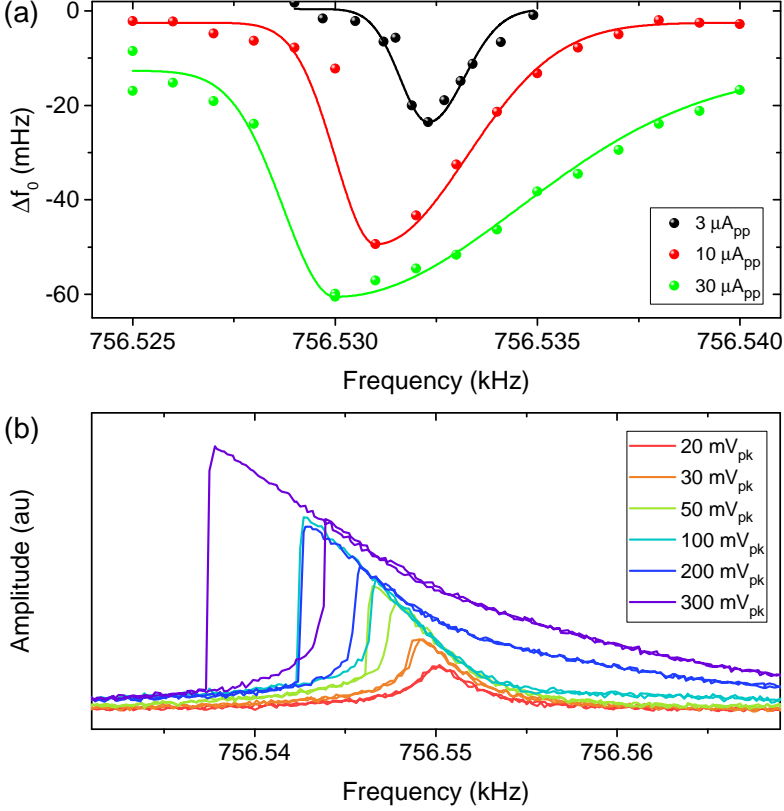


Figure B.2: (a) Direct frequency shift Δf_0 for various drive frequencies around the higher mode frequency. The amplitude of the RF currents are 3 μA_{pp} (black), 10 μA_{pp} (red), en 30 μA_{pp} (green). The solid lines are guides to the eye. An asymmetry of the signal and thus B_{RF} field generated by the higher mode indicates a strong non-linearity of the mode. (b) Response of the higher mode when driven by the cantilever piezo at various drive amplitudes far away from the sample. The drive frequency is swept from frequencies below the resonance to frequencies above the resonance and back. The signal is obtained from the magnetic field measured by the SQUID.

It is possible to convert the Q -factor to a dissipation constant. The shape of the higher vibrational modes of the cantilever induces a rotation of the magnet at the tip of the cantilever, which means we can calculate the dissipation constant using

$$\Gamma_n = \frac{\kappa_n}{Q\omega_n}, \quad (\text{B.6})$$

where κ_n is the torsional spring constant, given by

$$\kappa_n = \omega_n^2 I, \quad (\text{B.7})$$

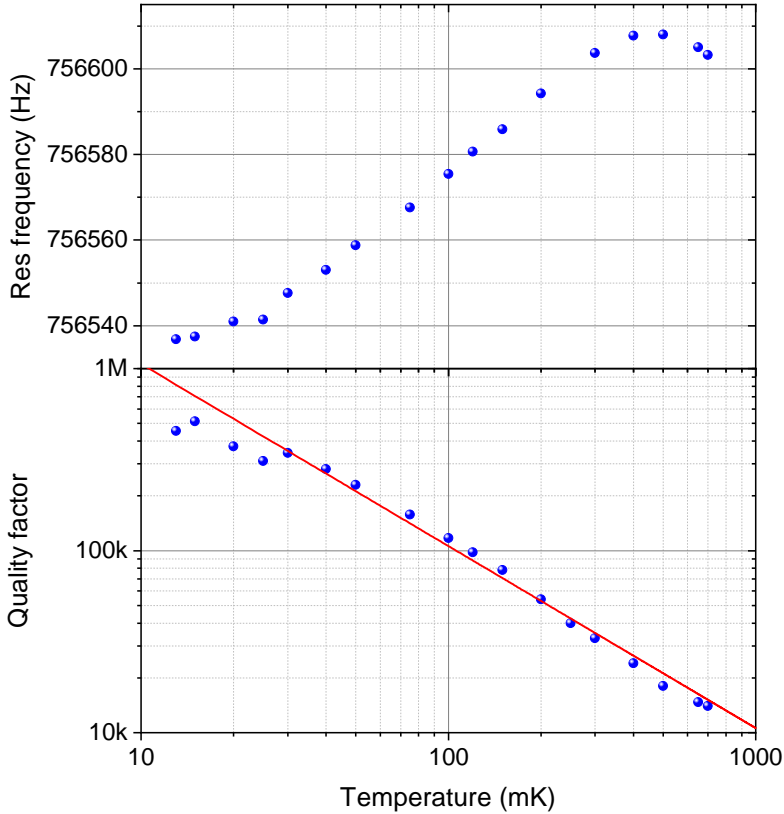


Figure B.3: (a) Resonance Frequency and (b) quality factor of the higher mode at 756 kHz measured for different temperatures of mass 3, when the magnetic particle is far away ($> 5 \mu\text{m}$) from the surface. The red solid line in (b) indicates a $1/T$ dependence.

with I the moment of inertia. When we assume the moment of inertia is dominated by the rotation of the heavy spherical magnet, it is given by $I = (2/5)mR_0^2$ with $m = 2 \cdot 10^{-13}$ kg the mass of the magnet and with $R_0 = 1.7 \mu\text{m}$ the radius. If we take the 6th higher mode at 756 kHz as an example, we find $\kappa_6 = 5 \cdot 10^{-12}$ Nm/rad, which at a temperature of 20 mK leads to a dissipation constant $\Gamma_6 = 3 \cdot 10^{-24}$ kg m²/s and a thermal torsional noise of about $2 \text{ yNm}/\sqrt{\text{Hz}}$. However, our detection sensitivity is not sufficient to detect the thermal motion for most of the higher modes.

C

QUENCHING OF SQUID MODULATION UNDER RADIO-FREQUENCY INTERFERENCE

In this appendix, we briefly expand upon the results presented in Ch. 6, in particular Fig. 6.5, to show the influence of the amplitude of the RF interference or crosstalk on the depth of the SQUID modulation, and the corresponding SQUID noise.

C.1 QUENCHED SQUID MODULATION

As we have seen in Ch. 6, the peak-to-peak amplitude of the SQUID modulation (ΔV_m) is reduced when the SQUID is exposed to a large RF flux. When we apply a test flux Φ_a to the SQUID in combination with RF interference Φ_{rf} , the time-dependent SQUID voltage response to Φ_a is given by [152]:

$$V(t) = \Delta V_m \cdot \cos \frac{2\pi\Phi_a}{\Phi_0} \cdot J_0 \left(\frac{2\pi\Phi_{\text{rf}}}{\Phi_0} \right), \quad (\text{C.1})$$

with $\Phi_0 = 2.068 \cdot 10^{-15}$ Wb the magnetic flux quantum, and J_0 the zeroth-order Bessel function. In Ch. 6 we only looked at the response of the SQUID voltage under a constant RF amplitude, but we can also reconstruct the entire response by varying the RF amplitude. The result of this measurement can be seen in Fig. C.1 for a constant frequency RF interference at 1908 kHz. We applied a test flux using the generator of the SQUID electronics with an amplitude of a little over $2\Phi_0$. The inset shows an example of the SQUID modulation for this applied test flux combined with RF flux at constant amplitude and constant frequency.

Since we have only measured the absolute amplitude, the data follows the absolute value of the zeroth-order Bessel function, shown as the red solid line. For a peak RF flux of $0.38\Phi_0$ the amplitude of the SQUID modulation is reduced to zero,

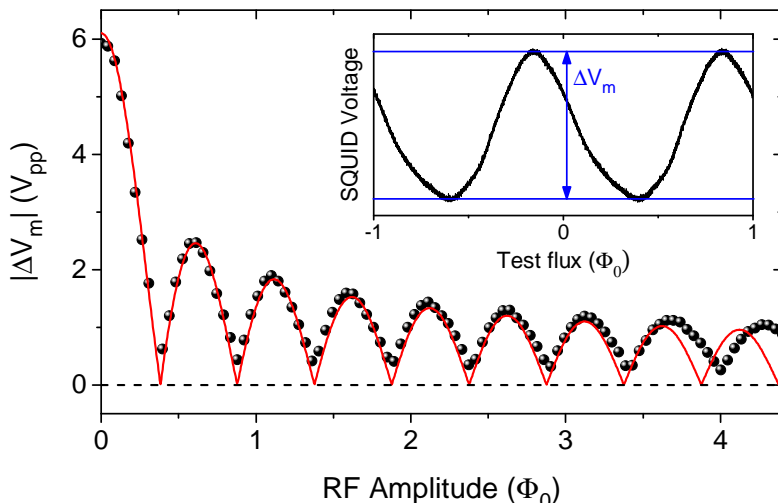


Figure C.1: Measured SQUID modulation depth as a function of the amplitude of the RF interference. This inset shows the way the modulation depth is extracted from the raw SQUID-flux response. The red solid line is a fit to Eq. C.1.

independent of the test flux Φ_a . For large RF amplitude we see that the period of the oscillation increases. An increasing period means that the amplitude of the RF interference reaching the SQUID reduces. We speculate that this is linked to the observed dissipation of power for high frequency, high amplitude RF fields, as described in Ch. 7. The idea behind this hypothesis is that we can make the data and fit match by stretching the horizontal axis by a value proportional to the RF amplitude squared. This scaling is consistent with the amplitude-dependent heating observed. An experimental check for this hypothesis would be to repeat the experiment at a higher RF frequency, as the dissipation of the RF wire scales as $f^{1.5}$ for high f . In that case, the deviation of the data from the fit should appear at lower RF amplitudes. This check has not been done yet.

C.2 POSSIBILITIES

The measurement presented in Fig. C.1 might have important consequences for SQUID-based MRFM experiments, if for some reason the compensation scheme presented in Ch. 6 cannot be used. For example in experiments on electrons, where the required GHz-range frequencies pose a challenge for the compensation. In those cases, the negative effects that the pulse has on the SQUID modulation can be reduced by selecting a suitable amplitude for the pulse.

Furthermore, one could use a measurement such as that presented in Fig. C.1 to check the amplitude of the magnetic field that we create at the location of the sample because the geometry of the pickup loop is known. Especially in the case of GHz pulses this cannot be done directly using the SQUID because of the limited bandwidth, but the amplitude of the pulse might show up in the amplitude of the SQUID modulation.

D

FABRICATION RECIPES

This appendix discusses some of the basic fabrication recipes used for the work presented in this thesis, as we believe this might be useful for future students.

D.1 DETECTION CHIP

We start the fabrication of the MRFM detection chips from 350 nm thick NbTiN films grown on top of a silicon wafer. All details about this film are given by Thoen et al. (our films are grown using the Nordiko 2000 Static) [55]. The pickup loop and RF wire are fabricated with a top-down approach using reactive-ion-etching (RIE). We use the following fabrication recipe:

Resist and spincoating:

- Resist: Negative E-beam resist AR-N 7700.18.
- Spincoat at 1500 rpm for a thickness of 0.65 μm .
- Bake at 80°C for 90 seconds on a closed hotplate.

Exposure using Raith EBPG 5000+ at the Kavli Nanolab Delft:

- E-beam dose 150 $\mu\text{C}/\text{cm}^2$.
- Spotsize 66 nm. With proximity effect correction (PEC).

Development after exposure:

- Postbake at 110°C for 120 seconds on a closed hotplate.
- MF321 developer, 180 seconds.
- H₂O, 30 seconds.
- Rinse with H₂O, dry with nitrogen.

Reactive-ion-etching using Leybold F2 at the Kavli Nanolab Delft:

- 13.5 sccm SF₆, 5.0 sccm O₂.
- 50 W forward RF power, 8 W backward RF power. 320 V_{DC} bias.
- Etching time: 335 seconds + 10 second overetch.
- O₂ plasma descum to help in resist removal.
- 20 sccm O₂, 30 W forward RF power, 100 seconds.

Stripping of the resist before dicing:

- PRS-3000 (positive-resist stripper), 40°C, sonicate for 15 minutes.
- Acetone, 40°C, sonicate for 5 minutes.
- IPA, 40°C, sonicate for 5 minutes.
- Rinse with IPA, dry with nitrogen.

Dicing of the detection chips at the Kavli Nanolab Delft:

- Apply positive photoresist S1805 to prevent surface damage during dicing.
- Spincoat at 4000 rpm.
- Bake at 110°C for 120 seconds on a closed hotplate.
- Dice using DAD 3220 wafer dicer.

Resist stripping after dicing:

- PRS-3000, heated to 85°C au bain-marie, 15 minutes.
- Move beaker to sonicator, sonicate for 5 minutes.
- Reheat to 85°C au bain-marie, 10 minutes.
- Move beaker to sonicator, sonicate for 5 minutes.
- Acetone, room temperature, sonicate for 5 minutes.
- IPA, room temperature, sonicate for 5 minutes.
- Rinse with IPA, dry with nitrogen.

Final measured thickness of the structures on the chip using DektakXT in Leiden: 400 nm, approximately 350 nm NbTiN and 50 nm overetch into the silicon substrate.

D.2 DOUBLE LAYER RESISTS FOR SPUTTERING

For sample fabrication using sputtering, a double resist layer with an undercut is required for proper lift-off and to prevent dog-ears. We identified 2 recipes which seem to work well with the available sputtering machines.

Recipe 1: thin samples.

Resist and spincoating:

- Spincoat PMMA 200k, AR-P 642.06, 4000 rpm. Thickness 0.2 μm .

- Bake at 180°C for 180 seconds on open hotplate.
- Spincoat PMMA 950k, AR-P 672.042, 4000 rpm. Thickness 0.25 μm .
- Bake at 180°C for 180 seconds on open hotplate.

Optimal E-beam dose: 280 $\mu\text{C}/\text{cm}^2$. Suitable for samples with a thickness of up to about 150 nm. Very large undercut due to large difference in polymer length.

Recipe 2: thick samples.

Resist and spincoating:

- Spincoat PMMA 600k, AR-P 662.06, 4000 rpm. Thickness 0.4 μm .
- Bake at 180°C for 180 seconds on open hotplate.
- Spincoat PMMA 950k, AR-P 672.042, 4000 rpm. Thickness 0.25 μm .
- Bake at 180°C for 180 seconds on open hotplate.

Optimal E-beam dose: 300 $\mu\text{C}/\text{cm}^2$. Suitable for samples with a thickness of up to about 350 nm, at the expense of a smaller undercut.

Development and lift-off.

Both options are developed following the same recipe:

- MIBK:IPA (1:3), 60 seconds.
- IPA (stopper), 30 seconds.
- Rinse with IPA, dry with nitrogen.

Liftoff after sample deposition:

- Acetone, 52°C, 20 minutes.
- Spray with acetone while keeping the chip submerged.
- Transfer to clean acetone, sonicate for 2 minutes.
- Inspection of the chip using an optical microscope, still submerged in acetone.
- When lift-off successful, sonicate in ethanol for 2 minutes.
- Sonicate in IPA for 2 minutes.
- Rinse with IPA, dry with nitrogen.

D.3 SPECIFIC SAMPLES

In this section, we will briefly discuss the recipes used for the specific samples used in the experiments presented in this thesis.

D.3.1 Copper

We aim for a sample consisting of about 100 nm of copper, capped with a 10-20 nm layer of gold to prevent oxidation. Deposition of both layers is done in a single session (without venting the system) using the Leybold Heraeus Z406 sputtering system in Leiden. Before sputtering, we do a 4-5 second long dip in hydrofluoric (HF) acid to remove oxides from the surface of the detection chip, followed by three H₂O baths. The chip is dried using nitrogen.

The chip is then loaded into the Z406 within minutes to prevent re-oxidation of the surface as much as possible. The chip is glued to the sample holder using silver paint to improve cooling. Sputtering is started from a background pressure of $5.5 \cdot 10^{-6}$ mbar. We use the following sputtering parameters:

- Cu layer: $5 \cdot 10^{-3}$ mbar argon, flow 49 sccm. RF voltage 1 kV. Pre-sputtering for 3 minutes, final sputtering for 10 minutes.
- Au layer: $5 \cdot 10^{-3}$ mbar argon, flow 49 sccm. RF voltage 1 kV. Pre-sputtering for 3 minutes, final sputtering for 90 seconds.

Measured thickness of the combined Cu/Au layer using DektakXT: 130 nm.

D.3.2 Calcium fluoride

We start from a sample ordered from Kurt J. Lesker, containing crystalline calcium fluoride pieces (1-4 mm) with a purity of 99.99%. The deposition was done using resistance evaporation, inspired by earlier work by Mamin et al. [14]. To improve thermalization, the CaF₂ is deposited on top of a thin layer of copper and gold. The copper and gold are deposited using e-beam evaporation in the Leybold Heraeus L560 at the Kavli Nanolab. The parameters for the different materials are:

- Cu layer: e-beam, 12 kV. Evaporation time 100 seconds at a rate of 0.8-1.2 Å/s.
- Au layer: e-beam, 12 kV. Evaporation time 375 seconds at a rate of 1.0-1.2 Å/s.
- CaF₂ layer: resistive heating, 25% power. Evaporation time 610 seconds at a rate of 3-5 Å/s.

Measured thickness of the Cu/Au layer using DektakXT: 40 nm. Measured thickness of the CaF₂ layer: 240 nm.

D.3.3 Palladium

Target ordered from ESPI: purity 99.99%, with less than 2 ppm Fe. The sputtering is done in the UHV sputtering system in Leiden. Before sputtering, we do a 4-5 second long dip in hydrofluoric (HF) acid to remove oxides from the surface of the detection chip, followed by three H₂O baths. The chip is dried using nitrogen. After the HF dip, the chip is loaded into the vacuum as soon as possible (< 20 minutes).

Sputtering is started at a chamber pressure of $7.7 \cdot 10^{-9}$ mbar. Sputtering is done using an argon pressure of $3.3 \cdot 10^{-3}$ mbar. The RF power is set to 100 mA, 401V. We pre-sputter for 5 minutes to clean the target, then do real sputtering on the sample for 20 minutes. The measured thickness of the palladium layer using the DektakXT is 108 nm.

D.4 CONSIDERATIONS FOR DOUBLE-LAYER DETECTION CHIPS

As discussed in Ch. 2, it is worth to invest time in the development of double-layer detection chips. This would enable the fabrication of on-chip transformers to boost the coupling efficiency between the pickup loop and SQUID input coil, and would also open the possibility to fabricate gradiometric pickup loops that cross the RF wire to reduce flux crosstalk. The first attempts to fabricate these double-layer devices were done by de Voogd [59]. In these attempts, the first layer was fabricated following a similar recipe as described in Sec. D.1 (RIE etching), while the second layer was made using a lift-off process. At the visual inspection after the sputtering of the second NbTiN layer, it was found that the resist was cracked. The measured critical current of the second layer, which was much lower than expected with only several

μA , confirms that the second layer was contaminated, probably from the resist which could not stand the high temperatures during sputtering.

From this we conclude that structures made by sputtering and lift-off might be more susceptible to contamination, resulting in a material with a lower critical current density. Hence, it is preferable to make the RF wire and the secondary coil of a transformer from the first (reactive-ion-etched) layer of high thickness NbTiN, as especially the RF wire should be able to carry large currents when used for an NMR experiment.

BIBLIOGRAPHY

- [1] Sidles, J. A. Noninductive detection of single-proton magnetic resonance. *Appl. Phys. Lett.*, 58(24):2854–2856, 1991.
- [2] Burley, S. K., Berman, H. M., Bhikadiya, C., Bi, C., Chen, L., Di Costanzo, L., Christie, C., Dalenberg, K., Duarte, J. M., Dutta, S., et al. Rcsb protein data bank: biological macromolecular structures enabling research and education in fundamental biology, biomedicine, biotechnology and energy. *Nucleic Acids Res.*, 47(D1):D464–D474, 2018.
- [3] Rugar, D., Yannoni, C. S., and Sidles, J. A. Mechanical detection of magnetic resonance. *Nature*, 360(6404):563, 1992.
- [4] Züger, O. and Rugar, D. First images from a magnetic resonance force microscope. *Appl. Phys. Lett.*, 63(18):2496–2498, 1993.
- [5] Rugar, D., Züger, O., Hoen, S., Yannoni, C. S., Vieth, H., and Kendrick, R. D. Force detection of nuclear magnetic resonance. *Science*, 264(5165):1560–1563, 1994.
- [6] Stowe, T. D., Yasumura, K., Kenny, T. W., Botkin, D., Wago, K., and Rugar, D. Attonewton force detection using ultrathin silicon cantilevers. *Appl. Phys. Lett.*, 71(2):288–290, 1997.
- [7] Chui, B. W., Hishinuma, Y., Budakian, R., Mamin, H. J., Kenny, T. W., and Rugar, D. Mass-loaded cantilevers with suppressed higher-order modes for magnetic resonance force microscopy. In *TRANSDUCERS, Solid-State Sensors, Actuators and Microsystems, 12th International Conference on, 2003*, volume 2, pages 1120–1123. IEEE, 2003.
- [8] Wago, K., Botkin, D., Yannoni, C. S., and Rugar, D. Force-detected electron-spin resonance: Adiabatic inversion, nutation, and spin echo. *Phys. Rev. B*, 57(2):1108, 1998.
- [9] Stipe, B. C., Mamin, H. J., Yannoni, C. S., Stowe, T. D., Kenny, T. W., and Rugar, D. Electron spin relaxation near a micron-size ferromagnet. *Phys. Rev. Lett.*, 87(27):277602, 2001.
- [10] Mamin, H. J., Budakian, R., Chui, B. W., and Rugar, D. Detection and manipulation of statistical polarization in small spin ensembles. *Phys. Rev. Lett.*, 91(20):207604, 2003.
- [11] Garner, S. R., Kuehn, S., Dawlaty, J. M., Jenkins, N. E., and Marohn, J. A.

- Force-gradient detected nuclear magnetic resonance. *Appl. Phys. Lett.*, 84(25):5091–5093, 2004.
- [12] Rugar, D., Budakian, R., Mamin, H. J., and Chui, B. W. Single spin detection by magnetic resonance force microscopy. *Nature*, 430(6997):329, 2004.
- [13] Mamin, H. J., Budakian, R., Chui, B. W., and Rugar, D. Magnetic resonance force microscopy of nuclear spins: Detection and manipulation of statistical polarization. *Phys. Rev. B*, 72(2):024413, 2005.
- [14] Mamin, H. J., Poggio, M., Degen, C. L., and Rugar, D. Nuclear magnetic resonance imaging with 90-nm resolution. *Nature Nanotechnol.*, 2(5):301, 2007.
- [15] Mamin, H. J., Oosterkamp, T. H., Poggio, M., Degen, C. L., Rettner, C. T., and Rugar, D. Isotope-selective detection and imaging of organic nanolayers. *Nano Lett.*, 9(8):3020–3024, 2009.
- [16] Degen, C. L., Poggio, M., Mamin, H. J., Rettner, C. T., and Rugar, D. Nanoscale magnetic resonance imaging. *Proc. Natl. Academy Sci.*, 106(5):1313–1317, 2009.
- [17] Rose, W., Haas, H., Chen, A. Q., Jeon, N., Lauhon, L. J., Cory, D. G., and Budakian, R. High-resolution nanoscale solid-state nuclear magnetic resonance spectroscopy. *Phys. Rev. X*, 8(1):011030, 2018.
- [18] Wago, K., Botkin, D., Yannoni, C. S., and Rugar, D. Paramagnetic and ferromagnetic resonance imaging with a tip-on-cantilever magnetic resonance force microscope. *Appl. Phys. Lett.*, 72(21):2757–2759, 1998.
- [19] Bruland, K. J., Dougherty, W. M., Garbini, J. L., Sidles, J. A., and Chao, S. H. Force-detected magnetic resonance in a field gradient of 250 000 tesla per meter. *Appl. Phys. Lett.*, 73(21):3159–3161, 1998.
- [20] Bartesaghi, A. and Subramaniam, S. Membrane protein structure determination using cryo-electron tomography and 3d image averaging. *Curr. Opin. Struct. Biol.*, 19(4):402–407, 2009.
- [21] Zhou, Z. H. Atomic resolution cryo electron microscopy of macromolecular complexes. In *Advances in protein chemistry and structural biology*, volume 82, pages 1–35. *Elsevier*, 2011.
- [22] Geelen, D., Thete, A., Schaff, O., Kaiser, A., van der Molen, S. J., and Tromp, R. eV-TEM: Transmission electron microscopy in a low energy cathode lens instrument. *Ultramicroscopy*, 159:482–487, 2015.
- [23] Crowther, R. A. The Resolution Revolution: Recent Advances in CryoEM, volume 579. *Academic Press*, 2016.
- [24] Murata, K. and Wolf, M. Cryo-electron microscopy for structural analysis of dynamic biological macromolecules. *Biochimica et Biophysica Acta (BBA)-General Subjects*, 1862(2):324–334, 2018.
- [25] Maletinsky, P., Hong, S., Grinolds, M. S., Hausmann, B., Lukin, M. D.,

- Walsworth, R. L., Loncar, M., and Yacoby, A. A robust scanning diamond sensor for nanoscale imaging with single nitrogen-vacancy centres. *Nature Nanotechnol.*, 7(5):320, 2012.
- [26] Mamin, H. J., Kim, M., Sherwood, M. H., Rettner, C. T., Ohno, K., Awschalom, D. D., and Rugar, D. Nanoscale nuclear magnetic resonance with a nitrogen-vacancy spin sensor. *Science*, 339(6119):557–560, 2013.
- [27] Müller, C., Kong, X., Cai, J.-M., Melentijević, K., Stacey, A., Markham, M., Twitchen, D., Isoya, J., Pezzagna, S., Meijer, J., Du, J. F., Plenio, M. B., Naydenov, B., McGuinness, L. P., and Jelezko, F. Nuclear magnetic resonance spectroscopy with single spin sensitivity. *Nature Commun.*, 5:4703, 2014.
- [28] Zhang, Z., Hammel, P. C., and Wigen, P. E. Observation of ferromagnetic resonance in a microscopic sample using magnetic resonance force microscopy. *Appl. Phys. Lett.*, 68(14):2005–2007, 1996.
- [29] Obukhov, Y., Pelekhov, D. V., Kim, J., Banerjee, P., Martin, I., Nazaretski, E., Movshovich, R., An, S., Gramila, T. J., Batra, S., and Hammel, P. C. Local ferromagnetic resonance imaging with magnetic resonance force microscopy. *Phys. Rev. Lett.*, 100(19):197601, 2008.
- [30] Lee, I., Obukhov, Y., Xiang, G., Hauser, A., Yang, F., Banerjee, P., Pelekhov, D. V., and Hammel, P. C. Nanoscale scanning probe ferromagnetic resonance imaging using localized modes. *Nature*, 466(7308):845, 2010.
- [31] Kinoshita, Y., Li, Y. J., Yoshimura, S., Saito, H., and Sugawara, Y. Magnetic resonance force microscopy using ferromagnetic resonance of a magnetic tip excited by microwave transmission via a coaxial resonator. *Nanotechnol.*, 28(48):485709, 2017.
- [32] Budakian, R., Mamin, H. J., and Rugar, D. Suppression of spin diffusion near a micron-size ferromagnet. *Phys. Rev. Lett.*, 92(3):037205, 2004.
- [33] Cardellino, J., Scozzaro, N., Herman, M., Berger, A. J., Zhang, C., Fong, K. C., Jayaprakash, C., Pelekhov, D. V., and Hammel, P. C. The effect of spin transport on spin lifetime in nanoscale systems. *Nature Nanotechnol.*, 9(5):343–347, 2014.
- [34] de Wit, M., Welker, G., de Voogd, J. M., and Oosterkamp, T. H. Density and t_1 of surface and bulk spins in diamond in high magnetic field gradients. *Phys. Rev. Appl.*, 10(6):064045, 2017.
- [35] Alexson, D. A., Hickman, S. A., Marohn, J. A., and Smith, D. D. Single-shot nuclear magnetization recovery curves with force-gradient detection. *Appl. Phys. Lett.*, 101(2):022103, 2012.
- [36] Saun, S.-B., Won, S., Kwon, S., and Lee, S. NMR spin-lattice relaxation time t_1 of thin films obtained by magnetic resonance force microscopy. *J. Magn. Reson.*, 254:71–74, 2015.

- [37] Wagenaar, J. J. T., den Haan, A. M. J., de Voogd, J. M., Bossoni, L., de Jong, T. A., de Wit, M., Bastiaans, K. M., Thoen, D. J., Endo, A., Klapwijk, T. M., Zaanen, J., and Oosterkamp, T. H. Probing the nuclear spin-lattice relaxation time at the nanoscale. *Phys. Rev. Appl.*, 6(1):014007, 2016.
- [38] Wagenaar, J. J. T. Magnetic resonance force microscopy for condensed matter. PhD thesis, Leiden University, 2017.
- [39] Bertero, M. and Boccacci, P. Introduction to inverse problems in imaging. *CRC press, Boca Raton, Florida, USA*, 1998.
- [40] Nguyen, H. L. and Marohn, J. A. Reverse Monte Carlo reconstruction of electron spin-label coordinates from scanned-probe magnetic resonance microscope signals. *arXiv preprint*, 2018.
- [41] Longenecker, J. G., Mamin, H. J., Senko, A. W., Chen, L., Rettner, C. T., Rugar, D., and Marohn, J. A. High-gradient nanomagnets on cantilevers for sensitive detection of nuclear magnetic resonance. *ACS Nano*, 6(11):9637–9645, 2012.
- [42] Tao, Y. Nanomechanical systems with small dissipation. PhD thesis, Massachusetts Institute of Technology, 2016.
- [43] Moores, B. A. J. Spanning the unbridged imaging regime: Advances in mechanically detected MRI. PhD thesis, ETH Zurich, 2015.
- [44] Poggio, M., Degen, C. L., Mamin, H. J., and Rugar, D. Feedback cooling of a cantilevers fundamental mode below 5 mk. *Phys. Rev. Lett.*, 99(1):017201, 2007.
- [45] H eritier, M., Eichler, A., Pan, Y., Grob, U., Shorubalko, I., Krass, M. D., Tao, Y., and Degen, C. L. Nanoladder cantilevers made from diamond and silicon. *Nano Lett.*, 18(3):1814–1818, 2018.
- [46] De Bonis, S. L., Urgell, C., Yang, W., Samanta, C., Noury, A., Vergara-Cruz, J., Dong, Q., Jin, Y., and Bachtold, A. Ultrasensitive displacement noise measurement of carbon nanotube mechanical resonators. *Nano Lett.*, 18(8):5324–5328, 2018.
- [47] Usenko, O., Vinante, A., Wijts, G. H. C. J., and Oosterkamp, T. H. A superconducting quantum interference device based read-out of a subattoneutron force sensor operating at millikelvin temperatures. *Appl. Phys. Lett.*, 98(13):133105, 2011.
- [48] Vinante, A., Kirste, A., den Haan, A. M. J., Usenko, O., Wijts, G. H. C. J., Jeffrey, E., Sonin, P., Bouwmeester, D., and Oosterkamp, T. H. High sensitivity SQUID-detection and feedback-cooling of an ultrasoft microcantilever. *Appl. Phys. Lett.*, 101(12):123101, 2012.
- [49] Vinante, A., Wijts, G. H. C. J., Usenko, O., Schinkelshoek, L., and Oosterkamp, T. H. Magnetic resonance force microscopy of paramagnetic electron spins at

- millikelvin temperatures. *Nature Commun.*, 2:572, 2011.
- [50] Wagenaar, J. J. T., den Haan, A. M. J., Donkersloot, R. J., Marsman, F., de Wit, M., Bossoni, L., and Oosterkamp, T. H. Mechanical generation of radio-frequency fields in nuclear-magnetic-resonance force microscopy. *Phys. Rev. Appl.*, 7(2):024019, 2018.
- [51] den Haan, A. M. J., Wagenaar, J. J. T., de Voogd, J. M., Koning, G., and Oosterkamp, T. H. Spin-mediated dissipation and frequency shifts of a cantilever at milliKelvin temperatures. *Phys. Rev. B*, 92(23):235441, dec 2015.
- [52] De Voogd, J. M., Wagenaar, J. J. T., and Oosterkamp, T. H. Dissipation and resonance frequency shift of a resonator magnetically coupled to a semiclassical spin. *Sci. Rep.*, 7:42239, February 2017. ISSN 2045-2322.
- [53] Wijts, G. H. C. J. Magnetic resonance force microscopy at milliKelvin temperatures. PhD thesis, Leiden University, 2013.
- [54] den Haan, A. M. J. Nuclear magnetic resonance force microscopy at milliKelvin temperatures. PhD thesis, Leiden University, 2016.
- [55] Thoen, D. J., Bos, B. G. C., Haalebos, E. A. F., Klapwijk, T. M., Baselmans, J. J. A., and Endo, A. Superconducting NbTiN thin films with highly uniform properties over a \varnothing 100 mm wafer. *IEEE T. on Appl. Supercond.*, 27(4):1–5, 2017.
- [56] Klimov, A., Słysz, W., Guziewicz, M., Kolkovsky, V., Zaytseva, I., and Malinowski, A. Characterization of the critical current and physical properties of superconducting epitaxial NbTiN sub-micron structures. *Physica C: Supercond. its Appl.*, 536:35–38, 2017.
- [57] Poggio, M., Degen, C. L., Rettner, C. T., Mamin, H. J., and Rugar, D. Nuclear magnetic resonance force microscopy with a microwave rf source. *Appl. Phys. Lett.*, 90(26):263111, 2007.
- [58] Griffiths, D. J. Introduction to Electrodynamics, Third Edition, International Edition. *Pearson Benjamin Cummings*, 2008.
- [59] de Voogd, J. M. Magnetic resonance force microscopy and the spin bath. PhD thesis, Leiden University, 2017.
- [60] Cleveland, J. P., Manne, S., Bocek, D., and Hansma, P. K. A nondestructive method for determining the spring constant of cantilevers for scanning force microscopy. *Rev. Sci. Instruments*, 64(2):403–405, 1993.
- [61] MEMSnet. material: Silicon (si), bulk. URL <https://www.memsnet.org/material/siliconsibulk/>.
- [62] Sidles, J. A., Garbini, J. L., Bruland, K. J., Rugar, D., Züger, O., Hoen, S., and Yannoni, C. S. Magnetic resonance force microscopy. *Reviews Mod. Phys.*, 67(1):249, 1995.
- [63] Mamin, H. J., Budakian, R., and Rugar, D. Superconducting microwave res-

- onator for millikelvin magnetic resonance force microscopy. *Rev. Sci. Instruments*, 74(5):2749–2753, 2003.
- [64] Yuan, M., Cohen, M. A., and Steele, G. A. Silicon nitride membrane resonators at millikelvin temperatures with quality factors exceeding 108. *Appl. Phys. Lett.*, 107(26):263501, 2015.
- [65] Opdam, D. Characterization of silicon nitride cantilevers and mechanical feedback cooling. Master’s thesis, Leiden University, 2018.
- [66] Jones, M. H. and Jones, S. H. The general properties of si, ge, sige, sio₂ and si₃n₄. *Virginia Semiconductor Inc.*, 2002.
- [67] van Velzen, M. New methods to improve the usability in magnetic resonance frequency microscopy. Master’s thesis, Leiden University, 2018.
- [68] Yazdanian, S. M., Marohn, J. A., and Loring, R. F. Dielectric fluctuations in force microscopy: Noncontact friction and frequency jitter. *The J. Chem. Phys.*, 128(22):224706, 2008.
- [69] Heeres, E. C., Katan, A. J., Van Es, M. H., Beker, A. F., Hesselberth, M., van Der Zalm, D. J., and Oosterkamp, T. H. A compact multipurpose nanomanipulator for use inside a scanning electron microscope. *Rev. Sci. Instruments*, 81(2):023704, 2010.
- [70] Nazaretski, E., Pelekhov, D. V., Martin, I., Zalalutdinov, M., Ponarin, D., Smirnov, A., Hammel, P. C., and Movshovich, R. Detection of localized ferromagnetic resonance in a continuous thin film via magnetic resonance force microscopy. *Phys. Rev. B*, 79(13):132401, 2009.
- [71] Berman, G. P., Borgonovi, F., Gorshkov, V. N., and Tsifrinovich, V. I. Modeling and simulations of a single-spin measurement using mrfm. *IEEE T. on Nanotechnol.*, 4(1):14–20, 2005.
- [72] Petersan, P. J. and Anlage, S. M. Measurement of resonant frequency and quality factor of microwave resonators: Comparison of methods. *J. Appl. Phys.*, 84(6):3392–3402, 1998.
- [73] JPE. Jpe - cryogenic linear actuator ”piezoknob”, 2018. URL <https://www.janssenprecisionengineering.com>.
- [74] Bian, L., Wen, Y., Li, P., Wu, Y., Zhang, X., and Li, M. Magnetostrictive stress induced frequency shift in resonator for magnetic field sensor. *Sens. Actuator. A: Phys.*, 247:453–458, 2016.
- [75] De Waele, A. T. A. M. Basic operation of cryocoolers and related thermal machines. *J. Low Temp. Phys.*, 164(5-6):179, 2011.
- [76] Chijioke, A. and Lawall, J. Vibration spectrum of a pulse-tube cryostat from 1hz to 20khz. *Cryogenics*, 50(4):266–270, 2010.
- [77] Den Haan, A. M. J., Wijts, G. H. C. J., Galli, F., Usenko, O., Van Baarle, G. J. C., Van Der Zalm, D. J., and Oosterkamp, T. H. Atomic resolution scanning

- tunneling microscopy in a cryogen free dilution refrigerator at 15 mk. *Rev. Sci. Instruments*, 85(3):035112, 2014.
- [78] Pan, S. H., Hudson, E. W., and Davis, J. C. ^3He refrigerator based very low temperature scanning tunneling microscope. *Rev. Sci. Instruments*, 70(2):1459–1463, 1999.
- [79] Moussy, N., Courtois, H., and Pannetier, B. A very low temperature scanning tunneling microscope for the local spectroscopy of mesoscopic structures. *Rev. Sci. Instruments*, 72(1):128–131, 2001.
- [80] Wiebe, J., Wachowiak, A., Meier, F., Haude, D., Foster, T., Morgenstern, M., and Wiesendanger, R. A 300 mk ultra-high vacuum scanning tunneling microscope for spin-resolved spectroscopy at high energy resolution. *Rev. Sci. Instruments*, 75(11):4871–4879, 2004.
- [81] Kambara, H., Matsui, T., Niimi, Y., and Fukuyama, H. Construction of a versatile ultralow temperature scanning tunneling microscope. *Rev. Sci. Instruments*, 78(7):073703, 2007.
- [82] Marz, M., Goll, G., and Löhneysen, H. v. A scanning tunneling microscope for a dilution refrigerator. *Rev. Sci. Instruments*, 81(4):045102, 2010.
- [83] Song, Y. J., Otte, A. F., Shvarts, V., Zhao, Z., Kuk, Y., Blankenship, S. R., Band, A., Hess, F. M., and Strosio, J. A. Invited review article: A 10 mk scanning probe microscopy facility. *Rev. Sci. Instruments*, 81(12):121101, 2010.
- [84] Misra, S., Zhou, B. B., Drozdov, I. K., Seo, J., Urban, L., Gyenis, A., Kingsley, S. C. J., Jones, H., and Yazdani, A. Design and performance of an ultra-high vacuum scanning tunneling microscope operating at dilution refrigerator temperatures and high magnetic fields. *Rev. Sci. Instruments*, 84(10):103903, 2013.
- [85] Singh, U. R., Enayat, M., White, S. C., and Wahl, P. Construction and performance of a dilution-refrigerator based spectroscopic-imaging scanning tunneling microscope. *Rev. Sci. Instruments*, 84(1):013708, 2013.
- [86] Roychowdhury, A., Gubrud, M. A., Dana, R., Anderson, J. R., Lobb, C. J., Wellstood, F. C., and Dreyer, M. A 30 mk, 13.5 t scanning tunneling microscope with two independent tips. *Rev. Sci. Instruments*, 85(4):043706, 2014.
- [87] von Allwörden, H., Eich, A., Knol, E. J., Hermenau, J., Sonntag, A., Gerritsen, J. W., Wegner, D., and Khajetoorians, A. A. Design and performance of an ultra-high vacuum spin-polarized scanning tunneling microscope operating at 30 mk and in a vector magnetic field. *Rev. Sci. Instruments*, 89(3):033902, 2018.
- [88] Machida, T., Kohsaka, Y., and Hanaguri, T. A scanning tunneling microscope for spectroscopic imaging below 90 mk in magnetic fields up to 17.5 t. *Rev. Sci. Instruments*, 89(9):093707, 2018.
- [89] Battisti, I., Verdoes, G., van Oosten, K., Bastiaans, K. M., and Allan, M. P.

- Definition of design guidelines, construction, and performance of an ultra-stable scanning tunneling microscope for spectroscopic imaging. *Rev. Sci. Instruments*, 89(12):123705, 2018.
- [90] Pelekhov, D. V., Becker, J. B., and Nunes Jr, G. Ultralow-temperature atomic force microscopy for the investigation of mesoscopic systems. *Appl. Phys. Lett.*, 72(8):993–995, 1998.
- [91] Gildemeister, A. E., Ihn, T., Barengo, C., Studerus, P., and Ensslin, K. Construction of a dilution refrigerator cooled scanning force microscope. *Rev. Sci. Instruments*, 78(1):013704, 2007.
- [92] Mamin, H. J. and Rugar, D. Sub-attoneutron force detection at millikelvin temperatures. *Appl. Phys. Lett.*, 79(20):3358–3360, 2001.
- [93] Björnsson, P. G., Gardner, B. W., Kirtley, J. R., and Moler, K. A. Scanning superconducting quantum interference device microscope in a dilution refrigerator. *Rev. Sci. Instruments*, 72(11):4153–4158, 2001.
- [94] Seo, Y., Cadden-Zimansky, P., and Chandrasekhar, V. Low-temperature high-resolution magnetic force microscopy using a quartz tuning fork. *Appl. Phys. Lett.*, 87(10):103103, 2005.
- [95] Schaefer-Nolte, E., Reinhard, F., Ternes, M., Wrachtrup, J., and Kern, K. A diamond-based scanning probe spin sensor operating at low temperature in ultra-high vacuum. *Rev. Sci. Instruments*, 85(1):013701, 2014.
- [96] Halbertal, D., Cuppens, J., Shalom, M. B., Embon, L., Shadmi, N., Anahory, Y., Naren, H., Sarkar, J., Uri, A., Ronen, Y., Myasoedov, Y., Levitov, L. S., Joselevich, E., Geim, A. K., and Zeldov, E. Nanoscale thermal imaging of dissipation in quantum systems. *Nature*, 539(7629):407, 2016.
- [97] Kleckner, D. and Bouwmeester, D. Sub-kelvin optical cooling of a micromechanical resonator. *Nature*, 444(7115):75, 2006.
- [98] Bassi, A., Lochan, K., Satin, S., Singh, T. P., and Ulbricht, H. Models of wavefunction collapse, underlying theories, and experimental tests. *Reviews Mod. Phys.*, 85(2):471, 2013.
- [99] Binnig, G., Rohrer, H., Gerber, C., and Weibel, E. Tunneling through a controllable vacuum gap. *Appl. Phys. Lett.*, 40(2):178–180, 1982.
- [100] Olivieri, E., Billard, J., De Jesus, M., Juillard, A., and Leder, A. Vibrations on pulse tube based dry dilution refrigerators for low noise measurements. *Nucl. Instruments Methods Phys. Res. Section A: Accelerators, Spectrometers, Detectors Associated Equipment*, 858:73–79, 2017.
- [101] Davidsson, P., Olin, H., Persson, M., and Pehrson, S. Design and operation of a low-temperature scanning tunneling microscope suitable for operation below 1 k. *Ultramicroscopy*, 42:1470–1475, 1992.
- [102] Ast, C. R., Assig, M., Ast, A., and Kern, K. Design criteria for scanning tun-

- neling microscopes to reduce the response to external mechanical disturbances. *Rev. Sci. Instruments*, 79(9):093704, 2008.
- [103] Foley, E. T., Yoder, N. L., Guisinger, N. P., and Hersam, M. C. Cryogenic variable temperature ultrahigh vacuum scanning tunneling microscope for single molecule studies on silicon surfaces. *Rev. Sci. Instruments*, 75(12):5280–5287, 2004.
- [104] Caparrelli, S., Majorana, E., Moscatelli, V., Pascucci, E., Perciballi, M., Puppo, P., Rapagnani, P., and Ricci, F. Vibration-free cryostat for low-noise applications of a pulse tube cryocooler. *Rev. Sci. Instruments*, 77(9):095102, 2006.
- [105] Pelliccione, M., Sciambi, A., Bartel, J., Keller, A. J., and Goldhaber-Gordon, D. Design of a scanning gate microscope for mesoscopic electron systems in a cryogen-free dilution refrigerator. *Rev. Sci. Instruments*, 84(3):033703, 2013.
- [106] Poggio, M. and Degen, C. L. Force-detected nuclear magnetic resonance: recent advances and future challenges. *Nanotechnol.*, 21(34):342001, 2010.
- [107] Fowles, G. R. and Cassiday, G. L. Analytical mechanics, 7th edition. *Thomson Learning, inc.*, 2005.
- [108] Campbell. Electrical receiving, translating, or repeating circuit, 1917.
- [109] Pobell, F. Matter and methods at low temperatures. *Springer Science & Business Media*, 2007.
- [110] Woodcraft, A. L. Recommended values for the thermal conductivity of aluminium of different purities in the cryogenic to room temperature range, and a comparison with copper. *Cryogenics*, 45(9):626–636, 2005.
- [111] Aspelmeyer, M., Kippenberg, T. J., and Marquardt, F. Cavity optomechanics. *Reviews Mod. Phys.*, 86(4):1391, 2014.
- [112] Vinante, A., Bahrami, M., Bassi, A., Usenko, O., Wijts, G. H. C. J., and Oosterkamp, T. H. Upper bounds on spontaneous wave-function collapse models using millikelvin-cooled nanocantilevers. *Phys. Rev. Lett.*, 116(9):090402, 2016.
- [113] Chen, L., Longenecker, J. G., Moore, E. W., and Marohn, J. A. Long-lived frequency shifts observed in a magnetic resonance force microscope experiment following microwave irradiation of a nitroxide spin probe. *Appl. Phys. Lett.*, 102(13):132404, 2013.
- [114] Nichol, J. M., Hemesath, E. R., Lauhon, L. J., and Budakian, R. Nanomechanical detection of nuclear magnetic resonance using a silicon nanowire oscillator. *Phys. Rev. B*, 85(5):054414, 2012.
- [115] Meyer, E. S., Silvera, I. F., and Brandt, B. L. Eddy current shielding and heating: Reduction of dissipation for very low-temperature experiments in the presence of magnetic field ripple. *Rev. Sci. Instruments*, 60(9):2964–2968, 1989.
- [116] Isaac, C. E., Gleave, C. M., Nasr, P. T., Nguyen, H. L., Curley, E. A., Yoder, J. L., Moore, E. W., Chen, L., and Marohn, J. A. Dynamic nuclear polarization

- in a magnetic resonance force microscope experiment. *Phys. Chem. Chem. Phys.*, 18(13):8806–8819, 2016.
- [117] Abragam, A. Principles of nuclear magnetism (International series of monographs on physics). *Clarendon Press, Oxford*, 1961.
- [118] Bloch, F. Nuclear induction. *Phys. Rev.*, 70(7-8):460, 1946.
- [119] Slichter, C. P. Principles of Magnetic Resonance, volume 1 of Springer Series in Solid-State Sciences. *Springer Berlin Heidelberg, Berlin, Heidelberg*, 1990.
- [120] Mulkern, R. V. and Williams, M. L. The general solution to the bloch equation with constant rf and relaxation terms: application to saturation and slice selection. *Med. Phys.*, 20(1):5–13, 1993.
- [121] Murase, K. and Tanki, N. Numerical solutions to the time-dependent Bloch equations revisited. *Magn. Reson. Imaging*, 29(1):126–131, 2011.
- [122] Herzog, B. E., Cadeddu, D., Xue, F., Peddibhotla, P., and Poggio, M. Boundary between the thermal and statistical polarization regimes in a nuclear spin ensemble. *Appl. Phys. Lett.*, 105(4):043112, 2014.
- [123] Hoepker, N., Lekkala, S., Loring, R. F., and Marohn, J. A. Dielectric fluctuations over polymer films detected using an atomic force microscope. *The J. Phys. Chem. B*, 115(49):14493–14500, 2011.
- [124] Yazdanian, S. M., Hoepker, N., Kuehn, S., Loring, R. F., and Marohn, J. A. Quantifying electric field gradient fluctuations over polymers using ultrasensitive cantilevers. *Nano Lett.*, 9(6):2273–2279, 2009.
- [125] Moore, E. W., Lee, S., Hickman, S. A., Wright, S. J., Harrell, L. E., Borbat, P. P., Freed, J. H., and Marohn, J. A. Scanned-probe detection of electron spin resonance from a nitroxide spin probe. *Proc. Natl. Academy Sci.*, 106(52):22251–22256, 2009.
- [126] Oosterkamp, T. H., Poggio, M., Degen, C. L., Mamin, H. J., and Rugar, D. Frequency domain multiplexing of force signals with application to magnetic resonance force microscopy. *Appl. Phys. Lett.*, 96(8):083107, 2010.
- [127] Moores, B. A. J., Eichler, A., Tao, Y., Takahashi, H., Navaretti, P., and Degen, C. L. Accelerated nanoscale magnetic resonance imaging through phase multiplexing. *Appl. Phys. Lett.*, 106(21):213101, 2015.
- [128] Grapengeter, H. H., Kosfeld, R., and Offergeld, H. W. Influences of paramagnetic impurities on the proton spin-lattice relaxation time T_1 of siloxane polymers. *Polymer*, 21(7):829–831, 1980.
- [129] Lounasmaa, O. V. Nuclear magnetism in copper, silver, and rhodium metals at positive and negative spin temperatures in the nano- and picokelvin regimes. *Matematisk-Fysiske Meddelelser*, pages 401–443, 1997.
- [130] Oja, A. S. and Lounasmaa, O. V. Nuclear magnetic ordering in simple metals at positive and negative nanokelvin temperatures. *Reviews Mod. Phys.*, 69(1):

- 1, 1997.
- [131] Bloembergen, N. On the interaction of nuclear spins in a crystalline lattice. *Physica*, 15(3-4):386–426, 1949.
- [132] Ofori-Okai, B. K., Pezzagna, S., Chang, K., Loretz, M., Schirhagl, R., Tao, Y., Moores, B. A., Groot-Berning, K., Meijer, J., and Degen, C. L. Spin properties of very shallow nitrogen vacancy defects in diamond. *Phys. Rev. B*, 86(8):081406, 2012.
- [133] Rondin, L., Tetienne, J. P., Hingant, T., Roch, J. F., Maletinsky, P., and Jacques, V. Magnetometry with nitrogen-vacancy defects in diamond. *Rep. on Prog. Phys.*, 77(5):056503, 2014.
- [134] Bar-Gill, N., Pham, L. M., Belthangady, C., Le Sage, D., Cappellaro, P., Maze, J. R., Lukin, M. D., Yacoby, A., and Walsworth, R. Suppression of spin-bath dynamics for improved coherence of multi-spin-qubit systems. *Nature Commun.*, 3:858, 2012.
- [135] Myers, B. A., Das, A., Dartiailh, M. C., Ohno, K., Awschalom, D. D., and Bleszynski Jayich, A. C. Probing surface noise with depth-calibrated spins in diamond. *Phys. Rev. Lett.*, 113(2):027602, July 2014.
- [136] Lee, D., Lee, K. W., Cady, J. V., Ouartchaiyapong, P., and Bleszynski Jayich, A. C. Topical review: Spins and mechanics in diamond. *J. Opt.*, 19(3):033001, 2017.
- [137] Luan, L., Grinolds, M. S., Hong, S. K., Maletinsky, P., Walsworth, R. L., and Yacoby, A. Decoherence imaging of spin ensembles using a scanning single-electron spin in diamond. *Sci. Rep.*, 5:8119, January 2015.
- [138] Romach, Y., Müller, C., Unden, T., Rogers, L. J., Isoda, T., Itoh, K. M., Markham, M., Stacey, A., Meijer, J., Pezzagna, S., Naydenov, B., McGuinness, L. P., Bar-Gill, N., and Jelezko, F. Spectroscopy of surface-induced noise using shallow spins in diamond. *Phys. Rev. Lett.*, 114(1):017601, jan 2015.
- [139] Rosskopf, T., Dussaux, A., Ohashi, K., Loretz, M., Schirhagl, R., Watanabe, H., Shikata, S., Itoh, K. M., and Degen, C. L. Investigation of surface magnetic noise by shallow spins in diamond. *Phys. Rev. Lett.*, 112(14):147602, apr 2014.
- [140] Grinolds, M. S., Warner, M., De Greve, K., Dovzhenko, Y., Thiel, L., Walsworth, R. L., Hong, S., Maletinsky, P., and Yacoby, A. Subnanometre resolution in three-dimensional magnetic resonance imaging of individual dark spins. *Nature Nanotechnol.*, 9(4):279–284, April 2014.
- [141] Bruno, A., De Lange, G., Asaad, S., Van der Enden, K. L., Langford, N. K., and DiCarlo, L. Reducing intrinsic loss in superconducting resonators by surface treatment and deep etching of silicon substrates. *Appl. Phys. Lett.*, 106(18):182601, 2015.
- [142] Pappas, D. P., Vissers, M. R., Wisbey, D. S., Kline, J. S., and Gao, J. Two

- level system loss in superconducting microwave resonators. *IEEE T. on Appl. Supercond.*, 21(3):871–874, 2011.
- [143] Casola, F., van der Sar, T., and Yacoby, A. Probing condensed matter physics with magnetometry based on nitrogen-vacancy centres in diamond. *Nature Reviews Mater.*, 3:17088, 2018.
- [144] Takahashi, S., Hanson, R., van Tol, J., Sherwin, M. S., and Awschalom, D. D. Quenching spin decoherence in diamond through spin bath polarization. *Phys. Rev. Lett.*, 101(4):047601, 2008.
- [145] Peddibhotla, P., Xue, F., Hauge, H. I. T., Assali, S., Bakkers, E. P. A. M., and Poggio, M. Harnessing nuclear spin polarization fluctuations in a semiconductor nanowire. *Nature Phys.*, 9(10):631–635, 2013.
- [146] Griffiths, D. J. Introduction to Electrodynamics, Third Edition. *Prentice Hall, Upper Saddle River*, 1999.
- [147] Stipe, B. C., Mamin, H. J., Stowe, T. D., Kenny, T. W., and Rugar, D. Noncontact friction and force fluctuations between closely spaced bodies. *Phys. Rev. Lett.*, 87(9):096801, 2001.
- [148] Kuehn, S., Loring, R. F., and Marohn, J. A. Dielectric fluctuations and the origins of noncontact friction. *Phys. Rev. Lett.*, 96(15):156103, 2006.
- [149] Vinante, A., Mezzena, R., Falferi, P., Carlesso, M., and Bassi, A. Improved noninterferometric test of collapse models using ultracold cantilevers. *Phys. Rev. Lett.*, 119(11):110401, 2017.
- [150] Koch, R. H., Foglietti, V., Rozen, J. R., Stawiasz, K. G., Ketchen, M. B., Lathrop, D. K., Sun, J. Z., and Gallagher, W. J. Effects of radio frequency radiation on the dc SQUID. *Appl. Phys. Lett.*, 65(1):100–102, 1994.
- [151] Mück, M., Dechert, J., Gail, J., Kreutzbruck, M., Schöne, S., and Weidl, R. Response of radio frequency superconducting quantum interference devices to electromagnetic interference. *Rev. Sci. Instruments*, 66(9):4690–4693, 1995.
- [152] Clarke, J. and Braginski, A. I. The SQUID handbook: Applications of SQUIDS and SQUID systems. *John Wiley & Sons*, 2006.
- [153] Webb, R. A. New technique for improved low-temperature SQUID NMR measurements. *Rev. Sci. Instruments*, 48(12):1585–1594, 1977.
- [154] Fan, N. Q., Heaney, M. B., Clarke, J., Newitt, D., Wald, L. L., Hahn, E. L., Bielecki, A., and Pines, A. Nuclear magnetic resonance with dc SQUID preamplifiers. *IEEE T. on Magn.*, 25(2):1193–1199, 1989.
- [155] Greenberg, Y. S. Application of superconducting quantum interference devices to nuclear magnetic resonance. *Reviews Mod. Phys.*, 70(1):175, 1998.
- [156] Clarke, J., Hatridge, M., and Möble, M. SQUID-detected magnetic resonance imaging in microtesla fields. *Annu. Rev. Biomed. Eng.*, 9:389–413, 2007.

- [157] Augustine, M. P., TonThat, D. M., and Clarke, J. SQUID detected NMR and NQR. *Solid State Nucl. Magn. Reson.*, 11(1-2):139–156, 1998.
- [158] McDermott, R., Lee, S., Haken, B. t., Trabesinger, A. H., Pines, A., and Clarke, J. Microtesla magnetic resonance imaging with a superconducting quantum interference device. *Proc. Natl. Academy Sci.*, 101(21):7857–61, 2004.
- [159] Matlachov, A. N., Volegov, P. L., Espy, M. A., George, J. S., and Kraus Jr, R. H. SQUID detected NMR in microtesla magnetic fields. *J. Magn. Reson.*, 170(1):1–7, 2004.
- [160] Buckenmaier, K., Rudolph, M., Back, C., Misztal, T., Bommerich, U., Fehling, P., Koelle, D., Kleiner, R., Mayer, H. A., Scheffler, K., et al. SQUID-based detection of ultra-low-field multinuclear NMR of substances hyperpolarized using signal amplification by reversible exchange. *Sci. Rep.*, 7(1):13431, 2017.
- [161] Ehnholm, G. J., Ekström, J. P., Loponen, M. T., and Soini, J. K. Transversal SQUID NMR. *Cryogenics*, 19(11):673–678, 1979.
- [162] Pasquarelli, A., Del Gratta, C., Della Penna, S., Di Luzio, S., Pizzella, V., and Romani, G. L. A SQUID based AC susceptometer for the investigation of large samples. *Phys. Med. Biol.*, 41(11):2533, 1996.
- [163] Pizzella, V., Della Penna, S., Del Gratta, C., and Romani, G. L. SQUID systems for biomagnetic imaging. *Supercond. Science Technol.*, 14(7):R79, 2001.
- [164] Quantum Design Inc. SQUID application note 1052-202a: Coupling magnetic signals to a SQUID amplifier, October 2001. URL <https://www.qdusa.com/sitedocs/appNotes/squids/1052-202.pdf>.
- [165] Garwood, M. and DelaBarre, L. The return of the frequency sweep: designing adiabatic pulses for contemporary NMR. *J. Magn. Reson.*, 153(2):155–177, 2001.
- [166] O’Dell, L. A. The WURST kind of pulses in solid-state NMR. *Solid State Nucl. Magn. Reson.*, 55:28–41, 2013.
- [167] Claridge, T. D. W. High-resolution NMR techniques in organic chemistry, volume 27. *Elsevier*, 2016.
- [168] Fagaly, R. Superconducting quantum interference device instruments and applications. *Rev. Sci. Instruments*, 77(10):101101, 2006.
- [169] Choi, W. S., Kim, M. J., Jeong, I. W., Kim, D. E., Park, H. C., and Park, K. H. Development of high-stability magnet power supply. *Nucl. Instruments Methods Phys. Res. A: Accelerators, Spectrometers, Detectors Associated Equipment*, 822:15–24, 2016.
- [170] van Waarde, B., Benningshof, O. W. B., and Oosterkamp, T. H. A magnetic persistent current switch at millikelvin temperatures. *Cryogenics*, 78:74–77, 2016.
- [171] Hortensius, H. L., Driessen, E. F. C., Klapwijk, T. M., Berggren, K. K., and

- Clem, J. R. Critical-current reduction in thin superconducting wires due to current crowding. *Appl. Phys. Lett.*, 100(18):182602, 2012.
- [172] Stoll, R. L. The analysis of eddy currents. *Clarendon Press*, 1974.
- [173] Popovic, Z. and Popovic, B. D. Introductory electromagnetics. *Prentice hall Upper Saddle River, NJ, USA.*, 2000.
- [174] Duthil, P. Material properties at low temperature. *arXiv preprint arXiv:1501.07100*, 2015.
- [175] Tinkham, M. Introduction to superconductivity. *Courier Corporation*, 2004.
- [176] Annett, J. F. Superconductivity, superfluids and condensates, volume 5. *Oxford University Press*, 2004.
- [177] Driessen, E. F. C., Coumou, P. C. J. J., Tromp, R. R., De Visser, P. J., and Klapwijk, T. M. Strongly disordered TiN and NbTiN s-wave superconductors probed by microwave electrodynamics. *Phys. Rev. Lett.*, 109(10):107003, 2012.
- [178] Abrikosov, A. A. On the magnetic properties of second kind superconductors. *Sov. Phys. JETP*, 5(6):1174–1182, 1957.
- [179] Kim, Y. B., Hempstead, C. F., and Strnad, A. R. Flux-flow resistance in type-II superconductors. *Phys. Rev.*, 139(4A):A1163, 1965.
- [180] Embon, L., Anahory, Y., Suhov, A., Halbertal, D., Cuppens, J., Yakovenko, A., Uri, A., Myasoedov, Y., Rappaport, M. L., Huber, M. E., Gurevich, A., and Zeldov, E. Probing dynamics and pinning of single vortices in superconductors at nanometer scales. *Sci. Rep.*, 5:7598, 2015.
- [181] Raes, B., Van de Vondel, J., Silhanek, A. V., de Souza Silva, C. C., Gutierrez, J., Kramer, R. B. G., and Moshchalkov, V. V. Local mapping of dissipative vortex motion. *Phys. Rev. B*, 86(6):064522, 2012.
- [182] Bardeen, J. and Stephen, M. J. Theory of the motion of vortices in superconductors. *Phys. Rev.*, 140(4A):A1197, 1965.
- [183] Yu, L., Newman, N., and Rowell, J. M. Measurement of the coherence length of sputtered NbTiN thin films. *IEEE T. on Appl. Supercond.*, 12(2):1795–1798, 2002.
- [184] Yu, L., Singh, R. K., Liu, H., Wu, S. Y., Hu, R., Durand, D., Bulman, J., Rowell, J. M., and Newman, N. Fabrication of niobium titanium nitride thin films with high superconducting transition temperatures and short penetration lengths. *IEEE T. on Appl. Supercond.*, 15(1):44–48, 2005.
- [185] Wilde, S., Valizadeh, R., Malyshev, O. B., Stenning, G. B. G., Hannah, A., Pattalwar, S., Pattalwar, N., Barradas, N. P., Alves, E., and Chesca, B. Physical vapour deposition of NbTiN thin films for superconducting RF cavities. *Loughborough University Institutional Repository*, 2017.
- [186] Stan, G., Field, S. B., and Martinis, J. M. Critical field for complete vortex

- expulsion from narrow superconducting strips. *Phys. Rev. Lett.*, 92(9):097003, 2004.
- [187] Gurevich, A. Enhancement of rf breakdown field of superconductors by multi-layer coating. *Appl. Phys. Lett.*, 88(1):012511, 2006.
- [188] Haugan, T., Barnes, P. N., Wheeler, R., Meisenkothen, F., and Sumption, M. Addition of nanoparticle dispersions to enhance flux pinning of the $\text{YBa}_2\text{Cu}_3\text{O}_{7-x}$ superconductor. *Nature*, 430(7002):867, 2004.
- [189] Maiorov, B., Baily, S. A., Zhou, H., Ugurlu, O., Kennison, J. A., Dowden, P. C., Holesinger, T. G., Foltyn, S. R., and Civale, L. Synergetic combination of different types of defect to optimize pinning landscape using BaZrO_3 -doped $\text{YBa}_2\text{Cu}_3\text{O}_7$. *Nature Mater.*, 8(5):398, 2009.
- [190] Fang, L., Jia, Y., Mishra, V., Chaparro, C., Vlasko-Vlasov, V. K., Koshelev, A. E., Welp, U., Crabtree, G. W., Zhu, S., Zhigadlo, N. D., Katrych, S., Karpinski, J., and Kwok, W. K. Huge critical current density and tailored superconducting anisotropy in $\text{SmFeAsO}_{0.8}\text{F}_{0.15}$ by low-density columnar-defect incorporation. *Nature Commun.*, 4:2655, 2013.
- [191] Córdoba, R., Baturina, T. I., Sesé, J., Mironov, A. Y., De Teresa, J. M., Ibarra, M. R., Nasimov, D. A., Gutakovskii, A. K., Latyshev, A. V., Guillamón, I., Suderow, H., Vieira, S., Baklanov, M. R., Palacios, J. J., and M., V. V. Magnetic field-induced dissipation-free state in superconducting nanostructures. *Nature Commun.*, 4:1437, 2013.
- [192] Wang, Y.-L., Glatz, A., Kimmel, G. J., Aranson, I. S., Thoutam, L. R., Xiao, Z.-L., Berdiyorov, G. R., Peeters, F. M., Crabtree, G. W., and Kwok, W.-K. Parallel magnetic field suppresses dissipation in superconducting nanostrips. *Proc. Natl. Academy Sci.*, 114(48):E10274–E10280, 2017.
- [193] Barends, R., Hortensius, H. L., Zijlstra, T., Baselmans, J. J. A., Yates, S. J. C., Gao, J. R., and Klapwijk, T. M. Contribution of dielectrics to frequency and noise of nbtin superconducting resonators. *Appl. Phys. Lett.*, 92(22):223502, 2008.
- [194] Bruno, A., Skacel, S. T., Kaiser, C., Wunsch, S., Siegel, M., Ustinov, A. V., and Lisitskiy, M. P. Investigation of dielectric losses in hydrogenated amorphous-silicon (a-si: H) thin films using superconducting microwave resonators. *Phys. Procedia*, 36:245–249, 2012.
- [195] Calusine, G., Melville, A., Woods, W., Das, R., Stull, C., Bolkhovsky, V., Braje, D., Hover, D., Kim, D. K., Miloshi, X., et al. Analysis and mitigation of interface losses in trenched superconducting coplanar waveguide resonators. *Appl. Phys. Lett.*, 112(6):062601, 2018.
- [196] Rosenberg, H. M. The thermal conductivity of germanium and silicon at low temperatures. *Proc. Phys. Soc. Section A*, 67(9):837, 1954.

- [197] Mamin, H. J., Rettner, C. T., Sherwood, M. H., Gao, L., and Rugar, D. High field-gradient dysprosium tips for magnetic resonance force microscopy. *Appl. Phys. Lett.*, 100(1):013102, 2012.
- [198] Nichol, J. M., Naibert, T. R., Hemesath, E. R., Lauhon, L. J., and Budakian, R. Nanoscale Fourier-transform magnetic resonance imaging. *Phys. Rev. X*, 3(3):031016, 2013.
- [199] Fong, K. C., Herman, M. R., Banerjee, P., Pelekhov, D. V., and Hammel, P. C. Spin lifetime in small ensembles of electron spins measured by magnetic resonance force microscopy. *Phys. Rev. B*, 84(22):220405, 2011.
- [200] Campanella, H., Del Real, R. P., Díaz-Michelena, M., Duch, M., Guerrero, H., Esteve, J., and Plaza, J. A. Focused-ion-beam-assisted magnet fabrication and manipulation for magnetic field detection applications. *ACS Appl. Mater. & Interfaces*, 1(3):527–531, 2009.
- [201] Overweg, H. C., Den Haan, A. M. J., Eerkens, H. J., Alkemade, P. F. A., La Rooij, A. L., Spreuw, R. J. C., Bossoni, L., and Oosterkamp, T. H. Probing the magnetic moment of FePt micromagnets prepared by focused ion beam milling. *Appl. Phys. Lett.*, 107(7):072402, 2015.
- [202] Longenecker, J. G., Moore, E. W., and Marohn, J. A. Rapid serial prototyping of magnet-tipped attonewton-sensitivity cantilevers by focused ion beam manipulation. *J. Vac. Science & Technol. B, Nanotechnol. Microelectronics: Materials, Processing, Measurement, Phenom.*, 29(3):032001, 2011.
- [203] Hickman, S. A., Moore, E. W., Lee, S., Longenecker, J. G., Wright, S. J., Harrell, L. E., and Marohn, J. A. Batch-fabrication of cantilevered magnets on attonewton-sensitivity mechanical oscillators for scanned-probe nanoscale magnetic resonance imaging. *ACS Nano*, 4(12):7141–7150, 2010.
- [204] Garner, S. R. Force-gradient detection of nuclear magnetic resonance. PhD thesis, Cornell University, 2005.
- [205] Donkersloot, R. Exploring a novel cantilever design for enhanced sensitivity in magnetic resonance force microscopy. Master’s thesis, Cornell University, 2016.
- [206] OConnell, A. D., Ansmann, M., Bialczak, R. C., Hofheinz, M., Katz, N., Lucero, E., McKenney, C., Neeley, M., Wang, H., Weig, E. M., Cleland, A. N., and Martinis, J. M. Microwave dielectric loss at single photon energies and millikelvin temperatures. *Appl. Phys. Lett.*, 92(11):112903, 2008.
- [207] Gao, J., Daal, M., Vayonakis, A., Kumar, S., Zmuidzinas, J., Sadoulet, B., Mazin, B. A., Day, P. K., and Leduc, H. G. Experimental evidence for a surface distribution of two-level systems in superconducting lithographed microwave resonators. *Appl. Phys. Lett.*, 92(15):152505, 2008.
- [208] Gao, J., Daal, M., Martinis, J. M., Vayonakis, A., Zmuidzinas, J., Sadoulet, B., Mazin, B. A., Day, P. K., and Leduc, H. G. A semiempirical model for

- two-level system noise in superconducting microresonators. *Appl. Phys. Lett.*, 92(21):212504, 2008.
- [209] Vissers, M. R., Kline, J. S., Gao, J., Wisbey, D. S., and Pappas, D. P. Reduced microwave loss in trenched superconducting coplanar waveguides. *Appl. Phys. Lett.*, 100(8):082602, 2012.
- [210] Oliver, W. D. and Welander, P. B. Materials in superconducting quantum bits. *MRS Bull.*, 38(10):816825, 2013.
- [211] Wendin, G. Quantum information processing with superconducting circuits: a review. *Rep. on Prog. Phys.*, 80(10):106001, 2017.
- [212] Wang, J., Zhang, W., Zhang, J., You, J., Li, Y., Guo, G., Feng, F., Song, X., Lou, L., Zhu, W., and Wang, G. Coherence times of precise depth controlled NV centers in diamond. *Nanoscale*, 8(10):5780–5785, 2016.
- [213] Brandenburg, F., Nagumo, R., Saichi, K., Tahara, K., Iwasaki, T., Hatano, M., Jelezko, F., Igarashi, R., and Yatsui, T. Improving the electron spin properties of nitrogen-vacancy centres in nanodiamonds by near-field etching. *Sci. Rep.*, 8(1):15847, 2018.
- [214] Martinis, J. M., Cooper, K. B., McDermott, R., Steffen, M., Ansmann, M., Osborn, K. D., Cicak, K., Oh, S., Pappas, D. P., Simmonds, R. W., and Yu, C. C. Decoherence in Josephson qubits from dielectric loss. *Phys. Rev. Lett.*, 95:210503, Nov 2005.
- [215] Sendelbach, S., Hover, D., Kittel, A., Mück, M., Martinis, J. M., and McDermott, R. Magnetism in SQUIDS at millikelvin temperatures. *Phys. Rev. Lett.*, 100:227006, Jun 2008.
- [216] Sendelbach, S., Hover, D., Mück, M., and McDermott, R. Complex inductance, excess noise, and surface magnetism in dc SQUIDS. *Phys. Rev. Lett.*, 103(11):117001, 2009.
- [217] Sank, D., Barends, R., Bialczak, R. C., Chen, Y., Kelly, J., Lenander, M., Lucero, E., Mariantoni, M., Megrant, A., Neeley, M., O’Malley, P. J. J., Vainsencher, A., Wang, H., Wenner, J., White, T. C., Yamamoto, T., Yin, Y., Cleland, A. N., and Martinis, J. M. Flux noise probed with real time qubit tomography in a josephson phase qubit. *Physycal Rev. Lett.*, 109:067001, Aug 2012.
- [218] Wang, C., Axline, C., Gao, Y. Y., Brecht, T., Chu, Y., Frunzio, L., Devoret, M., and Schoelkopf, R. J. Surface participation and dielectric loss in superconducting qubits. *Appl. Phys. Lett.*, 107(16):162601, 2015.
- [219] Chu, Y., Axline, C., Wang, C., Brecht, T., Gao, Y. Y., Frunzio, L., and Schoelkopf, R. J. Suspending superconducting qubits by silicon micromachining. *Appl. Phys. Lett.*, 109(11):112601, 2016.
- [220] Quintana, C. M., Megrant, A., Chen, Z., Dunsworth, A., Chiaro, B., Barends,

- R., Campbell, B., Chen, Y., Hoi, I.-C., Jeffrey, E., Kelly, J., Mutus, J. Y., O'Malley, P. J. J., Neill, C., Roushan, P., Sank, D., Vainsencher, A., Wenner, J., White, T. C., Cleland, A. N., and Martinis, J. M. Characterization and reduction of microfabrication-induced decoherence in superconducting quantum circuits. *Appl. Phys. Lett.*, 105(6):062601, 2014.
- [221] Dial, O., McClure, D. T., Poletto, S., Keefe, G., Rothwell, M. B., Gambetta, J. M., Abraham, D. W., Chow, J. M., and Steffen, M. Bulk and surface loss in superconducting transmon qubits. *Supercond. Science Technol.*, 29(4):044001, 2016.
- [222] Bosman, S. J. Delft Circuits b.v. URL <https://www.delft-circuits.com/>.
- [223] Ong, F. R., Orgiazzi, J.-L., de Waard, A., Frossati, G., and Lupascu, A. Insertable system for fast turnaround time microwave experiments in a dilution refrigerator. *Rev. Sci. Instruments*, 83(9):093904, 2012.
- [224] Wollersheim, O., Zumaqué, H., Hormes, J., Kadereit, D., Langen, J., Häußling, L., Hoessel, P., and Hoffmann, G. Quantitative studies of the radiation chemical behaviour of PMMA and poly(lactides). *Nucl. Instruments Methods Phys. Res. Section B: Beam Interactions with Mater. Atoms*, 97(1):273 – 278, 1995. ISSN 0168-583X.
- [225] Rangan, S., Bartynski, R. A., Narasimhan, A., and Brainard, R. L. Electronic structure, excitation properties, and chemical transformations of extreme ultraviolet resist materials. *J. Appl. Phys.*, 122(2):025305, 2017.
- [226] Thete, A., Geelen, D., van der Molen, S. J., and Tromp, R. M. Charge catastrophe and dielectric breakdown during exposure of organic thin films to low-energy electron radiation. *Phys. Rev. Lett.*, 119(26):266803, 2017.
- [227] Valiev, K. A. The physics of submicron lithography. *Springer Science & Business Media*, 2012.
- [228] Biercuk, M. J., Uys, H., Britton, J. W., VanDevender, A. P., and Bollinger, J. J. Ultrasensitive detection of force and displacement using trapped ions. *Nature Nanotechnol.*, 5(9):646–650, 2010.
- [229] Poot, M. and van der Zant, H. S. J. Mechanical systems in the quantum regime. *Phys. Rep.*, 511(5):273–335, 2012.
- [230] Moser, J., Güttinger, J., Eichler, A., Esplandiu, M. J., Liu, D. E., Dykman, M. I., and Bachtold, A. Ultrasensitive force detection with a nanotube mechanical resonator. *Nature Nanotechnol.*, 8(7):493–496, 2013.
- [231] Norte, R. A., Moura, J. P., and Gröblacher, S. Mechanical resonators for quantum optomechanics experiments at room temperature. *Phys. Rev. Lett.*, 116(14):147202, 2016.
- [232] Rocheleau, T., Ndukum, T., Macklin, C., Hertzberg, J. B., Clerk, A. A., and Schwab, K. C. Preparation and detection of a mechanical resonator near the

-
- ground state of motion. *Nature*, 463(7277):72–75, 2010.
- [233] Tao, Y. and Degen, C. L. Single-crystal diamond nanowire tips for ultrasensitive force microscopy. *Nano Lett.*, 15(12):7893–7897, 2015.
- [234] Garbini, J. L., Bruland, K. J., Dougherty, W. M., and Sidles, J. A. Optimal control of force microscope cantilevers. I. controller design. *J. Appl. Phys.*, 80(4):1951–1958, 1996.
- [235] Bruland, K. J., Garbini, J. L., Dougherty, W. M., and Sidles, J. A. Optimal control of force microscope cantilevers. ii. magnetic coupling implementation. *J. Appl. Phys.*, 80(4):1959–1964, 1996.
- [236] Marshall, W., Simon, C., Penrose, R., and Bouwmeester, D. Towards quantum superpositions of a mirror. *Phys. Rev. Lett.*, 91(13):130401, 2003.
- [237] Armour, A. D., Blencowe, M. P., and Schwab, K. C. Entanglement and decoherence of a micromechanical resonator via coupling to a cooper-pair box. *Phys. Rev. Lett.*, 88(14):148301, 2002.
- [238] Van Wezel, J. and Oosterkamp, T. H. A nanoscale experiment measuring gravity’s role in breaking the unitarity of quantum dynamics. In *Proceedings of the Royal Society A*, volume 468, pages 35–56. The Royal Society, 2012.
- [239] Cohadon, P.-F., Heidmann, A., and Pinard, M. Cooling of a mirror by radiation pressure. *Phys. Rev. Lett.*, 83(16):3174, 1999.

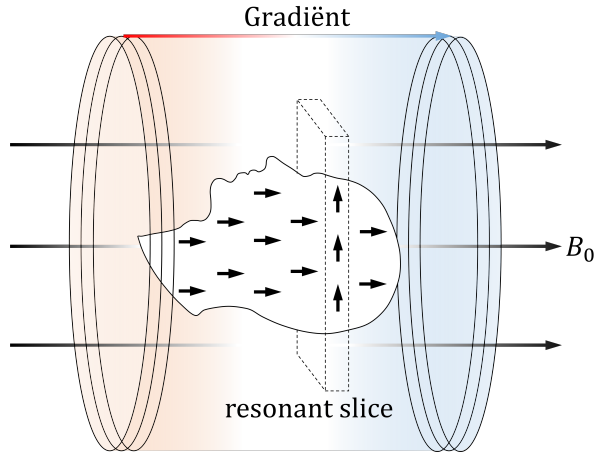
SAMENVATTING

De samenvatting is toegankelijk gemaakt voor een breed publiek. Hierom zijn sommige zaken vereenvoudigd en zijn er geen bronvermeldingen opgenomen. De wetenschappelijk geïnteresseerde lezer wordt verwezen naar de introductie in hoofdstuk 1.

DE NOODZAAK VOOR EEN NIEUWE TECHNIEK

Eiwitten spelen een cruciale rol in het lichaam, en het niet correct vouwen van deze eiwitten wordt in verband gebracht met een groot aantal ziektes, zoals Alzheimer en Parkinson. Het is belangrijk om de precieze ruimtelijke structuur van de eiwitten vast te kunnen stellen, zodat aan de hand hiervan een mogelijke behandeling kan worden bepaald. Het bestuderen van eiwitten wordt tot nu toe vooral gedaan met behulp van technieken zoals *kernspinresonantie* (NMR) en *röntgendiffractie*, maar om uiteenlopende redenen kan van lang niet alle eiwitten op deze manier de structuur worden ontrafeld. Er is daarom een sterke behoefte aan een nieuwe techniek om in volledig detail de structuur van individuele moleculen of virussen te bepalen.

Het klinkt erg aantrekkelijk om *magnetic resonance imaging* (MRI) voor dit doel te gebruiken. Deze techniek is in de medische wereld niet meer weg te denken, en stelt ons in staat om drie-dimensionale afbeeldingen te maken van het menselijk lichaam. Hierbij kan zelfs onderscheid gemaakt worden tussen verschillende weefsels. Echter, het is niet mogelijk om deze techniek direct ook toe te passen op veel kleinere biologische monsters, zoals bijvoorbeeld eiwitten, vanwege de beperkte gevoeligheid van MRI. Een lage gevoeligheid betekent dat er een relatief groot volume aan weefsel nodig is om voldoende signaal te krijgen, wat dus gelijk staat aan een lage beeldresolutie. In de jaren 90 is daarom een alternatieve techniek voorgesteld die de sterke punten van MRI zou moeten combineren met een veel hogere gevoeligheid en dus een hogere resolutie van de afbeeldingen: *magnetic resonance force microscopy* (MRFM). We gaan nu MRFM uitleggen via de analogie met MRI.

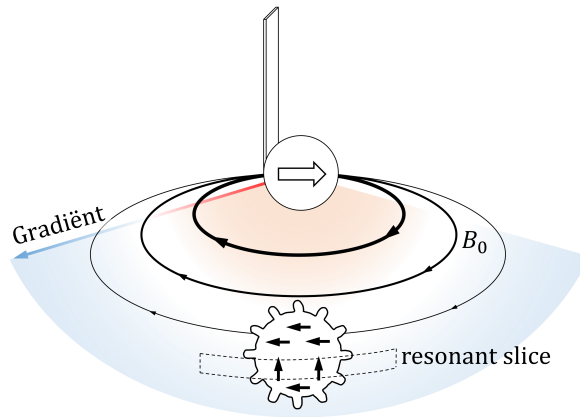


Versimpelde weergave van een MRI scanner. Een extern magnetisch veld (B_0) wordt gebruikt voor het polariseren van de spins in het monster, en een lineaire magnetische veld gradiënt wordt gebruikt om een platte *resonant slice* te definiëren.

MAGNETIC RESONANCE IMAGING: VAN MILLIMETERS...

Een MRI apparaat heeft drie cruciale componenten: een elektromagneet die gebruikt wordt voor het maken van een sterk, homogeen (overal gelijk) magnetisch veld (ook wel het B_0 veld genoemd), spoelen voor het aanleggen van een magnetische veld gradiënt (een verloop in de sterkte van het magnetisch veld in het monster), en een extra spoel om magnetische pulsen te sturen en signalen op te vangen. Om signaal te krijgen, maakt MRI gebruik van het feit dat bepaalde atoomkernen zich gedragen als een magneetje. Deze atoom-magneetjes worden ook wel *spins* genoemd. Wanneer deze spins in een magnetisch veld worden geplaatst, richten ze zich zo dat ze parallel aan het magnetisch veld komen te liggen. Het verschil tussen het aantal spins dat met het veld mee wijst en het aantal dat ertegenin wijst hangt af van de sterkte van het veld en de temperatuur, en wordt de *polarisatie* genoemd.

Een tweede bijzondere eigenschap van de spins is dat ze zich gedragen als kleine tolletjes: ze draaien rond het magnetisch veld, net zoals een tol die niet precies verticaal staat ook gaat draaien in het zwaartekrachtsveld. De frequentie waarmee ze draaien hangt af van de sterkte van het veld: hoe groter het veld, hoe sneller ze draaien. Wanneer we nu een magnetische puls sturen met een frequentie die precies overeenkomt met de frequentie waarmee de spins draaien, kunnen we de richting van de spin in het magnetisch veld veranderen. Deze verandering van de richting kan vervolgens worden gemeten met een van de detectiespoelen.



Versimpelde weergave van onze MRFM opstelling. Een klein magnetisch deeltje wordt tegelijkertijd gebruikt voor het maken van het magnetische veld B_0 en de gradiënt. Hierdoor ontstaat een dunne *resonant slice* in de vorm van een bolschil.

In een homogeen magnetisch veld worden alle spins beïnvloed door de magnetische puls, en kan dus niet gezegd worden waar de spins zich precies bevinden in het monster. Door het toevoegen van de veld gradiënt is dit wel mogelijk: spins op verschillende plekken voelen nu een net ander magnetisch veld, en draaien daardoor met een andere frequentie. De magnetische puls heeft nu dus alleen effect op een klein deel van het monster waar de frequentie van de puls overeenkomt met die van de spins. Het overeenkomen van de frequenties heet resonantie, en deze plek noemen we daarom de *resonant slice*. Door het kiezen van de frequentie van de magnetische puls, en met wat slim rekenwerk, is het nu dus ineens mogelijk om uit te vinden waar in het monster de spins precies zitten, en kan zo een drie-dimensionale afbeelding worden gevormd.

Het grote nadeel van MRI is echter de beperkte gevoeligheid. Om uiteenlopende redenen heeft een moderne MRI machine een resolutie die beperkt is tot ongeveer een tiende millimeter, ordes van grootte te laag voor onderzoek naar eiwitten en andere microstructuren.

...NAAR NANOMETERS: MRFM

Om de resolutie dusdanig te verbeteren dat het opvangen van signalen van veel kleinere monsters, zoals bijvoorbeeld eiwitten, mogelijk wordt, is MRFM bedacht. Het idee hierachter is dat MRFM de natuurkunde van MRI combineert met de technieken van

scanning probe microscopy (SPM), waarin kleine naaldjes gebruikt worden om een oppervlak te onderzoeken met extreem hoge resolutie. Een MRFM gebruikt daarom een hele slappe hefboom (een soort duikplankje dat verticaal staat) met aan het eind een klein magneetje. Dit magneetje zorgt voor zowel het B_0 veld als de gradiënt die het mogelijk maakt om spins op verschillende plekken te kunnen manipuleren. Door de microscopische afmetingen van het magneetje is de gradiënt extreem groot (ongeveer een miljoen keer sterker dan de gradiënt van MRI), waardoor we een hele smalle *resonant slice* krijgen, en dus een hele hoge resolutie. Door het magneetje te bewegen over het monster (scannen) kan het hele monster in kaart worden gebracht.

De signalen van de spins worden nu niet meer gemeten met een spoel, wat erg ongevoelig is, maar in plaats daarvan meten we direct de kracht die de spins in het monster uitoefenen op het magneetje (vandaar de term *force* in de naam). Deze krachten zijn extreem klein (ongeveer 10^{-20} Newton voor een waterstofatoom). Daarom zit het magneetje vast aan de hele gevoelige hefboom. De krachten zorgen voor een beweging van deze hefboom. Door de spins in het monster met magnetische pulsen meerdere keren om te draaien precies synchroon met de natuurlijke beweging van de hefboom, kan de uitwijking extra versterkt worden, en is het mogelijk deze kleine krachten te meten.

In **hoofdstuk 1** van dit proefschrift bespreken we kort de geschiedenis van de ontwikkeling van MRFM, en gaan we in detail in op de verschillende manieren waarop de gevoeligheid van de techniek verbeterd kan worden. Een van de methodes om dit te doen is het vergroten van de gradiënt van het magnetisch veld, bijvoorbeeld door nog kleinere magneetjes te gebruiken. Dit hebben wij proberen te doen door het maken van een nieuwe hefboom die magneten met verschillende afmetingen gebruikt, zoals beschreven in **hoofdstuk 8**. Echter, de focus van het Oosterkamp lab ligt op het verbeteren van de gevoeligheid door te meten bij extreem lage temperaturen.

EEN HONDERSTE GRAAD BOVEN HET ABSOLUTE NULPUNT

Het meten bij lagere temperaturen heeft een aantal voordelen. Zo zorgt het bijvoorbeeld voor een hogere *polarisatie* van de spins in het monster, wat bij bepaalde types MRFM metingen zorgt voor een sterker signaal (en dus de mogelijkheid om een kleiner volume met spins te detecteren). Daarnaast bieden lagere temperaturen de mogelijkheid om experimenten te doen waar het niet gaat om het afbeelden van een monster, maar juist om het onderzoeken van de natuurkundige eigenschappen. Veel materialen tonen deze exotische eigenschappen pas bij hele lage temperaturen.

Wij proberen onze metingen daarom te doen bij 10 mK, dus 1/100ste graad boven het absolute nulpunt. Onze groep doet daarmee de koudste MRFM experimenten ter wereld. Het meten bij deze temperaturen brengt een aantal problemen met zich mee, waarvan wij er in dit proefschrift een aantal hebben proberen op te lossen:

UITDAGING 1: HET UITLEZEN VAN DE BEWEGING VAN DE HEFBOOM. Dit wordt in andere MRFM opstellingen gedaan door een laser te laten weerspiegelen op het oppervlak van de hefboom, en te kijken naar het gereflecteerde licht. Echter, het gebruik van een laser zou bij onze lage temperaturen voor te veel opwarming zorgen. In plaats daarvan meten wij daarom de beweging door met een *Superconducting Quantum Interference Device* (SQUID) het magnetisch veld dat van het magneetje afkomt te meten. De SQUID is een extreem gevoelige magneetveld sensor die werkt met zulke lage vermogens dat dit niet tot extra opwarming leidt. Details over hoe we dit precies doen en de rest van de opstelling worden besproken in **hoofdstuk 2**.

UITDAGING 2: HET KRIJGEN VAN EEN KOUDE EN STILLE HEFBOOM. We willen onze hefboom in beweging krijgen door de interactie met de spins in het monster. Echter, de hefboom wordt ook in beweging gebracht door de trillingen die gemaakt worden door onze koelmachine en door trillingen die van buiten komen. Deze extra beweging van de hefboom verdoezelt het signaal dat wij willen meten. Om trillingen te dempen wordt vaak gewerkt met systemen waarin het experiment wordt opgehangen aan een massa en een veer. Het probleem van deze massa-veer vibratie-isolatie systemen is dat deze vaak een slechte warmtegeleiding hebben, en dat hierdoor de MRFM niet meer zo koud wordt als wij hem zouden willen hebben. In **hoofdstuk 3** beschrijven wij het massa-veer systeem dat wij speciaal ontwikkeld hebben om deze conflicterende eigenschappen zo goed mogelijk te combineren.

UITDAGING 3: HET ONDERSCHIEDEN VAN SIGNAAL EN OVERSPRAAK. Omdat wij zijn overgestapt naar een magnetische manier van het uitlezen van de beweging van de hefboom, zijn we een stuk gevoeliger geworden voor overspraak tussen onze detectie en onze bron van magnetische pulsen. De manier waarop wij dit probleem hebben opgelost staat beschreven in **hoofdstuk 6**. We doen dit door een techniek te gebruiken die erg lijkt op hoe noise-cancelling koptelefoons werken. Door de toevoeging van een klein extra circuit kunnen we de magnetische pulsen die we sturen direct opheffen voordat ze in onze SQUID terechtkomen. Hierdoor wordt het mogelijk om de superkleine signalen te blijven meten tijdens pulsen, iets wat absoluut noodzakelijk is voor veel van de protocollen in MRFM.

UITDAGING 4: HET MAKEN VAN DE MAGNETISCHE PULSEN ZONDER OPWARMING. Wij maken onze magnetische pulsen met een *radio-frequency* (RF) draad gemaakt van een supergeleider (een materiaal zonder elektrische weerstand). Wanneer we magnetische pulsen maken, meten we toch een toename van de temperatuur van de MRFM opstelling, wat erop duidt dat de RF draad warmte creëert (ook wel *dissipatie* genoemd) ondanks het feit dat de draad supergeleidend is. In **hoofdstuk 7** hebben we de dissipatie van onze RF draad gemeten, en bespreken we mogelijke oorzaken hiervan. We doen enkele suggesties hoe de dissipatie verminderd zou kunnen worden, maar helaas hebben we vooralsnog geen oplossing kunnen vinden. Wij beschouwen dit op dit moment als het grootste open probleem van MRFM bij lage temperaturen.

TOEPASSING VAN SQUID-GEDETECTEERDE MRFM

In dit proefschrift hebben we ons gefocust op het verbeteren van de SQUID-gedetecteerde MRFM opstelling. Hoewel deze verbeteringen bijdragen aan het succesvol afbeelden van biologische samples, hebben wij vooral gekeken naar materialen die interessant zijn vanuit een natuurkundig oogpunt.

In **hoofdstuk 4** beschrijven wij een nieuw experiment op koper. In dit experiment hebben we de *polarisatie* van de kernspins van koper in een heel klein deel van het koper helemaal verwijderd met een magnetische puls. Het verwijderen van de polarisatie leidt tot een verschuiving van de resonantiefrequentie van onze hefboom. Door te meten hoeveel deze frequentie verschuift en hoe lang het duurt voordat de frequentie na het uitzetten van de puls weer terug is op de oorspronkelijke waarde kunnen we bepaalde eigenschappen van het koper achterhalen. We hebben gebruik gemaakt van een combinatie van een nauwkeurigere theorie over het gedrag van de spins van de koperatomen tijdens een magnetische puls en de vele technische verbeteringen. Hierdoor zijn we in staat geweest experimenten te doen met een gevoeligheid die ongeveer 100 keer hoger is dan eerdere experimenten uit onze groep met een fractie van de dissipatie. Metingen bij lagere temperaturen en aan kleinere monsters zijn hierdoor mogelijk.

We hebben een hele andere aanpak gebruikt in **hoofdstuk 5**, waar we zonder gebruik te maken van magnetische pulsen de elektronenspins in en op diamant bestuderen. Door het magneetje vlak boven de diamant te hangen en onder verschillende omstandigheden de mechanische eigenschappen van de hefboom te meten is het mogelijk om de dichtheid van de spins in en op het diamant te bepalen. De mogelijkheid om dit te meten kan van grote waarde zijn, zoals we in de volgende sectie zullen

bespreken. Verder is het mogelijk om de relaxatietijd van de spins te meten, een indicatie voor de mate waarin de spins wisselwerken. Hieruit hebben we gevonden dat we de spins op het oppervlak van het diamant van elkaar kunnen isoleren door de hoge gradiënt van het magnetisch veld in de buurt van ons magneetje. Dit zou een methode kunnen zijn om de gevoeligheid van op diamant gebaseerde sensoren te verbeteren.

DE TOEKOMST: DE EASY-MRFM

Het is ondertussen duidelijk dat MRFM een gecompliceerde techniek is waarvoor veel componenten op hetzelfde moment moeten werken. Metingen op willekeurige monsters zijn ingewikkeld, omdat wij, vanwege onze detectiemethode gebaseerd op een SQUID, altijd structuren moeten aanbrengen op het monster, of het monster moeten plaatsen op speciaal ontwikkelde chips. Vanwege deze complexiteit is MRFM op lage temperaturen geen algemeen gebruikte techniek. In **hoofdstuk 9** bespreken wij onze poging om dit te veranderen door middel van de ontwikkeling van de zogenaamde Easy-MRFM. Dit is een versimpelde uitvoering van de volledige MRFM opstelling, waarin het monster volledig gescheiden is van alle cruciale MRFM componenten.

Met een eerste prototype van de Easy-MRFM hebben we laten zien dat de methode in principe werkt. Er wordt ondertussen gewerkt aan een verbeterde versie. Wanneer de Easy-MRFM volledig functioneel is, zou deze vaker gebruikt kunnen worden door vele onderzoeksgroepen, en bijvoorbeeld een bijdrage kunnen leveren aan het verbeteren van de prestaties van *qubits*, de bouwstenen van de kwantumcomputer.

CURRICULUM VITAE

Martin de Wit

Born on 19 January 1991 in Katwijk aan Zee (the Netherlands)

Education

2003 - 2009 HIGH SCHOOL,
Het Rijnlands Lyceum, Oegstgeest.

2009 - 2012 BSc. IN PHYSICS,
Leiden University, Leiden.

Final Project: The Lead Zeppelin Project: Development and testing of a force sensor, intended for MRFM, using magnetic levitation. (Supervision by Prof. dr. ir. T. H. Oosterkamp).

2012 - 2014 MSc. IN EXPERIMENTAL PHYSICS,
Leiden University, Leiden.

Project 1: On slippery ground: The search for superlubricity in macroscopic samples and the exploration of graphene as a friction lowering coating. (Supervision by Prof. dr. J.W.M. Frenken).

Project 2: Bismuth as topological insulator: Obtaining experimental evidence of the Quantum Spin Hall State in a bilayer of bismuth. (Supervision by Prof. dr. ir. S.J. van der Molen and Prof. dr. J.M. van Ruitenbeek).

2014 - 2019 PhD RESEARCH IN PHYSICS,
Leiden University, Leiden.

LIST OF PUBLICATIONS

PEER-REVIEWED PUBLICATIONS

- **M. de Wit**, G. Welker, J.J.T. Wagenaar, F.G. Hoekstra, & T.H. Oosterkamp. Feasibility of Imaging in Nuclear Magnetic Resonance Force Microscopy using Boltzmann polarization. *Journal of Applied Physics* **125**, 083901 (2019).
- **M. de Wit***, G. Welker*, K. Heeck, F.M. Buters, H.J. Eerkens, G. Koning, H. van der Meer, D. Bouwmeester, & T.H. Oosterkamp. Vibration isolation with high thermal conductance for a cryogen-free dilution refrigerator. *Review of Scientific Instruments* **90**, 015112 (2019).
- **M. de Wit**, G. Welker, F.G. Hoekstra, & T.H. Oosterkamp. Flux compensation for SQUID-detected Magnetic Resonance Force Microscopy. *Cryogenics* **98**, 67-70 (2019).
- **M. de Wit***, G. Welker*, J.M. de Voogd, & T.H. Oosterkamp. Density and T_1 of Surface and Bulk Spins in Diamond in High Magnetic Field Gradients. *Physical Review Applied* **10**, 064045 (2018).
- J.J.T. Wagenaar, A.M.J. den Haan, R.J. Donkersloot, F. Marsman, **M. de Wit**, L. Bossoni, & T.H. Oosterkamp. Mechanical Generation of Radio-Frequency Fields in Nuclear-Magnetic-Resonance Force Microscopy. *Physical Review Applied* **7**, 024019 (2017).
- J.J.T. Wagenaar, A.M.J. den Haan, J.M. de Voogd, L. Bossoni, T.A. de Jong, **M. de Wit**, K.M. Bastiaans, D.J. Thoen, A. Endo, T.M. Klapwijk, J. Zaanen, & T.H. Oosterkamp. Probing the Nuclear Spin-Lattice Relaxation Time at the Nanoscale. *Physical Review Applied* **6**, 014007 (2016).

* These authors contributed equally.

MISCELLANEOUS

- T.H. Oosterkamp, M. Beker, E. Hooijkamp, **M. de Wit**, G. Welker, D. van der Zalm, & G. Akkermans. Good Vibrations near Absolute Zero. *Mikroniek* **6**, 48-51 (2016).

IN PREPARATION

- G. Welker*, **M. de Wit***, T. Benschop, L. Bossoni, J. Mydosh, T. Prokscha, & T.H. Oosterkamp. Dilute spin densities on iron-doped palladium probed with Muon Spin Rotation, SQUID magnetometry and ultrasensitive Magnetic Force Microscopy. *In preparation*.

* These authors contributed equally.

ACKNOWLEDGEMENTS

I cannot say that the last four years have always been easy, but I can say for sure that I've never regretted starting this adventure. For a huge part, this is so because of the help and support I've had of the people around me. I will now try to acknowledge these people, hoping I won't forget too many.

First and foremost, I want to express my gratitude to my supervisor Tjerk Oosterkamp. You are truly one of the most interesting people I know. Your enthusiasm and grand vision is inspiring, and even though I will never admit this again, I actually like it when you're goofing around. Most of all I've enjoyed disagreeing with you on many subjects, even though more often than not, I had to admit my defeat after a few weeks (or sometimes months), loudly complaining how annoying it is that you always turn out to be right. I like to believe that in these last couple of months, I've been right once or twice as well.

I also want to thank my present and former group members: Jelmer, Marc, Arthur, Gesa, Tom, Bob, Lucia, Freek, and Olaf. You all had a big part in the great couple of years I've had in the lab, even when the results were meager. I still consider our trip to Iceland, Canada, and the USA as some of the best weeks of my life so far. I've also been lucky to be able to supervise several BSc and MSc students: Marnix, Guido, Joris, Daniel and Martijn. I know your projects didn't always go the way we had planned, but at least I hope that I've taught you to never give up and keep trying.

One of the more complicated aspects of working in a niche group like ours is that you have to be a jack of all trades. And as the saying goes, this means you are a master of none. For this reason, I've relied on a great number of people to help me, in a large variety of different fields.

Let's start with acknowledging the unsung heroes of the FMD and ELD, without whom this entire thesis would not exist, since I'm a poor theoretician, and it is very difficult to do experiments on an imaginary setup: Gert Koning, Merlijn Camp, Fred Schenkel, Dian van der Zalm, Harmen van der Meer, Ko Koning, Bert Crama, Peter van Veldhuizen, and all the others that have saved my ass every time I needed something at the last minute. At some point during my PhD I think I've spend more time in the workshop than in the lab, and I've always felt welcome. Additionally,

I would like to acknowledge Wilfred van der Geest for making sure we've had a seemingly endless supply of cryogenic liquids. For always being kind enough to help us magnetize our cantilever magnets, I want to thank Peter Gast and Mykhailo Azarkh.

A special place in this list is reserved for Kier Heeck. You have advised me about pretty much any electrical component in the setup, and played a pivotal role in the realization of the vibration isolation. On mornings where I decided to go to work early and you were already there, not much work was done, but the stories were more than worth it.

A particularly alien environment to me was the cleanroom, in which I would not have survived (probably literally) without the advice and assistance of many people. From Leiden: Amrita Singh, Marcel Hesselberth, Anne France Beker, and Douwe Scholma. From the TU Delft: Marco van der Krogt, Marc Zuiddam, Charles de Boer, Hozanna Miro, Eugene Straver, Anja van Langen-Suurling, and all the others that kept stuff working behind the scenes. Special thanks go out to Sal Bosman and David Thoen, who have been invaluable in the fabrication of our detection chips, crucial for the MRFM experiments.

However, none of the above fields is as complicated as the bureaucracy at Leiden University. Therefore, it cannot be understated how important Ellie van Rijsewijk has been for me. I'm ashamed to admit that I still don't know your phone-number by heart, even though I have called you so often to "Ask Ellie" about pretty much anything.

Now on to the people that made sure my PhD was never boring, both in and out of the lab. My close friends: Koen, Maarten, EJ, Oliver, Freek, Nigel, Tommie, and Jelmer (again). My former supervisors: Sense Jan van der Molen, Jan van Ruitenbeek, Joost Frenken, Johannes and Carlos, Geert, Andrea and Sasha, and Pavel and Dirk. And don't forget the other dwellers of the measurement hall and the floors above it: Tobias, Frank, Hedwig, Irene, Doohee, Wolfgang, Tjerk B, Vera, Kim, Mahesh, Sabine, Vincent, Willem, Daniël, Sumit, Remko, Kaveh, Daan, Jaap, Marcel Rost, Sander, Vitaly, Damianos, Luigi, Nikita, Milan, Federica, and many others.

I want to thank my parents, Henk and Trijnie, and my brother Henk Jr, for all the love and support you've given me my entire life, and for giving me the freedom to follow my own path.

Finally, Esther, thank you for all of your love. We've been together from the first day I've started studying physics, and you've always been there for me. I love you very much, and I hope that these last 9 years are only the beginning for us.